Noble metal catalysts for methane steam reforming

Jakobsen, Jon Geest

Publication date:
2010

Ph.D. Thesis

Noble metal catalysts for methane steam reforming

Jon Geest Jakobsen

May 2010

Center for Individual Nanoparticle Functionality

Department of Physics

Technical University of Denmark

Preface

This thesis is submitted in candidacy of the Ph.D. degree from the Technical University of Denmark (DTU). It represents results obtained during my work at the R&D division, Haldor Topsøe A/S and the Center for Individual Nanoparticle Functionality (CINF), Department of Physics, Technical University of Denmark. The work has been carried out from August 2006 to May 2010 under the supervision of Professor Ib Chorkendorff from CINF, DTU and Jens Sehested and Esben L. Sørensen, Haldor Topsøe. Within this period of time I was employed as a research fellow at Haldor Topsøe from December 2006 to June 2006. Financial support was provided by Haldor Topsøe A/S and the Danish Agency for Science, Technology and Innovation through the industrial Ph.D. fellowship Program.

The results obtained during my Ph.D. period have resulted in a number of international publications (see list of publications). The focus of the project has been on understanding industrial noble metal catalysts for methane steam reforming.

For many fruitful discussions during my Ph.D., I would especially like to thank my supervisors Jens Sehested and Ib Chorkendorff for excellent supervision.

Initially, I had great collaboration with Glenn Jones, CAMD, DTU in the group of Jens Nørskov on matching theoretical and experimental results. For the kinetic studies I have enjoyed working with two students, Martin Jakobsen and Tommy Jørgensen, in their pursuit of Bachelor and Master degree, respectively. This lead to good discussions on the kinetics of ruthenium and rhodium catalysts.

I would like to thank all my colleagues at Haldor Topsøe for creating an enjoyable working environment and for contributing to this project in a variety of ways. Especially, I would like to thank my project managers, Esben L. Sørensen and Niklas Jakobsson, for making my project relevant in ongoing industrial research. I thank Stig Helveg for assisting in all the microscopy work. And I would like to thank a dedicated group of technicians, Ulla Ebert, Michael Lehrmann, Mette Rosén, Henning Kosack and John Hartvig for helping me with synthesizing and test facilities in many out of normal experiments.

Abstract

This thesis contains experimental investigations of the methane steam reforming reaction on noble metal catalysts. These investigations are of great importance in connection with the conversion of natural gas to synthesis gas for the end production of liquid fuels such as diesel or methanol. Classic steam reforming catalysts are nickel based catalyst, but for certain low steam operating conditions, nickel catalyst are not suitable as it will form carbon that can deactivate the catalyst. Noble metals such as Ru, Rh, Ir, Pt and Pd are candidates for replacing nickel as they do not form carbon under similar conditions.

Characterization work by chemisorption and transmission electron microscopy (TEM) have been conducted on these catalysts. Sulphur chemisorption is found to be a tool for characterization of the metal surface area on the catalyst. TEM investigations of ruthenium based catalysts have shown that small metal particles (2-4 nm) form surface oxide and for proper TEM characterization, environmental TEM investigations in H_2 at elevated temperatures proves to be necessary. The steam reforming catalysts deactivates at an intermediate temperature range, which complicates measuring consistent rates. A long term treatment is implemented for reactivate the catalysts to eliminate the implications of this phenomenon.

Studies on the activity have shown that the order in turn-over frequency rates for the metals is Ru~Rh>Ni~Ir~Pt~Pd, which is supported by theoretical calculations. Investigations into improving long-term stability in the activity has shown that it might be possible to promote an active metal with a high surface energy promoter element. This have been investigated for a series of Ru, Rh, Ir and Pt catalysts with promoter atoms such as Mo, Re and W. There are theoretical and experimental indications of more sintering stable catalysts, but no conclusive results have been obtained.

Kinetic modelling and experimental studies have shown that the key elementary step for the reaction is the methane dissociative adsorption, but also that the activity is lowered by product inhibition of CO and H on the Ru, Rh and Ir catalysts. Kinetic models have been developed at atmospheric pressure for Ru and Rh describing this product inhibition.

Resumé

Denne afhandling omhandler *methane steam reforming* reaktionen på ædelmetal katalysatorer. Denne reaktion er vigtig i forbindelse med omdannelse af naturgas til flydende brændstoffer som diesel og træsprit. Traditionelt bruges der nikkel katalysatorer, men for specifikke eksperimentelle betingelser med et lavt dampindhold vil nikkel danne kul, som kan deaktivere katalysatoren. Ru, Rh, Ir, Pt og Pd er mulige ædelmetaller som kan erstatte en nikkel katalysator, da de ikke vil danne kul under lignende betingelser.

Adsorption målinger og *transmission electron microscopy* (TEM) undersøgelser har været brugt til karakterisering af ædelmetalkatalysatorerne. Det er blevet vist at svovladsorption er en brugbar teknik til at bestemme det aktive metal overflade areal på katalysatoren. TEM undersøgelser af små metalpartikler (2-4 nm) har vist at der dannes et overfladeoxidlag og undersøgelser er nødvendige at lave *in situ* i brint og ved højere temperaturer. *Steam reforming* katalysatorerne kan deaktivere i et temperaturområde omkring 550-650°C, som derved komplicerede det at opnå konsistente resultater. Der er implementeret en behandling ved høj temperatur og i reaktantgas for at formindske dette fænomen.

Aktivitetsstudier har vist at aktiviteten pr. overfladeatom for disse ædelmetaller er givet ved følgende rækkefølge Ru~Rh>Ni~Ir~Pt~Pd. Langtidsstabiliteten af katalysatoraktiviteten er forbedret ved at tilsætte et grundstof med høj overfladeenergi til et aktivt katalysatormetal, og derved kunne sænke sintringshastigheden. Dette er undersøgt for Ru, Rh, Ir og Pt som det aktive metal og med bl.a. Mo, Re og W som et promoteratom. Både teoretiske og eksperimentelle indikationer viser at der er mere sintringsstabilitet, men der er dog ikke opnået endelige beviser for fuldt ud at understøtte dette.

Kinetik modellering og eksperimentelle studier har vist at metan spaltning er den vigtigste elementærreaktion for *methane steam reforming* reaktionen. Produkt inhibition af CO og H sænker aktiviteten for både Ru, Rh og Ir. Kinetik modeller er udviklet ved atmosfærisk tryk for både Ru og Rh.

List of Included Papers

Paper I

First principles calculations and experimental insight into methane steam reforming over transition metal catalysts

G. Jones, J.G. Jakobsen, S.S. Shim, J. Kleis, M.P. Andersson, J. Rossmeisl, F. Abild-Pedersen, T. Bligaard, S. Helveg, B. Hinnemann, J.R. Rostrup-Nielsen, I. Chorkendorff, J. Sehested and J.K. Nørskov

Journal of Catalysis **259(1)** (2008) 147-160

Paper II

Steam and CO_2 reforming of methane over a Ru/ZrO_2 catalyst

J.G. Jakobsen, T.L. Jørgensen, I. Chorkendorff and J. Sehested

Applied Catalysis A – General **377** (2010) 158-166

Paper III

Methane steam reforming kinetics for a rhodium-based catalyst

J.G. Jakobsen, M. Jakobsen, I. Chorkendorff, J. Sehested

Catalysis letters, **submitted** (2010)

Other Publications

Experimental Measurements and Kinetic Modeling of CH_4/O_2 and $CH_4/C_2H_6/O_2$ Conversion at High Pressure

C.L. Rasmussen, J.G. Jakobsen, P. Glarborg

International Journal of Chemical Kinetics **40 (12)** (2008) 778-807

Business Report

Business report on innovation and the Ph.D. project in Haldor Topsøe's innovation strategy

J.G. Jakobsen

Danish Agency for Science, Technology and Innovation and Copenhagen Business School, June 2008

Contents

1. Introduction

Synthesis gas (syngas) is a key intermediate in the chemical industry compromised by a mixture of hydrogen, carbon monoxide and carbon dioxide. Steam reforming of hydrocarbons is the primary way of producing hydrogen and carbon monoxide on an industrial scale. Synthesis gas is used in a series of industrial applications for highly selective synthesis of chemicals and fuels, whereas pure hydrogen is used in the production of ammonia and in refineries for hydro treating and hydro cracking.

The hydrocarbon source can vary from natural gas to heavier oil products. The possible chemistry is reduced to a C_1 chemistry by the steam reforming reaction, hence obviously destroying functional groups, but providing great flexibility for producing chemical products. Fig. 1 shows the possibilities of the synthesis gas cycle. Gasification of coal is a way to produce synthesis gas directly from a solid based hydrocarbon [1], although steam reforming and water gas shift (WGS) is often needed to obtain the desired synthesis gas mixture. Steam reforming and auto thermal reforming (ATR) are the preferred ways of producing synthesis gas from light hydrocarbon sources on an industrial scale due to economical advantages [2].

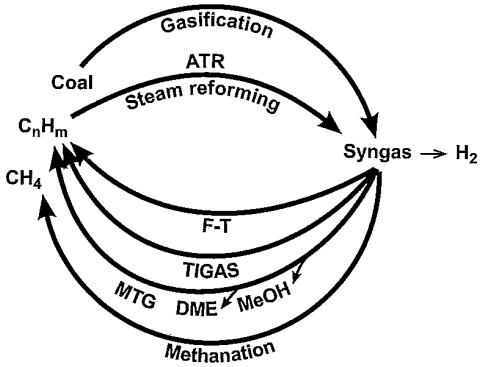

Figure 1. The synthesis gas cycle; from hydrocarbon through synthesis gas and back to a hydrocarbon [2].

From synthesis gas it is possible to form long chain hydrocarbons by the Fischer-Tropsch reaction [3], thereby providing a heavy hydrocarbon product stream ideal for diesel production. From the synthesis gas, it is also possible to form methanol [4], gasoline [5] or substituted natural gas (SNG) [6]. Direct routes from lower hydrocarbons such as natural gas to liquid fuels such as methanol or gasoline are very interesting, because the natural gas often is available in remote areas. This gas is present at locations without any connection to a natural gas distribution grid. Hence, forming liquid energy products, the transportation and distribution of the energy becomes economically feasible. A

competitive alternative for transporting natural gas is liquefied natural gas (LNG), which essentially cools the gas for naval transportation.

The natural gas is largely constituted by methane, and due to the high C-H bond energy of 439 kJ/mol for methane, it is difficult to directly form products with lower C-H bond energy directly without complete oxidation. Thus the synthesis gas production is an efficient intermediate utilising low value hydrocarbon carbon sources for upgrading to higher value hydrocarbon products. The steam reforming reaction is the reaction between a hydrocarbon and steam, here described by reaction of methane and steam

$$CH_4(g) + H_2O(g) \rightleftharpoons CO(g) + 3H_2(g) \qquad -\Delta H^{\circ}_{298} = -206\,kJ/mol \qquad (1)$$

The minor amounts of higher hydrocarbons in a natural gas feed are often processed in a pre-reformer at low temperature (400-500°C). The reactivity of these higher hydrocarbons is much higher than methane, due to lower C-C bond energies compared to C-H bond energies. The focus of this thesis is the conversion of methane to synthesis gas by steam reforming at conditions relevant for conversion of natural gas to liquid fuels. The water gas shift reaction runs in parallel with the steam reforming reaction

$$CO(g) + H_2O(g) \rightleftharpoons CO_2(g) + H_2(g) \qquad -\Delta H^{\circ}_{298} = 41\,kJ/mol \qquad (2)$$

The water gas shift reactivity is generally considered faster than the steam reforming reaction, an aspect that will be reviewed later. Thus, the synthesis gas of H_2, CO and CO_2 is produced by steam reforming and water gas shift. These two reactions serve as the basis for the subsequent discussion on methane steam reforming. In order to obtain sufficiently high reaction rates the steam reforming reaction has to be catalysed. Traditionally, the preferred metal for the steam reforming reaction has been a nickel based catalyst. This is due to the high activity and low cost for nickel. Alternatively, oxygen can be the oxidising agent and the reaction can proceed by the ATR reaction, at under-stoichiometric reaction conditions

$$CH_4(g) + \frac{1}{2}O_2(g) \rightleftharpoons CO(g) + 2H_2O(g) \qquad -\Delta H^{\circ}_{298} = 520\,kJ/mol \qquad (3)$$

Here the hydrocarbon is basically lean burned followed by a catalyst bed to equilibrate the gas stream by steam reforming and the water gas shift reaction.

1.1. Technology

There are several other possible ways for converting light hydrocarbons to synthesis gas. Catalytic partial oxidation (CPO) is another technique widely used [7] where the reaction between methane and oxygen is catalysed. Since the reaction takes place on a catalyst, there is no burning flame such as in ATR, hence obtaining a much lower reaction temperature in the catalyst bed. There are several medium scale industrial applications based on the use of CPO. The CPO technology provides an advantage with respect to the experimental equipment used, and furthermore it is a very versatile technology and can be used for many types of hydrocarbon fuels. However, due to the oxygen cost combined with expensive noble metal catalysts, it becomes expensive upon up-scaling.

Autothermal reformer technology (ATR) is a burner technology, where oxygen or air is mixed with a hydrocarbon feed through a nozzle making a flame. Below the flame a nickel based catalyst bed to adiabatically equilibrate the gas afterwards. This produces a mixture of CO, CO_2, CH_4, H_2O and H_2. The entry temperature to the catalyst bed is in the order of 1200-1300°C, providing the heat for the adiabatic reaction. The gas is equilibrated at the outlet at 900-1100°C and pressures up to 100 bar. Due to the high reactor temperatures, the process will run at low steam to carbon ratios (S/C) as low as 0.6 with no soot formation. It is not possible to run at lower S/C ratios due to whisker carbon formation. The steam to carbon ratio is a good measurement of the inlet conditions for the mixture of steam and carbon. It often covers the oxygen to carbon ratio as well, so it becomes slightly artificial when the oxidant is oxygen rather than steam. The steam to carbon ratio also gives simple information on the severity of the experiment for unwanted carbon formation.

The classical tubular reformer type for the steam reforming reaction is a multi tube reactor design with hundreds of 10-15 m long tubes aligned with side fired heaters. The tubes are 10-15 cm in diameter and filled with nickel catalyst pellets. Typically, the gas mixture consists of pre-reformed natural gas and steam that enters the reactor at 450-650°C and will exit at 800-950°C. The high exit temperature is necessary to obtain a high conversion. The mixed gas at the inlet is processed through a desulphurization unit and a prereforming unit to remove sulphur and higher hydrocarbons. If not removed, the higher hydrocarbons would crack at the inlet of the tubular reformer.

For gas to liquid (GTL) systems it has been shown to be advantageous using a two step solution of tubular reformer tube combined with ATR [8]. The high temperature ATR exist gas is heat exchanged with the inlet tubular reformer gas, increasing the overall energy efficiency. By combining these two reactors it is possible to obtain a solution close to the optimal for Fischer-Tropsch downstream process [8]. Energy optimization of this process proves that it is an advantage to run steam reformer operations in the low steam to carbon (S/C) ratio regime [8].

The combination of these two reactor setups gives new challenges to the steam reforming system. For the reaction to be economically feasible it is necessary to run the operation at conditions where the nickel catalyst cannot operate. At low S/C ratios the nickel catalyst will start forming carbon, due to the favourable thermodynamics for graphite formation [8]. Eventually this will destroy the catalyst and regeneration is not possible. To expand the limits downwards for the S/C ratio in methane steam reforming, it has been shown that noble metal catalysts can operate without carbon formation both at low S/C ratios and at conditions, where nickel is normally used [9]. Even though there is a thermodynamically driving force for graphite formation, the growth sites will form whisker carbon instead, which has a higher energy barrier. Thus, the whisker carbon formation therefore has an even higher energy barrier on noble metals compared to nickel. This emphasize the importance of understanding noble metal catalysts for the methane steam reforming. The scope of this two step synthesis gas application is rather limited at present, but with dwindling oil resources and relatively cheap sources of natural gas, this technology is likely to blossom in the future.

The steam reforming and the water gas shift reaction are governing the overall process. Thermodynamically, steam reforming should be conducted at low pressure, high temperatures and a high S/C ratio to ensure high methane conversion. The low pressure is due to more products forming than reactants in the steam reforming reaction (Eq. 1) and the endothermic steam reforming reaction is favoured by high temperature. The listed conditions are not all feasible for industrial applications where it is necessary to focus on a high output. The high temperature is obtainable to some extend and it is usually possible to reach outlet temperatures of 800-1000°C. Even though it is thermodynamically favourable to run at low pressures, it turns out economically unfavourable. The plant size would have to be huge and therefore pressures are set at 20-40 bar to ensure a high throughput. Furthermore, it can be necessary to have a low S/C ratio for the desired synthesis gas composition as described previously.

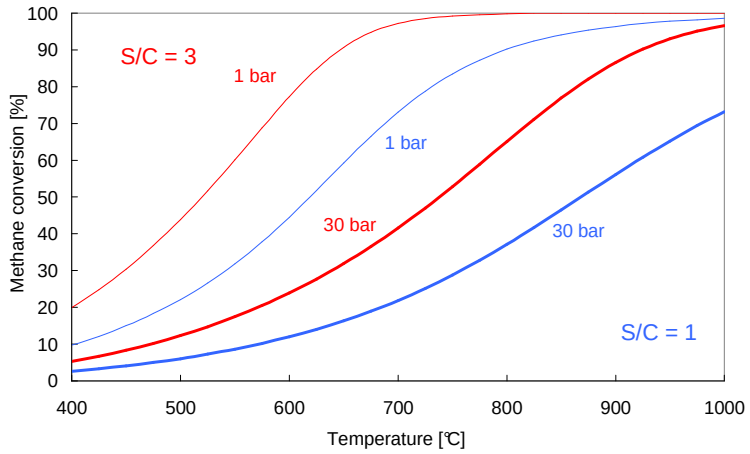

Figure 2. Thermodynamics for methane and steam reforming mixtures at S/C~1 or 3 and 1 or 30 bar total pressure as a function of temperature incl. equilibrium of the WGS reaction.

Fig. 2 shows equilibrium methane conversions for the steam reforming system. Traditionally, many hydrogen producing plants are running at S/C ratios of 2.5-4, a 20-30 bar total pressure, and an exit temperature of approximately 950°C. This yields near 100% conversion thermodynamically as seen by Fig. 2. The GTL application is running at S/C>1, a 20-40 bar total pressure and exit temperatures of 700-800°C, which yields completely different equilibrium conversions as also seen on Fig. 2. In the plant the tubular reformer is combined with ATR for higher methane conversion.

In the experiments conducted for this work, the main focus will be on low pressure experiment in order to understand the reaction at this level. It is then possible to perform the experiment further from equilibrium conversion by running at low S/C ratios. Low pressure experiments also simplify the testing facility for the reaction.

1.2. Catalysis

The reaction has been explained from a phenomenological perspective, but it is essential to use a catalyst for the reaction to proceed. In this section will follow a more general overview of catalysis with focus on steam reforming catalysts. A traditional heterogeneous catalyst consists of a metal oxide-supported material. Such an oxide could be Al_2O_3, ZrO_2, $CaO(Al_2O_3)_n$, $MgAl_2O_4$ or MgO. All these supports are used for steam reforming catalysts. Such a support should in general be inert, have high mechanical strength, high surface area and an efficient pore system. An efficient pore system allows gas to diffuse in and out of the pellet with only limited hindrance and has a minimal amount of encapsulated active catalytic material. The support is impregnated with an active material such as another oxide, metal or metal alloy. For steam reforming Ni, Pt, Pd, Ru, Rh and Ir are some

of the most active metals for the reaction. The chemical reaction occurs on the surface of this active material. The effect of the catalytic material is to lower the reaction barrier for the overall reaction, hence the catalytic material is not used in the process, but merely enables the reaction to proceed at lower energetically conditions often consistent with a lower temperature.

Overall kinetics is used as a mean to describe the reactions at a microscopic level on a macroscopic level. The kinetics describes how temperature, concentrations and pressures have influence on the macroscopic level, and the main focus of the kinetic description in this section will pertain to the methane steam reforming reaction

$$CH_4(g) + H_2O(g) \underset{k^-}{\overset{k^+}{\rightleftharpoons}} CO(g) + 3H_2(g) \tag{4}$$

A methane and a water molecule reacts and forms a CO molecule and three hydrogen molecules. This is an overall interpretation of the steam reforming reaction. It occurs in a single reaction step, where the rate of the overall reaction can be given by

$$r = -\frac{\partial[CH_4]}{\partial t} \tag{5}$$

Where r is the rate and t is time. To describe the reaction rate to a first approximation, it is possible to use a parameterization of the rate in terms of a power law rate expression given by Eq. 6.

$$r = k \cdot P_{CH_4}^{\alpha_{CH_4}} \cdot P_{H_2O}^{\alpha_{H_2O}} \cdot P_{CO}^{\alpha_{CO}} \cdot P_{H_2}^{\alpha_{H_2}} \tag{6}$$

It is possible to derive the reaction order, α_i, for each component thus observing that the reaction order can constitute any number. The individual order is derived in a log-log plot of the rate versus the partial pressure of the given component

$$\alpha_i = \frac{\partial \ln r_+}{\partial \ln(P_i)} \tag{7}$$

This simplified method will be used to describe and provide understanding for each individual component in the overall kinetics. The simple overall kinetic model can be expanded to give a more detailed description of the steam reforming reaction. A reaction scheme of the methane steam reforming is given by the following 9 elementary steps, ER1-ER9. The methane steam reforming reaction is a combination of a series of elementary steps, each constituting a micro-kinetic model. It is possible to have a larger scheme including more branching elementary reaction steps, but based on previous studies it is estimated that it does not add extra understanding to the reaction mechanism.

$$CH_4(g) + 2^* \underset{k_1^-}{\overset{k_1^+}{\rightleftharpoons}} CH_3^* + H^* \quad \text{(ER1)}$$

$$H_2O(g) + 2^* \underset{k_2^-}{\overset{k_2^+}{\rightleftharpoons}} OH^* + H^* \quad \text{(ER2)}$$

$$OH^* + {}^* \underset{k_3^-}{\overset{k_3^+}{\rightleftharpoons}} O^* + H^* \quad \text{(ER3)}$$

$$CH_3^* + {}^* \underset{k_4^-}{\overset{k_4^+}{\rightleftharpoons}} CH_2^* + H^* \quad \text{(ER4)}$$

$$CH_2^* + {}^* \underset{k_5^-}{\overset{k_5^+}{\rightleftharpoons}} CH^* + H^* \quad \text{(ER5)}$$

$$CH^* + {}^* \underset{k_6^-}{\overset{k_6^+}{\rightleftharpoons}} C^* + H^* \quad \text{(ER6)}$$

$$C^* + O^* \underset{k_7^-}{\overset{k_7^+}{\rightleftharpoons}} CO^* + {}^* \quad \text{(ER7)}$$

$$H^* \underset{k_8^-}{\overset{k_8^+}{\rightleftharpoons}} \frac{1}{2} H_2(g) + {}^* \quad \text{(ER8)}$$

$$CO^* \underset{k_9^-}{\overset{k_9^+}{\rightleftharpoons}} CO(g) + {}^* \quad \text{(ER9)}$$

This set of elementary reactions describes a possible route for the formation of CO and H_2. A surface site is denominated as * in the model (ER1-ER9), i.e. representing an active site on the catalyst. It is generally assumed to comprise all the surface sites when calculating an absolute turnover frequency (TOF). This assumption is not completely valid, as the surface will have different sites, with varying coordination numbers. Generally sites can be divided in three classes; terrace, step and kink sites. For the modelling it will be assumed that all sites are similar and for TOF calculations including all surface sites.

In the first step (ER1) methane is dissociatively adsorbing to the metal surface. This dissociative adsorption has been investigated on different metals, such as Ni [10,11] and other noble metals [12]. This elementary step plays a crucial role in the overall steam reforming reaction, and it is often being interpreted as the rate determining step for methane steam reforming on the various metals [13,14,15,16,17,18]. The reactivity of the methane dissociative adsorption on steps have been proven for Ni [10,19] to be significantly higher than at terrace sites. The second elementary step (ER2) is steam dissociative adsorption to two free sites. This step is significantly faster than the first step, due to easier dissociation of a water molecule compared to methane. The following steps (ER3-6) are the dehydrogenation steps of CH_x, where the last step of hydrogen removal (ER6) is likely to be dependent on the surface coverage of various adsorbents. The energy levels for CH → C + H are comparable to alternative sets of reaction steps such as

$$CH^* + OH^* \rightarrow CHOH^* + ^* \quad \text{(ER10)}$$

$$CHOH^* + ^* \rightarrow CHO^* + H^* \quad \text{(ER11)}$$

$$CHO^* + ^* \rightarrow CO^* + H^* \quad \text{(ER12)}$$

or

$$CH^* + O^* \rightarrow CHO^* + ^* \quad \text{(ER13)}$$

$$CHO^* + ^* \rightarrow CO^* + H^* \quad \text{(ER14)}$$

These reactions have been calculated by DFT calculations on Ni(111) where both alternative pathways are found to be possible [20,21]. No direct experimental evidence have been found experimentally for the presence of a CHO^* or COH^* molecule under reaction conditions. Similarly for the reverse reaction of methanation, pathways through CHO^* or COH^* have been proposed [22]. Thus it is likely that these pathways do exists and that they may be competing at some level. In this investigation the main focus will remain on the initial 9 elementary steps. For the remaining steps (ER7-9), both CO and hydrogen desorb as well as a reaction cycle have been completed on the catalyst. More elaborate implications of this kinetic model will be given in section 5.2.

1.3. Surface reactivity

In catalysis, the interaction between an adsorbate and a surface is crucial for the catalytic behaviour of the reaction. The weakest form of adsorption, physisorption, have little relevance for catalysis directly, however it can be very useful as a characterization tool it can be very useful, e.g. gas adsorption on solids for surface area determination.

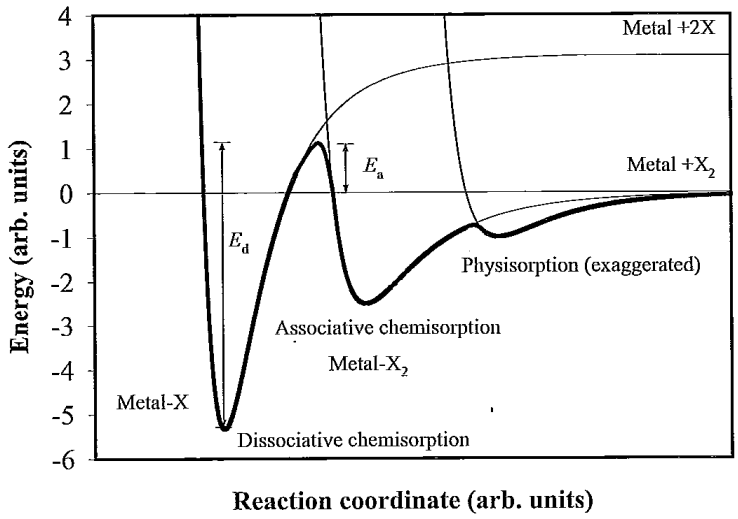

Figure 3. Potential energy diagram with a molecule X_2 physisorption by van der Waals forces, followed by associative chemisorption and finally dissociative chemisorption [23].

In Fig. 3 it is shown that after physisorption chemisorption is the next step, whether it being associative or dissociative. The chemical bond between an adsorbate and a metallic surface can be qualitative described. The solid surface of metals has extended outer *s* or *p* orbitals, which provide a continuum band, whereas the *d* orbitals have minor overlap, hence the interaction is weaker and the *d* band is narrower. The *d* band is the compilation of molecular orbitals and is almost empty at the left of the periodic system, e.g. Ca, while more noble metals, e.g. Cu, have an almost completely filled *d* band. The combination of orbitals on a solid surface can be combined as energy levels in density of states (DOS), where the electrons are filled up to the Fermi level.

The interactions between a molecule and metal surface can be described by the Newns-Anderson model. If the anti-bonding orbitals of a molecule are filled due to the interaction, the molecule internal bonds might be so weak that it will dissociate. This is essential for understanding the molecule-surface interaction. Overall, the bond strength between the metal *d* band and the adsorbate can be determined as a function of

- The degree of filling of the *d* band
    - A higher degree of filling gives a more noble metal and less bond strength to adsorbates
- The energy difference between the centre of the *d* band and the original election level of the adsorbate
    - The centre of the *d* band decreases to the right of the periodic system, lowering the bond strength
- Interaction between the electron wave function of the adsorbate and the metal *d* state wave function
    - Large interaction enhance predominant trend from the previous two points

This notion of *d* band model can be exemplified by the ammonia synthesis reaction from N_2 and H_2. This is illustrated in Fig. 4, where it is seen that Ru is the most active catalyst. A volcano type plot of the activity as a function of the *d* band occupancy is obtained.

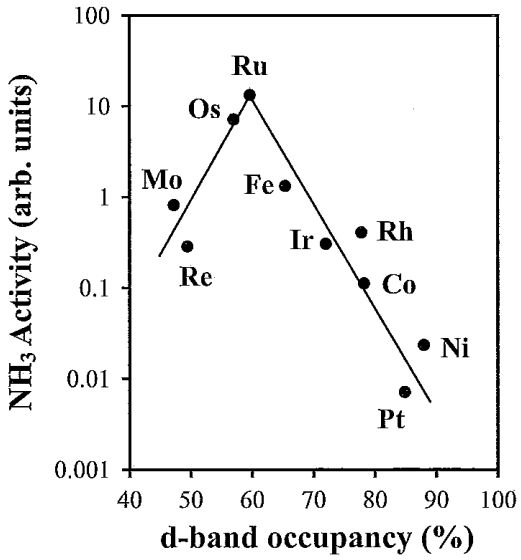

Figure 4. Catalytic activity of various supported metals for the production of ammonia [23].

The interaction between the surface and the adsorbates has an optimum depending on the factors described above. To the left of Ru the reactants and products adsorbs too strongly with the surface due to the lower degree of *d* band filling. This effectively blocks the surface of the catalyst lowering the activity. To the right of Ru, the reactants does not interact strongly enough with the surface due

to the high degree of *d* band filling. The surface is effectively clean due to the low adsorbance of reactants. Hence, an optimal catalyst exists for each reaction depending on the interplay between the gas phase and the solid catalyst. This generalisation will also be used for understanding the steam reforming catalyst relative activity.

1.3.1. **Theoretical catalysis**

The catalysis field has developed tremendously over the previous centuries with a big amount of empirical data. The ammonia synthesis catalyst required some 2500 catalytic material samples to be tested before an optimal catalyst was obtained [23]. In an effort to reduce the number of experiments, computer modelling of catalytic reactions have proven to be able to explain catalytic phenomena [12,22,24,25]. Density functional theory (DFT) is one of the main methods for studying catalysis by theoretical calculations and is based on the importance of active sites for catalysis and use of models of 20-100 atoms. As for many other reactions, methane steam reforming is largely thought to be independent on direct support effects [14,12]. This gives a good opportunity to calculate the physical properties of the steam reforming reaction. When modelling a reaction, the specific site chosen for the calculation is essential. For methane steam reforming on nickel, it has been found that the turnover frequency is two orders of magnitude higher on steps than on terrace sites [10]. This was shown both experimentally and by DFT calculations. This shows the importance in distinguishing between different sites, whether it being terrace or step sites.

It has been found that there is a linear relationship between the activation energy of dissociation, E_a, and the adsorption energy of dissociated atoms [26]. Such linear relationships are called Brønsted-Evans-Polanyi (BEP) relations. The activation energy for methane on steps is plotted against the adsorption energy of carbon, ΔE_C, in Fig. 5. The relationship depends on the surface structure and the values used for this plot have been obtained by DFT calculations.

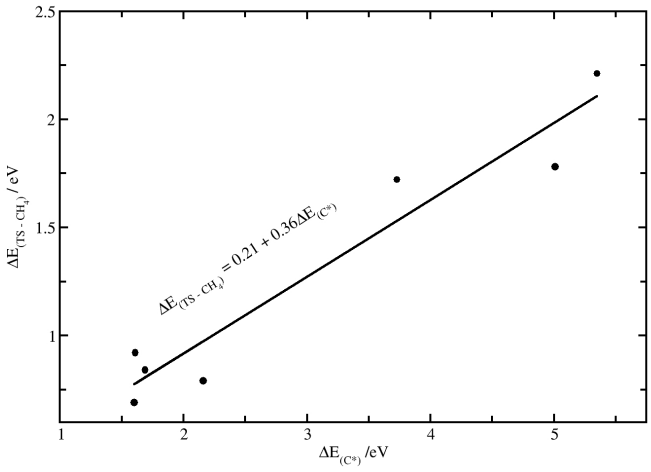

Figure 5. Calculated transition state energies (E_a) of methane on steps as a function of C adsorption energies (ΔE_C) [12].

To simplify the equation obtained above with adsorption energies of CH_3 and H, linear scaling relationships between adsorption energies can be used. For hydrogen containing species, it is possible to show that there exists a linear relationship between the adsorption energy of C and CH_x. This is irrespectively of the metal, although dependent on the surface structure.

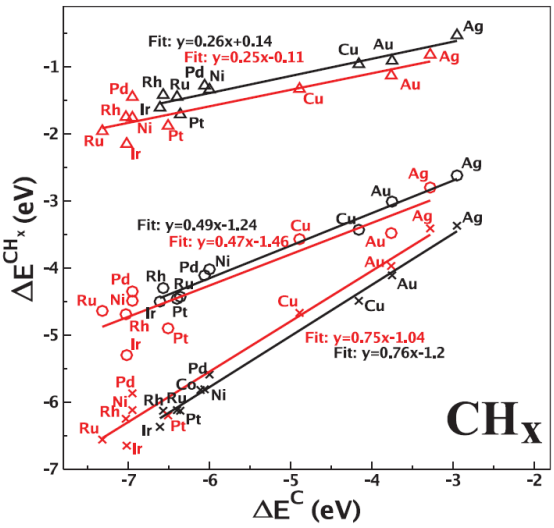

Figure 6. Adsorption energies of CH_X intermediates plotted against adsorption energies of C. The data represent closed-packed (black) and stepped (red) surfaces [27].

In Fig. 6 such a dependency is shown for C and the hydrogenated species CH, CH_2 and CH_3. The linear relationship is called scaling relation and the slope depends on the valency of the adsorbate.

This correlates back to the *d* band model inferring that the coupling to the *d* states scale with the valency of the adsorbate [27]. Further relationships are necessary for the steam reforming reaction and it can be shown that the adsorption energy of CO relates to C and O and the adsorption energy of H to C [12]. The activation barrier for methane dissociation can now be given as a linear function of the C adsorption energy on a metal based on linear scaling relationships and BEP relations. This has been applied theoretically determine to the steam reforming activity as given in section 5.2.1.

1.4. Summary

The methane steam reforming reaction can be viewed at different levels. From a full scale industrial GTL plant to a theoretical calculation of a CH_x specie adsorption energy. Both aspects are equally important when understanding the steam reforming process. This work will attempt to include syntheses of catalysts that could be used for industrial applications, to test the catalysts in setups that required reactor modelling, to derive an overall kinetic expression and try to deduct the underlying mechanism.

This will be combined with characterization of the catalyst to get a better understanding of the catalyst properties for the analysis. A key parameter at the large industrial scale is the long term activity, so beyond finding the most active catalyst among the different metals, it is also attempted to stabilize active catalysts towards sintering.

2. Experimental

2.1. Setups

From the more theoretical part to the experiments conducted in this project. A wide range of experimental setups have been used for the investigations conducted. After catalyst preparation, the samples have been reduced in a reduction setup. The reduction setup is along with the other setups, steel tube plug-flow reactors. There have been used several different sizes of test reactors, but all with the same basic principle as shown in Fig. 7.

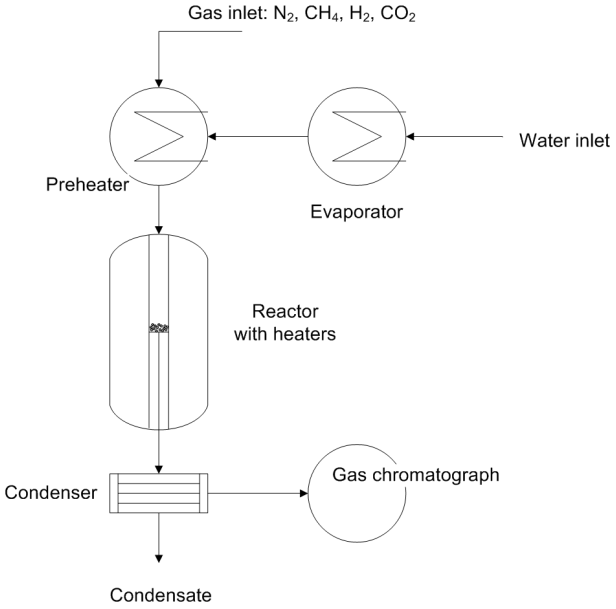

Figure 7. Schematic drawing of a test reactor setup.

The central reactor is a stainless steel tube with an inner diameter of either 2.6, 7.2 or 8.5 mm depending on the reactor system. Three reactor systems were used for the experimental work. Kinetic data were obtained with the largest reactor setup, 8.5 mm inner diameter. There is a continuous radial heat input to these reactors. A temperature measurement is placed in the near vicinity of the catalyst bed. The setups include gas inlets through mass flow controllers, where it is possible to add N_2, CH_4, CO_2 and H_2. Water is added through an evaporator.

Table 1. Properties of the two reactor setups.

Reactor system	Testing purpose	Inner diameter	Outer diameter	Reactor length	Thermo well placement	Operating temperature	Catalyst bed length	Details
1	Screening	2.6 mm	3 mm	310 mm	10-20 mm above bed	350-550°C	20-30 mm	No condenser
2	Kinetic	8.5 mm	9.5 mm	930 mm	In thermo channel, at bed height	450-850°C	13-17 mm	
3	Absolute activities	7.1 mm	8.5 mm	600 mm	In thermo channel, at bed height	450-800°C	11-12 mm	

The outlet gas is analysed after the reactor by a gas chromatograph, where the mole fractions of H_2, N_2, CO, CO_2 and CH_4 are measured. In test reactor 1 is the H_2O concentration also measured. For this setup it is possible to measure steam by gas chromatography due to the low steam content used in experiments for this setup. The test system 1 is a 10 reactor parallel screening reactor with narrow reactors (2.6 mm inner diameter) and a heating block supplying the heat. Due to the size of the small reactor, the temperature measurement is placed above the reactor bed. In this way it is not possible to determine temperature changes due to chemical reaction. But the setup is mainly for a screening study of catalysts, hence comparison between each experiment is valid.

In reactor system 2 three heating zones provide a stable temperature in the reactor. A thermo well is placed inside a thermo channel, allowing the thermo well to be placed at the centre of the catalyst bed. Due to the wider reactor tube, the radial heat gradient becomes more important and needs to be taken into consideration for the setup if running at significant high conversions for the endothermic methane steam reforming reaction. Reactor system 3 is similar to reactor system 2 with the exception of having a smaller inner diameter.

2.2. Catalyst preparation

The support materials are important for obtaining a good performance of a catalyst. It should be a support material that has a high surface area, to ensure well distributed metal particles. The support should have good strength, but at the same time has efficient diffusion properties for reactants and products. It is in most cases inert to chemical reaction, so the desired catalytic reaction only can occur on the catalytic active particle. For the steam reforming reaction it should be stable under

severe reaction conditions; high partial pressures of steam in combination with high temperatures will have a sintering effect on most high surface area support materials. These properties are fulfilled by support materials such as $MgAl_2O_4$, Al_2O_3 and ZrO_2. In the case of Al_2O_3 there exist several forms of alumina, where γ-alumina can be desirable for low temperature (400°C), the alumina will eventually form α-alumina with a lower surface area at higher temperatures. It is therefore desirable to use an α-alumina from the beginning to avoid support sintering during experiments. As given by table 2 ZrO_2 is stabilised by 3 wt% Y_2O_3 for the experiments performed to obtain the high temperature stability.

Table 2. List of support materials and their basic properties.

	Stabilisator	**Surface area**	**Pore volume**	**Peak pore diameter**
$MgAl_2O_4$	-	60 – 70 m^2/g	~0.4 ml/g	100 Å
α-Al_2O_3	-	5 m^2/g	~0.5 ml/g	1500 Å
ZrO_2	Y_2O_3	10-15 m^2/g	~0.2 ml/g	300 Å

The supports are impregnated by an incipient wetness method, where the aqueous solutions of metal salts are mixed with support material. Due to capillary forces, the liquid will wet the entire inner surface of the catalyst. The main issues regarding this procedure is gradient impregnation and support dissolving. The aqueous solution will sometimes be acidic or alkaline to ensure high metal content in the solution. This can cause the support to start dissolving, which will reduce the surface area and change the morphology. During impregnation the metal will bind relatively strongly to the surface, sometimes resulting in a metal gradient through the catalyst, with a higher metal loading at the surface compared to the centre of the pellet. This can be reduced by impregnating smaller support pellets. In this thesis, catalyst pellets sizes are in different size fraction between 2.0-4.5 mm. The specific value is chosen as a compromise between not having the support material as powder with little pore structure left and having too large particles that will give concentration gradients. The metal salts used for impregnation have been listed in table 3.

Table 3. The metal salts used in the incipient wetness impregnation.

Metal	**Ni**	**Ru**	**Rh**	**Pt**	**Pd**	**Ir**
Solution	$Ni(HCOO)_2$ $Ni(NO_3)_2$	$Ru(NO)(NO_3)_3$	$Rh(NO_3)_3$	$Pt(NH_3)_4(NO_3)_2$	$Pd(NH_3)_4(HCO_3)_2$	$IrCl_3 \cdot 4H_2O$

The amount of solution used is determined from pore volume measurements by water as given in table 2. There is used a 10% surplus of the solutions for the desired loading due to spillage.

After impregnation of the support, the samples are dried at 80°C to ensure a good distribution of the metal atoms. The metal is now present as an oxide. Some metal oxides are volatile at elevated temperatures; especially RuO_2 is a volatile and carcinogenic compound. The subsequent heating to remove the remaining water and ions are done in pure hydrogen at 400-600°C for Ru catalysts. Other catalysts were calcined at 400°C for 4 hours in air before reduction at 400-600°C. The metal atoms are now well distributed in small metal particles on the support surface. To obtain a catalyst which is more resistant to sintering, a high temperature ageing procedure is applied. The catalysts are heated to 750-800°C in a H_2O/H_2 (ratio ~ 1) at 30 bar for approximately 10 days. This procedure should give a stable catalyst. As will be evident, this is only partly true, as a reversible deactivation phenomena occurred at 550-650°C, which will be described in section 3.3.

2.3. Characterization

For characterization of the catalyst several methods have been used. The main focus has been on estimating the metal surface area. The metal surface area or dispersion can be used to calculate the turnover frequency representing the activity per site. Hydrogen chemisorption, sulphur chemisorption, x-ray diffraction (XRD) and transmission electron microscopy (TEM) have been used in determining the metal surface area.

Volumetric H_2 chemisorption at 40°C was used to determine metal surface area. Samples were reduced at 400°C for 2 h and then evacuated 1 h and finally cooled to 40°C before hydrogen chemisorption measurement began. An isotherm was measured between 2.5 and 112 kPa H_2 and extrapolated to zero hydrogen pressure. The dispersion was obtained by assuming 1:1 stoichiometry between a metal atom and an adsorbed H atom.

The sulphur chemisorption has served two purposes. It is used in a similar way as hydrogen chemisorption to determine dispersions. There have also been done experiments on Ru, Rh, Pt, Ir and Ni catalysts to determine sulphur isotherms. The measurements were performed in a H_2S/H_2 gas mixture with catalysts placed in series in a plug flow reactor. The experiment continues until

saturation of the samples. After sulphidation, the sulphur content in the catalyst is determined by high temperature oxidation measurement of SO_2. The sulphur chemisorption capacity (s_{cap}) has been used to determine the dispersion and surface-average metal particle diameter. It has been shown for Ni that the maximum coverage of sulphur is 0.5 [28]. It is assumed that similar coverages are valid for Rh, Ru, Ir and Pt. From the sulphur chemisorption it is possible to determine the average particle diameter by Eq. 8 for an fcc metal [12].

$$d = \theta_s \frac{M_s}{M_x} \frac{X}{s_{cap}} \frac{6v}{s} 10^4 \qquad (8)$$

Where M_s is the molar mass of sulphur, M_x is the molar mass of metal x, θ_s is the coverage of sulphur, X is the weight percentage of the metal, v and s are the volume and surface area of the metal.

Characterization of catalysts by x-ray diffraction (XRD) give an estimate of the volume averaged surface area for the metal particles. At low metal loadings, XRD is not a feasible technique as the signals are not sufficient for good measurements. The XRD measurements were performed on a Philips X'Pert Pro θ–θ diffractometer with Bragg–Bretano geometry, a variable divergence slit and a graphite monochromator using CuKα radiation. Average metal crystallite sizes were obtained from the line broadenings of the Rh(200) diffraction line, corrected for the instrumental broadening, using the Scherrer equation.

Characterization of catalysts has been done with transmission electron microscopy (TEM) to determine particle sizes. Measurements have been done *ex situ* using a Philips CM200 FEG and a Philips CM300 FEG electron microscope. A TEM sample is prepared at ambient conditions by crushing the sample and covering a Cu grid with a holey carbon film. TEM images were recorded using a 1k x 1k CCD camera at different magnifications corresponding to an image pixel size in the range of 0.08 nm to 0.45 nm. The *ex situ* studies should be sufficient to have good description of the catalyst. But some inconsistencies were observed for Ru based catalysts. *In situ* studies of Ru catalysts were undertaken, which revealed that there is surface oxidation of the metal particles at ambient conditions. When performing measurement at *in situ* conditions, much smaller particles are visible. This oxidised surface at *ex situ* condition rendered it difficult to determine actual particle sizes. Environmental transmission electron microscopy (ETEM) were done using a Philips CM300 FEG electron microscope equipped with an environmental cell [29]. For the ETEM experiments the

sample was distributed on a Mo TEM grid and exposed to 2.0 mbar H_2 at 500°C for 1 h to reduce the surface of the sample.

From the TEM or ETEM images, the metal nanoparticle diameters are determined from the projected area of the particles assuming that the particles are spherical. The resulting particle size distributions allow surface-averaged and volume-averaged particle diameters to be calculated and compared to the average particle diameters obtained by the sulphur chemisorption and XRD methods. The surface-averaged particle diameter is given by

$$d_s = \frac{\sum n_i d_i^3}{\sum n_i d_i^2} \tag{9}$$

Where d_i is the diameter of the i´th particle. Likewise, the volume-averaged particle diameters are given by

$$d_v = \frac{\sum n_i d_i^4}{\sum n_i d_i^3} \tag{10}$$

The dispersion can then be determined from the total surface area (A_{tot}) and the total volume (V_{tot}) determined from the particle size distributions by the following equation

$$D = \frac{A_{tot}}{V_{tot}} \cdot \frac{v}{s} = 6 \cdot \frac{\sum n_i d_i^2}{\sum n_i d_i^3} \cdot \frac{v}{s} \tag{11}$$

Where v is the atomic volume and s is the surface area per atom. If it is assumed that the close-packed surfaces have the lowest surface energies are dominant, then it is possible to calculate the dispersion for an fcc(111) metal particle by

$$D = \frac{\sum n_i d_i^2}{\sum n_i d_i^3} \cdot \frac{6a}{\sqrt{3}} \tag{12}$$

and for an hcp(0001) metal particle by

$$D = \frac{\sum n_i d_i^2}{\sum n_i d_i^3} \cdot 3 \cdot c \tag{13}$$

With *a* and *c* being the lattice parameters.

2.4. Reactor modelling

If the catalytic activity is sufficiently slow, no influence of intra-particle diffusion or heat gradients in the system then it would relatively easy to analyse the data. But the reaction is strongly endothermic, the porous support has a high surface area and the reaction needs to be run to a certain conversion to observe kinetic changes. The incorporation of mass and heat transfer need to be taken into consideration since it will be evident that the experiments are not conducted at intrinsic conditions, but only at near intrinsic conditions.

In Fig. 8 is sketched a plug flow reactor resembling the reactors used in the experiments. The modelling of the reactor is done by a differential reactor model to calculate the pressure, temperature and conversion profiles of a fixed bed catalytic reactor. Effectiveness factors are used through the catalyst bed to incorporate the heat and mass transfer in the catalyst pellets. The integration is done over length steps through the reactor. In each integration step, the heat and mass transfer are calculated and evaluated.

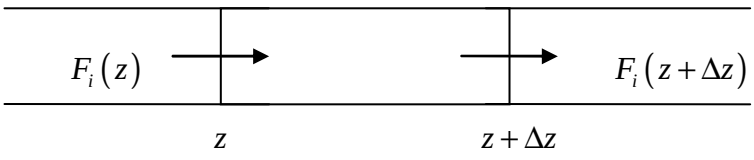

Figure 8. Setup for plug flow reactor with the change in molar flows for Δz

The important aspect to review is the conversion, X_i, both for the steam reforming and the water gas shift reactions. They are given as a function of the molar flow F_i in Eq. 14 and 15.

$$X_1 = \frac{F_{CH_4,in} - F_{CH_4}}{F_{CH_4,in}} \tag{14}$$

$$X_2 = \frac{F_{CO} - F_{CO,in}}{F_{CH_4,in}} \tag{15}$$

The water gas shift reaction is assumed to be in equilibrium as described in section 5.1. So the conversion, X_2, is therefore directly a function of X_1 and K_p (WGS). The water gas shift equilibrium is ensured numerically by using a sufficiently high water gas shift reaction rate. By assuming the water gas shift reaction is in equilibrium then it is possible to do a full description of CO_2 reforming as well with the conversions, X_1 and X_2. For numerically modelling the CO_2 reforming reaction it is necessary to include a small amount of steam in the feed for convergence, since there is either H_2 or steam for initial conversion in the first integral step. Since there is no steam dependency on the forward steam reforming reaction, X_1 is also a descriptor for the conversion of methane for the CO_2 reforming experiments.

This conversion is used as a variable for modelling the mass transfer. In Fig. 8 the change in molar flows as a function of length, *z*, is sketched. A general mole balance can be constructed and in the limit of Δz and it gives a differential equation in Eq. 16 for the molar conversion of a given component.

$$\frac{\partial F_i}{\partial z} = R_1 \nu_{i,1} + R_2 \nu_{i,2} \tag{16}$$

Where $v_{i,j}$ is the stoichiometric coefficient for compound *i* in reaction *j*. If this differential equation is evaluated for methane then it is possible to relate the steam reforming reaction rate directly to the conversion by Eq. 17. The reaction rate is an analytical expression which will be constructed based on the kinetic modelling.

$$\frac{\partial\left(F_{CH_4,in}\left(1-X_1\right)\right)}{\partial z} = -R_1 \quad \Rightarrow \quad \frac{\partial X_1}{\partial z} = \frac{R_1\left(X_1, K_p\left(WGS\right)\right)}{F_{CH_4,in}} \tag{17}$$

Obviously, the reaction rate will depend on the reactant concentrations and therefore also the conversions.

2.4.1. **Energy balance**

Due to the strongly endothermic steam reforming reaction and resulting temperature change, the energy balance has to be taken into consideration. The change in temperature will have a significant effect on the reaction and therefore the modelling, especially at high conversion and temperature. The energy balance is modelled as in Fig. 9 where an inlet flow to a differential area contains an amount of energy, $\sum_{i=1}^{N}\left(F_i H_i\right)_z$, and together with the heat input through the reactor wall, ΔQ, this has to be balanced with the produced heat and exit flow, $\sum_{i=1}^{N}\left(F_i H_i\right)_{z+\Delta z}$.

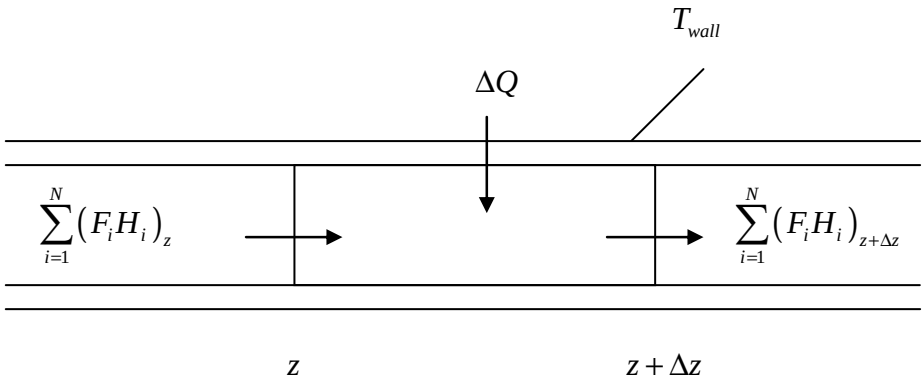

Figure 9. The heat transfer in the bed. H_i is the enthalpy of the individual component.

A simple one dimensional model is applied in the axial direction. Since the catalytic sample is highly diluted, combined with the flow velocity, it is assumed that the temperature change in the radial direction is constant. The heat balance is given by Eq. 18.

$$U\left(T_{wall}-T\right)\cdot a\cdot\frac{\Delta z}{\rho_{bulk}\cdot\omega_{bed}}+\sum_{i=1}^{N}\left(F_i H_i\right)_z-\sum_{i=1}^{N}\left(F_i H_i\right)_{z+\Delta z}=0 \qquad (18)$$

Where a is a geometric factor representing the ratio between the area of the inner wall and the volume of the bed (e.g. m^2 inner wall/m^3 bed), ρ_{bulk} is the bulk density of the bed, U is the overall heat transfer, T is the bed temperature and ω_{bed} is the mass fraction of catalyst in the bed. Eq. 18 can be rewritten as Eq. 19, where the change in enthalpy can be given by the specific heat capacity, $C_{p,i}$, and the change in temperature by Eq. 20.

$$U\left(T_{wall}-T\right)\cdot\frac{a}{\rho_{bulk}\cdot\omega_{bed}}-\left(\sum_{i=1}^{N}\frac{\partial F_i}{\partial z}\cdot H_i+\sum_{i=1}^{N}\frac{\partial H_i}{\partial z}\cdot F_i\right)=0 \tag{19}$$

$$\frac{\partial H_i}{\partial z}=C_{p,i}\frac{\partial T}{\partial z} \tag{20}$$

The final energy balance can be written in Eq. 21 where ΔH_i is change in enthalpy.

$$\frac{\partial T}{\partial z}=\frac{U\cdot\left(T_{wall}-T\right)\cdot\frac{a}{\rho_{bulk}\cdot\omega_{bed}}-\sum_{i=1}^{N}R_i\Delta H_i}{\sum_{i=1}^{N}F_iC_{p,i}} \tag{21}$$

Converting the general Eq. 21 into the specific for the steam reforming reaction in Eq. 22.

$$\frac{\partial T}{\partial z}=\frac{U\cdot\left(T_{wall}-T\right)\cdot\frac{a}{\rho_{bulk}\cdot\omega_{bed}}-R_1\Delta H_1-R_2\Delta H_2}{F_{T,in}\left(\overline{C_{p,in}}+y_{CH_4,in}X_1\Delta C_{p,1}+y_{CH_4,in}X_2\Delta C_{p,2}\right)} \tag{22}$$

Where $\overline{C_{p,in}}$ is the average heat capacity at inlet conditions and $\Delta C_{P,j}$ is the change in heat capacity for reaction *j*. This equation describes the heat changes in the reactor when assuming heat input from the outer wall.

2.4.2. **Heat transfer coefficients**

It was assumed that there was no temperature change in the radial direction this still holds for the bed, but the temperature from the wall to the bed has a temperature drop due to film effects. The heat transfer coefficients for the resistances can be evaluated as follows. Firstly, it is assumed that the heat transfer through the reactor wall is high and does no play a significant part. This energy transport due to the radial heat transport is sketched in Fig. 10. Here the outer wall, the packed bed and the thermo well is shown. The heat is transported through an inner wall film and then into the catalytic bed. The resistance in the packed bed, Ω_{bed}, and the inner wall film, $\Omega_{inner\ wall}$, are decisive for the total heat transfer. In total this can be summarized by Eq. 23.

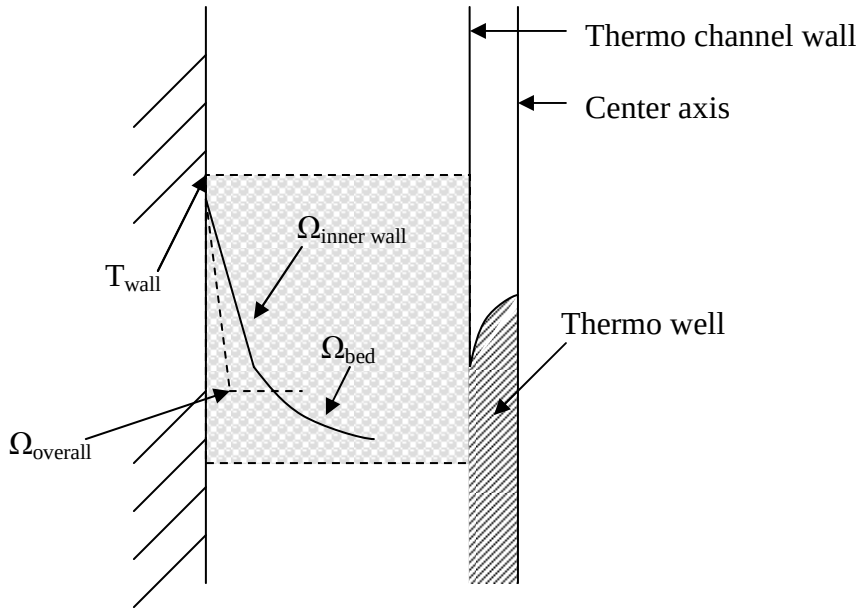

Figure 10. Heat transfer from the wall through the inner wall film and the packed bed. Overall it is described by the overall resistance, $\Omega_{overall}$= 1/U.

$$\frac{1}{U} = \Omega_{inner\ wall} + \Omega_{bed} \tag{23}$$

The two resistances can be given by Eq. 24 and 25. By combining the two resistances it is possible to simplify the temperature change in the axial direction. The radial heat change is then calculated based solely on the overall heat coefficient.

$$\Omega_{inner\ wall} = \frac{1}{h_{inner\ wall}} \tag{24}$$

$$\Omega_{bed} = \frac{D_{tube,eff}}{8 \cdot \lambda_{er}} \tag{25}$$

Where $h_{inner\ \ wall}$ is the heat transfer at the inner wall, $D_{tube,eff}$ is the effective tube diameter and λ_{er} is the effective thermal conductivity. An axial temperature has been measured as given in Fig. 10. This temperature measurement is placed inside a thermo channel. The temperature should be equal to the inlet and wall temperature at zero conversion and is used as reference temperature. Because of the endothermic reaction the axial temperature will decrease at increasing conversion. The heat transfer between z and z + Δz can then be calculated as in Eq. 26.

$$\Delta Q = U \cdot \left(T_{wall} - T_{bed}\left(z\right)\right) \cdot \frac{a \cdot \Delta z}{\rho_{bed} \cdot \omega_{bed}} \tag{26}$$

Where ΔQ is the heat transferred to the differential zone and $T_{bed}(z)$ is the mean temperature which depends on the independent variable z. It is assumed that the overall heat transfer coefficient, U, will be constant through the short reactor bed.

The gas flow along the catalytic bed wall has laminar flow conditions. So calculations should be made for laminar flow. If the flow near the wall is considered, it can be approximated as flow around a sphere [30]. This theory was developed for the film around a sphere in a packed bed. The sphere was suspended in an infinite fluid and overall the system corresponds well the flow around the wall of this packed bed.

$$h_{inner\ wall} = C_{wall} \cdot \frac{\lambda_{gas}}{D_{p,av}} \cdot \left(2 + 0.6 \cdot \sqrt[3]{\mathrm{Pr}}\sqrt{\mathrm{Re}}\right) \tag{27}$$

A correction factor C_{wall} is added to the equation of a simple sphere due to the large artificial particle (the wall) which is introduced in this system. The effective thermal conductivity is necessary for determining the heat transfer in the bed. It is assumed to be constant for the entire reactor bed. The transfer coefficient can be calculated based on a turbulent and stagnant part as given in Eq. 28 [31].

$$\lambda_{er} = \lambda_{turb} + \lambda_{stag} \tag{28}$$

The detailed calculations are given in appendix A along with the calculations based on the inlet conditions. It can be shown that the stagnant contribution surpasses the turbulent contribution due to the low Reynolds number flow (Re~1).

The temperature measurement in the thermo channel T_{TC} has so far been assumed to be equivalent to the bed temperature. But since the outer wall has been considered having high heat conductivity, similar considerations must be taken for the thermo channel. Heat can be transported in the thermo channel and between the thermo channel and the bed. In appendix A is given the detailed calculations for this effect to the heat balance. By adjusting C_{wall}, the data obtained from the axial temperature can be compared to the calculated temperature in the thermo channel at the centre of the reactor by Eq. 29.

$$SSQ = \sum_{i=1}^{N} \left(T_{i,axial,meas} - T_{TC,calc} \right)^2 \tag{29}$$

The heat balance is adjusted to the experimental setup by the C_{wall} parameter that largely is determined by the flow velocity, which is kept constant.

2.4.3. **Pore diffusion**

Pore diffusion is an important aspect of the catalytic performance. A general way of including the pore diffusion in relation to the reaction rate is by the effectiveness factor given in Eq. 30 [30]. The effect of the effectiveness factor is multiplied to the rate.

$$\eta = \frac{actual\ mean\ reaction\ rate\ within\ pore}{bulk\ rate} \tag{30}$$

The pore distribution of a standard ZrO_2 based catalyst is shown in Fig. 11 and determined by Hg porosimetry. For a relative strong support such as ZrO_2 it is feasible to apply Hg porosimetry without destroying the catalyst. Calculation of the effectiveness factor can be done through equation 31 – 33.

$$D_{eff} = \frac{D \cdot \varepsilon}{\tau} \tag{31}$$

$$\varphi = L \sqrt{\frac{k}{D_{eff}}} \tag{32}$$

$$\eta = \frac{3}{\varphi} \left(\frac{1}{\tanh(\varphi)} - \frac{1}{\varphi} \right) \tag{33}$$

Where φ is the Thiele modulus for the reaction given by Eq. 32, L is a characteristic size of the catalyst particle, k is the rate constant and D_{eff} is the effective diffusion coefficient. D_{eff} is derived

from the molecular diffusion coefficient D, by the porosity ε and a tortusity factor τ that describes the overall pore system.

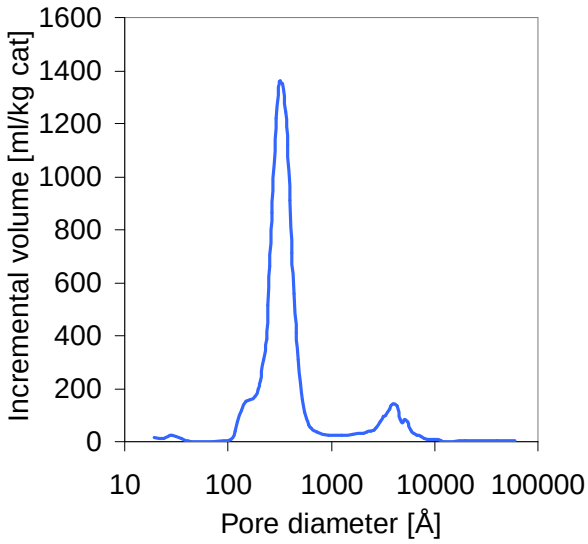

Figure 11. Pore distribution for standard ZrO_2 support material used for noble metal catalysts. Obtained by Hg porosimetry.

In appendix A an example of calculating the effectiveness factor for a standard experiment at 500°C is given. The effectiveness factor is at those conditions 0.97, close to intrinsic conditions, but enough to consider when analyzing the kinetic data.

2.4.4. **Model optimization**

From the gas chromatography data it is possible to determine the experimental conversion. For methane steam reforming this is done by Eq. 34, while for CO_2 reforming it can be done by Eq. 35.

$$X_{1,out} = \frac{y_{CO,meas} + y_{CO_2,meas}}{y_{CH_4,meas} + y_{CO,meas} + y_{CO_2,meas}} \tag{34}$$

$$X_{1,out} = \frac{y_{H_2,meas} + y_{CO,meas}}{4 \cdot y_{CH_4,meas} + y_{H_2,meas} + y_{CO,meas}} \tag{35}$$

It is possible to compare the obtained conversion data from experiments and model. The optimization has been done by applying Eq. 36 where the modelled outlet conversions are optimized by changing the kinetic rate expression parameters.

$$SSQ = \sum_{i=1}^{N} \left(X_{1,out,meas,i} - X_{1,out,calc,i} \right)^2 \quad (36)$$

This describes the model optimization. The modelling results gives temperature profiles as shown by Fig. 12, where axial profiles are shown of the thermo channel temperature, bed temperature and the methane conversion rate. It is seen that the bed temperature decreases significantly at inlet due to the endothermic reaction. The large bed temperature decrease at inlet present is due to the high rate, where there is a high methane partial pressure and low product inhibition. The thermo channel temperature decreases also slightly, but is compensated by the heat conductivity in the channel wall.

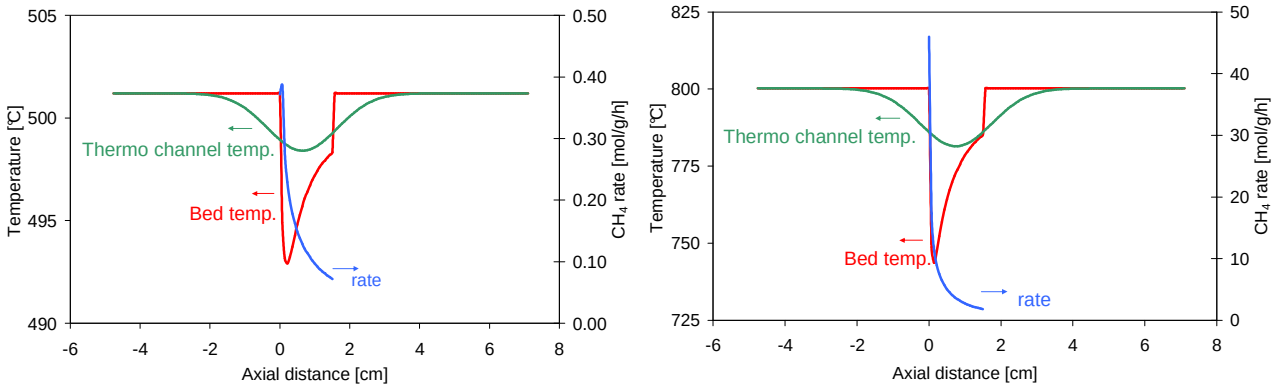

Figure 12. Reactor profile with the thermo channel temperature, the bed temperature and the methane conversion rate as a function of the axial distance. Flow direction from left towards right. (left)Experimental conditions of 500°C, 0.18 bar N_2, 0.18 bar CH_4, 0.72 bar H_2O and 7.0% conversion. (right) Experimental conditions of 800°C, 0.20 bar N_2, 0.20 bar CH_4, 0.80 bar H_2O and 62.1% conversion.

The high temperature experiment shown in Fig. 12(right), gives fundamentally the same results as in low temperature experiment, but there is a significant drop in bed temperature of 50°C. This drop is not reflected in the actual temperature measurement in the thermo channel, where the temperature decrease is closer to 20°C. These figures represent the reactor behaviour as represented by the model. The big drop in temperature affects the reaction rate and it is therefore necessary to include the modelling. Not relating the different temperatures would give a wrong model result. It also shows the importance for fully understanding the strongly endothermic reaction in the reactor setup. The central measured temperature does not always present the expected result.

As will be given later by the kinetic model, the catalyst has significant product inhibition through the reactor and there are large differences in reactivity even at low conversion as given by Fig. 12

(left). An analytical expression would not have been able to capture the development of the reaction rate due to the strong product inhibition.

3. Characterization results

3.1. Sulphur adsorption

As given earlier, sulphur chemisorption plays an important role for steam reforming. In a traditional hydrocarbon feed gas there is sulphur impurities and it is necessary to remove these in a desulphurization unit. Only small amounts of sulphur are necessary for sulphur poisoning of the catalyst. The sulphur atoms adsorb to the metal surface with a high binding energy and thereby reducing the methane steam reforming activity. This investigation is partly uncovering some of the aspects for determining sulphur content limits the gas phase, which will help designing desulphurization units. The sulphur adsorption can also be used as an advantage. The surface area of the metal particles can be estimated based on the total sulphur adsorption and the metal loading in the catalyst. This estimation has previously been shown for nickel to give a reasonable estimate of the specific surface area [28]. This technique proves advantageous or multiple sampling compared to more individual sample characterization techniques such as TEM or H_2 chemisorption. Since sulphur on the metal surface is in equilibrium with H_2S as given by Eq. 37, then it is possible to have multiple samples in one H_2S gas stream. When the system has reached equilibrium conditions overall, then the experiment is finished and the samples can be analysed individually for their sulphur content.

$$Me + H_2S \rightleftharpoons Me - S + H_2 \tag{37}$$

So both as an impurity and for characterization the sulphur adsorption is interesting. The specific sulphur adsorption in weight ppm, S_{cap}, representing the sulphur capacity of a given catalyst for a given set of experimental conditions. In this investigation, the sulphur is added to the gas phase as H_2S. Most other sulphur containing compounds will be converted to H_2S on the steam reforming catalyst in the presence of H_2. It can therefore be assumed that sulphur is present as H_2S. For nickel at 500°C, half a monolayer of sulphur ($\theta_s = 0.5$) corresponds to the equilibrium of H_2S/H_2 by Eq. 37 to $H_2S/H_2 = 1.6 \cdot 10^{-12}$ [28]. When discussing sulphur adsorption or H_2S then it is always referring to the idealized H_2S/H_2 system. Measurement is therefore performed under idealized and strongly reducing conditions. To experimentally obtain sulphur coverages lower than full coverage, it is

necessary to perform experiments at very low H_2S concentrations and elevated temperatures to the gain knowledge about sulphur adsorption.

For nickel catalysts it has been observed that there is a strong interaction between sulphur atoms on the Ni surface. The sulphur atoms binds both fourfold and twofold to Ni sites and the maximum coverage observed is approximately half a monolayer [32], hence at complete sulphur adsorption on the surface the actual nickel surface area is twice the corresponding sulphur surface area. At high sulphur concentrations (>1000 ppm H_2S/H_2) it becomes favourable to form nickel sulphide, Ni_3S_2. The strong impact of sulphur has both electronic and geometrical effect on the catalytic activity. It can effectively block sites [33], restructure the surface [32] or induce shift in the surface energy of the active catalyst metal [32].

There is operating conditions at which sulphur content in the feed stream can be an advantage. Due to the high sulphur adsorption energy (table 4) then it is more favourable than carbon adsorption. So with a specific amount of sulphur in the feed gas it is possible to suppress the carbon formation, while retaining sufficient steam reforming activity. This technique is applicable when running under severe experimental conditions of low S/C ratio which is prone to form carbon under normal operating conditions. This geometrical effect hinders the formation of stable carbon structures which is necessary for significant carbon formation [33].

Table 4. Sulphur adsorption energies and sulphide formation energies [34,35,36,37,38,39].

Metal	**Sulphur adsorption energy [kJ/mol][1]**	**Sulphide formation energy (per sulphur atom) [kJ/mol]**
Ni	-247	-173
Ru	-215	-168
Rh	-166	-148
Ir	-219	-135
Pt	-177	-147

[1] *Reference (1/2) $S_2(g)$*

Sulphur adsorption studies have been done by Rostrup-Nielsen [40], who measured the chemisorption of H_2S on nickel supported catalyst for temperatures between 550-645°C. The sulphur uptake is given as a function of H_2S/H_2 ratio; saturation layer is observed above 5 ppm H_2S and bulk sulphide (Ni_3S_2) is observed above 1000 ppm H_2S. To validate the sulphur chemisorption experiments, H_2 chemisorption measurements were performed. It was estimated that the maximum sulphur coverage is 0.5 sulphur atom per nickel atom. Alstrup et al. [41] performed additional

experiments at high temperature. The experiments covered a larger temperature span (500-750°C) and a large H_2S/H_2 ratio (7.5-50 ppm). By combining their experiments with McCarty et al. [37], an adsorption isotherm was suggested as given by Eq. 38.

$$\frac{p_{H_2S}}{p_{H_2}} = \exp\left(\Delta H^0 \left(1-\alpha\theta\right)/RT - \Delta S^0/R\right) \tag{38}$$

Where ΔH^0 (-289 kJ/mol) is the sulphur adsorption energy, ΔS^0 (19 J/K) is the change in entropy, α (0.69) is the coverage factor and θ is the sulphur coverage determined by $\theta = s/s_0$. s and s_0 are the actual and the saturation amount of adsorbed sulphur, respectively. The values are determined experimentally based on both the data by Alstrup et al. [41] and McCarty et al. [37]. This equation describes the relationship between the experimental conditions given by the H_2S/H_2 ratio and the sulphur coverage, θ.

Since sulphur also binds strongly to other transition metals, it is speculated if this method could be expanded to other relevant steam reforming metals, such as Rh, Ru, Pt, Ir and Pd [12]. Ru, Pt and Pd all have surface metal sulphides with qualitative similar structures as those of Ni [42]. McCarty and Wise have produced a series of investigations, analysing the H_2S chemisorption on Ni [37], Ru [36], Fe [43], Co [43], Pt [35] and Ir [34]. The investigations have been done at very low partial pressure of H_2S (0.1 ppb – 1 ppm) on various catalyst samples. In this investigation the applicability of the sulphur adsorption on noble metals and the precise adsorbance will be reviewed.

3.1.1. **Experimental**

The sulphur adsorption experiments have been conducted in a plug flow reactor (40 mm inner diameter). In the reactor a series of containers are placed above each other for a length of 80 cm. There are three heating zones in the reactor setup, which makes it possible to have a temperature gradient axially in the reactor by setting the three different temperatures. The gas enters at the top where the highest temperature is, and then the temperature decrease as the gas flows downwards. The temperature gradient can have up to 300°C in difference between the highest and lowest temperature. Catalyst samples of 2-3 g are placed at 4-5 different locations through the reactor and the local temperature is measured by a thermo well inside a centred thermo channel.

Ni-0 (14.4wt% $Ni/MgAl_2O_4$), Pt-0 (4wt%$Pt/MgAl_2O_4$), Ir-0 (4wt%$Ir/MgAl_2O_4$), Rh-0 (4wt%$Rh/MgAl_2O_4$) and Ru (4wt%$Ru/MgAl_2O_4$) samples have been used for the experiment.

The temperature gradient was kept constant throughout the experiment. First the samples are re-reduced in H_2 and then exposed to the experimental gas mixture of H_2S and H_2 (total flow 335 Nl/h). The gas flow was kept constant until a sulphur amount corresponding to 3-4 times full saturation for a 100% dispersed sample have passed through the reactor setup. It is assumed that this is enough to ensure equilibrium conditions as given by Eq. 37. After the experiment the reactor was cooled in standing H_2S/H_2 gas. The samples were analysed by high temperature oxidation and IR measurement of SO_2 signal. In the two sets of conditions, 0.75 and 2 ppm H_2S/H_2 gas mixtures were measured. They would evidently be close to each other, but should show consistent adsorption behaviour.

3.1.2. **Results**

The coverages are presented in Fig. 13, where there decreasing coverage of sulphur at increasing temperatures is observed. The data for Ir and Pt have some uncertainty due to their low absolute adsorption as given in Appendix B. But for especially Rh and Ru there is a good correlation between the temperature and the coverage. The data obtained for the experiments are not precise enough to produce good models that describe the data. The results though give a good qualitative description of the sulphur adsorption on noble metal catalysts. The obtained data for sulphur adsorptions have been converted to coverages based on a standard reference experiment (12 ppm H_2S/H_2, 550°C) that ensures full coverage.

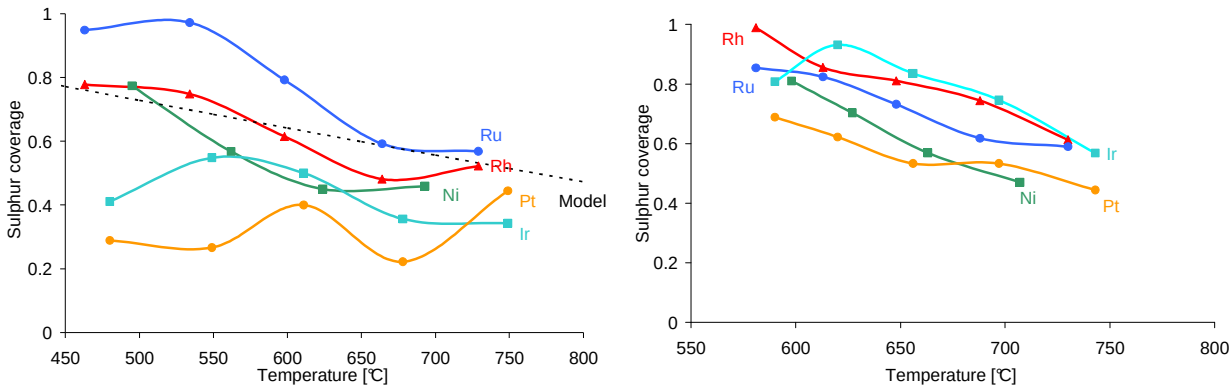

Figure 13. Coverage plotted as a function of temperature for 0.75 (left) and 2.0 ppm (right) H_2S/H_2 gas mixture. Full coverage is given by low temperature and high H_2S/H_2 ratio, see appendix B. The model is given for Ni in work by McCarty and Wise. [37]

The H_2S/H_2 ratios were chosen based on the data by McCarty and Wise [32,37,34,36,35], so it is affirming that for this sulphur gas concentration a temperature effect would be expected. The obtained results compares qualitatively with data reported by McCarty and Wise on Ru, Ni, Pt and Ir based catalysts.

The catalyst sinters during the experiment and it was seen by subsequent standard sulphur adsorption measurements on certain samples that there is sintering up to 15% at the highest temperature. This further complicates the data and the uncertainty has to be included when analysing the data. Overall the data confirms the expected trends and levels for sulphur chemisorption, but more precise measurements are needed to make a model that precisely can describe the sulphur coverage as a function of temperature and H_2S/H_2 ratio.

3.2. Carbon formation

The interest in noble metals for steam reforming catalysts stem from the lower risk of carbon formation. Basically there are three forms of carbon formation that can be critical for the steam reforming process. Polymer film ("gum"), pyrolytic coke or whisker carbon.

Table 5. The possible formation of carbon, where the whisker carbon is most relevant for this study [2].

Carbon type	**Phenomena**	**Critical parameters**
Gum	Blocking of metal surface	Low S/C ratio, low temperature, higher hydrocarbons
Pyrolytic coke	Encapsulation of catalyst pellets	High temperature, residence time
Whisker carbon	Breakup of catalyst pellets	Low S/C, high temperature, olefins

At low temperatures hydrocarbons might adsorb to the surface and can slowly transform into a polymer film equivalent of gum, which effectively blocks the Ni surface. At high temperatures, pyrolysis of higher hydrocarbons may lead to pyrolytic coke. This coke can encapsulate the catalyst pellets. The most critical carbon formation for methane steam reforming is carbon whiskers. Carbon whiskers grows from a metal particle as a tube, and for the special case of one graphene layer in the tube it is also referred to as carbon nanotubes. Adsorbed carbon atoms diffuse on the surface, where step-edge sites act as growth centres for graphene layers on the metal surface. Additional carbon atoms diffuse to the continued growth of these carbon whiskers. The mechanical strength of graphene effectively destroys the catalyst pellets. This will increase the pressure drop through the reactor, eventually stopping the process. The whisker carbon has a higher energy than graphite due to the high surface area of the structure, so the conditions for whisker growth cannot be determined

directly from graphite thermodynamics. The dependency of the thermodynamics on the metal particle size makes it only possible to determine experimentally.

There are three main factors determining the whisker growth; the particle size, the carbon potential and the specific metal. The geometry is important for the growth of carbon whiskers. Larger terrace areas are necessary for a full graphene layer to develop. It is observed that on small metal particles, carbon have minor affinity for whisker growth compared to larger particles [2]. Carbon deposition can come from three main reactions by Eq. 39 – 41.

$$CH_4 \rightleftharpoons C + 2H_2 \qquad \Delta H = 75 \text{ kJ/mol} \qquad (39)$$

$$2CO \rightleftharpoons C + CO_2 \qquad \Delta H = -172 \text{ kJ/mol} \qquad (40)$$

$$CO + H_2 \rightleftharpoons C + H_2O \qquad \Delta H = -131 \text{ kJ/mol} \qquad (41)$$

The three reactions are methane decomposition, the Boudouard reaction and the CO reduction reaction. The main focus will be on the methane decomposition reaction, since this is most relevant for the experiments performed. To evaluate the potential for whisker formation, the whisker equilibrium constant K_{pw} can be taken into consideration

$$K_{pw} = \frac{P_{H_2}^2}{P_{CH_4}} \qquad (42)$$

This is an experimental K_{pw} value for the whisker thermodynamics. It is valid qualitatively for similar systems but cannot be generally applied to other catalysts with a different metal or different metal particle sizes.

3.2.1. **Experimental**

A ruthenium catalyst has been tested in a thermo gravimetric (TGA) setup. The setup consisted of a glass tube with a glass basket attached to a micro-balance. The formation of carbon has been tested using both a mixture of CH_4 and H_2 for methane decomposition studies. Furthermore has CH_4/H_2O equilibrated gas mixtures been used for studying the influence of oxygen containing species. There is used a single large pellet of 1wt% Ru/ZrO_2 catalyst to ensure full conversion of the gases and

thereby having equilibrated gas in the entire catalyst pellet. The pellet is placed in the open structured basket, so there is easy interaction between the gas flow and the pellet.

The measurements have been conducted in the temperature range of 500-750°C. For the majority of the experiments, the catalyst have been exposed to a H_2O/H_2 gas mixture (ratio 1:1) at 750°C for approximately 2 hours to ensure no carbon residue and stable weight. The temperature was adjusted and the inlet flow was set at either a high H_2O/CH_4 or high H_2/CH_4 ratio. Then the methane flow was increased by a concurrent similar decrease in inert N_2 flow. The stable total flow ensures no artificial influence on the microbalance. When the methane level reaches a certain flow compared to the H_2O or H_2 flow, then carbon starts forming and this carbon limit is observable by the weight increases. The catalyst pellet has a total weight of 450 mg and the uncertainty of the microbalance is 0.1 mg. The methane flow gradient is kept significantly slow to ensure that it is possible to determine the carbon limit for the catalyst. The time frame for each of these experiments therefore has been in the order of 10-30 hours.

3.2.2. **Results**

Thermodynamically, graphite is the most favourable carbon type that can be formed. So when comparing data in Fig. 14, then the carbon formation limit is compared to graphite formation. The actual whisker carbon have a significantly higher energy and hence more difficult to form. In Fig. 14 is seen the carbon limits for a 1 wt%Ru/ZrO_2 catalyst, where it is evident that the limits are significantly lower than graphite formation. There is also a difference between the potential for carbon formation depending on the presence of oxygen containing species. It is assumed that the CH_4/H_2O gas mixture is in equilibrium and the equilibrium CH_4 and H_2 concentrations are calculated for these experiments to estimate the K_{pw} value.

If this reaction should not be in equilibrium, then the equilibrium constant for carbon formation for the CH_4/H_2O data would be expected to above the CH_4/H_2 data due to lower H_2 concentration in the CH_4/H_2O experiments. So oxygen containing species apparently play a role in lowering the carbon formation limit.

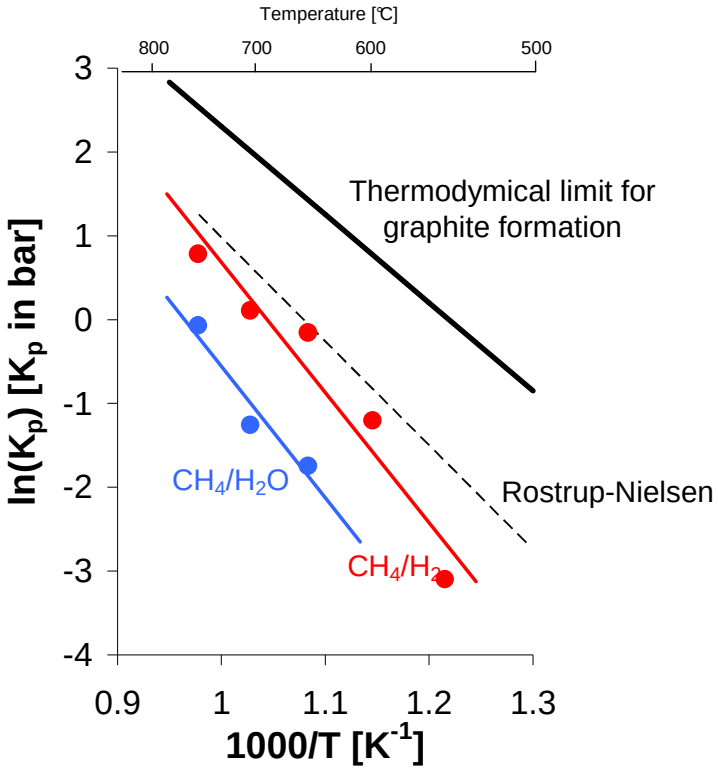

Figure 14. The carbon formation limit as a function of temperature. K_{pw} is for the methane decomposition reaction is calculated for both reactions. Reference by Rostrup-Nielsen [9].

The values for the CH_4/H_2 experiments correlates very well with similar experiments obtained in a study by Rostrup-Nielsen and Hansen [9]. That investigation also shows the particle size has a significant influence on the carbon limit, and that small particles are less prone to carbon formation. This is likely due to the carbon structure, which is forming on terrace sites, since it needs to be a stable whisker carbon structure that can be expanded.

Experiments have also been done on a pre-carborized sample and the carbon limits have been measured qualitatively on the ruthenium catalyst to form carbon at a higher equilibrium value. This supports the notion of having a carbon structure that continuously grows. The initial carbon formation is the threshold for the actual carbon formation on a ruthenium catalyst. The obtained results supports the investigation by Rostrup-Nielsen and Hansen [9], which shows similar results for the carbon formation on other noble metals. Their results show that all noble metals (Ru, Rh, Ir, Pt and Pd) have significantly lower affinity for carbon formation than nickel does. Post characterization by TEM analysis of the sample showed clearly the formation of whisker carbon, which support that this type of carbon formation is responsible for the weight increase.

3.3. Stabilisation of catalytic activity

Heterogeneous catalysts can deactivate in different ways. It can be due to sintering, poisoning or loss of catalytic material in the reactant stream. These phenomena are usually possible to model, either by a simple linear model or more complex models. But overall it is possible to predict the activity as a function of time.

In the steam reforming catalyst research a deactivation has been observed as sketched in Fig. 15, which is not possible to model directly. Basically the catalyst deactivates in a medium temperature regime of 550-700°C. This happens when the temperature is increased in a standard steam reforming gas mixture, e.g. 20% CH_4 and 80% H_2O. For such experimental conditions the catalyst will deactivate. In this section it will be attempted to explain this phenomenon and derive a way to ensure stable activities. The basis will be in Fig. 15 sketching the deactivation and subsequent reactivation. Time plays a crucial part for the deactivation phenomenon. The time factor for the conditions applied is in the order of hours. With such time lengths it is difficult to obtain similar results for similar experiment and fluctuations have been observed. Another independent variable is the catalyst pellet size. When using large pellets this phenomenon is not observed, while significantly smaller pellets are prone to this deactivation. At the reactor conditions used here, the deactivation is observed for a pellet size range of 125-300 μm. Larger particles in the size range of 300-500 μm did not show the same deactivation phenomenon. The biggest difference between different size fractions is the conversion inside the pellet. In larger pellets there is more equilibrated gas in the centre of pellet, whereas for smaller size fractions the rate will be almost independent of location in the pellet. It will be evident that this feature is also central to understand the phenomenon.

The experiments are done with 30 min between each gas measurement, though 60 min between each temperature. With three gas measurements at each temperature it gives 120 min between the first measurements for each temperature. Interestingly the catalyst reactivates at higher temperature of 700-800°C as also shown in Fig. 15. For the reactivation there is also a time dependency, where it takes hours if not days for full reactivation. At present three theories will be proposed to explain the observed phenomenon.

- Metal support interaction
- Carbon deposition
- Poisoning

There is neither direct evidence for either of the theories, but indications towards that metal support interactions form the strongest arguments for the explanation of the observed deactivation.

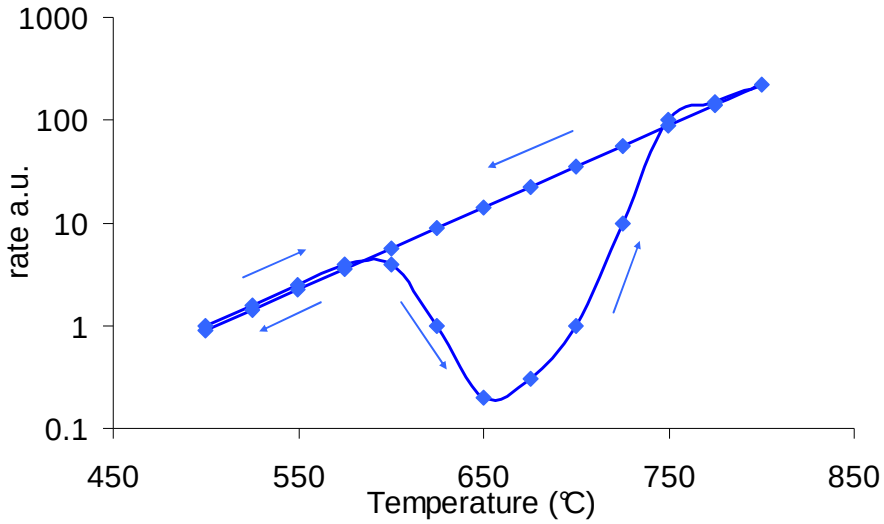

Figure 15. Sketch of the deactivation phenomenon based on experimental observations. Temperature increase from 500 to 800°C and reverse down in temperature. Deactivation in medium temperature range (600-650°C) with increasing temperatures, reactivation at higher temperatures >700°C. No deactivation on the return path.

The phenomenon has been observed for the following catalysts: Rh/ZrO_2, $Rh/MgAl_2O_4$, Ru/ZrO_2, Ru/Al_2O_3, $Ru/MgAl_2O_4$ and $Ir/MgAl_2O_4$. So the phenomenon is not limited to either a specific metal or a specific support. The phenomenon can be regarded as a general issue. The deactivation gives a lot of constrains for kinetic measurements of the steam reforming reaction. It can be very difficult to achieve stabile activities in the medium temperature range of 550-700°C and it is difficult to replicate experiments. It is possible to obtain stable activities after the first temperature cycle given by Fig. 15, where the catalyst remains stable in most circumstances. The temperature can be cycled up and down in temperature with expected activities. So it is possible to obtain a stable catalyst for measuring intrinsic or near intrinsic activity by applying this deactivation and reactivation cycle.

3.3.1. **Results**

Here is presented the obtained results demonstrating the steps for achieving stable activities. The results will be shown with rates as a function of temperature. This rate is determined by assuming a

simple first order kinetics and then analytically calculate the inlet reaction rate. This does not include any kinetic effect except the first order in methane partial pressure, but due to the large difference in activity this will be an acceptable way of presentation. The second cycle will also be shown in some instances, where it can be seen that the catalyst is usually stable after the first temperature cycle. In Fig. 16 is seen the first experimental results obtained by cycling the temperature. If the 8 mg 5%Rh/$MgAl_2O_4$ experiment is followed, then it starts deactivating at 550°C and continues deactivating until 650°C. From 750°C the catalyst starts reactivating again. On the downward temperature ramp there is no deactivation. The second cycle (grey) then makes an increase and decrease in temperature without any significant change in activity. In Fig. 16 it is seen that the effect of changing the amount of rhodium catalyst for similar flow conditions. The deactivation starts at a higher temperature for a larger catalyst amount, so likely the conversion have an influence on the deactivation.

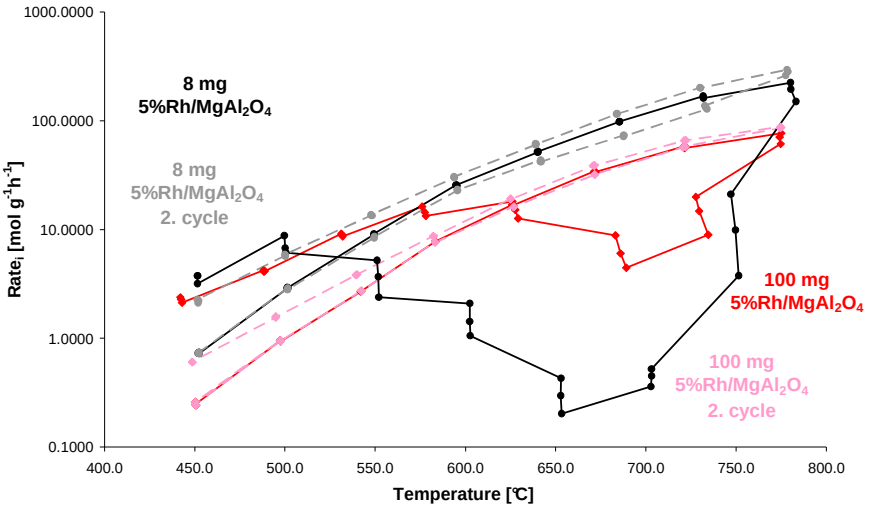

Figure 16. Deactivation experiments for rhodium catalysts for different catalyst amounts (8 and 100 mg). Inlet feed is 2 Nl/h CH_4 and 8 Nl/h H_2O apart from at 450-550°C where 0.8 Nl/h H_2 was added.

For low temperature kinetic studies it can be necessary to have a high catalyst amount, as it is necessary to achieve a higher activity than the low 2.cycle activity (light red) observed in Fig. 16. In the experiments in Fig. 17, the holding time at 800°C is altered significantly and three time length of 2 and 77 hours are used. It is evident that longer holding times yield a higher final activity. It would more likely be expected that long holding times at these conditions would cause sintering hence having the reverse final activities. This is not observed, so time is important for the full rearrangement of the support material.

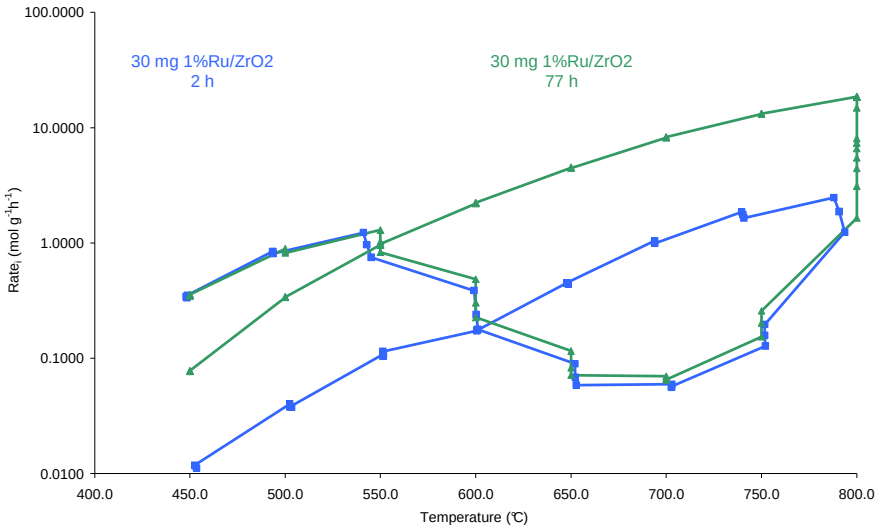

Figure 17. Deactivation of ruthenium catalysts as a function of holding time at 800°C. Inlet feed is 2 Nl/h CH_4 and 8 Nl/h H_2O apart from at 450-550°C where 0.8 Nl/h H_2 was added.

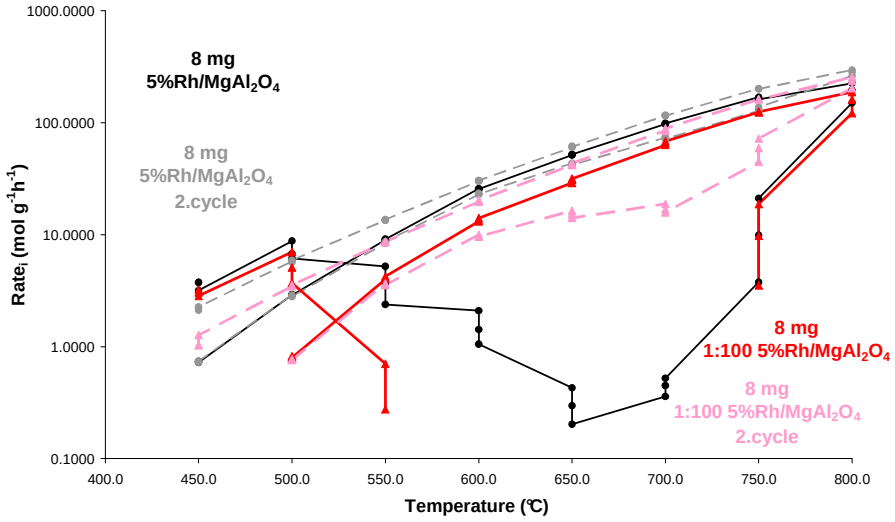

Figure 18. Deactivation for rhodium catalysts as a function of the dilution. Inlet feed is 2 Nl/h CH_4 and 8 Nl/h H_2O apart from at 450-550°C where 0.8 Nl/h H_2 was added.

The effect of diluting the catalyst is shown in Fig. 18, where the catalyst sample have been diluted by a factor of 100. There is still the same amount of catalyst in the sample. The catalyst have been crushed to grains (<45µm) and retabletted mixed with inert. This results in effectively having smaller catalyst grains but similar size pellets, catalyst amount, and increases the deactivation phenomenon substantially. The main effect of this dilution is on the gas mixture near the catalyst,

where the diluted catalyst experience more inlet gas conditions, whereas the undiluted catalytic material observed a more equilibrated gas mixture. So the deactivation is faster in inlet gas than in more equilibrated gas. The highly diluted sample also slightly deactivates in the second temperature cycle, so it is more difficult to keep the small grains with a stable activity even after one temperature cycle. There has likely not been a full rearrangement of the support at the high temperature, which is necessary for obtaining a stable catalytic activity.

Overall, the steam reforming catalysts will have a stable activity if they are exposed to a temperature of 800°C for at least 75 hours in a H_2O/CH_4 gas mixture for ruthenium. For other noble metals it has been found that similar long time periods are necessary for full reactivation. The deactivation, reactivation and stable activity conclusions are valid for this specific methane steam reforming system.

3.3.2. **Discussion**

There is no conclusive evidence on the origin of the observed deactivation. To add to the complexity then similar observations have been done on a different reactor system with the same results, so it is not linked to this specific reactor system. Neither has it direct link with gas impurities as gases have been changed during the experimental period. As given in the introduction; poisoning, carbon deposition and metal-support interactions are possible explanations.

If poisoning is considered at first then it could be sulphur, alkali metals or oil residue from sources such as the support, inlet gases or the reactor system. This explanation is in agreement with the observations that it is only present in the first cycle and not for the second. But the observation that catalyst grain size makes a difference makes it difficult to imagine that a poison should be dependent on the diffusion in the catalyst pellet to this degree.

Carbon formation could origin from methane or other carbon containing species, e.g. CO. As the severity seems to increase in inlet gas conditions rather than equilibrated gas conditions then methane could be the cause of the deactivation. Though the observation that it is only present in the first cycle and not in the second cycle is at first not coherent with the methane decomposition reaction. Studies by Beretta et al. [44,45] on Rh/Al_2O_3 catalysts for CPO activity shows strong deactivation around 500-600°C for the first runs, especially dominant for the first two runs out of a total of eight runs. The sample then reactivates and becomes stable at a high activity. This observation is only valid for the wet impregnation with $Rh(NO_3)_3$, whereas $Rh_4(CO)_{12}$ impregnation in n-hexane of Al_2O_3 renders no deactivation phenomenon. So the impregnation is clearly a factor

for their phenomenon. It is proposed that a fast build-up of carbon occurs due to CO dissociation. The carbon build-up is supported by CO_2 formation in subsequent TPO analysis. It is proposed that in the subsequent runs the rhodium surface is modified and the number of low-coordinated sites is reduced, which will reduce the CO dissociation rate. This could also be the case for methane decomposition, but it does not explain the absence of deactivation for the second cycle, as all low-coordinated sites should disappear.

At present the best explanation for understanding the phenomenon is metal-support interaction. There have previously been conducted extensive studies of the strong metal-support interaction (SMSI) [46]. The metal-support interaction is in this case likely not due to reduction of the surface, hence hydrogen provided no extra deactivation and the inlet gas (CH_4/H_2O) has an increasing effect on the deactivation rate. Instead of surface reduction phenomenon, it is more likely that the rearrangement of the support and/or the metal is the reason for this phenomenon.
Studies of similar systems have shown rearrangement of support due to the temperature and gas effects. Chen et al. [47] studied Rh supported on Al_2O_3 on a Mo(110) surface using EELS of absorbed CO, CO TPD and Auger spectroscopy of the system before and after heating to 827°C in vacuum. They found that Rh lost the ability to adsorb CO after this treatment, but the Rh Auger signal is still present indicating that Rh is still present near the surface. The gas did not play a role, but some short length rearrangement has apparently occurred. Bernal et al. [48] have studied Rh/Y_2O_3 catalyst by SEM showing that the impregnation have a significant influence on the support morphology. It changes from crystalline structure to an amorphous structure by impregnation with an aqueous solution of $Rh(NO_3)_3$. Wong and McCabe [49] studied Rh/Al_2O_3 catalysts by high temperature oxidation (HTO, 5%O_2, 800°C), reduction (HTR, 5%H_2, 800°C) and re-oxidation (RO, 5%O_2, 500°C) for the influence on H_2 chemisorption and CO oxidation activity and they studied the samples using ETEM and IR. The HTO treatment resulted in low H_2 chemisorption, low CO oxidation and low IR CO adsorption band intensity. These observations were best explained by subsurface diffusion of Rh, though other explanations were possible. Subsequent HTR treatment results in more rhodium being visible and finally the RO produces nearly all the rhodium from the fresh sample. Whether a re-dispersion is taking place or another mechanism, it is clear that there is strong interaction between the support and the Rh.

Based on the results compiled a simple model for the deactivation and reactivation phenomenon is proposed in Fig. 19. In the model the metal particle is adhering to the surface. In the first heat treatment at 500-600°C there occurs some interference between the metal particle and the support. This can cause a full deactivation phenomenon as sketched and the activity is recovered by a high temperature treatment uncovering the metal particle.

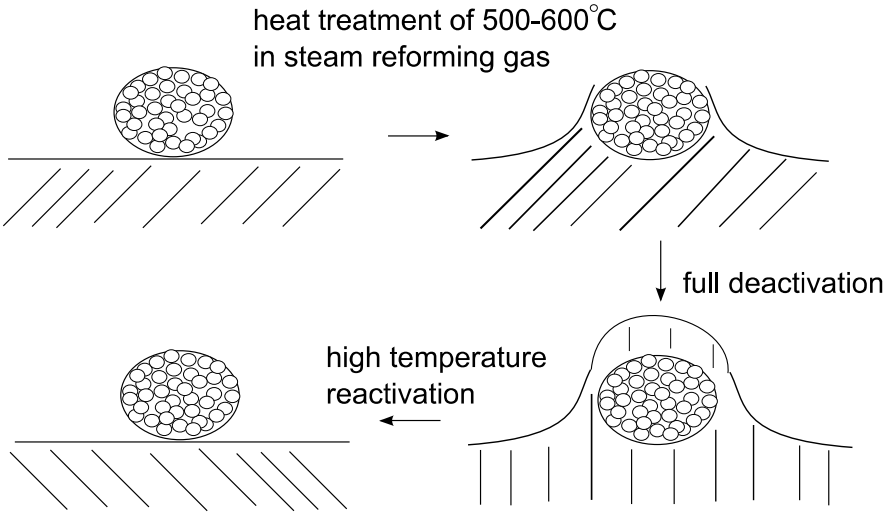

Figure 19. Proposed deactivation sequence, where there are two stable forms of support material. The second one is formed through a heat treatment that deactivates the catalytic activity.

In the second cycle there is not observed significant deactivation and it is possible that there exist different configurations of supports. It is proposed that an amorphous support is present initially, probably due to the impregnation by strongly acidic noble metal solutions. Energetically, surface oxides have an energy in the order of 0.5 J/m^2 equivalent to about 20 kJ/mol, while surface energies of metals are of the order of 2 J/m^2 corresponding to 80 kJ/mol. To cover the surface as sketched in Fig. 19 it is necessary to move support surface group, like –OZrOH from the support to the metal surface. This will cost approximately 20 kJ/mol if it is replaced by a –OH group on the ZrO_2 surface. It is then assumed that the binding energy of the –OZrOH is equivalent to an –OH group on the metal. Binding –OH groups on noble metal steps as in Eq. 43 have been calculated to be -61, -34 and -26 kJ/mol for Ru, Ir and Rh respectively [26].

$$H_2O + Me_{step} \rightleftharpoons Me_{step} - OH + \frac{1}{2}H_2 \qquad (43)$$

By an overall combination it is an exothermic reaction. It is possible to cover the metal surface by oxide as the entropy change will likely be negative as well, due to a more disordered system. So it is

necessary to have sufficient oxidizing conditions to form –OH groups on the oxide, but not too oxidizing conditions that the metal will oxidize. This can be fulfilled by the steam reforming gas mixture. Some kinetic energy is necessary for the support to start moving, which will be dependent on the exact support and the gas mixture. At the applied conditions this is observed to be 550-650°C. There is a competing reaction of methane dissociation taking place as well. At this intermediate temperature the conditions favours the deactivation kinetics. At higher temperatures the methane dissociation will start taking place at some of the free terrace sites. Products will start forming and carbon containing species such as CO have a high binding energy to the low-coordinated sites. It can be speculated that this will eventually force the support of the metal particle. The final state of the support has to be different than the original. The strong rearrangement that has taken place from an amorphous structure to a crystalline structure, will give a more stable support structure that is not as prone to rearrangement.

This model is highly speculative and these overall considerations do not take strain in the oxide layer over the metal or in the metal into account. The energy difference between the bond strengths of Me_{step}-OH and Me_{step}-OZrOH and the additional surface energy of small noble metal particles. However even though these issues have not been taken into considerations the experiments show that the trends are generally valid for a wide rage of metals and supports.

3.4. Summary

Characterization of the catalysts is important as it is necessary to understand the activity at relatively precise range. The sulphur characterization is a good way to relatively simple analyse multiple samples and the obtained results proves to be in line with previous reported data. For full utilisation of this results, more comparison with other techniques such as H_2 chemisorption and TEM is necessary. The catalyst activity in terms of stability have been addressed, where a description of the obtained method for stabilisation is presented. Furthermore, it is possible to explain the stable catalyst activity by the proposed metal-support interaction mechanism.

4. Sintering – promoted catalysts

Sintering or the growth of the supported metal particles results in loss of active surface area and is of great importance for high temperature catalysts. A significant part of the loss in activity for catalytic systems arises from sintering and therefore understanding the mechanism is essential in trying to minimize this issue. Generally there have been proposed two mechanisms to describe the sintering process

- Ostwald ripening
    - Atoms can self-detach from metal particles, and then diffuse on a support surface until they reach another metal particle, where they can attach again. It is assumed that the metal particles are stationary in the process. There will be a driving force for atoms migrating from smaller crystallites to larger crystallites, due to the higher vapour pressure for smaller particles.
- Particle migration and coalescence
    - This mechanism describes the migration of entire particles and the metal particles on the support surface due to metal surface atom mobility. The atom movement is due to instability of the metal atoms on the surface of metal particles. The atoms diffuse on the metal surface, effectively causing a movement of the metal particles, when enough particles have moved to one side of the metal particle. Eventually the particles will collide and coalescence.

These two sintering routes are generally used to describe the sintering process. At higher temperatures it would also be possible to have atom evaporation followed by gas diffusion and re-adsorption on other different locations on the support.
The atmosphere around the particles has a significant influence on the sintering process, since it is changing the chemical potential of the surface. Since sintering is usually an irreversible process, it is more easily prevented than reversed. Though there have been reports of re-dispersion for both platinum and rhodium metal particles through oxidation and re-reduction procedures [50,51,52,53].

The principal factors influencing the sintering process are temperature, atmosphere, metal type, metal dispersion, support and support surface area. Sintering rates are exponentially dependent on the temperature, since the surface diffusion of atoms is determining the sintering process. For

metals relevant for the steam reforming reaction, experiments in different types of atmospheres have been carried out. In H_2, the sintering rate generally increases with decreasing metal melting temperature, Ru > Ir > Rh > Pt > Ni, where as in an oxygen atmosphere the order is Rh > Pt > Ir > Ru due to oxide formation [42]. Hence the atmosphere will have a significant influence on the sintering rate.

Generally metal-support interactions are weak in comparison with metal-metal interactions, but some supports have significant influence on the thermal stability. Furthermore, sintering rates are lower on highly porous supports compared to non-porous supports, both due to pore dimensions, defects and surface area. The most important sintering factor for heterogeneous catalysts is the geometrical hindrance caused by the support structure. A large surface area of a support constitutes the biggest geometrical hindrance for sintering. Support rearrangement is therefore an important aspect for the sintering process. Trying to include all these parameters in one simple model is not directly possible. But it can be attempted to combine all these factors into empirical models.

A sintering model for Ni steam reforming catalysts has been proposed by Sehested et al. [54,55,56,57]. The study has been conducted on Al_2O_3 and $MgAl_2O_4$ supports and the determining parameters are time, temperature and P_{H2O}/P_{H2} ratio. It is suggested that Ni_2-OH complexes are the major transport species on the metal surface in a H_2O/H_2 atmosphere enhancing the particle migration and coalescence rate, which is the predominant mechanism at low temperatures (<600°C). At higher temperatures (>600°C) the Ostwald ripening mechanism is favoured via atom migration on the support. The equation that describes the model is given by Eq. 44.

$$\frac{d_{Ni}}{d_{Ni,0}} = \left(1 + a \cdot e^{-E_a/RT} \cdot \left(\frac{P_{H_2O}}{P_{H_2}^{0.5}} \right)^m \cdot t \right)^{-1/(n-1)} \tag{44}$$

Where d_{Ni} is the Ni average diameter, $d_{Ni,0}$ is the initial Ni average diameter, a is a temperature-independent pre-exponential factor, E_a is the activation energy of the sintering process, m denotes the effect of the atmosphere on the sintering rate and n is the time-dependence in terms of a number related to the type of sintering mechanism. The time-dependence, n, was found to change from 8.6 at low temperature to approximately 4 at high temperature, indicating a shift from particle migration and coalescence at low temperature to Ostwald ripening at higher temperature [57].

When reviewing the parameters that are possible to change, the temperature and atmosphere is usually set by the actual process. The support is a key parameter for reducing sintering, by having a high surface area support for sintering reduction. This can be done by geometrical hindrance by either changing support or support preparation method. Additives could also be used for extra geometrical hindrance. Fe have been observed to suppress Cu sintering on a water gas shift catalyst [58]. Generally the methods for reducing sintering are often system specific. There exists few general methods to reduce sintering; hence the specific experiment usually sets the necessary operating conditions.

The main goal in dealing with sintering is to have well-dispersed metal particles, which must be taken as a prerequisite for further discussion in this section. In the next section a possible method of reducing the sintering for steam reforming catalysts operating at steam reforming conditions is proposed.

4.1.1. **Promoted catalysts**

A general approach is to consider limiting the diffusion of metal atoms with regards to atom surface diffusion on the metal particle and atoms leaving the particle to start diffusing on the oxide support. This is the starting points for the sintering mechanisms and could be obtained by alloying an active host metal with a high surface energy element. The surface energy of this new element (promoter atom) should be relatively high compared to a host atom located at the same position. The high surface energy element (promoter) should be located in the bulk of the host metal particle as sketched in Fig. 20. When the metal atoms starts diffusing at high temperatures the host metal atoms can move freely among other host metal atoms, but it is not energetically favourable for a promoter atom to be exposed at the surface due to the high surface energy. Consequently reducing the mobility of the alloyed particle, since it is controlled by detachment of surface atoms should diminish the sintering process. There will be no changes in the understanding of which metals are active for the steam reforming reaction, so Ru, Rh, Pt and Ir will be experimentally tested to investigate this theory. This is not regarded as a surface alloy phenomenon for increased activity, just increased long-term stability due to reduced sintering. This model is controlled by a series of factors that determines whether an element is a good promoter for a catalytic active metal in the steam reforming process. Some of the considerations needed for promoted catalysts are given by

- Segregation energy

- Surface energy
- Phase diagram / alloy
- Heat of formation
- Oxidation potential
- Atom size mismatch

The promoter atom should have positive segregation energy in the alloy, hence staying in the bulk and preventing sintering. It should alloy with the host metal, so it forms a mixed particle and not be significantly influenced by reactants (H_2O, CO, CO_2, H_2) at relevant reaction conditions. For steam reforming, a significant factor is the possible oxidation.

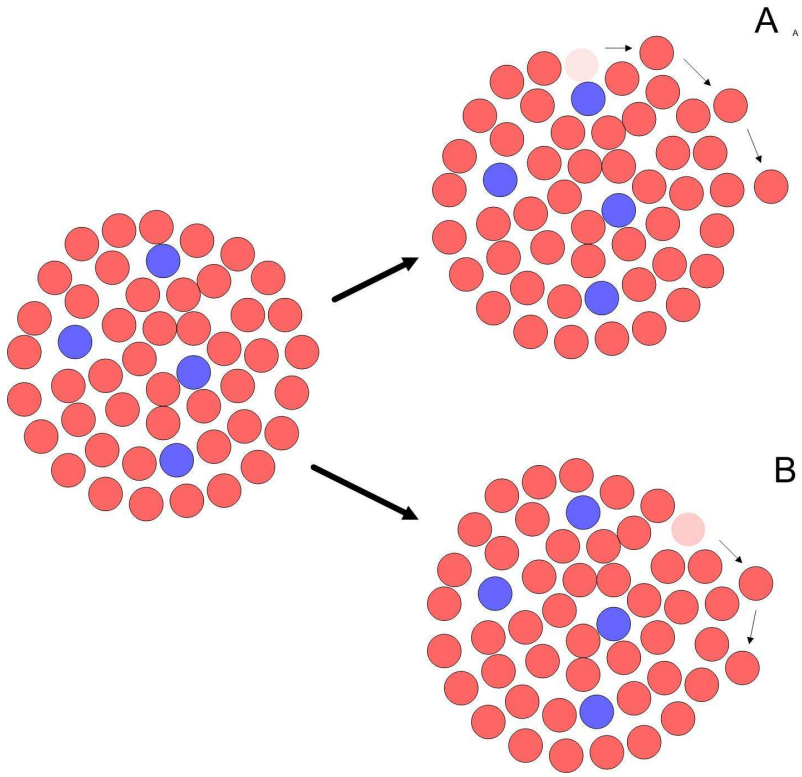

Figure 20. Promotion effect: An active host material (red), such as Ru, Rh, Pt or Ir, with a promoter (blue). Atoms will not diffuse as in pathway A, since the promoter have a higher surface energy than possible for the diffused atom. Pathway B will occur, but eventually pathway A needs to occur for actual sintering.

4.1.2. **Thermodynamics for surfaces**

First some general thermodynamics for surfaces are considered. The thermodynamic properties of a surface is defined as the excess of the bulk thermodynamics, due to the presence of the surface

surrounding the condensed phase [59]. The total free energy of a system *G* can be expressed by Eq. 45.

$$G = NG^{\circ} + \alpha G^{s} \tag{45}$$

Where G° and G^{s} are the free energy per atom and per unit area of surface respectively, *N* is the total number of atoms in the solid and α is the surface area. To increase the surface area or expose new bulk atoms in the surface, it is necessary to move an atom from bulk and at the same time move a surface atom along the surface to accommodate the new surface atoms. The reversible work δWs that is required to increase the surface area under constant temperature *T* and pressure *P* is given by Eq. 46.

$$\delta W^{s}_{T,P} = \gamma \cdot d\alpha \tag{46}$$

Where γ is the surface tension. In a bulk fcc metal, each atom have 12 nearest-neighbour atoms. For the fcc(111) closed packed surface, there is 3 missing bonds at the surface, so if a bulk atom should evaporate, then it would be necessarily have 12 broken bonds, whereas it only takes 3 broken bonds to create a new surface atom

$$\gamma a = \gamma_m \approx \frac{3}{12}\Delta H_{subl} = 0.25\Delta H_{subl} \tag{47}$$

Where γ_m is the molar surface tension. Experimentally, there is established a correlation between the heat of sublimation ΔH_{subl} and the surface tension γ_m [60] for a series of metals including Ni and Pt, but not including Rh, Ru and Ir, which gives a good understanding for the surface tension of solid metals. This correlation is given by Eq. 48.

$$\gamma_m \approx 0.16\Delta H_{subl} \tag{48}$$

This correlation does not take into consideration the crystal plane orientations, which will have different surface tensions. It only describes the overall surface tension from metal supported particles. It is not necessary to evaporate an atom completely to create a new surface. In Eq. 47, the

relaxation of a freshly prepared sample in which the atoms will approach an equilibrium surface structure is not taking into consideration. This relaxation can lower the surface tension appreciably. The surface tension γ can be set equal to the specific surface free energy G^s, hence the creation of surface always results in a positive free energy of formation. The surface energy will always be minimized by restructuring to the lowest specific surface free energy. This is usually equal to the closest packing of the atoms.

As an overview, the energies for a binary promoter-host system are given in Fig. 21. In this figure are shown the sublimation, adsorption, solution and segregation energies for a promoter metal B that is dissolved at low concentrations in a host metal A. Due to the equilibrium between the bulk and the surface, there will always be some B present at the surface. If B forms a strong bond in the bulk, then the surface concentration of B is minimized. The extent of the surface segregation depends on the surface structure of A.

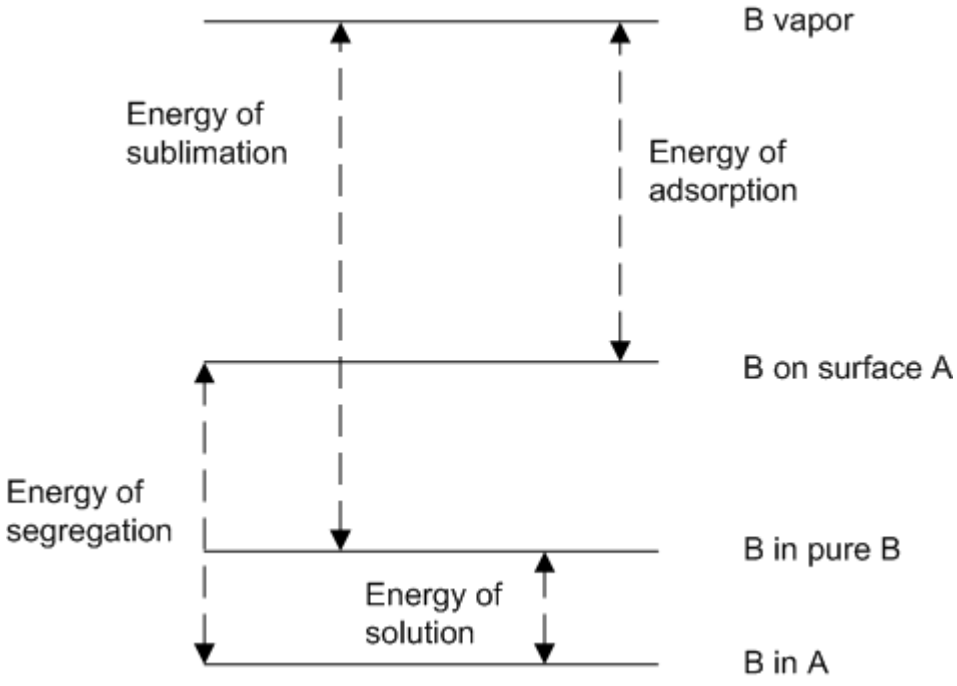

Figure 21. Relative energies of sublimation, solution, segregation and adsorption of promoter metal B with a host metal A.

If such a promoter-host system is created, then the segregation energy is the energy that is needed for promoter to be moved from the bulk phase to the surface of the particle. If the segregation energy is negative, then it is favourable for the promoter, to be at the surface of the particle. However, if the segregation energy is positive, then it is favourable for the promoter atom to remain within the bulk. The segregation energy depends on the concentration in the alloy and the difference

in surface energies between the pure elements. For the dilute systems it is possible to calculate the segregation energy, either by ab initio methods [61] or tight-binding scheme for transition metals [62].

4.1.3. **Ideal binary alloy systems – surface segregation**

When considering bulk chemistry, the chemical potential decreases for ideal binary alloy systems as compared to the chemical potential of a pure metal. The surface segregation depends on the difference in binding energies between two different atoms and two identical atoms. The driving force for this surface segregation gives rise to a change in the surface tension of the binary system compared to the surface tension of the individual constituents. The relationship between the surface mole fractions, x_A^s *and* x_B^s, and the bulk mole fractions, x_A^b *and* x_B^b, at ideal conditions can be derived to [59]

$$\frac{x_B^s}{x_A^s} = \frac{x_B^b}{x_A^b} \exp\left(\frac{(\gamma_A - \gamma_B)a}{RT} \right) \tag{49}$$

Where γ_A and γ_B are the surface tensions of the pure components and a is surface area covered by one mole of an individual component, assuming equal surface area for the two components. The term, $(\gamma_A - \gamma_B)a$, can be considered to be the segregation energy, $-\Delta H_{segr}$, to a first approximation. At increasing temperatures the difference between the surface tension becomes less important due to entropy effects, hence the surface concentrations will approach bulk concentrations. If the surface tension is not available, then it is possible to correlate the surface tension to the thermodynamic property of sublimation energy as in Eq. 48.

$$\frac{x_B^s}{x_A^s} \simeq \frac{x_B^b}{x_A^b} \exp\left(\frac{0.16\left(\Delta H_{subl_A} - \Delta H_{subl_B}\right)}{RT} \right) \tag{50}$$

This equation shows that the metal with the lowest sublimation energy will accumulate at the surface in excess to bulk conditions. The surface composition furthermore depends on an exponential function, not only in the difference of sublimation energy, but also in the temperature. At higher temperatures the bulk and surface concentrations will approach each other.

So far, it has been assumed that the bond energy is similar for all bonds, though it is necessary to include the enthalpy of mixing in Eq. 50. The surface composition in the regular solution monolayer approximation [59] is given by

$$\frac{x_B^s}{x_A^s} = \frac{x_B^b}{x_A^b}\exp\left(\frac{(\gamma_A - \gamma_B)a}{RT}\right)\exp\left(\frac{\Omega(l+m)}{RT}\left[\left(x_A^b\right)^2 - \left(x_B^b\right)^2\right] + \frac{\Omega l}{RT}\left[\left(x_B^s\right)^2 - \left(x_A^s\right)^2\right]\right) \tag{51}$$

Where l is the fraction of nearest neighbours to an atom in the plane, m is the fraction of nearest neighbours below the layer containing the atom and Ω is given by

$$\Omega = \frac{\Delta H_m}{x_A^b\left(1 - x_A^b\right)} \tag{52}$$

Eq. 51 describes the difference in surface concentration by including the enthalpy of mixing, ΔH_m. The irregularities of solid surfaces especially for particles where steps and kinks are present have been included by the values for l and m, the fraction of in-plane and out-of-plane nearest neighbours. This also shows that the effect of promoting will be minor for smaller metal particles due to the increase in low-coordinated sites. Finally the reduction in strain can be included, since a large mismatch in atomic size will create a strain in the lattice. The strain energy is given by Eq. 53 [60].

$$24\pi\frac{K_{sm}G_{sm}}{3K_{sm}r_B + 4G_{sm}r_A}r_A r_B\left(r_B - r_A\right)^2 \tag{53}$$

Where K_{sm} is the bulk shear modulus of the promoter, G_{sm} is the shear modulus of the host metal, and r_A and r_B are the radii for the host metal and promoter, respectively. At the surface there is less strain for an atomic mismatch compared to a promoter atom placed in the bulk. In total the segregation energy can be given by

$$\begin{aligned}\Delta H_{segr} = {} & (\gamma_A - \gamma_B)a + \frac{\Omega(l+m)}{RT}\left[\left(x_B^b\right)^2 - \left(x_A^b\right)^2\right] + \frac{\Omega l}{RT}\left[\left(x_B^s\right)^2 - \left(x_A^s\right)^2\right] \\ & - 24\pi\frac{K_{sm}G_{sm}}{3K_{sm}r_B + 4G_{sm}r_A}r_A r_B\left(r_B - r_A\right)^2\end{aligned} \tag{54}$$

This includes the difference in surface tension, enthalpy of mixing, coordination number and the induced strain. It is possible to make qualitative calculations that show the effect of segregation on the surface concentration on the promoter atom. Since metal particles consist of an array of steps and kinks it is not possible to make a reasonable quantitative estimation of the effect.

The surface concentration changes due to the surface tension, mixing energy and the promoter radii are given in Fig. 22. Here it is observed that the surface concentration of the host metal A increases by increased promoter surface tension, whereas there is minor effects of the mixing energy. Within the normal radii then there is not a significant effect, but for large differences between the promoter and host metal then the promoter will segregate to lower the strain.

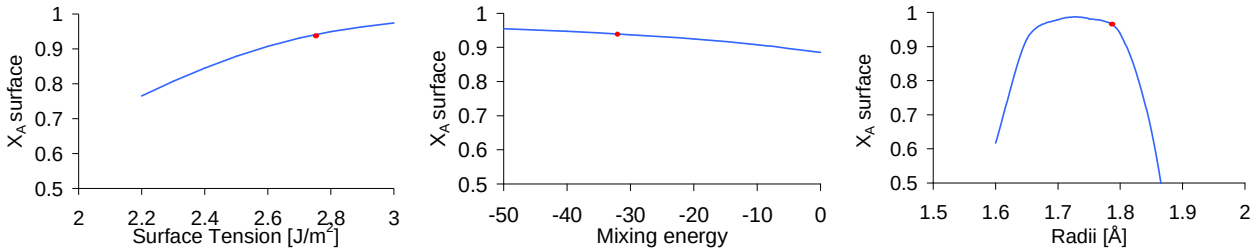

Figure 22. Surface concentrations of the host metal A. The promoter effect of surface tension, mixing energy and the atom radii is given. The red dot represents the Rh(host)/Ir(promoter) system.

These equations and observations for the promotion effect gives a good description of the effects. For more precise results it is necessary to use theoretical methods such as DFT to obtain the desired precision. But for a screening study, the considerations done here is sufficient for obtaining a series of possible sintering stable catalysts.

4.1.4. **Adsorbed inducing restructuring**

The gas atmosphere will also have an influence on the surface energy and hence the distribution of promoter atoms; giving an overall effect on the sintering. One key aspect is the possible oxidation, especially of promoter atoms. The oxidation potential is low for the steam reforming catalysts at relevant conditions, whereas promoter metals such as W, Mo and Re could potentially oxidize and reduce the promoting effect. It is therefore necessary to evaluate the oxidation potential of these metals.

Other adsorbate effects could come from CO, H_2O, CH_4, CO_2, H_2 or dissociation products of these. These adsorbates will to some extend influence the metal-metal bonds, inducing a restructuring

phenomenon. For traditional steam reforming nickel catalysts it is known that H_2O have an enhancing effect on the sintering rate, due to interactions with the metal particles. Estimating these effects is difficult and will be very system specific in terms of partial pressure of the gasses, binary metal mixture and temperature.

4.1.5. **Phase diagrams**

One possible way to evaluate the possible alloying of multiple metals is by phase diagrams that describes miscibility of metals. Phase diagrams describe alloy behaviour at a macroscopic level, therefore it is questionable if these diagrams provides an accurate description of nano size particles. However, in the following it will be assumed that phase diagrams can be used as guidelines as to whether two nano size particles are miscible.

At nano size range, there will generally be a better miscibility of two elements. It has been observed that bulk systems which are immiscible, were in specific cases miscible when particle size reaches a certain nano scale size [64]. Hence the phase diagrams can be used as a minimum criterion for the miscibility. In relation to the phase diagrams, the heat of formation can also be used for evaluating the potential mixture of formation.

4.2. Promoted noble metal catalysts

This chapter describes the actual process of rationally designing promoted noble metal catalysts. Four metals have been selected as possible candidates for new catalysts, which is ruthenium, rhodium, iridium and platinum, and are all active for the methane steam reforming process. It has been shown that Ru and Rh are more active than Ir and Pt catalysts [12], although the relative activity were within a few orders of magnitude. Thus, by stabilising a catalyst against sintering, it would still be an interesting catalyst if the metals could be promoted in such a way that the activity remains high even after long-term sintering.

If sintering is considered for these metals first, there exist limited systematic surveys of the sintering behaviour relative to each other. Studies show that in a reducing environment the ranking of the thermal stabilities of the four metals are Ru > Ir > Rh > Pt [42]. As described earlier there is a series of factors determining the sintering process including atmosphere and temperature as some of the most predominant factors. At first, it is possible to look at the melting temperatures of the metals as given in table 6 and it is seen that the noble metals have a higher melting point than a traditional nickel catalyst, which give more stability against sintering.

Table 6. The melting temperature [65] and surface tension [66] of a series of metals.

Metal	Rh	Ru	Pt	Ir	Mo	Re	W	Ni
Melting temperature	1964°C	2034°C	1768°C	2446°C	2623°C	3185°C	3422°C	1455°C
Surface tension [J/m^2]	2.70	3.05	2.48	3.00	3.00	3.60	3.68	2.450

An extra factor to be taken into consideration is the possible compounds formed under various gas conditions experienced during both stable operation and start-up procedures. A well known phenomena is the higher mobility of RuO_4 [42], compared to metallic Ru particles. The oxide can be formed during oxidizing conditions in the atmosphere at elevated temperatures. Another atmosphere induced issue is the formation of carbonyls. Nickel carbonyls are known to form at low temperatures (200-400°C) and CO partial pressures, but also Ru have been observed to form carbonyls [67]. The specific knowledge of the gas atmosphere influence is limited by the full understanding of the sintering process for these noble metals. Overall even noble metals with high melting temperatures and low metal loading on a high surface area oxide support will eventually sinter. So the challenge will be to reduce the level of sintering as much as possible.

4.2.1. **Promoters**

For each of the four noble metals (Ru, Rh, Ir and Pt) it is possible to review the segregation for possible promoters. It is essential that the promoter and host metal will not segregate; hence the segregation energy should be positive. The evaluation is done on the basis of the work by Ruban et al. [61]. Here the segregation energies are estimated by single impurities at close packed surfaces using DFT calculations at vacuum and 0 K conditions. Table 7 provide an overview of the possible configurations for promoted catalyst following the database of segregations energies, where the criteria is set at $E_{seg} > -0.05$. It is assumed that by choosing this level of segregation energy all possible promoters are included.

Table 7. List of possible promoters for the noble metals, based on calculated segregation energies [61].

Host metal	Possible promoter
Ru	V, Cr, Mo, Tc, W, Re, Os
Rh	Ti, V, Cr, Fe, Co, Nb, Mo, Tc, Ru, Ta, W, Re, Os, Ir
Ir	Ti, V, Cr, Fe, Co, Ni, Nb, Mo, Tc, Ru, Ta, W, Re, Os
Pt	Ti, V, Cr, Fe, Co, Ni, Cu, Zr, Nb, Mo, Tc, Ru, Rh, Pd, Hf, Ta, W, Re, Os, Ir

There is obviously a significant uncertainty associated with this method of selecting potential promoters. The promoter should be present at a reasonable low amount in order not to influence the activity of the catalyst, but also high enough amounts to make an impact on the metal particle. An essential issue for the promoters is the possibility of oxidation. The mixture used in the process will mainly consist of methane and steam, with a low partial pressure of hydrogen at the inlet. The oxidation potential can be estimated as

$$B\,H_2O + A\,Me \rightleftharpoons Me_AO_B + B\,H_2 \tag{55}$$

Typically, steam will be the predominant source of oxidation of the promoter. So the ratio for oxidation of the promoter can be estimated by Eq. 56.

$$\Delta G^{ox} = RT \ln\left(\left(\frac{P_{H_2}}{P_{H_2O}}\right)^B\right) \tag{56}$$

The hydrogen concentration is the lowest at the inlet of the reactor. When the reaction progresses the ratio increase and the oxidation potential is reduced. The gas ratio can be converted into an oxidation potential, taking the most stable metal oxide into consideration. The limit for the oxidation have been set at $\Delta G^{ox} \geq -25\,kJ/mol$ at 500°C to give a certain margin. This limit is equivalent of a P_{H_2}/P_{H_2O} ratio of 1/50. Formation and segregation energies have not been taken into consideration. This margin of oxidation is set to include all relevant elements and not exclude pre-emptively. The value does not equal zero since oxidation still has to overcome the segregation energy barrier and the oxidation potential has to be sufficiently high for pulling the promoter atoms out of the metal particle. The oxidation potential has not increased since the promoter will be

present as an oxide before reduction and it should be possible to reduce the promoter for incorporation in the metal particle. Below is seen a separation of the elements prone to oxidation and those that are not

Y, Sc, La, Zr, Hf, Ti, Ta, Mn, Nb, V, Cr < -25 kJ/mol < Mo, Os, W, Fe, Co, Ni, Re, Ru, Cu, Rh, Ir, Pd, Pt (57)

At this point before considering heat of formation and alloying, a few of the suggested promoter elements given by the right hand side of Eq. 57 have the possibility of forming carbon at the relevant reaction conditions. The carbon formation is the essential critical issue for choosing the noble metals as catalytic active material. The carbon can act in the same way as oxidation, effectively pulling some of the promoter elements out of the metal particles. This is a critical issue and the reason that noble metals have been chosen. Thus, Ni, Co and Fe are therefore excluded as they are known to form carbon at the relevant conditions of low steam/carbon ratio [68]. As this is a critical issue, it is the reason why noble metals have been chosen. Another element that is excluded is osmium due to formation of the highly volatile OsO_4 which is a poisonous compound. In table 8 a summary of possibilities for promoted catalysts is presented.

Table 8. List of possible promoters for the noble metals, based on calculated segregation energies [61].

Host metal	**Possible promoter**
Ru	Mo, W, Re
Rh	Mo, Ru, W, Re, Ir
Ir	Mo, Ru, W, Re, Ir
Pt	Mo, Ru, Rh, Pd, W, Re, Ir

4.2.2. **Stability and alloying**

To estimate the stability of the promoted catalysts, the predicted enthalpies are shown in table 9 for alloy formation of the possible promoted catalysts. Entropic effects are not included in these calculations, but would have yielded higher formation energies. The values are based on a 1:1 mixture, significantly different than a promoted catalyst, where there would a be significant surplus of the active host metal. Due to limited available data of diluted alloy systems, these values are given as even mixtures, although an evaluation done on data for diluted mixture would correspond better.

Table 9. Predicted enthalpy of formation (ΔH^{for}) for binary alloy (1:1) formation in kJ/mol [66].

Promoter / **Host**	*Mo*	*Ru*	*Rh*	*Pd*	*W*	*Re*	*Ir*
Ru	-22				-15	-1	
Rh	-23	2			-14	1	1
Ir	-32	-1			-23	-5	
Pt	-42	-2	-2	3	-30	-7	1

It is still believed that there is a reasonable correlation between the equal mixture and a more diluted mixture. Furthermore these energies are included in the phase diagrams for the alloys. These data are presented in table 10 and generally supports the stability information obtained from the formation energy data.

Table 10. Extract from phase diagrams of bulk mixtures [69].

Promoter / **Host**	*Mo*	*Ru*	*Rh*	*Pd*	*W*	*Re*	*Ir*
Ru	Solid solution at <35% Mo, $\Delta H^{solution}<0$				Solid solution at <30% W	Solid solution at all Re concentrations	
Rh	Solid solution at <10% Mo	Solid solution at <35% Ru			Solid solution at <15% W	Solid solution at <10% Re	Solid solution at <20% Ir, $\Delta H^{solution}<0$
Ir	Solid solution at <22% Mo	Solid solution at <38% Ru			Solid solution at <5% (high certainty)	Solid solution at <20% Re	
Pt	Solid solution at <20% Mo	Solid solution at <62% Ru	Solid solution at <10%Rh	Solid solution at all Pd concentrations	Solid solution at <33% W	Solid solution at <20% Re(high certainty)	Solid solution at <5% Ir

When combining these two datasets it is seen that it is possible to alloy most of the promoted catalysts proposed in table 9 and based on this screening study it is suggested to experimentally test these promising promoted catalysts.

4.3. Experimental

Based on the theoretical considerations, there are made a series of promoted catalysts. In table 11 an overview of the promoted catalysts which have been made for testing of the stability with respect to sintering is shown.

Table 11. Overview of the catalysts tested for sintering stability. A total of 36 catalysts have been produced, including two promoter concentrations and pure reference samples.

Host \ **Promoter**	*Mo*	*Ru*	*Rh*	*W*	*Re*	*Ir*	*Pt*
Ru	■			■	■		
Rh	■	■		■	■	■	
Ir	■	■		■	■		
Pt	■	■		■	■		

The support material is a standard $MgAl_2O_4$ (45 m^2/g). It is possible to achieve higher surface area of the support, but here it was favoured to have a relative stable oxide support. Hence it was calcined at 1050°C for 4 hours to reduce the surface area to 45 m^2/g. The support were then crushed and fractionized to a range of 2-2.8 mm.

To ensure a thorough investigation of the promoter effects, both 3 and 7 mol% of the promoter relative to the host metal is chosen for the test. The metal weight percentage of active metal is 4 wt% after reduction. The total weight percentage is slightly above 4 wt%. In appendix C the list of chemicals used in preparation of the catalysts is shown. A part of each sample have been exposed to sintering conditions of 830°C in a H_2O/H_2 (1:1 mixture) for 225 h at 30 bar pressure. This procedure ensures the sintering at a fairly high rate, enabling a measurable effect.

The activity measurements have been performed in reactor system 1. The system is a parallel screening unit with 10 reactors. The gases are mixed and distributed evenly through the reactors, by having an alumina powder resistance. The reactors consist of steel tubes (2.6 mm inner diameter) and samples (2-80 mg, 125-300 µm) are placed on top of quartz wool. To ensure consistent operating conditions, the samples are diluted up to 80 mg in total with inert high surface area $MgAl_2O_4$ as there a large difference in intrinsic activities between the metals. A thermocouple is place above the catalytic bed. The screening study of the catalysts was preformed in the range 350-500°C and with H_2O/CH_4 ratio of 0.6-2. The gas mixture was diluted with nitrogen (55-85% N_2) to

optimise the experimental conditions and measurement accuracy. Chemical compositions were measured with an Agilent 3000 micro gas chromatograph with nitrogen as internal standard.

4.3.1. **Results**

The main output of the results is the relative activity of the promoted catalysts. Each noble metal have been prepared both with and without promoters, hence it is possible to compare the level of sintering for a promoted sample compared to a pure metal. The methane steam reforming activity was decreased by a factor of 2-4 due to the sintering as seen in Fig. 23, hence there is a clear effect of the sintering process. It is seen that there is clear activity difference between the metals, with an order of Ru > Rh > Ir > Pt. Furthermore, it should be noted that the sintering order decreases as follows Rh > Ir > Pt > Ru.

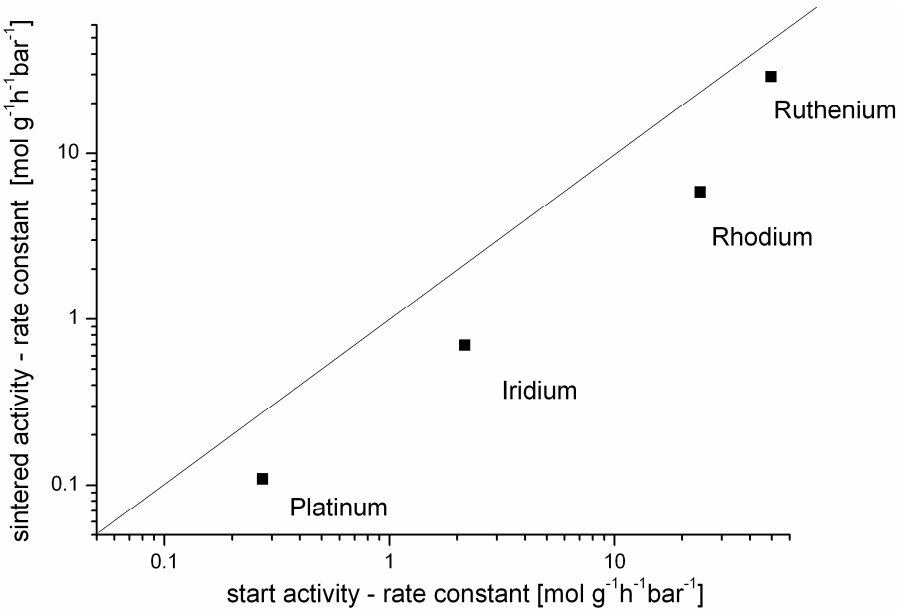

Figure 23. The start and sintered activities of the pure noble metal catalysts. The catalysts have decreased in activity by factors of Ru (1.7), Rh (4.1), Ir (3.1) and Pt (2.5) in a 30 bar and H_2O/H_2~1 atmosphere for 225 h. Overall rate constants at 450°C in a gas mixture of 6.3%CH_4, 8.9% H_2O, 84.8%N_2 at 1 bar total pressure.

During preparation of a sample, there will be variance in the actual impregnation of the oxide support due to different in the liquid solutions, giving a different distribution and size range of the active metal particles. This difference will be evident in the following data when comparing start activities. The main comparison is therefore a combination of absolute activity and the relative

sintering of the catalysts. The relative sintering is the main parameter and shown by a line on the graphs in the following sections.

First the activities of promoted iridium catalysts in Fig. 24 is shown. The iridium catalyst have been promoted with Re, Mo, W and Ru. There is a fair scattering in the start activities of the iridium catalysts, though the line can be used to distinguish between the experiments. Below the line is a higher degree of sintering than the pure sample (none promoted). The Ru promoter catalysts should obviously be handled with caution since Ru by itself is very active for catalysing the methane steam reforming reaction. Otherwise it is seen that especially 7%Re seems to have a significant effect on the stability of the catalysts. This Re promoted catalyst has been reproduced with the same long term stability. In absolute activities then the 3%W is also a promising catalyst, since it has a high sintered activity. Otherwise there is a limited effect of the remaining promoters and the effects must be considered within the experimental uncertainty.

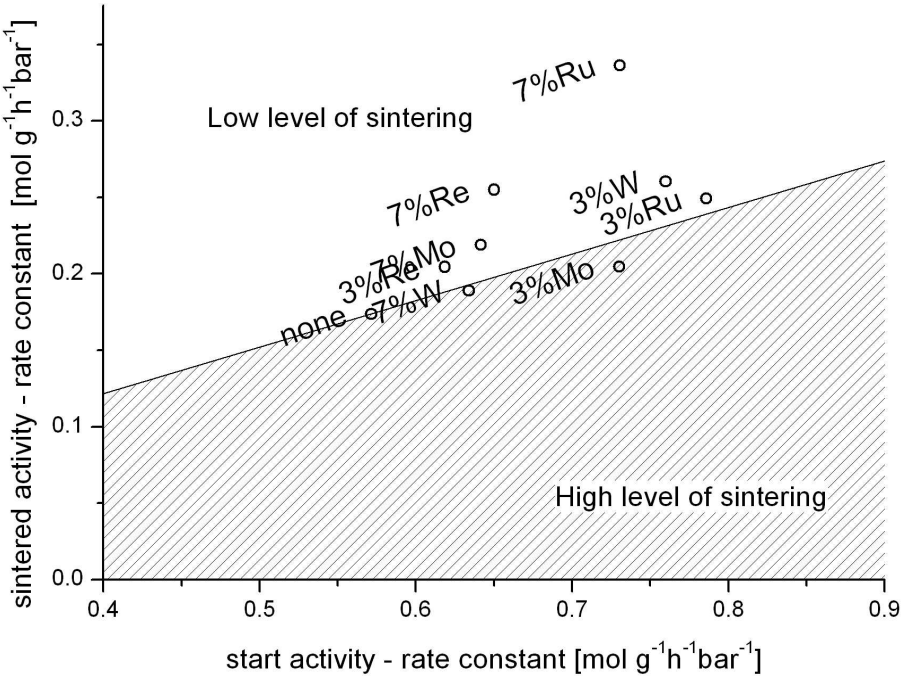

Figure 24. Promoted iridium catalysts, tested at 450°C and H_2O/CH_4 ~ 0.75.

Platinum is the least active element for methane steam reforming of the four tested catalytic materials. In Fig. 25 is seen the effect of the promoters (Ru, Re, Mo and W) used for enhancing the stability of platinum catalysts. Again it is noted that there is an effect of using Ru as a promoter, though it is most likely that it is the activity of Ru itself that is responsible for the better activity after sintering. There also seems to be an effect of Re as a promoter, stabilising both with 3 and 7%

Re. The remaining promoters (W and Mo) seem to have a negligible influence on the stability of platinum catalysts.

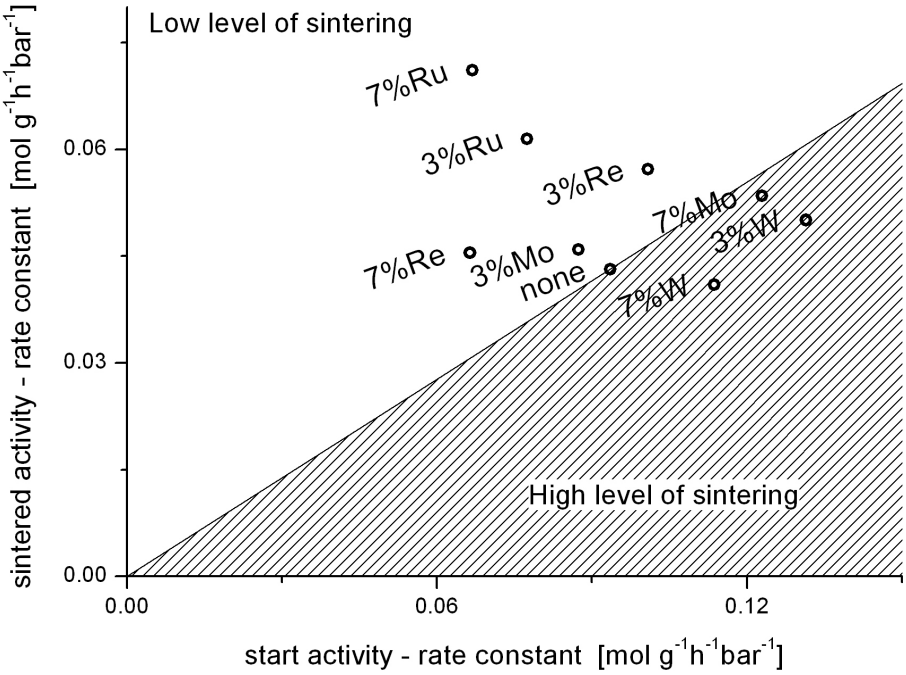

Figure 25. Promoted platinum catalysts, tested at 500°C and H_2O/CH_4 ~ 0.75

Rhodium is the second in the ranking of active catalytic metals for the reaction. In Fig. 26 the promoted rhodium catalysts, with the Re, W, Mo, Ir and Ru promoters is shown. It is noted that the Re (7%) promoted rhodium catalyst has retained a high activity after sintering, though the activity is not higher than the pure Rh sample. This is likely due to influence of rhenium on the start activity. Hence it is not believed that there is a promoting effect in enhancing the stability of this catalyst. The Ru-promoted catalysts have again this extra added activity that is due to the activity of Ru. Mo-promoted catalyst have a high start activity and retains the activity relative to the non-promoted Rh sample, so there is possibly an effect of Mo on the obtained high activity after sintering. The remaining catalysts show no significant enhanced stability.

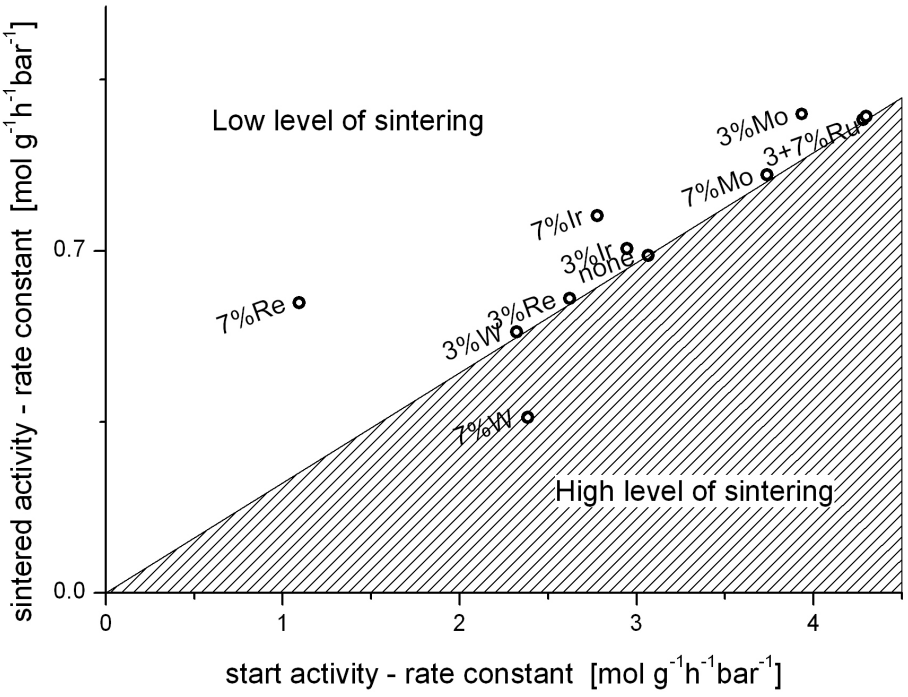

Figure 26. Promoted rhodium catalyst. Tested at 450°C and H_2O/CH_4 ~ 2.

The most active pure metals is ruthenium. As seen in Fig. 27, ruthenium has been promoted with 3 different metals (Mo, W and Re). The non-promoted catalyst show the highest activities, both start and sintered. A small amount of Re and W seem to have minor stabilising effect on the ruthenium based catalysts, unfortunately this trend could not be reproduced at the same level (data not shown) and this effect seems to very limited. A Mo-promoted Ru catalyst appears to have a significant deactivation during sintering. In appendix C the absolute segregation energies is given, where it is seen that Mo have minimal segregation energy in a Mo-Ru alloy. This could explain the deactivation effect which is observed here.

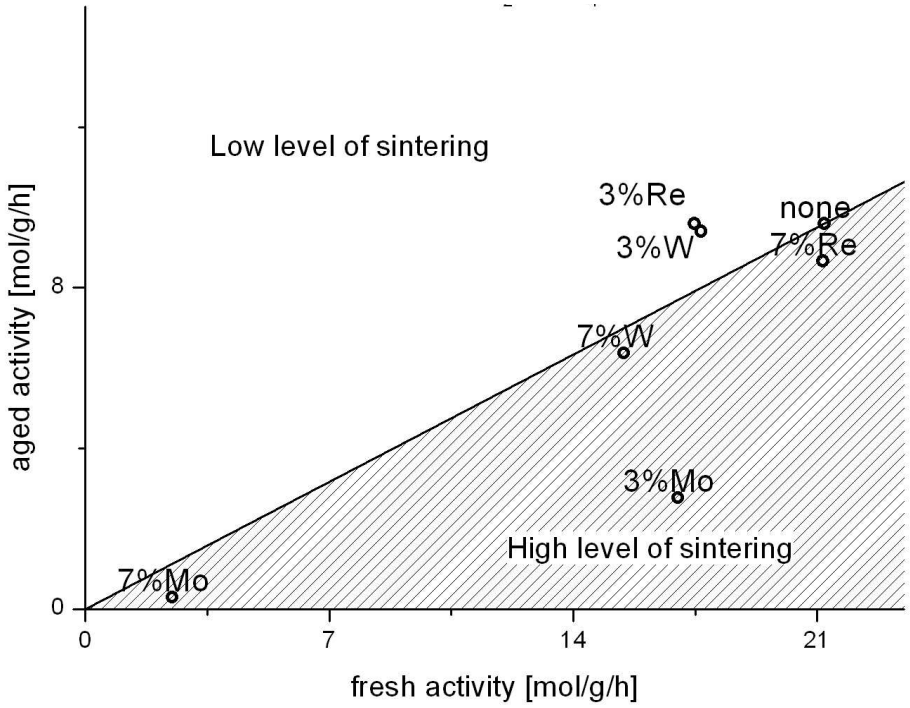

Figure 27. Promoted ruthenium catalysts. Tested at 450°C and H_2O/CH_4 ~0.75.

4.4. Summary

The previous sections have provided an overview of the results obtained for a range of promoted noble metal catalysts. The effect should be a higher activity after sintering for the promoted catalysts relative to non-promoted catalysts. Based on the theoretical considerations, the promoters should have a large surface energy compared to the active noble metals and following the concepts of segregating, low oxidation potential and alloying. These criteria have been followed in deciding which catalysts should be experimentally tested. A group of 4 pure catalysts and 16 promoted catalysts have been estimated to fulfil these criteria. The experimental and calculation errors have been included for a good margin for each of these criteria.

Even though it is theoretically possible to make these promoted catalysts, then there is an unknown interplay between the parameters in estimating the actual properties of these catalytic nanoparticles. Especially the thermodynamic properties of nanoparticles are a topic of uncertainty and the possible extension of bulk material thermodynamic properties.

So the concepts have been experimentally tested and especially Re seems to have some promoting effect on the stability of the noble metal catalysts. A slight effect is seen on Ru and Pt catalysts, whereas a more significant effect is seen with regards to the Ir based catalysts. The other promoters (W, Mo, Ir, and Ru) have negligible or deactivating effects on the long term stability of the noble

catalysts. Based on this study it is noted that ruthenium is the most active catalyst and could not have enhanced long term activity. The effects observed for all the metals are not substantially large enough to continue with further studies. It is still believed that the procedure is feasible and may have better compliance with other catalyst systems.

The catalyst have not been characterized to obtain exact turn-over frequency rates, but merely on a weight basis. So the absolute difference in activity between the metals should be take with some caution as will be shown by the following chapter.

5. Steam reforming catalysts activity

The methane steam reforming activity is traditionally performed over nickel based catalysts, but the use of noble metal catalysts requires a better understanding of the absolute activity and the kinetics for these metals. This is due to the economical aspect of using noble metal catalyst, which requires that almost every metal atom is active for conversion of methane. Hence understanding the precise activity in absolute and relative terms is essential. In this section the focus will be on the absolute activity of the various metals for the methane steam reforming reaction. In the following sections the focus will be on the kinetics of some of these noble metals. One of the first studies of ranking within steam reforming activity was done by Kikuchi et al. [70], where they measured the relative order in activity at atmospheric conditions and 350-600°C and observed the following order

Rh~Ru > Ni > lr > Pd ~ Pt >> Co, Fe.

Kikuchi et al. [70] proposed that the kinetics should depend on methane and steam as $r = k(P_{CH4})^0(P_{H2O})^{0.5}$, arguing that there should be no methane dependency on the rate. Even though this kinetics is most likely not correct, later studies have confirmed the activity trend reported by Kikuchi et al. Rostrup-Nielsen and Hansen [9] made similar studies at 550°C and atmospheric conditions of the methane steam reforming activity. They reported the relative activities to be

Ru~ Rh > Ir > Ni > Pt~Pd.

Studies by Qin et al. [71] performed similar experiments as Rostrup-Nielsen et al. [72] with noble metals on a MgO support at a temperature range of 600-800°C and atmospheric pressure and found an almost identical activity relationship for the noble metal catalysts as the two previous mentioned studies

Ru > Rh > Ir > Pt > Pd.

The above-mentioned studies seem to point to a general trend for the order of reactivity among the noble metals. Of the pure metal catalysts Ru and Rh are the most active, Ni and Ir are intermediate and Pd and Pt are less active. However, a series of thorough kinetic studies on Pt, Ir, Rh, Ru and Ni

catalyst by Wei and Iglesia [73,13,14,15,16,17,18] showed different results for the methane steam reforming reaction at 600°C. It was found that the relative reactivity order is

Pt > Ir > Rh > Ru, Ni.

Here Pt was found to be the most active metal and Ru determined to be the least active metal. All the studies presented have been done at more or less similar conditions in plug flow type reactors. The investigations by Wei and Iglesia have been performed more thoroughly than previous investigations and all results are based on a turnover frequency (TOF) rate rather than a weight based activity. This was possible since characterization by H_2 chemisorption and TEM were done. It was found that the TOF is dependent on the metal particle size, so that TOF increases with the dispersion. It is also generally found that the surface is clean at all reaction conditions. To confirm either of the activity orders, measurements were performed of the absolute activity for a series of steam reforming catalysts.

5.1. Absolute activity

To estimate the steam reforming activity of metal catalysts there has been prepared eighteen catalysts. Three different support materials were used in the preparation, an yttrium (3 mol%) stabilised ZrO_2 support, a θ-Al_2O_3 support and a $MgAl_2O_4$ spinel support. The impregnation and pre-treatment were done as described in section 2.2. To obtain varying particle sizes, six 5wt% Rh/ZrO_2 catalysts were aged for up to 600 h at different temperatures between 600 and 830°C in H_2O/H_2 mixtures (H_2O:H_2=1:1) at 31 bar total pressure. Samples of 1wt% Rh/ZrO_2, 1wt% Ir/ZrO_2, 1wt% Ru/ZrO_2 and 1wt% Pt/ZrO_2 were aged at 1103 K for 228 h in a similar gas mixture. The ageing procedures rendered a total of 18 catalysts, which are listed in table 12.

Table 12. Overview of the catalysts investigated in this study. The varying treatments is given by aging time and temperature. This give rise to varying particle sizes and dispersions. The activity is given as a turnover frequency (TOF).

Catalyst	Support	Aging time [h]	Aging temperature [°C]	Average particle diameter [nm]	Dispersion [%]	TOF at 773 K [s^{-1}]
1wt% Rh-1	ZrO_2	-	-	2.7/2.2[#]	32.3	12.5
1wt% Rh-2	ZrO_2	228	830	8.4	10.6	1.8
5wt% Rh-3	ZrO_2	-	-	4.5	21.0	7.4
5wt% Rh-4	ZrO_2	72	830	8.2	11.0	3.6
5wt% Rh-5	ZrO_2	600	619	6.5	12.7	6.2
5wt% Rh-6	ZrO_2	600	673	7.0	12.8	4.7
5wt% Rh-7	ZrO_2	600	794	9.8	9.5	2.5
5wt% Rh-8	ZrO_2	600	823	11.1	7.6	2.0
1wt% Ir-1	ZrO_2	-	-	1.4/1.7[#]	82.2	2.3
1wt% Ir-2	ZrO_2	228	830	2.9	28.4	2.1
1wt% Ru-1	ZrO_2	-	-	4.2/2.1[#]	48.1	19.9
1wt% Ru-2	ZrO_2	228	830	7.2	10.8	1.1
1wt% Pt-1	ZrO_2	-	-	1.9/2.3[#]	58.4	2.5
1wt% Pt-2	ZrO_2	228	1103	3.9	23.8	0.5
1wt% Pd-1	Al_2O_3	-	-	2.1	54.1	1.3
14.8wt% Ni-1	$MgAl_2O_4$	-	-	6.1	20.0	1.0
2.4 wt% Ni-2	Al_2O_3	-	-	2.7/2.8[#]	35.9	1.9
10wt% Ni-3	Al_2O_3	-	-	2.6	40.5	2.0

[#]*ex situ/in situ measurements.*

The catalysts were crushed to a fraction of 300-500 µm and mixed with inert $MgAl_2O_4$ for a total weight of 300 mg. The catalysts were tested in reactor system 3, where the methane steam reforming activity was measured at 500°C using a gas mixture for 19% CH_4, 74% H_2O and 7% H_2 at ambient pressure and a total flow of 21.6 Nl/h. The overall conversion in the reactor was used to calculate the inlet methane steam reforming rate, *r*, as given by Eq. 58.

$$r = k(T) P_{CH_4} \tag{58}$$

The conversions are kept low (<15%) to ensure that reactivity is not close to equilibrium. To calculate the rate as a turnover frequency it is necessary to characterize the metal surface area, which is done by TEM, H_2 chemisorption, sulphur chemisorption and XRD. The method descriptions are given in chapter 2. The dispersion can be determined from *ex situ* TEM images as shown in Fig. 28 of fresh and aged samples. From these images it is possible to derive particle size distributions, which consist of more than 400 individual particles each.

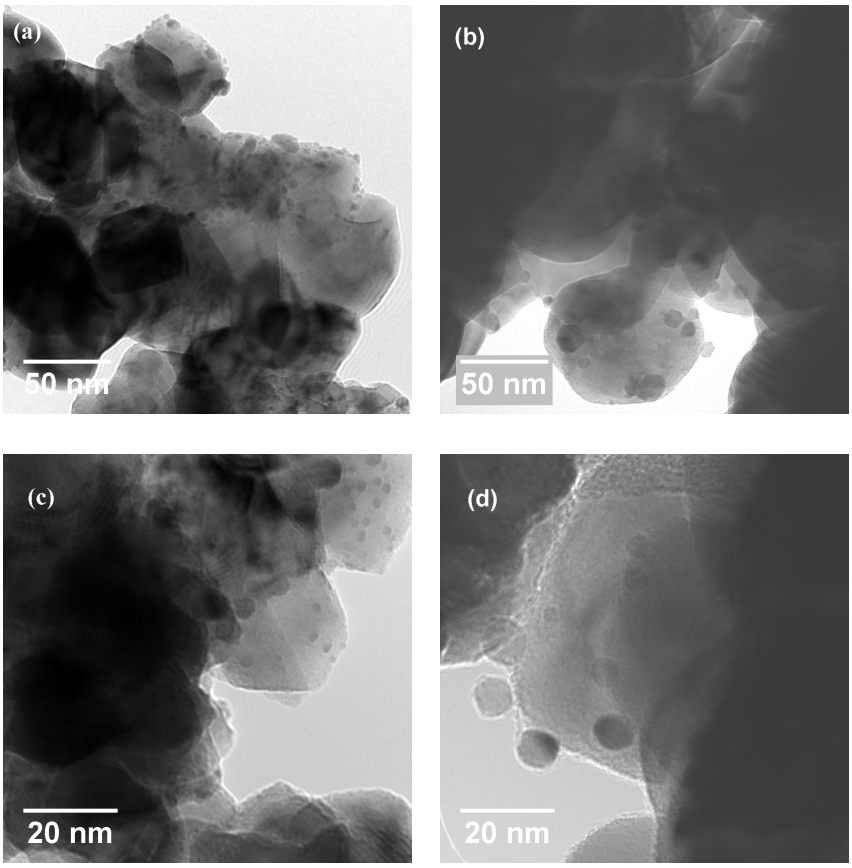

Figure 28. TEM images of Rh/ZrO_2 catalysts showing the effect of ageing. (a) Fresh 5wt% Rh-3 and (b) aged 5wt% Rh-8 (600 h/823°C) with the average particle diameters of 4.5 and 11.1 nm, respectively. (c) Fresh 1wt% Rh-1 and (d) aged 1wt% Rh-2 (228h/830°C) with average particle diameters of 2.7 and 8.4 nm, respectively.

The particle size distributions are exemplified by Fig. 29 and they can be used to calculate the number-averaged particle sizes and dispersions as given in table 12. The TEM images in Fig. 28 and results in table 12 show that the fresh samples contained metal particles with an average diameter in the range 1-6 nm. The particle diameters increased and the dispersion decreased correspondingly with ageing of the catalysts.

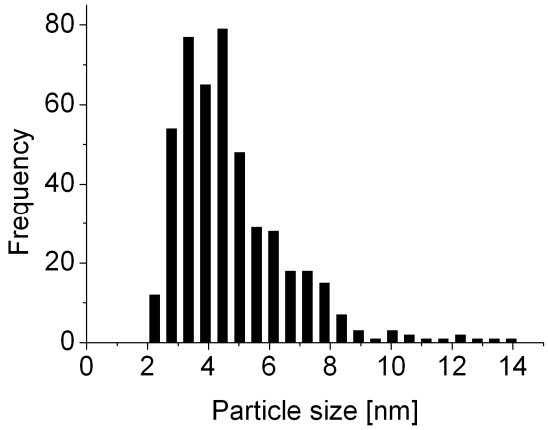

Figure 29. The particle size distribution of the Rh-3 catalyst with an average particle size of 4.5 nm (i.e. 21% dispersion). A total of 466 particles are included.

Most of the particle size distributions reported have been done by *ex situ* TEM measurements. The average particle diameter for the Ru catalyst is larger than for the other metals as noted in table 12. It is well-known that Ru easily surface oxidize [74] and therefore environmental TEM (ETEM) measurements were conducted to image the fresh catalyst with 1wt% metal loading under reducing conditions. The surface oxidation would be most pronounced for the smallest metal particle sizes. These *in situ* images were done at 1.2-1.4 mbar H_2 and 500°C and analyses were performed for average particle size and dispersion. Fig. 30a and 30b show representative TEM images of the Ru sample obtained *ex situ* and *in situ* that shows more small particles were present during *in situ* observations. The finding is furthermore confirmed by the results presented in table 12, which reveal that the average particle size for the fresh Ru sample (Ru-1) was reduced by a factor of two to 2.1 nm in the ETEM experiment. In comparison, the fresh Rh, Pt, Ni, Pd, and Ir catalysts have also been investigated thoroughly by ETEM. For these catalysts, the results show no difference between the *ex situ* and *in situ* determination of the average particle sizes (table 12).

Since Ru seems to be the only metal affected by surface oxidation, the aged Ru catalyst (Ru-2) was also investigated *in situ* in the H_2 environment by ETEM. Fig. 30c and 30d indicate that the Ru particles in the aged catalyst apparently had similar size in the *ex situ* and *in situ* observations and that the average particle size was large (Ru-2: 7.2±0.3 nm), hence independent of whether the measurements were performed *in situ* or *ex situ*. The surface oxidation only affects the visibility of

2-4 nm wide Ru particles whereas the effect was less significant for the other metals and larger Ru particles. In order to accurately determine the TOF and dispersion of the fresh ruthenium catalyst, the average particle size is obtained from *in situ* observations using ETEM. For the other catalysts the particle diameters obtained *ex situ* were used.

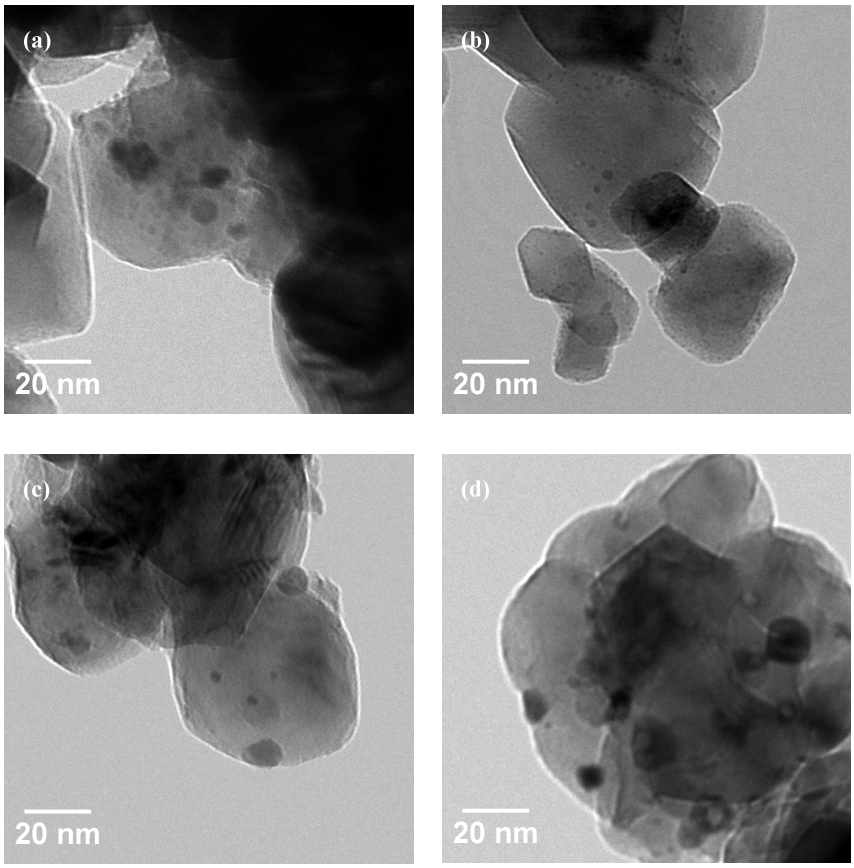

Figure 30. Ex situ and *in situ* microscopy of Ru/ZrO_2. (a) TEM image and (b) ETEM image (1.4 mbar H_2, 500°C) of the fresh Ru catalyst (1wt% Ru-1). The average particle size was 4.2 nm and 2.1 nm under *ex situ* and *in situ* conditions, respectively. (c) TEM image and (d) ETEM image (1.4 mbar H_2, 500°C) of the aged Ru catalyst (1wt% Ru-2). The average particle size was 7.2 nm and 7.5 nm under *ex situ* and *in situ* conditions, respectively.

The data obtained by TEM can be confirmed by other characterization techniques. Sulphur chemisorption and XRD studies were performed to validate the surface areas for Rh catalysts. Fig. 31 (left) shows the sulphur chemisorption measurements for 5wt% Rh and the surface-averaged diameter obtained by TEM. This data correlates well to each other as would also be expected based on the sulphur chemisorption observations for determining isotherms. Fig. 31 (right) shows the average crystal size diameter by XRD that is compared to the volume-averaged diameter obtained

by TEM. The discrepancy of smaller sizes obtained by XRD are likely linked to twinning of the individual Rh particles that will effectively show the metal particles as polycrystals reducing the average crystal size [12]. Within this assumption there is otherwise fairly good correlation between the particle diameters.

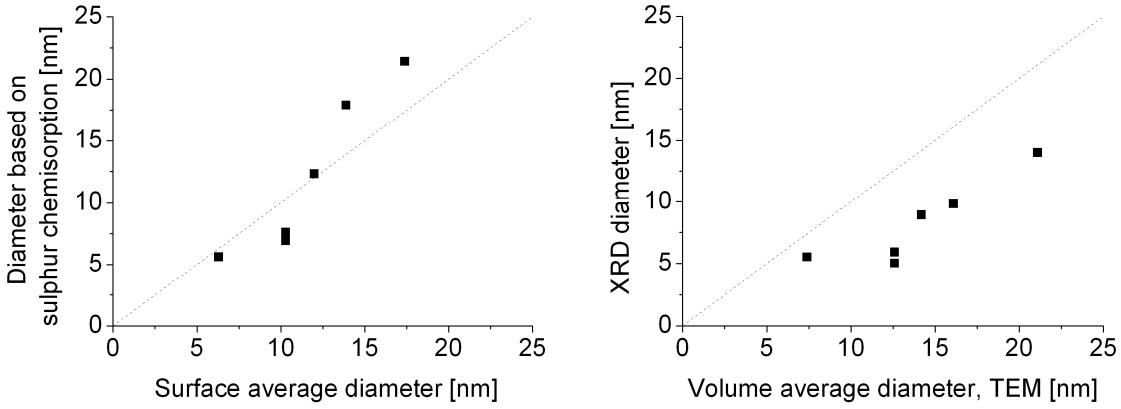

Figure 31. Diameter by sulphur chemisorption vs. surface average diameter (left). Diameter by XRD vs. volume averaged diameter (right).

All catalysts were tested for their methane steam reforming activity. The series of Rh catalysts was prepared to obtain a variation in particle sizes so that any structural effect on the activity could be revealed. The remaining Ru, Ir, Pt, Pd and Ni catalysts were tested to allow a ranking of the different metals with respect to their TOF. Table 12 gives the turnover rates for all the tested catalysts and plotted versus dispersion in Fig. 32. There is a pronounced dispersion effects for especially the large set of Rh data with increasing turnover rates as a function of dispersion. This finding indicates that the activity depends on the detailed surface structure of the nanoparticles and that the low-coordinated surface sites play an important role for the relative activity of the active metals for steam reforming because smaller particles are expected to expose a larger fraction of low-coordinated sites than larger particles [75,76]. It is particularly interesting to note that for Rh, the turnover rate increases nearly linearly with dispersion. When comparing the TOF in Fig. 32 at a given dispersion, e.g. 0.4, then the ranking is given by Rh~Ru>Ni~Pt~Ir~Pd.

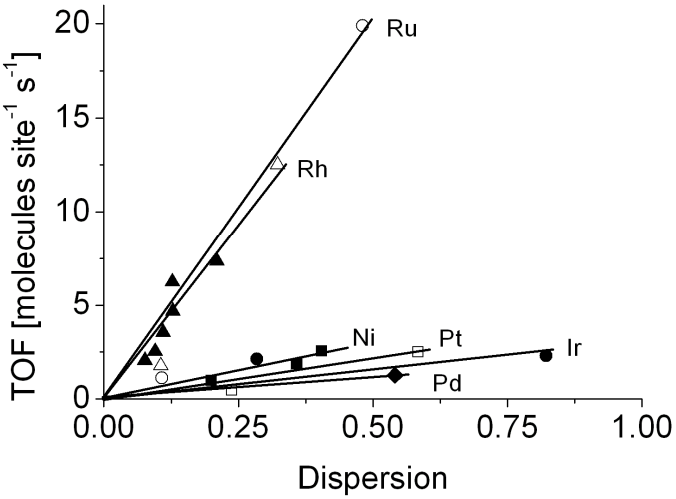

Figure 32. Reaction rate as a function of dispersion for CH_4-H_2O reforming (500°C, 0.19 bar CH_4, 0.74 bar H_2O, 0.07 bar H_2). Ru (○), 5wt%Rh (▲), 1 wt% Rh (Δ), Ni (■), Pt (□), Ir (●) and Pd (♦).

The TOF data in Fig. 32 is based on the assumption that all surface sites are active on the metal, i.e. TOF = r / A, where r is the rate and A is the surface area. It is also seen that there is a clear linear dependency between the TOF and dispersions. It can be estimated that the TOF would be constant if terrace sites were dominant, while if steps are dominant, it would increase linearly and if corners are dominant it would increase by the square of the dispersion. The data presented in Fig. 32 clearly shows that the reactivity is dominated by steps and low-coordinated sites. It has been shown that methane dissociates much faster on steps than on terrace sites [10] due to low-coordination effects. The data obtained here for the relative activities agrees much better with the obtained data by Kikuchi et al. [70], Rostrup-Nielsen and Hansen [9] and Qin [71]. It differs though significantly from the data obtained by Wei and Iglesia [14].

For the experiments shown in Fig. 32 there is a variance in support material used. There is observed no direct influence of the type of support used. As also reported by Wei and Iglesia [14] the support only has an indirect influence due to the difference in metal particle size, whereas any other effects are insignificant. This is valid for the tested supports such as ZrO_2, Al_2O_3 and $MgAl_2O_4$. Studies of Ru/La_2O_3 catalysts have shown that for CO_2 reforming there is an interaction between the CO_2 and the La oxide support [77]. Other support effects have also been proposed to stem from OH radials on the support surface [78]. While these effects are likely present they are negligible for most supports when measuring the activities of the steam reforming reaction.

Before dealing with the kinetics of the steam reforming reaction, it is necessary to discuss the water gas shift reaction. Few water gas shift experiments have been done at temperatures of 500°C and above. Indirect measurements have been done in connection with steam and CO_2 reforming experiments. For both Ru [15] and Rh [79] it have been reported that there is sufficient high rates for keeping the water gas shift reaction in equilibrium. Low temperature studies (270°C) of the transition metals indicates that the remaining interesting metals have similar rates and it is assumed to be valid at higher temperatures [80]. The kinetic experiments conducted of the noble metals in this study have all shown to be near equilibrium for the water gas shift reaction under all conditions.

5.2. Kinetics

After determining the absolute activities for the methane steam reforming, then the focus will be on the kinetics for the two most active metals, Ru and Rh. Though the starting point is to continue the kinetic model development started in section 1.2. Here a nine elementary step model was proposed. Based on DFT studies it is estimated that both methane dissociation, ER1, and the CO formation reaction ER7, could be rate determining for the steam reforming reaction [12]. So the overall rate when assuming steady state can be written as Eq. 59.

$$r_{overall} = r_1 = r_7 = k_1^+ P_{CH_4} \theta_*^2 - k_1^- \theta_{CH_3} \theta_H = k_7^+ \theta_C \theta_O - k_7^- \theta_{CO} \theta_* \quad (59)$$

From the expressions for the equilibrium constants it is possible to replace θ_{CO}, θ_O and θ_C at the right side of Eq. 59

$$\theta_{CO} = P_{CO} \theta_* / K_9 \quad (60)$$

$$\theta_O = K_2 K_3 K_8^2 P_{H_2O} \theta_* / P_{H_2} \quad (61)$$

$$\theta_C = K_4 K_5 K_6 K_8^3 \theta_{CH_3} / P_{H_2}^{\frac{3}{2}} \quad (62)$$

At the left side of the expression for the overall reaction rate, θ_H equals

$$\theta_H = P_{H_2}^{1/2} \theta_* / K_8 \quad (63)$$

θ_{CH_3} can be expressed as a function of θ_* by setting the kinetic model

$$\theta_{CH_3} = \frac{(A+B)}{(C+D)}\theta_* \tag{64}$$

where

$$A = k_1^+ P_{CH_4} \tag{65}$$

$$B = k_7^- P_{CO} \Big/ K_9 \tag{66}$$

$$C = k_1^- P_{H_2}^{1/2} \Big/ K_8 \tag{67}$$

$$D = K_2 K_3 K_4 K_5 K_6^5 k_7^+ P_{H_2O} \Big/ P_{H_2}^{5/2} \tag{68}$$

where θ_* now can be determined,

$$\theta_* = \frac{1}{1+\sum_i \theta_i} \tag{69}$$

By combining Eq. 60-69 in the overall rate expression it is possible to obtain a rate expression based on ER1 and ER7 being rate determining steps and where the remaining steps are quasi equilibrated. This model will be used in the following section of theoretical results for the steam reforming reaction.

5.2.1. **Theoretical results**

The methane steam reforming reaction has been modelled in a collaboration project with the measured absolute rates presented [12]. The theoretical calculations are done by G. Jones and co-workers at CAMD (Technical University of Denmark) using DFT as implemented in the computer code DACAPO using the RPBE exchange correlation functional [81]. For further details on exact calculation procedure is referred to the article [12]. The calculation has been done on steps as shown is important by Fig. 32. For Ni it has been estimated that the turnover frequency is a factor of 200 higher for steps compared to terrace sites [10] at 225 °C, supporting the notion of steps being the most important sites. The data presented here is based on the theoretical description from section 1.3.

First, the calculations will be shown to address some of the key parameters for the reaction. This will start from a simple energetic picture and then adding information such as pressure, temperature and kinetics to get the full picture of the methane steam reforming reaction from a theoretical perspective. First scaling relationships are used to construct an energy diagram for the steam reforming reaction. Fig. 33 describes the overall trends in steam reforming activity of the pure metals by having an overall energy diagram. The diagram shows that there is an overall energy increase; this is due to the endothermic nature of the reaction. When entropy effects start being important then the free energy of the reaction becomes negative at sufficiently high temperature. The path between reactants and products are given by the specific metal due to the binding energies of the intermediates. It is seen that it is difficult to bind on the most noble metals, Au, Ag and Cu. So they become unsuitable for the reaction as nothing will bind to the surface. Likewise for very strongly binding metal surfaces such as W, the surface will be completely covered by species reducing the reactivity. There is essentially a band between Pt and Ru that looks reasonably favourable for the reaction to occur. These metals are also the ones that have experimentally been observed to be the active catalyst for the methane steam reforming reaction.

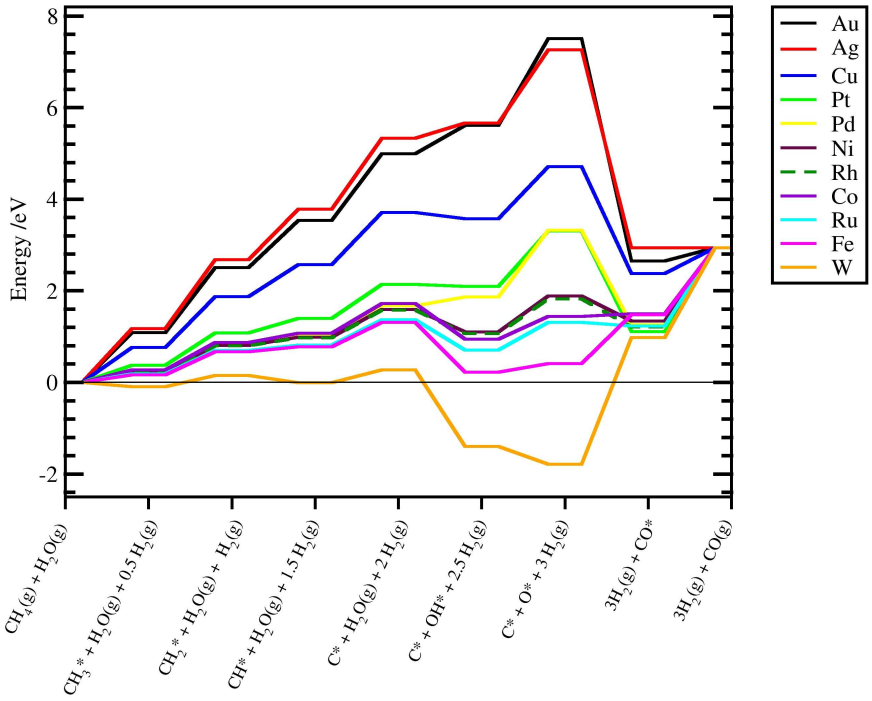

Figure 33. The potential energy diagram for steam reforming, as determined from the linear scaling relationships. Here a range of metals from noble to highly reactive are considered [12].

For Ni and Ru there have been included the pressure and temperature in Fig. 34, which represent a total energy diagram including the energy barriers for each step intermediate step. It is seen that at the conditions modelled here there is similar energy barriers for the methane dissociation reaction and the CO formation reaction. At increasing temperatures the methane dissociation barrier increases due to the entropic contribution relative to the reactants free energy.

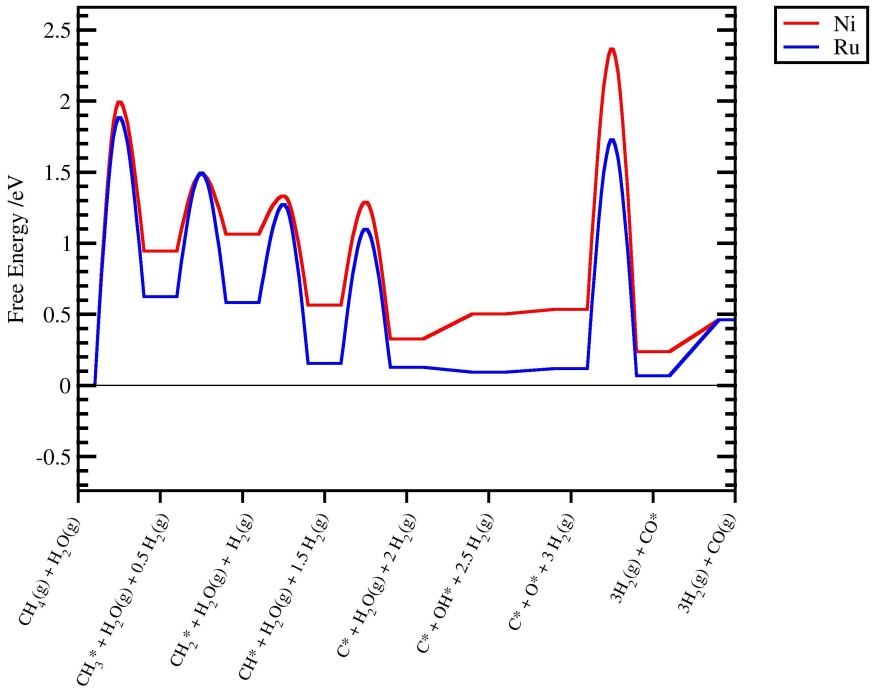

Figure 34. Reaction free energy scheme including reaction barriers for steam reforming over stepped Ru and Ni. The plot has been constructed using DFT calculations and normal-mode analysis for the total free energies at 500°C.

The two barrier kinetic model from section 5.2 is applied where the rate constants and equilibrium constants are determined from DFT calculations of ruthenium [12]. The adsorption energies of C and O can be used to describe all the remaining adsorption energies and reactions barriers from scaling relations and BEP relations. Rather than just calculating rates for discrete points given by the specific elements of the Periodic Table, it is possible to obtain the rate as a function of these two independent variables, the adsorption energies of carbon and oxygen (ΔE_C , ΔE_O). This allows us to probe the rate of steam reforming in all of the T, P and adsorption energy phase space. One particular advantage of the scaling method is that it allows us to probe not only the influence of temperature and pressure on the reaction for each metal, but also permits variation of the adsorption energy of oxygen and carbon and hence rationalise their effect. Fig. 35 depicts the 2-D plot comparing the influence of the C and O adsorption energy on the rate at 500°C, 1 bar of pressure

having a conversion of 10%. It is seen that the peak of the volcano plot (i.e. where the rate is highest) lies close to the region of the Ni, Rh and Ru adsorption energies. The peak lies in the region where the influence of the CO formation and CH_4 adsorption are roughly balanced and that there is competition between these two processes. This is as expected from inspection of the BEP relations where the CH_4 dissociation barrier scales with the C adsorption energy, yet both the C and O energy are required to describe the CO formation barrier correctly.

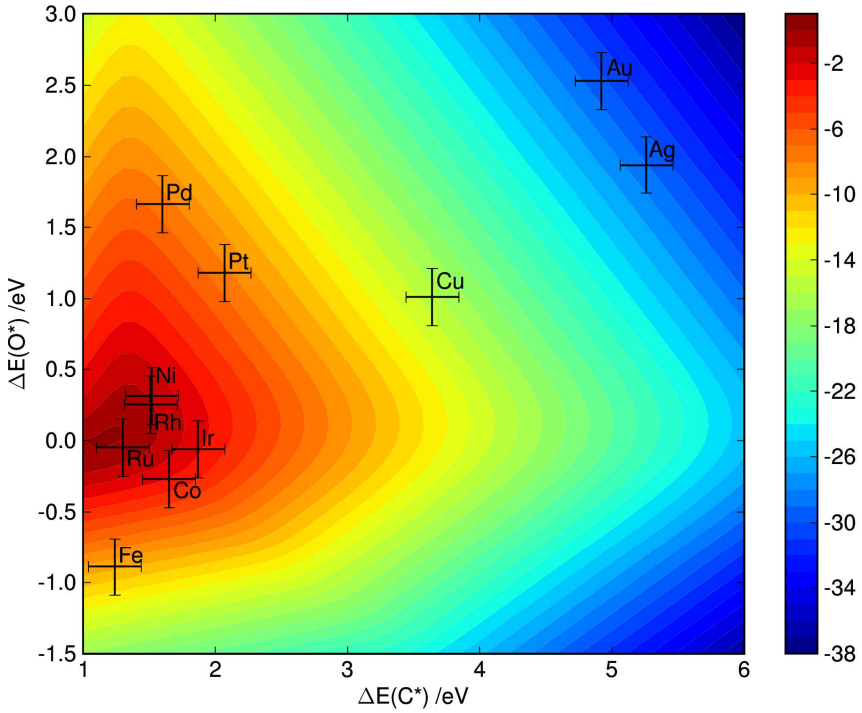

Figure 35. Two-dimensional volcano-curve of the turnover frequency (log_{10}) as a function of O and C adsorption energy. T = 500°C, P = 1 bar; 10% conversion. The error bars include an estimated 0.2 eV (20 kJ/mol) uncertainties in the adsorption energies.

The absolute activities estimated by the model show the same trend as the obtained experimental results. The results given by Fig. 35 shows large differences in absolute activities and especially Pt and Pd that have been measured in the experimental study show slow theoretical activity. The remaining activities for Ru, Rh, Ni and Ir match fairly well with the obtained experimental results. It should be noted that the calculation error of the DFT calculations will be more pronounced further away from the maximum. At the maximum there exists significant compensation effect between different elementary reactions giving a better estimation of the absolute activity. Furthermore, the main obstacle for the low Pt and Pd rate is the CO formation rate as dependent on the O adsorption energy. Instead the proposed pathways of ER10-12 and ER13-14 through CHO

species could have an influence with lower energy barriers. So the absolute difference in activity given by Fig. 35 is not completely representative of the actual process. If the modelling is carried out assuming the CO formation reaction to be quasi equilibrated then the results are as given in Fig. 36.

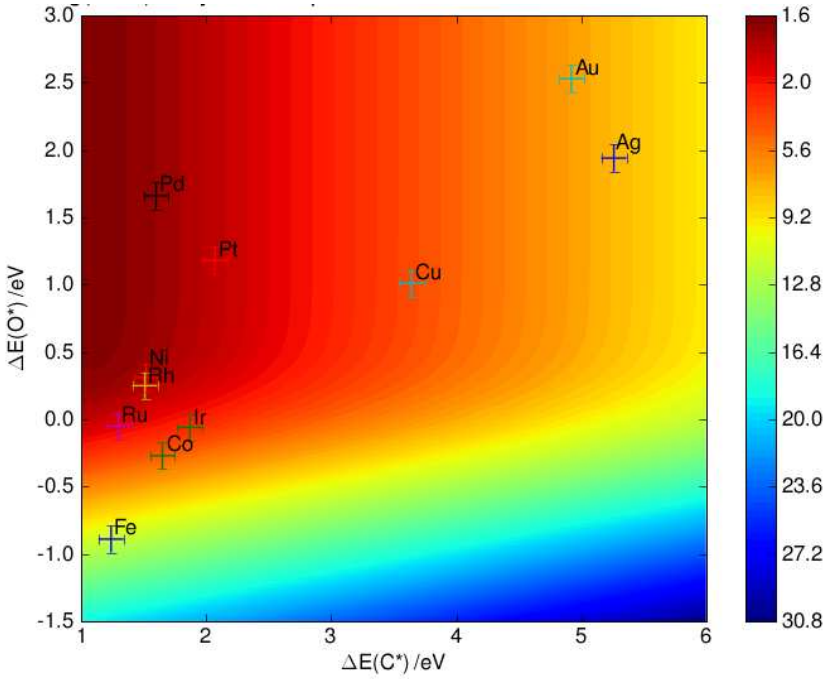

Figure 36. Two-dimensional volcano-curve of the turnover frequency ($\log_{10}$) as a function of O and C adsorption energy for the methane dissociation adsorption as the rate limiting step. T = 500°C, P = 1 bar; 10% conversion. The error bars include an estimated 0.2 eV (20 kJ/mol) uncertainties in the adsorption energies.

Here it is seen that the absolute activities for Pt is much closer to the rates for the other noble metals. Experimental investigations to determine the kinetics is performed in the next sections.

5.3. Kinetics – adsorbate effects

The discussion on the influence of the CO formation step is investigated experimentally. As given by Eq. 70 it can be estimated that the rate should scale with the pressure of hydrogen to the power of -3. This has not been observed experimentally at low temperatures (500°C) for either Rh or Ru. There is no other literature supporting this notion of high negative order dependency of hydrogen.

$$r \propto \frac{P_{CH_4} P_{H_2O}}{P_{H_2}^3} \tag{70}$$

So the proposed model by Eq. 59-69 is simplified by assuming that only methane dissociation is the rate limiting step. Again this is likely due to the pre-requisite that there is limited coverage and that the CHO reaction paths are not taken fully into consideration for the theoretical calculations. It can simply be derived that the rate for this model is given by

$$r = k_1^+ P_{CH_4} \left(1 - \beta_{SR}\right) \theta_*^2 \tag{71}$$

Where β_{SR} is the approach to equilibrium given by

$$\beta_{SR} = \frac{P_{CO} P_{H_2}^3}{P_{CH_4} P_{H_2O}} \cdot \frac{1}{K_{P,SR}} \tag{72}$$

So then the rate should be a simple first rate expression with respect to the partial pressure of methane. Though it has been assumed previously that the metal surface is clean the following experiments will show that there is a no simple first order dependency, but rather a complicated dependency from various factors. So based on previous studies that showed that there was a significant difference in activity between CO_2 and steam reforming explained by a CO adsorption term [9] and the experiment performed here it is believed that it is necessary to include surface species in the equation and the θ_* cannot be assumed to be one. There is a series of possible adsorbents that can lower the steam reforming activity, such as CO, H, C, CH, CH_2 or CH_3. It could also be speculated that O or OH would adsorb on the surface, but based on the measurements, the trends in activity is opposite of expression having these as adsorbing species. The equations of the models are given by appendix D.

5.4. Ruthenium kinetics

In this section the focus will be on using the models obtained for the methane steam reforming reaction on a ruthenium catalyst. This new Ru-3 catalyst is 1wt% Ru catalyst on ZrO_2 made as described in section 2.2. The catalyst is aged at 750°C for 336 hours in H_2O/H_2 (ratio ~ 1) atmosphere at 31 bar total pressure. The experiments are performed in reactor system 2 and all the experiments were carried out far from equilibrium as the approach to equilibrium for steam and

CO_2 reforming was $\beta_{SR} < 9.6 \cdot 10^{-3}$ and $\beta_{CO_2\ reforming} < 1.4 \cdot 10^{-3}$ under all conditions. As a control of the stability of the catalyst, standard activity measurements were made between each series of variations. A standard activity measurement corresponds to the following conditions at the entrance of the catalyst bed: 16.7% CH_4, 16.7% N_2, and 66.6% H_2O at 500°C and 1.3 bar. The standard activity measurements showed that the catalyst deactivation was small during the experiments. During a measurement period of 14 days, the total deactivation of the catalyst as amounted to 16%, which was compensated for by a linear correction of the rates followed by calculations of the conversions.

Characterization by TEM and environmental TEM was done on the Ru catalyst to determine the particle size distribution for the Ru/ZrO_2 catalyst. According to the previous results it is necessary to study the catalyst *in situ* to image small Ru particles. The resulting surface average particle size was compared to the results from H_2 and sulphur chemisorption measurements.

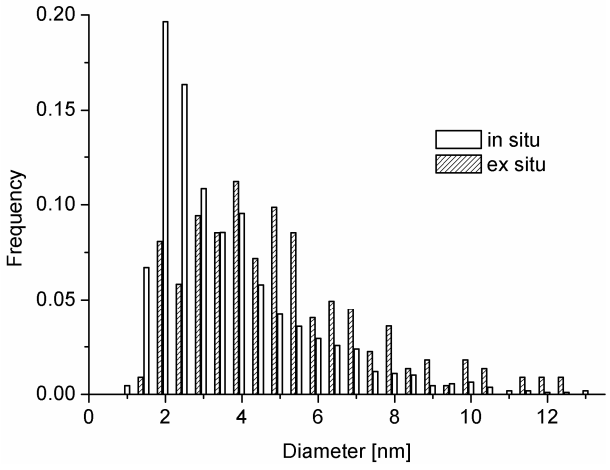

Figure 37. Particle size distributions (PSD) for the Ru-3 catalyst obtained from *ex situ* measurements (white) and from *in situ* measurements at reducing conditions, i.e. 500°C and 1.5 mbar H_2 (striped). Average particle sizes are 4.9 and 3.5 nm, respectively. The PSDs were based on 223 (*ex situ*/white) and 1042 (*in situ*/striped) measured particles, respectively.

The particle size distributions (PSD) for the Ru-3 catalyst are presented in Fig. 37. The data obtained at *ex situ* conditions show a broad distribution of particle sizes and an average particle diameter of 4.9 nm. The equivalent particle size distribution obtained at reducing conditions is

much sharper and has an average particle diameter of 3.5 nm. There is a significant difference between the particle size distributions for the same sample obtained under different conditions.

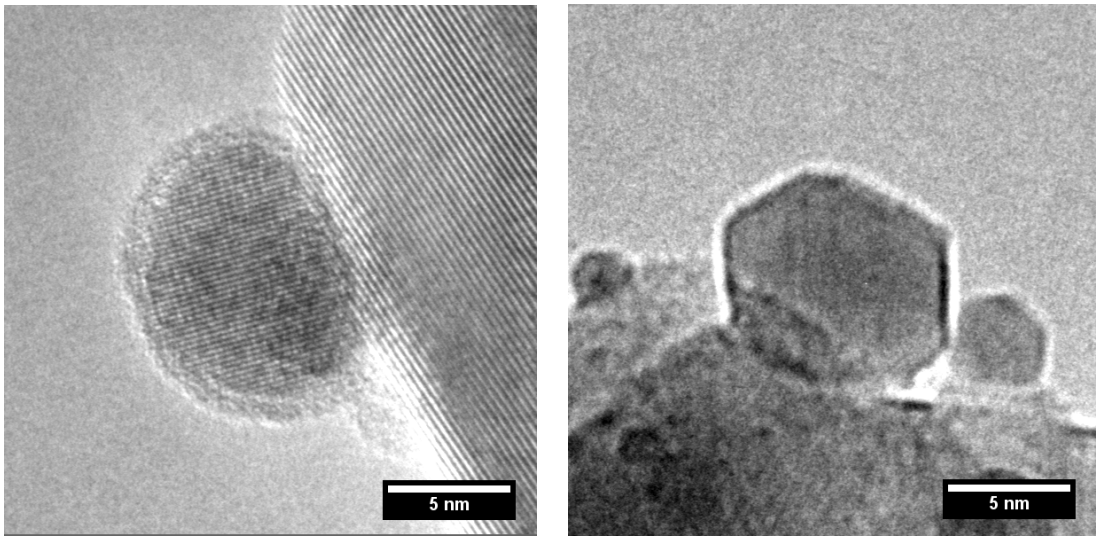

Figure 38. 22x22 nm TEM images obtained with 200kx magnification. At *ex situ* conditions of Ru-3 a 1 nm layer of RuO_2 is observed at the edge of the Ru particle (left). At *in situ* ETEM conditions of 1.5 mbar H_2 and 500°C a faceted Ru particle is observed (right).

The ruthenium particle on the ZrO_2 support in Fig. 38 (left) has a 1 nm edge of amorphous material at *ex situ* conditions. The amorphous material is assumed to be ruthenium oxide, and the inner core of the particle is seen to be crystalline. In the ex-situ measurements the particle size includes the oxide surface, which yields further complications during size estimation. A similar size particle at reducing conditions of 500°C and 1.5 mbar H_2, Fig. 38 (right) does not have the amorphous layer and the particle appear faceted. The resolution is lower due to the presence of a relative high gas pressure in the *in situ* cell. Therefore the PSD obtained using 60kx ETEM images will be used in the following, and the average diameter and dispersion were determined to be 3.5 nm and 20%, respectively. The Ru/ZrO_2 catalyst was also characterized by H_2 chemisorption and sulphur chemisorption, and the dispersions were determined to be 32% and 23%, respectively.

5.4.1. **Results**

In total 62 experiments were used in the model fitting (both steam and CO_2 reforming experiments). The difference between the rate models was the appearance of the denominator of θ_*. The following species were tried out in the denominator of θ_* : Clean surface, CO, H, C, CH, CH_2, CH_3, and CO + H. Effectively coverage effects of the possible surface species were thus studied by modelling the

experimental results. In the following only the results based on the reaction rate models of Clean surface, CH, CH_2, and CO + H in the denominator of θ_* will be commented as the latter three models provide the best agreement with the experimental data, and the clean surface will be included as a reference for these models. In table 13 the pre-exponential factor A_1^+, the activation energy $E_{a,1}$, and the adsorption parameters are provided for the reaction rate models of Clean surface, CH, CH_2, and CO + H in the denominator of θ_*. The corresponding sum of square as given by Eq. 36 is also shown for each fit.

Table 13. Results of fitting the overall rate model to the experimental kinetic data for the Ru-3 catalyst. In total 62 experiments were used in the model fitting. The pre-exponential factor, activation energy and adsorption parameters are provided for the reaction rate models containing Clean surface, CH, CH_2, and CO + H in the denominator of θ_*. The corresponding sum of squares as given by Eq. 36 are also shown.

Reaction species in denominator of θ_*	A_1^+ $\left[\frac{\text{mole}}{\text{g}\cdot\text{h}\cdot\text{bar}}\right]$	$E_{a,1}$ $\left[\frac{kJ}{mole}\right]$	A_{CH}, A_{CH_2} or A_{CO} [$bar^{-3/2}$, bar^{-2} or bar^{-1}]	ΔH_{CH}, ΔH_{CH_2} or ΔH_{CO} $\left[\frac{kJ}{mole}\right]$	A_H [$bar^{-1/2}$]	ΔH_H $\left[\frac{kJ}{mole}\right]$	SSQ [$\%^2$]
Clean surface	$1.38\cdot10^{7}$	102.3	-	-	-	-	247.58
CH	$1.74\cdot10^{8}$	118.0	$6.01\cdot10^{-12}$	-213.2	-	-	21.59
CH_2	$3.35\cdot10^{8}$	122.0	$6.93\cdot10^{-10}$	-195.5	-	-	24.12
CO and H	$4.39\cdot10^{7}$	107.9	$2.19\cdot10^{-5}$	-87.4	$7.31\cdot10^{-6}$	-71.0	10.98

The comparison between the experimental results and the modelling results is given in Fig. 39-41. Here is seen the methane conversion as a function of the initial pressures of CH_4, H_2 and H_2O. Furthermore is Fig. 41 showing the temperature influence on conversion for methane steam and CO_2 reforming. All models fairly well describe the conversion as a function of the methane partial pressure given in Fig. 39 (left), where as the strong negative effect of the inlet partial pressure of hydrogen observed in Fig. 39 (right) is not equally well modelled. Especially using a clean surface model gives poor results not catching the trend that is experimentally observed.

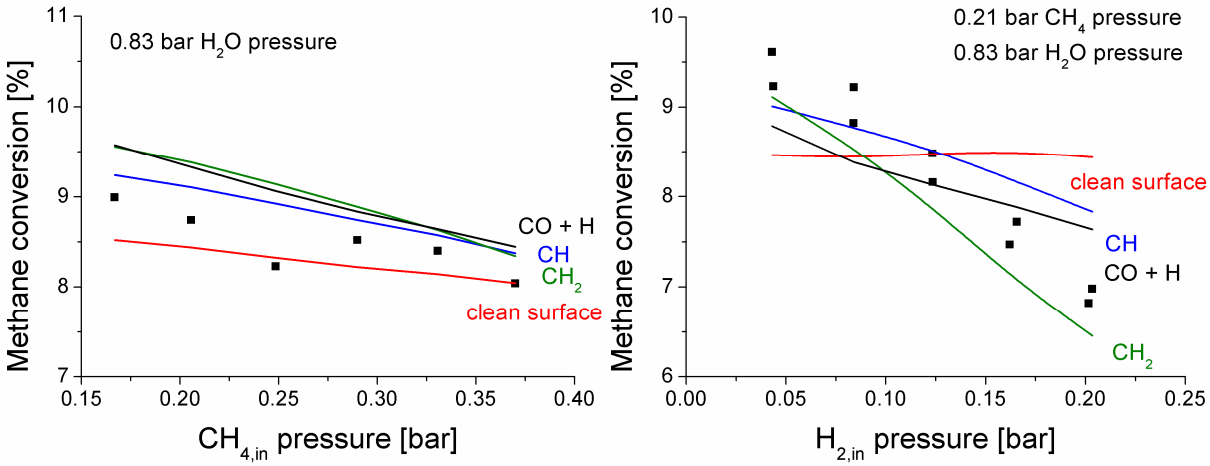

Figure 39. Experimental conversions and global model data by 4 models; Clean surface, CH, CH_2 and CO + H in the denominator of θ_*. Predictions of methane conversions at varying methane partial pressure (left) and H_2 partial pressure (right). The total inlet flow rate was $v_{T,\,in}$ = 12.1 Nl/h. Total pressure P = 1.3 bar, N_2 balance. T_{in} = 500 °C.

The model that describes the results best can be seen by reviewing Fig. 40, which shows the conversion as a function of the inlet partial pressure of steam. Here it is clearly seen that at low steam concentrations there is no experimental dependency of the inlet steam concentration. The model that assumes CH_x adsorption are strongly dependent on the partial pressure of steam as shown by the figure.

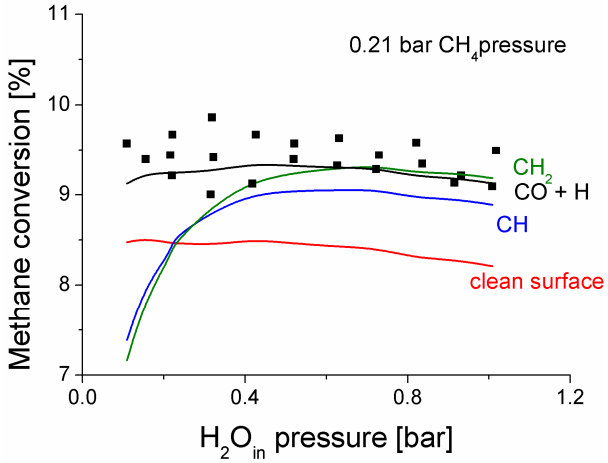

Figure 40. Experimental conversions and global model data by 4 models; Clean surface, CH, CH_2 and CO + H in the denominator of θ_*. Predictions of methane conversions at varying steam partial pressure. The total inlet flow rate was $v_{T,\,in}$ = 12.1 Nl/h. Total pressure P = 1.3 bar, N_2 balance. T_{in} = 500°C.

For otherwise similar reaction conditions, it is seen by Fig. 41 that there is a clear difference in steam and CO_2 reforming activities. The clean surface model predicts too low conversions for most

of the steam reforming experiments, while it predicts too high conversions for the CO_2 reforming experiments.

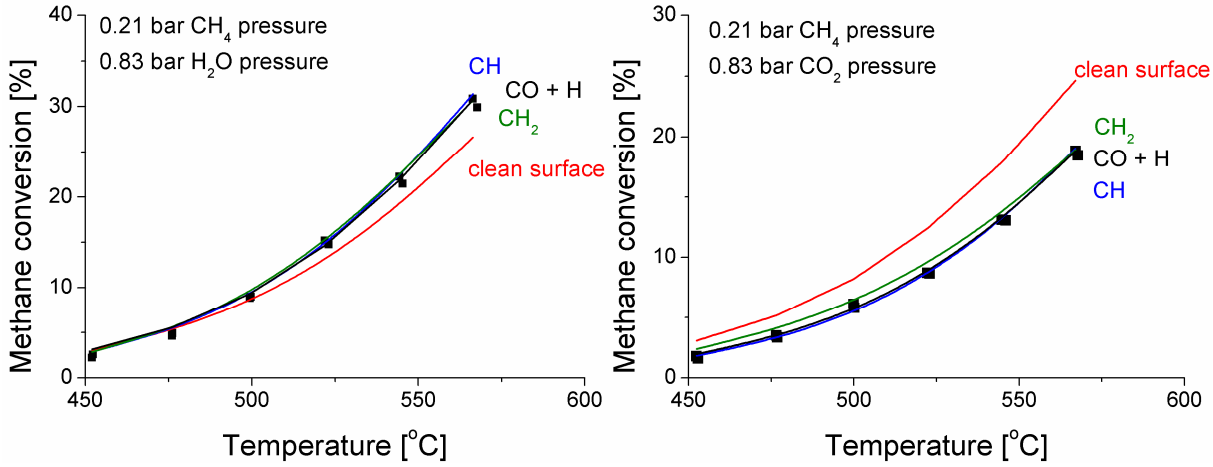

Figure 41. Prediction of methane conversions during steam reforming (left) and CO_2 reforming (right). Experimental conversions and global model data by 4 models; Clean surface, CH, CH_2 and CO + H as the denominator of θ_*. The total inlet flow rate was $v_{T,\,in} \approx 12.1$ Nl/h, P = 1.3 bar, N_2 balance and with varying temperatures (425-575°C).

Of the models considered, the CO and H model provides the best fit to the overall dataset because this model estimates the conversions at low partial pressures of steam correctly. Furthermore, this model provides a good agreement with the measured conversions during both temperature variations, and it also captures the negative influence of H_2 addition with reasonable accuracy. The model is given in its complete form by Eq. 73.

$$r = \frac{4.39\cdot 10^{7}\left[\frac{mole}{g\cdot h\cdot bar}\right]\exp\left(\frac{-108[kJ/mole]}{RT}\right)\cdot P_{CH_4}\cdot(1-\beta_{SR})}{\left(1+2.19\cdot 10^{-5}\left[bar^{-1}\right]\exp\left(\frac{87[kJ/mole]}{RT}\right)\cdot P_{CO}+7.31\cdot 10^{-6}\left[bar^{-1/2}\right]\exp\left(\frac{71[kJ/mole]}{RT}\right)\cdot P_{H_2}^{1/2}\right)^{2}} \qquad (73)$$

The final model with CO and H inhibition rightly contains 6 parameters, whereas especially the two other models (CH and CH_2) only have 4 parameters. One should be critical when adding parameters for modelling experimental data. However, it is still believed that it captures the right trends and makes a solid theoretical basis at the actual reaction conditions.

5.4.2. **Discussion**

First, the dispersions were determined by TEM, H_2 chemisorption, and sulphur chemisorption. The three methods give slightly different dispersions, and an average of the dispersions was used together with the activity to obtain a good estimate of the turnover frequency (TOF) for comparison with previous results. The average dispersion is 25%, and the resulting TOF for Ru-3 is 11.1 s^{-1} at 500°C. When comparing absolute rates of methane reforming, it has been found that the TOF agrees within a 20% uncertainty with the data presented in Fig. 32. So the absolute activity is larger than those observed in the study of Wei and Iglesia [15], which has determined TOF at 0.83 s^{-1} (at 44% dispersion and 500°C) for similar conditions. From the data of Wei and Iglesia [15] the CH_4 sticking coefficient can be estimated

$$S(T) = kN_o\sqrt{2\pi m k_B T} \tag{74}$$

where k is the experimental rate constant of the methane dissociation (which under the assumption that the surface is free of adsorbates) is equivalent to the TOF in $s^{-1}Pa^{-1}$ and N_o is the area density of the exposed metal atoms on the catalyst at the hcp closed packed surface (e.g. $1.57x10^{19}$ m^{-2} for Ru(0001)). This gives a sticking coefficient value of $0.25x10^{-7}$. Wei and Iglesia suggest that there is a large discrepancy between the CH_4 sticking probabilities measured on single crystal Ru(0001) [82] and those extracted from their rate data. The sticking coefficient measurements on single crystals were carried out at 223-423°C [82]. Using the measured activation energy of E_a = 0.55eV for the single crystal experiment, this value has been extrapolated to 500°C to give a sticking coefficient of $76x10^{-7}$. As pointed out by Wei and Iglesia this is two orders of magnitude larger than their value. A similar procedure can be used to extract a sticking coefficient from the rate data in this study. In the case of Ru at 500°C the sticking coefficient can be estimated to be $6.9x10^{-7}$, much closer to the single crystal value.

The CH_4 dissociation rate measured by Wei and Iglesia for methane decomposition over Ru is considerably lower than the one extracted from our catalytic data, which is in reasonable agreement with the single crystal data. Abbott and Harrison [83] suggested that the experimental conditions used during the methane decomposition measurement of the sticking coefficient of CH_4 on ruthenium by Wei and Iglesia [15] will lead to an underestimation.

The results by Wei and Iglesia were derived from experiments in the temperature range, 550-700°C, using total pressures of 1-5 bar. No dependency on steam or CO_2 was observed, hence the rates of

steam and CO_2 reforming were equal. The difference between the results presented here and that obtained by Wei and Iglesia can to some level be explained by the temperature difference. It can be found that the level of site blockage in the steam and CO_2 reforming experiments reported by Wei and Iglesia [7] is in the order of 10% at 600°C at their conversion used using the proposed model.

So there is an agreement on the first order dependency in methane, though the reaction conditions are very dependent on whether this will be experimentally measured. Studies by Berman et al. of methane steam reforming over ruthenium at different temperatures (450, 500 and 700°C) show a significant variation of the reaction order of methane [84]. At low temperatures (450/500°C), the reaction order of methane was found to be significantly below 1, while at higher temperatures (700°C) the reaction rate was proportional to the methane partial pressure. This is in good agreement with the observed results in this study.

The kinetic studies of steam reforming over ruthenium reported in the literature and the work presented here point to methane dissociative adsorption as the rate determining step. At high temperature the active surface is free, but at lower temperatures CO and hydrogen are present at the surface and reduces the activity due to blockage of the active sites. Thus, there is a qualitative agreement between the kinetic model reported here and the data obtained by Rostrup-Nielsen and Bak-Hansen [9].

So the adsorption of CO is important for understanding the kinetics of the steam reforming reaction on Ru. When CO is adsorbed on a ruthenium surface, it is predominantly molecularly adsorbed [85]. Adsorption experiments using both single crystals and nanoparticles show a large difference in adsorption energies for low and high CO coverages. The initial CO binding energy is about 150-175 kJ/mol but decrease to about 100 kJ/mol for higher CO coverages, see table 14. A CO adsorption energy of 87 kJ/mol is found using the obtained model, which reasonably agrees with the high-coverage values of the CO adsorption energy found in the literature. There may be two reasons for this. First, the obtained value most likely corresponds to the high-coverage adsorption energy of CO as ΔH_{CO} was mainly determined by the data at the relative high coverages of CO during CO_2 reforming. Second, even though the binding energy of CO is in the low end of the range reported in the literature, the temperature independent factor of the CO adsorption constant is relatively high, 2.19×10^{-5} bar^{-1}. For example the temperature independent factor for CO adsorption to nickel is about two orders of magnitude lower [86]. The low-temperature independent factor could be due to a compensation effect between the pre-factor and the adsorption energy [87].

Table 14. Experimental CO adsorption/desorption energies (kJ/mol).

Ru surface	ΔH_{CO} at low coverage (kJ mol^{-1})	ΔH_{CO} at high coverage (kJ mol^{-1})	Analytical method	Ref
$Ru\left(10\bar{1}0\right)$	-145		TPD	[88]
$Ru\left(109\right)$	-165	-50	FTIR and TPD	[89]
$Ru\left(10\bar{1}0\right)$	-157	-100	TPD	[90]
$Ru\left(11\bar{2}0\right)$		-103	TPD	[91]
Ru/HOPG[a]		-113	TPD	[85]
Ru/Al_2O_3	-175	-115	FTIR and adsorption model	[92]
Ru/ZrO_2		-87	Kinetic model	This work

[a]*Highly ordered pyrolytic carbon*

The adsorption energies of CO reported in table 14 were mainly derived using temperature programmed desorption (TPD). Few studies of the energetics of CO adsorption at high temperatures i.e. of the order of 500°C have been carried out, but Dulaurent et al. [92] studied Ru/Al_2O_3 catalysts and CO adsorption in the temperature range of 100-430°C and at a constant background pressure of 1000 Pa CO. The CO coverage was studied by FTIR spectroscopy and significant coverages were obtained even at high temperatures. By using their model at the current conditions (both steam and CO_2 reforming at 500°C), CO coverages of 10-40% are obtained, which explain the observed differences in activity between steam and CO_2 reforming.

As table 15 shows the H adsorption energy of 71 kJ/mol found here is higher than the energy obtained in single crystal and nanoparticle studies. DFT calculations [93] suggest that at the gas and temperature conditions used in this study, the surface will be partly covered by hydrogen. Therefore it is likely that the kinetics will also be influenced by hydrogen as found in this study. Furthermore, the temperature independent factor for H atom adsorption at nickel is estimated to be approximately 2 orders of magnitude higher than obtained here [86]. These deviations from the literature values are most likely due to a compensation effect as the overall adsorption constant is well determined, whereas the temperature independent factor and the activation energy are highly correlated. At the experimental conditions in this study, the model predicts hydrogen coverages in the range of 2-20%, with the highest coverage when hydrogen was added at the inlet and lowest during CO_2 reforming.

The potential importance of the interaction between CO and H should also be considered. Co-adsorption of CO and H at ruthenium catalysts were studied in some detail [94,95,96,97,98], and it is observed that for CO there is either no influence [97,98] or weaker CO bonding [96] in the presence of hydrogen. Furthermore, the studies reported in the literature do not agree on whether the CO-H interaction is repulsive [97] or attractive [94]. It is likely that the binding of H atoms is more affected than CO in this co-adsorption situation [97,98]. Generally, it cannot be concluded with certainty that there is any significant co-adsorption effect.

Table 15. Experimental H adsorption energies (kJ/mol) at low H coverage.

Ru surface	**ΔH_H (kJ mol^{-1})**	**Analytical method**	**Ref**
$Ru\left(10\bar{1}0\right)$	-40	TPD	[32]
$Ru\left(0001\right)$	-46	TPD	[33]
$Ru\left(0001\right)$	-62	TPD	[34]
$Ru\left(0001\right)$	-54	TPD	[35]
Ru/SiO_2 nanoparticles	-40	Calorimetric	[36]
$Ru\left(0001\right)$	-35	TPD	[37]
Ru/ZrO_2	-71	Kinetic model	This work

5.5. Rhodium kinetics

Kinetic investigations have also been performed for a Rh based catalyst. As for ruthenium there is not observed an apparent first order dependency in methane partial pressure. In this investigation for rhodium there have been measured the dependency of methane and steam at various temperatures of 500, 600 and 800°C in comparison to only 500°C for Ru. This will be shown to add information to the understanding of rhodium kinetics. Here the Rh-2 catalyst as presented earlier is used for the kinetic experiments. The Rh catalyst is supported on a ZrO_2 support and with Rh particle diameter of 8.4 nm as determined by transmission electron microscopy corresponding to a metal dispersion of 10.6%. To circumvent transport restrictions during the kinetic measurements, the catalyst pellets were crushed to less than 45 µm and mixed 1:10 with inert ZrO_2 support and pressed to tablets. The final catalyst particle size of the diluted particles was 125-300 µm. The kinetic experiments were performed on reactor system 2 and the bulk effectiveness factors (η) were

calculated to be above 0.8 for 90% of the measurements; hence the intrinsic rate controls the majority of the measurements. For the remaining measurements, η is larger than 0.6.

As given by section 3.3 there is a strong deactivation phenomenon, which makes a pre-treatment procedure at high temperatures necessary to obtain stable catalytic activity. This has been especially pronounced for this testing of rhodium based catalysts, where the high temperature treatment at 850°C for several hours reduced the problem, but it did not completely solve the problem. The catalyst activity have been stabilized, but at different stable activity levels. The differences between the absolute activities for the different set of experiments were included in the modelling procedure by using a factor multiplied to A_1 in Eq. 13, when modelling the experimental data. These factors were determined by standard measurements before and after each experimental series.

5.5.1. **Results**

The kinetic experiments done on rhodium based catalyst can be shown to depend on production inhibition in the same way as for ruthenium. The different models given by section 5.3 have been tested for optimizing the kinetics and the adsorption of CO and H gives the best description of the experimental results.

$$rate = \frac{A_1 \cdot \exp(\frac{-E_1}{RT}) \cdot p_{CH_4} \cdot (1-\beta)}{\left(1 + A_{CO} \cdot \exp\left(\frac{-\Delta H_{CO}}{RT}\right) p_{CO} + A_H \cdot \exp\left(\frac{-\Delta H_H}{RT}\right) p_{H_2}^{½}\right)^2} \quad (75)$$

So the rate is given by a similar expression in Eq. 75. Modelling of the results is divided in steam reforming and CO_2 reforming experiments separately. A total of 62 steam reforming measurements will be modelled initially using Eq. 75 and the results are given by table 16 and Fig. 42-45.

Table 16 Results of fitting the overall rate model to the experimental data. In total 62 steam reforming measurements were fitted by the model. The prefactor, activation energy and adsorption parameters are provided by the reaction rate model. The corresponding sums of squares (SSQ) as given by Eq. 3 are also shown.

Reaction species in denominator of θ_*	**A_1** [mol/g/h/bar]	**E_1** [kJ/mol]	**A_{CO}** [bar^{-1}]	**ΔH_{CO}** [kJ/mol]	**A_H** [$bar^{-½}$]	**ΔH_H** [kJ/mol]	**SSQ** [$\%^2$]
Clean surface	$2.04 \cdot 10^9$	147.7	-	-	-	-	2556
CO and H	$6.89 \cdot 10^6$	89.2	$2.29 \cdot 10^{-5}$	-126.6	$1.99 \cdot 10^{-5}$	-82.1	30.29

Table 16 compares the results obtained using a simple first order dependency with no coverage dependence to those obtained by Eq. 74. As shown by the big difference in SSQ, a simple first order model is too simple to give a reasonable fit to the data. In Fig 42 (a) is shown the rate as a function of the inlet partial pressure in a logarithmic form. The apparent reaction order can then be directly derived from the results. The observed reaction order in methane increases with temperature and decreases with conversion. These observations are ascribed to indirect effects of changes in CO and H coverages. When comparing experiments at 500°C for high (9-22%) and low (5-11%) conversions, the effect of higher CO and H_2 partial pressures for higher conversions results in a lower observed reaction order in methane. This can also be seen by the CO and H coverages in Fig. 42 (b), where there are significantly more free sites for the low conversions than the high conversions. Similarly, orders increase with temperature in the observed reaction as the coverage of CO and H decreases with T. The observed reaction orders in methane are only phenomenological as the reaction is temperature and coverage dependent.

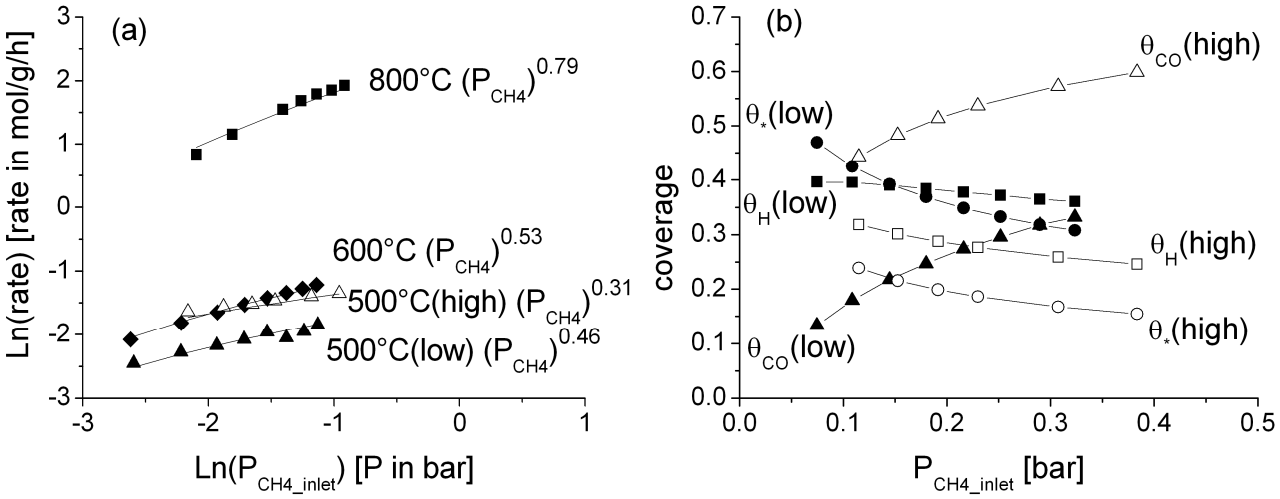

Figure 42. (a) Comparison between the model and the measured overall apparent CH_4 steam reforming rates. The observed reaction orders of methane are shown. The inlet pressure of H_2O was 0.66 bar and N_2 was used as the balance. (b) The average CO and H coverages based on the model are shown for low and high conversions at 500°C, respectively.

Fig. 43 shows the effect of steam partial pressure on the reaction rate. The observed reaction order is observed to be minimal. There is a reasonable agreement between the modelled results and the experimental data. The effect of steam corresponded to previously observed results for rhodium

steam reforming catalysts, where steam was found to have a minimal effect on the steam reforming rate [18,79].

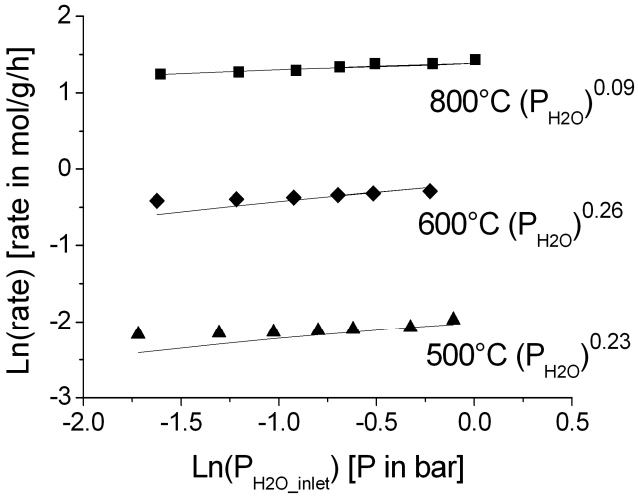

Figure 43. Comparison between model results and experimental data. Overall apparent CH_4 steam reforming rate plotted as a function of the partial pressure of steam with 0.17 bar CH_4 and balance N_2.

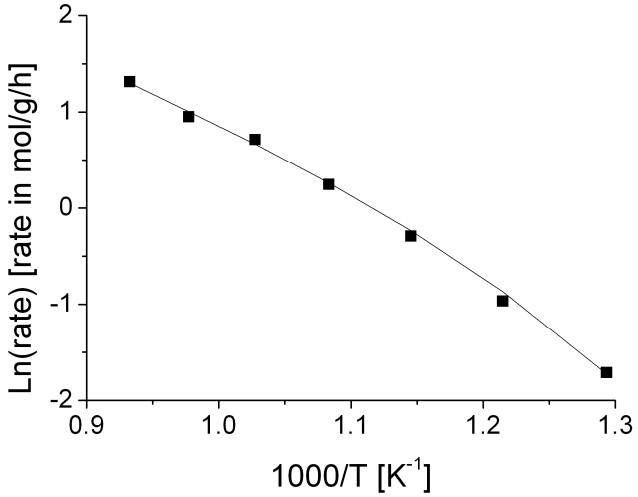

Figure 44. Observed temperature dependency of the steam reforming rate plotted as a function of 1000/T. The gas composition consists of 0.8 bar H_2O, 0.2 bar CH_4 and balance N_2.

The temperature dependency of the rate is shown in Fig. 44. The results are obtained in the temperature range of 500-800°C with corresponding conversions between 3% (500°C) and 62% (800°C). The change of the rate with temperature, CO and H partial pressures give a slightly curved graph when plotting ln(rate) vs. 1/T. In a typical Arrhenius plot, the gradient can be converted to an

observed activation energy. Here the observed activation energy can be estimated to vary between 91 kJ/mol (500°C) and 46 kJ/mol (800°C). These values are valid for the specific conditions used in this experimental set, but serve as a good indication of the difficulty in estimating the activation energy. Detailed modelling as shown here is critical to describe the change in the reaction rate with temperature.

Finally, the effect of H_2 at low temperature was measured. Additional hydrogen was added at the reactor inlet to obtain higher H_2 partial pressures through the reactor. As shown in Fig. 45 the model and the experimental data both show a clear negative effect of hydrogen on the methane steam reforming rate. This was ascribed to the adsorption term for hydrogen in Eq. 74.

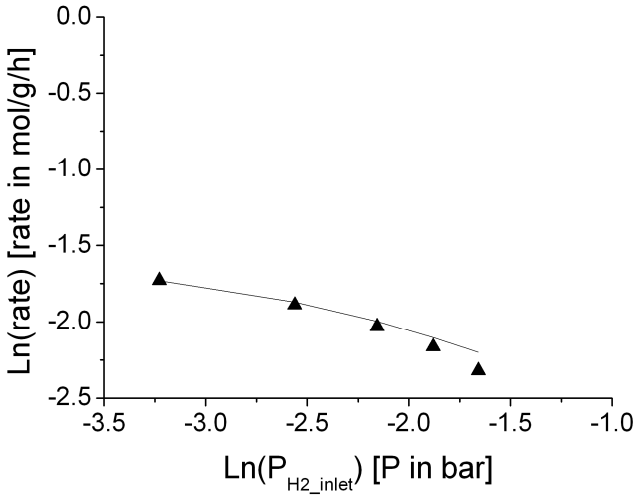

Figure 45. Comparison between model results and experimental data. Average CH_4 steam reforming rate as a function of the inlet H_2 partial pressure. (0.8 bar H_2O, 0.17 bar CH_4, balance N_2)

Until this point only steam reforming experiments have been reported and this is due to a different observed kinetic regime observed when performing CO_2 reforming experiments at the conditions applied here. For CO_2 reforming there is a significant increase in the partial pressure of CO in the gas phase, hence the concentration of adsorbed CO also increases. When attempting to model the CO_2 reforming data with the model obtained by fitting the steam reforming data, but the model gave too low activities. This can likely be explained by too high adsorption energy of CO, though when the CO concentration increases the average CO adsorption energy will decrease due to the CO interaction on the rhodium surface. One way to solve this apparent discrepancy was to adjust the CO adsorption energy and take the remaining values in the models from table 16. The CO_2 reforming data at 500°C and 600°C can be modelled well with an average CO adsorption energy

that is 16.3 kJ/mol lower than that obtained from the steam reforming data with low CO levels. As shown in Fig. 46, the model gives a good description of the experimental data. The average CO coverage is between 0.75 and 0.8, and minimal H coverages for all the CO_2 reforming experiments are obtained.

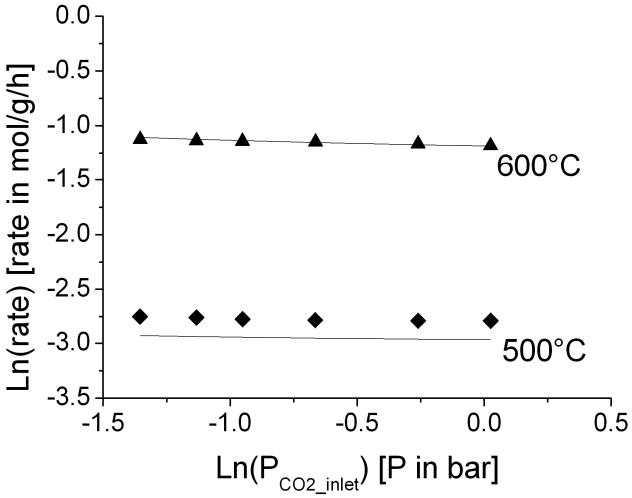

Figure 46. Comparison between model results and experimental data. Average CO_2 reforming rates as a function of inlet CO_2 partial pressure. 0.2 bar CH_4, N_2 balance. The model is given by Eq. 13 and the data in table 1, except ΔH_{CO} = -110.3 kJ/mol.

5.5.2. **Discussion**

In the results and modelling there is found a dependency of the CO and H adsorption on the steam reforming and CO_2 reforming activity on rhodium catalysts. This is in contrast to previous investigations that observe a first order dependency of methane investigations of CO_2 reforming by Bhat and Sachtler at 600°C and that there is no influence of the CO_2 partial pressure [99]. Likewise gave investigations of steam and CO_2 reforming at 550-700°C by Wei and Iglesia the same conclusions as Bhat and Sachtler – i.e. the reaction is first order in CH_4 and no other species influence the reaction rate [18]. These results are not necessarily incorrect, but the exact outcome of the experiments depend strongly on the conversion and hence the possible product hindrance that is observed in this study.

Other studies have been done where similar CO and H effects have been found. In the kinetic model developed in a paper by Maestri et al. [79]. This is due to the adsorption of CO and H that both have a significant influence at low temperatures (<600°C). The inhibition effect of CO on rhodium-based steam reforming catalysts is also been noted elsewhere [9,100].

The adsorption energy estimated in this study of 126.3 kJ/mol is in good accordance with other CO adsorption results [101,102]. Studies of Rh catalysts at ambient conditions show that there is a significant CO coverage at temperatures of around 450°C [101]. It was estimated that a 1%CO/He at 450°C corresponded to 65% CO coverage on a Rh catalyst, which would be equivalent to approximately 30% at 500°C and 7% conversion for a standard experiment in this study, matching fairly well the modelled coverages.

The CO adsorption energy has been shown to depend on the CO surface coverage [101,103]. The initial adsorption energy is determined to 195 kJ/mol for a Rh/Al_2O_3 catalyst [101] and 165-175 kJ/mol [103] on another Rh/Al_2O_3 catalyst. In Fig. 47 the CO adsorption energy is shown as a function of CO coverage for rhodium [103]. For a Rh/Al_2O_3 catalyst, a plateau between θ = 0.05-0.6 shows a constant adsorption energy (115-120 kJ/mol) and at higher coverages (θ = 0.6-0.9) this levels off to approximately 95 kJ/mol [103]. These values are in good agreement with the observations in this study at the different plateaus. The relative difference in adsorption energy at low and high coverage of approximately 16 kJ/mol found in the modelling of the steam and CO_2 reforming experiments.

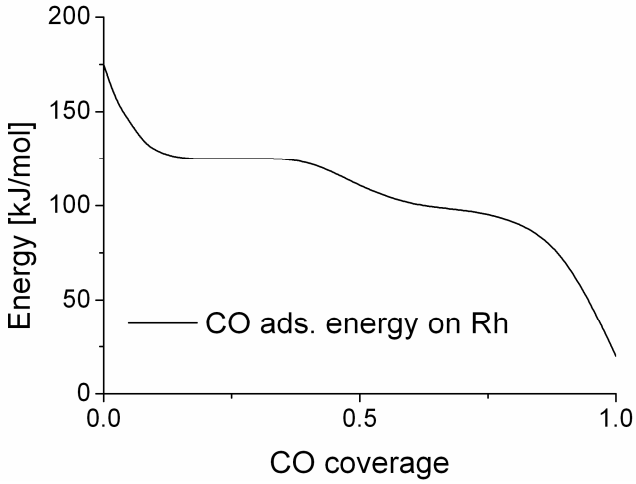

Figure 47. The CO adsorption data for Rh/Al_2O_3 [103].

There is also observed an effect of hydrogen on the overall activity, but to a smaller extent than CO. The adsorption energy in this study has been estimated to 82.1 kJ/mol, where the adsorption energy of hydrogen have been reported to be up to 80 kJ/mol at low coverages and level out to approximately 35-50 kJ/mol at a coverage of θ = 0.4-0.6 [103].

At the hydrogen concentrations and the experimental conditions there have not been reported any specific measurements of the H surface coverage. However, detailed DFT and kinetic modelling

were carried out and it is estimated that there is a significant coverage of hydrogen on rhodium at atmospheric pressure of H_2 at 500°C [93]. These models were confirmed by experimental TPD and metal-hydrogen binding energies [93].

The coadsorption of CO and hydrogen is included in the model, whereas any interaction was disregarded. Studies of coadsorption of CO and hydrogen on Rh(100) show that hydrogen is destabilised and that some of the hydrogen desorbs at a lower temperature due to the interaction [104]. When there are a low number of free sites, the surface will predominantly be covered by CO. This model predicts that the coverages for the two species, CO and H, are similar at steam reforming conditions as shown on Fig. 42(b), but that CO is dominating for CO_2 reforming conditions.

Different values of the activation energy for steam reforming were reported. While the model had an activation energy of 89 kJ/mol, the observed activation energy was in the range of 46-91 kJ/mol at the reaction conditions of this study. Wei and Iglesia's study found an activation energy of 109 kJ/mol [18] for an assumed clean surface, which is not too far from what is found in this study. Maestri et al. included coverage effects in determining the activation energy and estimated an activation energy of 62 kJ/mol at θ_{CO} = 0.15 and θ_H = 0.2, which corresponds well with the observed values that also include a partly coverage of CO and H.

5.6. Noble metal kinetics

The main focus of the experimental study has been on the kinetics for Ru and Rh. Few experiments have also been conducted on a Ir catalyst to make a last comparison between the different noble metal kinetics. The 4wt%Ir/$MgAl_2O_4$ catalyst has been prepared according to section 2.2 and tested on reactor system 2.

5.6.1. **Results**

Fig. 48 and 49 show reforming rates as a function of the methane and steam partial pressures. The results are given for Rh, Ru and Ir. The data for Rh and Ru are taken from the previous results and converted to arbitrary units together with the iridium data. Conversions are comparable around 5-20% and the data have been fitted with a power law model to deduct the differences in trends.

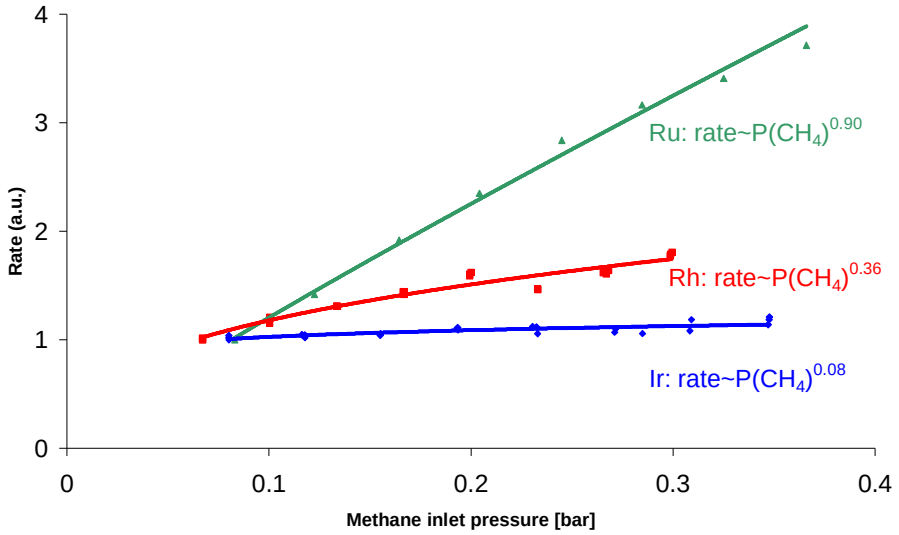

Figure 48. Comparison of the rate (a.u) between Ir, Rh and Ru as a function of the inlet partial pressure of methane at 500°C.

Fig. 48 shows the methane dependency and the large difference for the metals at 500°C. Whereas Ru is only slightly influenced by the product inhibition then the Ir catalyst is strongly inhibited. It is presumed that similar product inhibition exists for Ir as fro the two other noble metals. The Rh catalyst is in between the two other metals. On Fig. 49 is seen the dependency of the inlet partial pressure of steam and it is observed that at these experimental conditions there is negligible influence of the partial pressure of steam for all three metals.

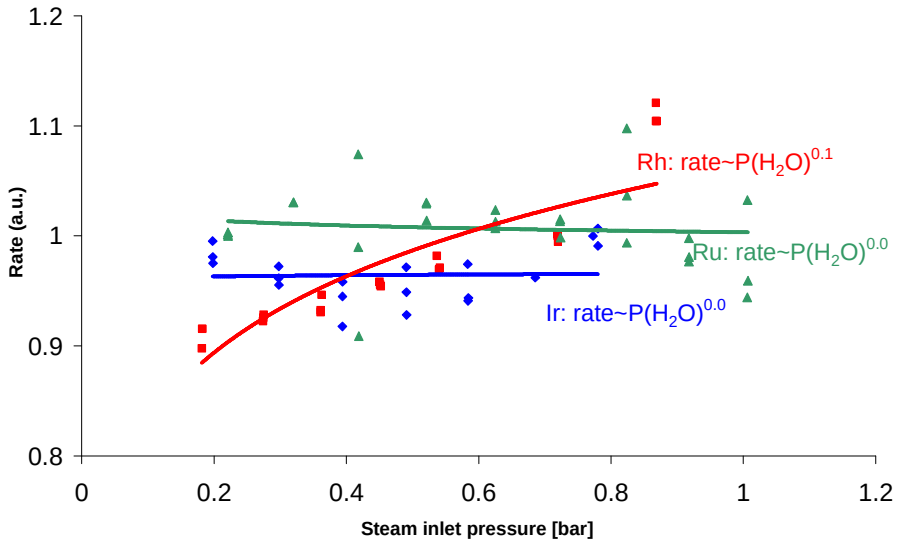

Figure 49. Comparison of the rate (a.u) between Ir, Rh and Ru as a function of the inlet partial pressure of steam at 500°C.

5.6.2. **Discussion**

It is found experimentally that there is a stronger adsorption of CO on Rh than on Ru. On Ru, CO adsorption energy is found to be 87 kJ/mol, where the adsorption energy was largely controlled by CO_2 reforming experiments with an average CO coverage of 0.4-0.5 [10]. It was not necessary to take the adsorption energy dependency of the CO coverage into consideration for the Ru kinetics, probably because the coverages of CO on Ru were below 0.5 during CO_2 reforming. The adsorption energy of CO on Ru corresponded well with other high CO coverage adsorption energies for Ru.

The stronger adsorption of CO on Rh than on Ru is also evident from temperature-programmed desorption (TPD) experiments at similar conditions. On single crystal closed packed surfaces, CO are adsorbed on Ru(0001) [105] and Rh(100) [104]. The experimental conditions are almost equal, making ground for a fair comparison. In Fig. 50 the CO TPD experiments with medium and high initial coverages are shown. The relative strength of CO adsorption on Ru and Rh is supported theoretically by adsorption and desorption calculations on closed packed surfaces at low coverages. These show that CO binds more strongly to Rh than to Ru [106].

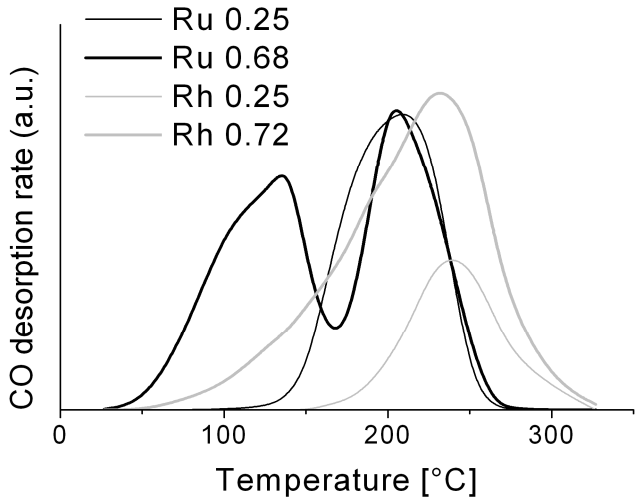

Figure 50. CO TPD data for Ru(0001) [30] and Rh(100) [31]. CO is pre-adsorbed at temperatures below -143°C for both sets of experiments. Initial CO coverages of 0.25 and ~0.7 (0.68 for Ru and 0.72 for Rh) were used. β = 5 °C/s.

The sparse data for Ir does not provide enough to make a full scale modelling. The inhibition order of Ir>Rh>Ru can also be deducted from CO adsorption data, which shows the same trend at 500°C [101,92,107]. Here similar CO adsorption studies have been performed and they show also this trend, supporting the order in inhibition effect. A high heating rate (50°C/s) combined CO and H TPD experiment showed that that is CO desorbs later than what is observed for Ru and Rh in Fig.

50 [108]. This experiment were conducted on a Ir foil, where the last CO is observed to desorb at 500°C well above the observed temperatures in Fig. 50 even for a high heating rate TPD experiment.

5.7. Summary

The methane steam reforming activity of noble metals can be described as a function of the adsorption energies of carbon and oxygen on the metals and the ranking in turn-over frequency of the metals is Ru~Rh>Ni~Ir~Pt~Pd. Generally, it is found that the water gas shift reaction is in equilibrium and the support effect is negligible. It is found by reactor and kinetic modelling that CO and H inhibits the activity of the reaction, where the dominating specie of CO have a great impact on the observed rates. Decreasing adsorption energy of CO leads to a higher observed reaction order in methane and Ru is the least influenced by CO product inhibition followed by Rh and lastly Ir.

Measuring methane steam reforming rates on noble metal catalysts is dependent on the actual experimental conditions, as product inhibition have a great influence. The exact conversion and also the flow rate have a direct impact and without proper modelling it is not possible to derive this kinetic features. This can lead to very different experimental results for the kinetics at various setups and conditions.

6. Conclusion and outlook

In the present thesis work kinetic modelling and reactor modelling have been used to address the methane steam reforming reaction. The goal of developing steam reforming catalysts for low steam/carbon gas mixtures is investigated by characterization of noble metal catalysts, studies into addressing sintering stability, obtaining absolute activities and determining kinetic modelling for noble metal catalysts.

Characterization of noble metal catalysts have shown that similar sulphur adsorption models as for nickel can be taken into consideration. For ruthenium based catalysts carbon resistance is better than expected due to oxygenated species. Furthermore it has been shown that ruthenium based catalysts easily surface oxidize, an important feature when analysing by TEM. This can be addressed by using ETEM facilities at reducing and elevated temperature conditions.

Obtaining stable activities are important, but a deactivation phenomenon has been observed for small catalyst pellets at the temperature region of 550-650°C. Though the catalyst reactivates at higher temperature, it strains the possible operating mode for obtained stable measurements. The deactivation phenomenon is possibly caused by metal-surface interaction phenomenon.

Preventing sintering is a difficult task. A method of anchoring the catalytic active metal particles with high surface energy promoter elements have been attempted. Based on thermodynamic considerations this method should be feasible. The experimental results indicate that this method possibly works, but no conclusive evidence have been obtained.

Thorough description of the steam reforming reaction on noble metal catalyst has been done. It shows that ruthenium and rhodium are the most active catalyst followed by Ni, Ir, Pt and Pd. The activity is strongly dependent on low-coordinated sites as there is a linear dependency of the dispersion. The steps dissociate methane as the key elementary step. The steam reforming kinetics show strong product inhibition for ruthenium and rhodium catalysts, where adsorbance of CO and H is strongest on Rh compared to Ru. Simple investigations of Ir have shown even higher product inhibition than for the first two metals.

Studies in literature of the steam reforming reaction have proven to yield different results. By comparing theoretical modelling with experimental work the rankings and kinetics for the methane steam reforming reaction have been determined. The actual conditions of operation at which the experiments have been conducted is very important to obtain correct kinetics. Differences in actual reaction conditions is the likely explanation for previous discrepancy between kinetic models.

Appendix A – Reactor Modelling

A.1 Example for calculation of effectiveness factor

Calculation of effectiveness factor at 500°C and high reaction rate. The example is a fresh high loaded (5 wt%) ruthenium sample with a rate of 6.6 mol/g/h, at relative low conversion (8.0 %) and 0.2 bar CH_4 (8.923 mol/m^3):

$$k = \frac{rate}{C_{CH_4}} = \frac{6.6\left(mol/g/h\right)\cdot 1.37\cdot 10^6\left(g/m^3\right)\cdot 1/3600\left(h/s\right)}{8.923\left(mol/m^3\right)} = 281.5\left(s^{-1}\right) \quad \text{(A1)}$$

The effective diffusion can be estimated from the diffusion coefficient in gas phase, the porosity and the tortusity factor. The diffusion coefficient is dependent on the gas mixture and calculated based on the gas mixtures at 500°C [65]. The porosity is measured by Hg porosimetry and the tortusity factor is an estimate from the pore system.

$$D_{eff} = \frac{D\cdot\varepsilon}{\tau} = \frac{1.2\cdot 10^{-4}\left(m^2/s\right)\cdot 0.54}{2.5} = 2.59\cdot 10^{-5}\left(m^2/s\right) \quad \text{(A2)}$$

The Thiele modulus:

$$\varphi = L\cdot\sqrt{\frac{k}{D_{eff}}} = 212.5\left(\mu m\right)\cdot\sqrt{\frac{281.5\left(s^{-1}\right)}{2.59\cdot 10^{-5}\left(m^2/s\right)}} = 0.70 \quad \text{(A3)}$$

$$\eta = \frac{3}{\varphi}\left(\frac{1}{\tanh\left(\varphi\right)} - \frac{1}{\varphi}\right) = \frac{3}{0.70}\left(\frac{1}{\tanh\left(0.70\right)} - \frac{1}{0.70}\right) = 0.97 \quad \text{(A4)}$$

So here the effectiveness factor is 0.97. There is a minor effect on the rate that needs to be taken into consideration even though it is close to intrinsic conditions.

A.2 Packed bed calculation

The underlying equations for calculating the heat conductivity in the bed is given here. Firstly is given the turbulent contribution for the heat conductivity in Eq. A5.

$$\lambda_{turb} = \frac{1.15 \cdot \rho_{gas} \cdot u_{gas} \cdot C_{p,gas} \cdot D_{p,av}}{Pe} \tag{A5}$$

Where u_{gas} is the velocity, $C_{p,gas}$ is the heat capacity for the gas, $D_{p,av}$ is the average particle diameter and Pe is the Peclet number (Dimensionless number for momentum transfer relative to the heat transfer). In the following is given the calculation of the stagnant gas contribution based on the theory by Zehner and Schlunde [31]. B is a dimensionless number in the calculation based on the bed porosity.

$$B = 1.25 \cdot \left(\frac{1-\varepsilon_{bed}}{\varepsilon_{bed}} \right)^{10/9} \tag{A6}$$

The void fraction for a standard ZrO_2 catalyst in the catalyst bed is 0.25, which can relatively easy be measured.

$$\lambda_{rad} = \frac{0.04 \cdot C_s}{\frac{2}{emis} - 1} \cdot \left(\frac{T}{100} \right)^3 \cdot D_{p,av} \tag{A7}$$

$$\frac{\lambda_{stag}}{\lambda_{gas}} = \left(1-\sqrt{1-\varepsilon_{bed}}\right) \cdot \left(1+\frac{\lambda_{rad}}{\lambda_{gas}}\right) + \sqrt{1-\varepsilon_{bed}} + \left(\frac{2}{1-\frac{\lambda_{gas}}{\lambda_{particle}} \cdot B} \cdot \left(\frac{\left(1-\frac{\lambda_{gas}}{\lambda_{particle}}\right) \cdot B}{\left(1-\frac{\lambda_{gas}}{\lambda_{particle}} \cdot B\right)^2} \cdot \ln\left(\frac{\lambda_{particle}}{\lambda_{gas} \cdot B}\right) - \frac{B+1}{2} - \frac{B-1}{1-\frac{\lambda_{gas}}{\lambda_{particle}} \cdot B} \right) + \frac{1}{\frac{\lambda_{gas}}{\lambda_{rad}} + \frac{\lambda_{gas}}{\lambda_{particle}}} \right) \tag{A8}$$

The stagnant part contributes by a factor approximately 250 times more to the heat conductivity in the bed than the turbulent part.

A.3 Thermo channel temperature

The calculations for the temperature changes in the thermo channel is presented in this section. In Fig. A.1 is sketched the heat balance for the thermo channel wall.

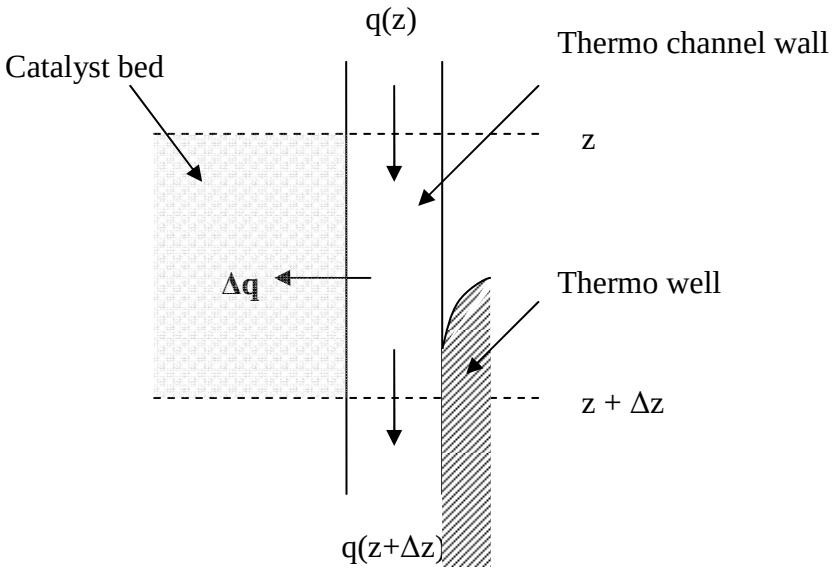

Figure A.1. Sketch of the reactor with the catalyst bed, the thermo channel wall and the thermo well. Heat is transported axially in the thermo channel wall from the gas phase above and below the catalyst bed. Heat is transported in the radial direction from the thermo channel wall to the catalyst bed.

The heat balance can be given by Eq. A9 and expanded to Eq. A10.

$$q(z) = q(z + \Delta z) + \Delta q \tag{A9}$$

$$\lambda_{TC} \cdot A_{cross} \cdot \left(\frac{\partial T_{TC}}{\partial z} \right)_{z+\Delta z} = \lambda_{TC} \cdot A_{cross} \cdot \left(\frac{\partial T_{TC}}{\partial z} \right)_{z} + h_{inner\ wall} \cdot (T_{TC} - T_{bed}) \cdot D_{TC} \cdot \pi \cdot \Delta z \tag{A10}$$

Where λ_{TC} is the heat conductivity in the thermo channel (20 kcal/h/m/k), A_{cross} is the cross sectional area for the thermo channel wall and D_{TC} is the thermo channel outer diameter. It is possible to obtain Eq. A11, which describes the temperature gradient in the thermo channel.

$$\frac{\partial^2 T_{TC}}{\partial z^2} = \frac{h_{inner\ wall} \cdot (T_{TC} - T) \cdot D_{TC} \cdot \pi}{\lambda_{TC} \cdot A_{cross}} \tag{A11}$$

It is assumed that the thermo channel temperature gradient will have a normal distribution, so that Eq. A12 can be set up as a constrain for the equation.

$$\frac{\partial T_{TC}}{\partial z} = 0 \text{ for } z \to -\infty \tag{A12}$$

The second constrain is to ensure that the temperature outside the catalyst bed area will be similar for the thermo channel and the gas temperature. This is achieved by imposing Eq. A13.

$$T_{TC} = T_{inlet} \text{ for } z \to -\infty \tag{A13}$$

Now a temperature profile is obtained that describes the thermo channel and a correct factor of C_{wall} can be determined, so the $h_{inner\ wall}$ is described for both the reactor wall and the thermo channel wall.

Appendix B – Characterization results

B.1 Sulphur

Results for adsorption of sulphur on the samples in the experiments. The catalysts used for these experiments have been

- 4 wt% $Rh/MgAl_2O_4$
- 4 wt% $Ru/MgAl_2O_4$
- 4 wt% $Pt/MgAl_2O_4$
- 4 wt% $Ir/MgAl_2O_4$
- 14.4 wt% $Ni/MgAl_2O_4$

The nickel catalyst is primarily used as a reference catalyst for the noble metal catalyst. In table B.1 is shown the obtained data for the sulphur adsorption at the given temperature. The reference measurement at which the coverages have been normalised to is also presented.

Table B.1. The obtained sulphur adsorption data (S_{cap}) in weight ppm of the catalyst sample. Last column is the reference data for full coverage at 12 ppm H_2S/H_2 and 550°C.

Metal	**0.75 ppm H_2S/H_2 for 864 hours.**						**2.0 ppm H_2S/H_2 for 192 hours.**						**Full coverage**
Rh	T [°C]	463	534	598	664	729	T [°C]	581	613	648	688	730	2700
	S_{cap}	2100	2020	1660	1300	1410	S_{cap}	2670	2310	2190	2010	1655	
Ru	T [°C]	463	534	598	664	729	T [°C]	581	613	648	688	730	2500
	S_{cap}	2370	2430	1980	1480	1420	S_{cap}	2135	2060	1830	1545	1475	
Pt	T [°C]	480	549	611	678	749	T [°C]	590	620	656	697	743	225
	S_{cap}	65	60	90	50	100	S_{cap}	155	140	120	120	100	
Ir	T [°C]	480	549	611	678	749	T [°C]	590	620	656	697	743	730
	S_{cap}	300	400	365	260	250	S_{cap}	590	680	610	545	415	
Ni	T [°C]	495	562	624	693		T [°C]	598	627	663	707		3400
	S_{cap}	2630	1930	1530	1560		S_{cap}	2755	2390	1935	1600		

Appendix C – Promoted catalysts

The reference data used to determine the promoter elements based on the segregation energies (figure C.1 and table C.1), heat of sublimation data (table C.2) and atoms radius data (table C.3). A list of chemicals and experimental procedures for dissolvent in the impregnation is given by table C.4.

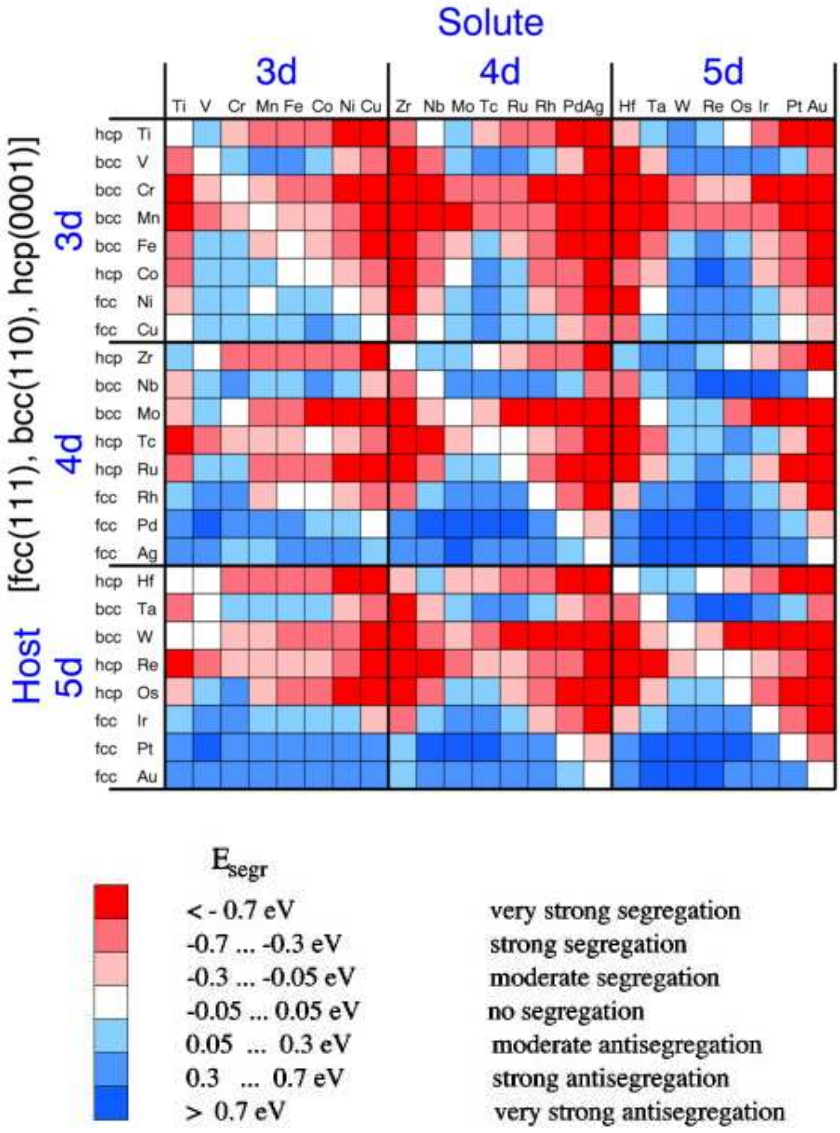

Figure C.1. Surface segregation energies on closed-packed surfaces from Ruban et al. [61].

Table C.1. The values from figure A.1 presented in as numerical values for the relevant promoted catalysts. Surface segregation energies (kJ/mol) for promoters at closed packed surfaces [61].

Promoter / Host	Cu	Mo	Ru	Rh	Pd	W	Re	Os	Ir	Pt
Ru (0001)		9.6				23.2	35.7	22.2		
Rh		42.5	29.9			63.7	68.5	54.0	22.2	
Ir		33.8	22.2			45.3	46.3	30.9		
Pt	30.9	89.7	57.9	25.1	0	111.9	107.1	83.0	42.5	

Table C.2. Heat if sublimation [109]:

Metal	**Rh**	**Ru**	**Pt**	**Ir**	**Mo**	**Re**	**W**	**Ni**
Heat of sublimation at 0 K [cal/mol] [110]					155550	186850	191900	
Heat of Sublimation at 298.15 K [cal/mol]	133100	155000	134970	160000		186100	202400	102670

Table C.3. It is assumed that the lattice parameter is equivalent with the atom size. Since the atom size have an influence on the strain in the alloy system, and then larger atoms will have a tendency to segregate to the surface.

	Preferred configuration	**Fcc lattice parameter**	**Hcp lattice parameter**	**Bcc lattice parameter**
Ru	Hcp	x	2.71/4.28[23]	
Rh	Fcc	3.80[23]		
Ir	Fcc	3.84[23]		
Pt	Fcc	3.92[23]		
Pd	Fcc	3.89[23]		
Mo	Bcc	4.01[111]	X	3.15[23]
W	Bcc	X	X	3.16[23]
Re	Hcp	3.893[112][1]	2.76/4.46[23]	

[1] MEAM calculations

List of chemicals used for promoted catalysts excluding table 3.

Re – **NH_4ReO_4** (Re_2O_7 volatile above 300°C, ReO_2, ReO_3 not volatile) (s)

W – **$(NH_4)_6[H_2W_{12}O_{40}] \cdot 4\,H_2O$** ($WO_x$ not volatile) (s)

Mo – **$(NH_4)_6Mo_7O_{24} \cdot 4H_2O$**, ($MoO_x$ slightly volatile above 700°C) (s)

Table C.4. Overview of the solutions used in the preparation of the catalysts.

Host metal / **Promoter**	**Rh**	**Ru**	**Pt**	**Ir**
Re	Re dissolved at 50°C. One solution.	Re dissolved at RT. One solution.	Re+Pt dissolved at 80°C+acetic acid. One solution.	Re+Ir dissolved at RT. One solution.
W	W dissolved at RT One solution.	W dissolved at RT. One solution.	Pt dissolved at RT+acetic acid. Imp, dried, calcined. W dissolved at RT, second impregnation.	W+Ir dissolved at RT One solution.
Mo	Mo dissolved at RT. One solution.	Mo dissolved at RT. One solution.	Pt dissolved at RT+acetic acid. Imp, dried, calcined. Mo dissolved at RT, second impregnation.	Mo+Ir dissolved at RT. One solution.
Ru	One solution.		Pt dissolved at RT+acetic acid. One solution.	Ir dissolved at Rt. One solution.
Ir	Ir dissolved at RT. One solution.			

Ir-catalysts:

- It seems that there is an uneven distribution of metals through the pellets. Probably a phenomenon of the drying process.

Pt-catalysts

- W and Mo catalysts could not be prepared in one solution, since the precipitation of one of salts was inevitable. Then Pt was impregnated was for these catalysts, then dried and calcined at 450°C (1 hour), followed by impregnation with the promoter.
- The Re promoted Pt catalysts, were impregnated at 80°C.
- During reduction, the acetic acid caused varies problems in the system. All Pt samples was therefore calcined at 300°C/1 hour [100°C/hour] at ambient conditions to oxidize the acetic acid.

Appendix D – Adsorbate models

Overview of possible adsorbants used to test the models.

Model number	Reaction intermediate in denominator of θ_*	Reaction rate expression from derivation	Reaction rate expression simplified
1	None	$k_1^+ P_{CH_4}\left(1-\beta_{SR}\right)$	$k_1^+ P_{CH_4}\left(1-\beta_{SR}\right)$
2	CO	$\frac{k_1^+ P_{CH_4}\left(1-\beta_{SR}\right)}{\left(1+P_{CO}/K_9\right)^2}$	$\frac{k_1^+ P_{CH_4}\left(1-\beta_{SR}\right)}{\left(1+A_{CO}\exp\left(\frac{-\Delta H_{CO}}{RT}\right)P_{CO}\right)^2}$
3	H	$\frac{k_1^+ P_{CH_4}\left(1-\beta_{SR}\right)}{\left(1+P_{H_2}^{½}/K_8\right)^2}$	$\frac{k_1^+ P_{CH_4}\left(1-\beta_{SR}\right)}{\left(1+A_H\exp\left(\frac{-\Delta H_H}{RT}\right)P_{H_2}^{½}\right)^2}$
4	C	$\frac{k_1^+ P_{CH_4}\left(1-\beta_{SR}\right)}{\left(1+\frac{1}{K_2K_3K_7K_8^2K_9}\frac{P_{CO}P_{H_2}}{P_{H_2O}}\right)^2}$	$\frac{k_1^+ P_{CH_4}\left(1-\beta_{SR}\right)}{\left(1+A_C\exp\left(\frac{-\Delta H_C}{RT}\right)\frac{P_{CO}P_{H_2}}{P_{H_2O}}\right)^2}$
5	CH	$\frac{k_1^+ P_{CH_4}\left(1-\beta_{SR}\right)}{\left(1+\frac{1}{K_2K_3K_6K_7K_8^3K_9}\frac{P_{CO}P_{H_2}^{3/2}}{P_{H_2O}}\right)^2}$	$\frac{k_1^+ P_{CH_4}\left(1-\beta_{SR}\right)}{\left(1+A_{CH}\exp\left(\frac{-\Delta H_{CH}}{RT}\right)\frac{P_{CO}P_{H_2}^{3/2}}{P_{H_2O}}\right)^2}$
6	CH_2	$\frac{k_1^+ P_{CH_4}\left(1-\beta_{SR}\right)}{\left(1+\frac{1}{K_2K_3K_5K_6K_7K_8^4K_9}\frac{P_{CO}P_{H_2}^2}{P_{H_2O}}\right)^2}$	$\frac{k_1^+ P_{CH_4}\left(1-\beta_{SR}\right)}{\left(1+A_{CH_2}\exp\left(\frac{-\Delta H_{CH_2}}{RT}\right)\frac{P_{CO}P_{H_2}^2}{P_{H_2O}}\right)^2}$
7	CH_3	$\frac{k_1^+ P_{CH_4}\left(1-\beta_{SR}\right)}{\left(1+\frac{1}{K_2K_3K_4K_5K_6K_7K_8^5K_9}\frac{P_{CO}P_{H_2}^{5/2}}{P_{H_2O}}\right)^2}$	$\frac{k_1^+ P_{CH_4}\left(1-\beta_{SR}\right)}{\left(1+A_{CH_3}\exp\left(\frac{-\Delta H_{CH_3}}{RT}\right)\frac{P_{CO}P_{H_2}^{5/2}}{P_{H_2O}}\right)^2}$
8	CO and H	$\frac{k_1^+ P_{CH_4}\left(1-\beta_{SR}\right)}{\left(1+\frac{P_{CO}}{K_9}+\frac{P_{H_2}^{½}}{K_8}\right)^2}$	$\frac{k_1^+ P_{CH_4}\left(1-\beta_{SR}\right)}{\left(1+A_{CO}\exp\left(\frac{-\Delta H_{CO}}{RT}\right)P_{CO}+A_H\exp\left(\frac{-\Delta H_H}{RT}\right)P_{H_2}^{½}\right)^2}$

References

1. Gasification Technologies Council (2009) http://www.gasification.org/default.aspx

2. J.R. Rostrup-Nielsen, J. Sehested, J.K. Norskov, *Adv. Catal.* 47 (2002) 65-139.

3. M.E. Dry, *Catal. Today* 71 (2002) 227-241.

4. J.-H.B. Hansen and P.E.H. Nielsen, *Handbook of Heterogenous Catalysis, Methanol synthesis vol. 6* (2008) 2920-2949.

5. J. Topp-Jørgensen, *Stud. Surf. Sci. Catal*. 36 (1988) 293-305.

6. J.R. Rostrup-Nielsen, K. Pedersen, J. Sehested, *Appl. Catal. A-Genl* 330 (2007) 134-138.

7. V. Papavassiliou, P. Pacouloute, K.T. Wu, R. Drnevich, D. Vlachos, J. Hemmings, L. Bonnel, *Industrial & Engineering Chemistry Research* 49 (2010) 94-103.

8. P.K. Bakkerud, *Catal. Today* 106 (2005) 30-33.

9. J.R. Rostrup-Nielsen and J.-H.B. Hansen, *J. Catal.* 144 (1993) 38-49.

10. F. Abild-Pedersen, O. Lytken, J. Engbaek, G. Nielsen, I. Chorkendorff, J.K. Norskov, *Surf. Sci*. 590 (2005) 127-137.

11. H. Larsen and I. Chorkendorff, *Surf. Sci. Rep.* 35 (1999) 163-222.

12. G. Jones, J.G. Jakobsen, S.S. Shim, J. Kleis, M.P. Andersson, J. Rossmeisl, F. Abild-Pedersen, T. Bligaard, S. Helveg, B. Hinnemann, J.R. Rostrup-Nielsen, I. Chorkendorff, J. Sehested, J.K. Nørskov, *J. Catal.* 259 (2008) 147-160.

13. J.M. Wei and E. Iglesia, *J. Catal.* 224 (2004) 370-383.

14. J.M. Wei and E. Iglesia, *J. Phys. Chem. B* 108 (2004) 4094-4103.

15. J.M. Wei and E. Iglesia, *J. Phys. Chem. B* 108 (2004) 7253-7262.

16. J.M. Wei and E. Iglesia, *Angewandte Chemie-Int. Ed.* 43 (2004) 3685-3688.

17. J.M. Wei and E. Iglesia, *Abstr. Papers Amer. Chem. Soc.* 227 (2004) U1072-U1072.

18. J.M. Wei and E. Iglesia, *J. Catal.* 225 (2004) 116-127.

19. R.C. Egeberg, S. Ullmann, I. Alstrup, C.B. Mullins, I. Chorkendoff, *Surf. Sci.* 497 (2002) 183-193.

20. D.W. Blaylock, T. Ogura, W.H. Green, G.J.O. Beran, *J. Phys. Chem. C* 113 (2009) 4898-4908.

21. S.G. Wang, X.Y. Liao, J. Hu, D.B. Cao, Y.W. Li, J.G. Wang, H.J. Jiao, *Surf. Sci.* 601 (2007) 1271-1284.

22. M.P. Andersson, F. Abild-Pedersen, I.N. Remediakis, T. Bligaard, G. Jones, J. Engbæk, O. Lytken, S. Horch, J.H. Nielsen, J. Sehested, J.R. Rostrup-Nielsen, J.K. Norskov, I. Chorkendorff, *J. Catal.* 255 (2008) 6-19.

23. I. Chorkendorff and J.W. Niemantsverdriet, *Concepts of Modern Catalysis and Kinetics* Wiley-VCH (2007)

24. F. Abild-Pedersen, J. Greeley, J.K. Norskov, *Catal. Lett.* 105 (2005) 9-13.

25. Y.A. Zhu, D. Chen, X.G. Zhou, W.K. Yuan, *Catal. Today* 148 (2009) 260-267.

26. T. Bligaard, J.K. Norskov, S. Dahl, J. Matthiesen, C.H. Christensen, J. Sehested, *J. Catal.* 224 (2004) 206-217.

27. F. Abild-Pedersen, J. Greeley, F. Studt, J. Rossmeisl, T.R. Munter, P.G. Moses, E. Skulason, T. Bligaard, J.K. Norskov, *Phys. Rev. Lett.* 99 (2007)

28. J.R. Rostrup-Nielsen *Catalytic Steam Reforming* in *Catalysis, Science and Technology.* (Eds.) J.R. Anderson and M. Boudart, Springer (1984)

29. P.L. Hansen, S. Helveg, A.K. Datye, *Adv. Catal.* 50 (2006) 77-95.

30. O. Levenspiel, *Chemical Reaction Engineering* John Wiley & Sons (1999)

31. P. Zehner and E.U. Schlunde, *Chemie Ingenieur Technik* 42 (1970) 933-&.

32. H. Wise, J.G. McCarty, J. Oudar, *Sulfur and Carbon Interactions with Metal Surfaces* In: *Deactivation and poisoning of catalysts* (Eds.) J. Oudar and H. Wise, Marcel Dekker (1985)

33. H.C. Dibbern, P. Olesen, J.R. Rostrupnielsen, P.B. Tottrup, N.R. Udengaard, *Hydrocarbon Processing* 65 (1986) 71-74.

34. J.G. McCarty and H. Wise, *J. Catal.* 94 (1985) 543-546.

35. J.G. McCarty, K.M. Sancier, H. Wise, *J. Catal.* 82 (1983) 92-97.

36. J.G. McCarty and H. Wise, *J. Chem. Phys.* 74 (1981) 5877-5880.

37. J.G. McCarty and H. Wise, *J. Chem. Phys.* 72 (1980) 6332-6337.

38. J. Bénard, J. Oudar, N. Barbouth, E. Margot, Y. Berthier, *Surf. Sci.* 88 (1979) L35-L41.

39. R.I. Hegde and J.M. White, *J. Phys. Chem.* 90 (1986) 296-300.

40. J.R. Rostrup-Nielsen, *J. Catal.* 11 (1968) 220-227.

41. I. Alstrup, J.R. Rostrup-Nielsen, S. Røen, *Appl. Catal.* 1 (1981) 303-314.

42. C.H. Bartholomew, *Appl. Catal. A-Gen.* 212 (2001) 17-60.

43. J.G. McCarty and H. Wise, *J. Chem. Phys.* 76 (1981) 1162-1167.

44. A. Beretta, T. Bruno, G. Groppi, I. Tavazzi, P. Forzatti, *Appl. Catal. B-Env.* 70 (2007) 515-524.

45. A. Beretta, A. Donazzi, G. Groppi, P. Forzattl, V. Dal Santo, L. Sordelli, V. De Grandi, R. Psaro, *Appl. Catal. B-Env.* 83 (2008) 96-109.

46. S.J. Tauster, *Acc. Chem. Res.* 20 (1987) 389-394.

47. J.G.G. Chen, M.L. Colaianni, P.J.J. Chen, J.T. Yates, G.B. Fisher, *J. Phys. Chem.* 94 (1990) 5059-5062.

48. S. Bernal, J.J. Calvino, M.A. Cauqui, J.M. Gatica, C.L. Cartes, J.A.P. Omil, J.M. Pintado, *Catal. Today* 77 (2003) 385-406.

49. C. Wong and R.W. McCabe, *J. Catal.* 119 (1989) 47-64.

50. H. Lieske, G. Lietz, H. Spindler, J. Völter, *J. Catal*. 81 (1983) 8-16.

51. E. Ruckenstein and Y.F. Chu, *J. Catal.* 59 (1979) 109-122.

52. T. Wang and L.D. Schmidt, *J. Catal.* 70 (1981) 187-197.

53. Y. Nagai, K. Dohmae, Y. Ikeda, N. Takagi, T. Tanabe, N. Hara, G. Guilera, S. Pascarelli, M.A. Newton, O. Kuno, H.Y. Jiang, H. Shinjoh, S. Matsumoto, *Angewandte Chemie-Int. Ed.* 47 (2008) 9303-9306.

54. J. Sehested, *J. Catal.* 217 (2003) 417-426.

55. J. Sehested, J.A.P. Gelten, I.N. Remediakis, H. Bengaard, J.K. Norskov, *J. Catal.* 223 (2004) 432-443.

56. J. Sehested, *Catal. Today* 111 (2006) 103-110.

57. J. Sehested, J.A.P. Gelten, S. Helveg, *Appl. Catal. A-Gen.* 309 (2006) 237-246.

58. C.S. Chen, W.H. Cheng, S.S. Lin, *Chem. Comm.* (2001) 1770-1771.

59. G.A. Somarjai, *Introduction to surface chemistry and catalysis* John Wiley and Sons (1994)

60. S.H. Overbury, P.A. Bertrand, G.A. Somorjai, *Chem. Rev.* 75 (1975) 547-560.

61. A.V. Ruban, H.L. Skriver, J.K. Norskov, *Phys. Rev. B* 59 (1999) 15990-16000.

62. H. Dreysse and R. Riedinger, *Phys. Rev. B* 28 (1983) 5669-5674.

64. J.H. Sinfelt, *Science* 195 (1977) 641-646.

65. R.D. Lide *CRC Handbook of Chemistry and Physics, 88th Edition (Internet Version 2008).* CRC Press/Taylor and Francis (2008)

66. F.R. de Boer, R. Boom, W.C.M. Mattens, A.R. Miedema, A.K. Niessen, *Cohesion in metals* Elsevier Science (1988)

67. J. Goodwin, D.O. Goa, S. Erdal, F.H. Rogan, *Appl. Catal.* 24 (1986) 199-209.

68. J.R.Rostrup-Nielsen, *Steam reforming catalysts* Danish Technical Press Inc (1975)

69. B. Predel, *Phase Equilibria, Crystallographic and Thermodynamic Data of Binary Alloys* Springer-Verlag (1993)

70. E. Kikuchi, S. Tanaka, Y. Yamazaki, Y. Morita, *Bulletin of The Japan Petroleum Institute* (1974) 95-98.

71. D. Qin and J. Lapszewicz, *Catal. Today 21* (1994) 551-560.

72. J.R. Rostrup-Nielsen, *J. Catal.* 31 (1973) 173-199.

73. J.M. Wei and E. Iglesia, *Phys. Chem. Chem. Phys.* 6 (2004) 3754-3759.

74. P.G.J. Koopman, A.P.G. Kieboom, H. van Bekkum, *J. Catal.* 69 (1981) 172-

75. C.J.H. Jacobsen, S. Dahl, P.L. Hansen, E. Tornqvist, L. Jensen, H. Topsoe, D.V. Prip, P.B. Moenshaug, I. Chorkendorff, *J. Mol. Catal. A-Chem.* 163 (2000) 19-26.

76. K. Honkala, A. Hellman, I.N. Remediakis, A. Logadottir, A. Carlsson, S. Dahl, C.H. Christensen, J.K. Norskov, *Science* 307 (2005) 555-558.

77. C. Carrara, J. Munera, E.A. Lombardo, L.M. Cornaglia, *Top. Catal.* 51 (2008) 98-106.

78. P. Ferreira-Aparicio, I. Rodriguez-Ramos, J.A. Anderson, A. Guerrero-Ruiz, *Appl. Catal. A-Gen.* 202 (2000) 183-196.

79. M. Maestri, D.G. Vlachos, A. Beretta, G. Groppi, E. Tronconi, *J. Catal.* 259 (2008) 211-222.

80. A. Boisen, T.V.W. Janssens, N. Schumacher, I. Chorkendorff, S. Dahl, *J. Mol. Catal. A-Chem.* 315 (2010) 163-170.

81. B. Hammer, L.B. Hansen, J.K. Norskov, *Phys. Rev. B* 59 (1999) 7413-7421.

82. R.C. Egeberg, S. Ullmann, I. Alstrup, C.B. Mullins, I. Chorkendoff, *Surf. Sci.* 497 (2002) 183-193.

83. H.L. Abbott and I. Harrison, *J. Catal.* 254 (2008) 27-38.

84. A. Berman, R.K. Karn, A. Epstein, *Appl. Catal. A-Gen.* 282 (2005) 73-83.

85. R.M.Nielsen, *The Structure and Reactivity of Ruthenium Nanoparticles*, Ph.D. thesis Technical University of Denmark (2009)

86. J. Sehested, S. Dahl, J. Jacobsen, J.R. Rostrup-Nielsen, *J. Phys. Chem. B* 109 (2005) 2432-2438.

87. T. Bligaard, K. Honkala, A. Logadottir, J.K. Norskov, S. Dahl, C.J.H. Jacobsen, *J. Phys. Chem. B* 107 (2003) 9325-9331.

88. M. Kiskinova and M. Tikhov, *Surf. Sci.* 194 (1988) 379-396.

89. T. Zubkov, G.A. Morgan, J.T. Yates, O. K³hlert, M. Lisowski, R. Schillinger, D. Fick, H.J. Jänsch, *Surf. Sci.* 526 (2003) 57-71.

90. G. Lauth, T. Solomun, W. Hirschwald, K. Christmann, *Surf. Sci.* 210 (1989) 201-224.

91. J. Wang, Y. Wang, K. Jacobi, *Surf. Sci.* 488 (2001) 83-89.

92. O. Dulaurent, M. Nawdali, A. Bourane, D. Bianchi, *Appl. Catal. A-Gen.* 201 (2000) 271-279.

93. F. Faglioni and W.A. Goddard, *J. Chem. Phys.* 122 (2005)

94. H.M. Miura, M.L. Mclaughlin, R.D. Gonzalez, *J. Catal.* 79 (1983) 227-232.

95. N.M. Gupta, V.P. Londhe, V.S. Kamble, *J. Catal.* 169 (1997) 423-437.

96. D.L. King, *Prepr. - Am. Chem. Soc. , Div. Pet. Chem.* 23 (1978) 482-494.

97. I.M. Ciobica, A.W. Kleyn, R.A. van Santen, *J. Phys. Chem. B* 107 (2003) 164-172.

98. D.W. Goodman, T.E. Madey, M. Ono, J.T. Yates, *J. Catal.* 50 (1977) 279-290.

99. R.N. Bhat and W.M.H. Sachtler, *Appl. Catal. A-Gen.* 150 (1997) 279-296.

100. I. Tavazzi, A. Beretta, G. Groppi, P. Forzatti, *J. Catal.* 241 (2006) 1-13.

101. O. Dulaurent, K. Chandes, C. Bouly, D. Bianchi, *J. Catal.* 192 (2000) 262-272.

102. D.N. Belton and S.J. Schmieg, *Surf. Sci.* 202 (1988) 238-254.

103. A. Maroto-Valiente, I. Rodriguez-Ramos, A. Guerrero-Ruiz, *Catal. Today* 93-5 (2004) 567-574.

104. M.M.M. Jansen, J. Gracia, B.E. Nieuwenhuys, J.W. Niemantsverdriet, *Phys. Chem. Chem. Phys.* 11 (2009) 10009-10016.

105. H. Pfnur, P. Feulner, D. Menzel, *J. Chem. Phys.* 79 (1983) 4613-4623.

106. E.D. German and M. Sheintuch, *J. Phys. Chem. C* 112 (2008) 14377-14384.

107. A. Bourane, M. Nawdali, D. Bianchi, *J. Phys. Chem. B* 106 (2002) 2665-2671.

108. V.V. Savkin and N.U. Kislyuk, *Kin. Catal.* 41 (2000) 411-414.

109. R. Hultgren, R.L. Orr, P.D. Anderson, K.K. Kelley, *Selected Values of Thermodynamics of Metals and Alloys* John Wiley & Sons (1963)

110. A.N. Nesmeyanov, *Vapor pressure of the chemical elements* Elsevier (1963)

111. G.F. Wang, M.A. Van Hove, P.N. Ross, M.I. Baskes, *J. Phys. Chem. B* 109 (2005) 11683-11692.

112. G.F. Wang, M.A. Van Hove, P.N. Ross, M.I. Baskes, *J. Chem. Phys.* 121 (2004) 5410-5422.

Journal of Catalysis 259 (2008) 147–160

Contents lists available at ScienceDirect

Journal of Catalysis

www.elsevier.com/locate/jcat

First principles calculations and experimental insight into methane steam reforming over transition metal catalysts

Glenn Jones [a], Jon Geest Jakobsen [b,c], Signe S. Shim [b,c], Jesper Kleis [a], Martin P. Andersson [a], Jan Rossmeisl [a], Frank Abild-Pedersen [a], Thomas Bligaard [a], Stig Helveg [c], Berit Hinnemann [c], Jens R. Rostrup-Nielsen [c], Ib Chorkendorff [b], Jens Sehested [c], Jens K. Nørskov [a,*]

[a] Center for Atomic-Scale Materials Design (CAMD), Department of Physics, Building 307, Technical University of Denmark, DK-2800 Kgs. Lyngby, Denmark
[b] Center for Individual Nanoparticle Functionality (CINF), Department of Physics, Building 312, Technical University of Denmark, DK-2800 Kgs. Lyngby, Denmark
[c] Haldor Topsøe A/S, Nymøllevej 55, DK-2800 Kgs. Lyngby, Denmark

ARTICLE INFO

Article history:
Received 22 May 2008
Revised 31 July 2008
Accepted 5 August 2008
Available online 3 September 2008

Keywords:
DFT
Steam reforming
TEM
Kinetics
Reactivity trends
Noble metals
Surfaces
Nanoparticles

ABSTRACT

This paper presents a detailed analysis of the steam reforming process from first-principles calculations, supported by insight from experimental investigations. In the present work we employ recently recognised scaling relationships for adsorption energies of simple molecules adsorbed at pure metal surfaces to develop an overview of the steam reforming process catalyzed by a range of transition metal surfaces. By combining scaling relationships with thermodynamic and kinetic analysis, we show that it is possible to determine the reactivity trends of the pure metals for methane steam reforming. The reaction is found to be kinetically controlled by a methane dissociation step and a CO formation step, where the latter step is found to be dominant at lower temperatures. The particle size of the metal catalysts particles have been determined by transmission electron microscopy (TEM) and the turn over frequency observed to be linearly dependent on the dispersion, supporting the theoretical notion that the active sites are most likely present as one dimensional edges. It has been found that determination of the correct particle size distribution of small (2–4 nm) Ru particles requires *in situ* TEM measurements under a hydrogen atmosphere. The overall agreement between theory and experiment (at 773 K, 1 bar pressure and 10% conversion) is found to be excellent with Ru and Rh being the most active pure transition metals for methane steam reforming, while Ni, Ir, Pt, and Pd are significantly less active at similar dispersion.

1. Introduction

Our dependence on fossil fuels can be found in areas such as energy production and manufacture of nearly all man-made bulk chemicals. In spite of the necessity to move towards bio- and renewable chemical sources in the future [1–3], the importance of large fossil fuel based industrial processes cannot be over-emphasized and will remain central for a number of years to come. The need for cleaner and more efficient catalysis technologies is therefore greater than ever. Steam reforming is an industrial process of key importance. Natural gas and other liquid hydrocarbons are converted into synthesis gas or hydrogen which can subsequently be transformed to higher value chemicals. The process is a first step in converting natural gas resources to valuable products like petroleum, diesel, methanol, and ammonia. Moreover, steam reforming processes can act as a source of hydrogen and are therefore potentially important in any emerging hydrogen economy. A detailed review of this reforming process and its applications can be found in reference [4].

Steam reforming is traditionally performed over Ni-based catalysts [4] in tubular reformers with the catalyst placed inside 10–12 m long tubes situated in a fired oven. The temperatures vary from 450 °C at the inlet up to 950 °C at the outlet. The effectiveness factor of the catalyst is high (1–0.2) at the inlet but falls below 0.1 after 2 m from the inlet when reaching approximately 600 °C [5]. Noble metals such as Ru [6,7], Rh [7,8], Pd [7], Ir [7,9,10], and Pt [7,11] are also active for steam reforming but these metals are normally too expensive to be used in conventional industrial reformers.

There have been a number of studies that have addressed the order of reactivity between the different transition metals. Rostrup-Nielsen [12] and Kikuchi et al. [13] performed some of the first detailed studies of steam reforming over transition metal catalysts in the early nineteen-seventies. Rostrup-Nielsen [12], measured the rate of steam reforming of ethane at atmospheric pressure and 773 K, which correlated directly with the rate of steam reforming of methane. The relative activity was found to be:

Rh, Ru > Ni, Pd, Pt > Re > $Ni_{0.7}Cu_{1.3}$ > Co.

* Corresponding author. Fax: +45 45253175.
E-mail address: norskov@fysik.dtu.dk (J.K. Nørskov).

0021-9517/$ – see front matter
doi:10.1016/j.jcat.2008.08.003

Kikuchi et al. [13] studied steam reforming of methane at atmospheric pressure in the temperature range 623–873 K and observed a similar sequence of the relative activity between the group VIII metals,

$$\text{Rh–Ru} > \text{Ni} > \text{Ir} > \text{Pd} \sim \text{Pt} \gg \text{Co, Fe.}$$

Kikuchi et al. [13] proposed that the kinetics should follow dependencies on methane and water as $r = k(P_{CH_4})^0(P_{H_2O})^{0.5}$, arguing that there should be no methane dependency of the rate on Ru and Rh pure metals. This kinetic expression is not in agreement with the most recent published activity measurements by Wei and Iglesia as discussed below.

Rostrup-Nielsen and Hansen [7] conducted a series of experiments with Ru, Rh, Pd, Ir, Ni and Pt on MgO supports, measuring steam reforming activity at 823 K and atmospheric pressure. The relative activities were reported to be:

$$\text{Ru, Rh} > \text{Ir} > \text{Ni} > \text{Pt, Pd.}$$

Qin et al. [14] performed similar experiments as Rostrup-Nielsen et al. [7] with noble metals on a MgO support and found an almost identical activity relationship for the noble metal catalysts as the two previous mentioned studies under reaction conditions with a temperature range of 873–1173 K and atmospheric pressure:

$$\text{Ru} > \text{Rh} > \text{Ir} > \text{Pt} > \text{Pd.}$$

It should be noted that support effects were shown to be minimal, with Pd, Pt and Rh on Ceria having a similarly high rate compared to a silicate support [15].

It thus appears that there is a reasonably general consensus regarding the trend in the order of reactivity. Of the pure metal catalysts Ru and Rh are the most active, Ni and Ir are intermediate and Pd and Pt are less active. However, Wei and Iglesia [6,8–11,16] have recently made carefully designed kinetic investigations of a series of metal catalysts for methane steam reforming. It was surprisingly found for the metals investigated (Ru [6], Rh [8], Pt [11], Ir [9,10], and Ni [16]) that the relative activity order was:

$$\text{Pt} > \text{Ir} > \text{Rh} > \text{Ru, Ni.}$$

Interestingly, Wei and Iglesia found that Pt is the most active and that Ir is also more active than Rh and Ru. Wei and Iglesia also showed that the turnover frequency increases with increasing dispersion indicating that the detailed metal nanoparticle structure must play a role for the activity—an observation that could be important for the comparison with previous work. Furthermore Harrison et al. [17] have highlighted a discrepancy in the measured sticking coefficient for single crystal Ru [18], this will be subject to discussion later in the paper.

The kinetics of the steam reforming reaction has been the subject of numerous interpretations and discussions as illustrated lately [16]. The thorough investigations by Wei and Iglesia showed that dissociation of methane is the rate-determining step for both steam and CO_2 reforming of methane. This mechanism was verified at 873 K and various pressures for a range of metals (Ni, Ru, Pt, Rh, and Ir) [16]. It has been shown by other authors that for different transition metals there was a difference between steam and CO_2 reforming reactivity, attributing this to blocking of the active sites by CO [7]. There is a general trend in previous studies, showing that the reaction kinetics are first-order with respect to methane. However, different studies invoke various parameters to be included in the kinetic expression in order to readily explain other phenomena, such as the H_2O dependency [19] or pressure dependency [2]. Therefore, it may be that the activity is not governed by a single rate determining step, but several rate determining steps depending on the reaction conditions [4].

This paper will present a detailed analysis of the methane steam reforming process from first-principles calculations, and compare the results with experimental investigations of the reactivity of supported nanoparticles. Several groups have published results from calculations for CH_4 activation [20–39], however these have not dealt with the full catalytic process of steam reforming under industrial conditions. In the present work we employ recently recognised scaling relationships for adsorption energies (of hydrogenated atoms) adsorbed at pure metal surfaces, to develop an overview of the trends underlying the steam reforming process catalyzed by transition metals. These relationships allow total energies of reaction intermediates to be estimated and used in a complementary fashion alongside detailed density functional theory calculations. Once the detailed energetics are established, thermodynamic analysis can be applied to the total energies in order to account for temperature and pressure effects. The approach is particularly important because the entropic effects become significant at the high reaction temperatures necessary for the steam reforming process. Finally, the thermodynamic analysis allows us to parameterize a kinetic model from which we can determine turn-over frequencies (TOF) for a range of pure metals. This opens up both the possibility of establishing a detailed understanding of the relative rates of pure metal catalysts, as well as the possibility for a future rational search for improved steam reforming alloy catalysts.

To validate and expand the theoretical model, we combine the first principles calculations with experimental investigations of the steam reforming process. The experimental work will report on the steam reforming activity for a series of catalysts (Ni, Pt, Ru, Rh, Ir, Pd), primarily supported on ZrO_2 and Al_2O_3. The activity experiments are performed at atmospheric pressure and 773 K, at conditions far from equilibrium. The activities are correlated with structural information in terms of the metal dispersions of the catalysts, which are determined from (environmental) transmission electron microscopy (TEM) and supported by sulphur chemisorption and X-ray powder diffraction (XRPD). From the dispersions and the activities it is possible to evaluate the relative turn-over frequencies (TOF) for the metal catalysts studied here. The results show a clear dependency of the steam reforming activity on different types of metals and a significant increase in the activity with increasing dispersion. The experimental determination of the TOF and the dispersion allows direct comparison and benchmarking of the theoretical results.

2. Theoretical methodology

DFT is used as implemented in the computer code DACAPO using the RPBE exchange correlation functional [40]. Previous work has shown that the important active sites for a number of catalytic processes are the steps [33,41–44]. That this is also the case for methane dissociation was also recently demonstrated for a stepped Ni(111) surface where it was possible to separate the reactivity of the steps from that of the terraces. The ratio of turn over frequencies was found to be a factor of 200, which was in good agreement with theoretical calculations [45]. Steps thus present a lower activation barrier for steam reforming than close-packed terrace sites and the results presented here have therefore been calculated on stepped surfaces. In order to establish the adsorption energetics of hydrogenated intermediates scaling relationships were combined with the relative energies from Ref. [46] for adsorption on the fcc{211} surface for the close-packed (fcc and hcp) metals and bcc{210} surface for the bcc metals.[1] Unit cells of (2×1) periodicity were used with a depth of 10 atomic layers and a vacuum

[1] Experience has shown that modelling hcp with fcc stepped surface provides a good model and captures the desired trends. However using bcc metals in an fcc

region of 10 Å. An electronic plane wave cut-off of 340 eV was used, with the Brillouin zone being sampled by a Monkhorst–Pack [47] mesh of $\{4 \times 4 \times 1\}$. Pseudopotentials of the Vanderbilt [48] type were used to describe the electronic core regions.

Linear scaling relationships were used as discussed in reference [49]. In brief, the basic theory shows that an estimate of the adsorption energy of a given species is obtained from a linear relationship having a slope given by the valency parameter γ. If we have calculated the energy of all reaction intermediates, $\Delta E_{\mathrm{M1}}^{\mathrm{AH}_x}$, for one metal, M1, we can therefore estimate the energy, $\Delta E_{\mathrm{M2}}^{\mathrm{AH}_x}$, of the same intermediate on another metal, M2, from the adsorption energies of atom A on the two metals as:

$$\Delta E_{\mathrm{M2}}^{\mathrm{AH}_x} = \Delta E_{\mathrm{M1}}^{\mathrm{AH}_x} + \gamma(x)\left(\Delta E_{\mathrm{M2}}^{\mathrm{A}} - \Delta E_{\mathrm{M1}}^{\mathrm{A}}\right), \tag{1}$$

where γ is given by $(x_{\max} - x)/x_{\max}$, where $x_{\max}$ is the number of hydrogen atoms required to provide sufficient electrons to fulfill the octet rule of a given atomic species and x is the number of hydrogen atoms in the species for which the adsorption energy is determined.

This approach allows us to screen a wide range of metals [50], achievable through the knowledge of either the adsorption energy of the parent atom in question and the knowledge of all the species on a single metal. This paper has used values calculated from full DFT calculations carried out on Ru $\{10\bar{1}5\}$ surfaces for M1, and used a database of adsorption energies [46] to obtain the values for M2.

Two further relationships are necessary to fully parameterise the adsorption energies required for the steam reforming process. They relate the adsorption energy of CO to C and also the adsorption of H to C. For the purposes of this paper they are presented in a phenomenological fashion and further details, along with the calculated DFT energies can be found in the supporting material.

In order to determine scaled values for the transition state, it is also possible to use linear energy relationships determined from DFT calculations. An example of such a class is the so-called Brønsted–Evans–Polanyi relationship (BEP) [51]. The transition state barrier for a process is plotted against ΔE of the elementary step or another suitable descriptor. It is often found that a linear scaling does exist and the dependence on the barrier height to the descriptor can thus be obtained. This approach has been used to determine an expression for the CO formation step [52]:

$$\Delta E_{\mathrm{C^*+O^*\rightarrow CO^*}}^{\mathrm{Act.}} = \alpha \Delta E_{\mathrm{CO^*-C^*-O^*}} + \beta, \tag{2}$$

where $\Delta E_{\mathrm{C^*+O^*\rightarrow CO^*}}^{\mathrm{Act.}}$ is the activation barrier for CO formation, $\Delta E_{\mathrm{CO^*-C^*-O^*}}$ is the energy of reaction for the formation of adsorbed CO from adsorbed C and O, α and β are parameters from the straight-line fit. The relationship determining the CH_4 dissociation barrier is derived from the BEP relationship between the activation barrier for CH_4 dissociation, $\Delta E_{\mathrm{CH_4(g)\rightarrow CH_3^*+H^*}}^{\mathrm{Act.}}$, and the energy of reaction for the dissociative adsorption of CH_4, $\Delta E_{\mathrm{CH_3^*-H^*-CH_4(g)}}$:

$$\Delta E_{\mathrm{CH_4(g)\rightarrow CH_3^*+H^*}}^{\mathrm{Act.}} = \alpha \Delta E_{\mathrm{CH_3^*-H^*-CH_4(g)}} + \beta. \tag{3}$$

The equation is based on a linear relationship between the adsorption energy of C and the adsorption energies of both CH_3 and H and that the energy of CH_4(g) is constant. By plotting the barrier height for CH_4 dissociation against the adsorption energy of C we obtain a linear relationship, which to a first approximation gives us the activation barrier for a particular metal. The supporting information should be consulted for diagrams and tables describing these relationships.

structure is often more problematic, hence the need to model them explicitly with a bcc surface.

Thermodynamic analysis can be carried out using the total energies (E) obtained from either full DFT or scaling methods as input. In this study free energies have been calculated by employing standard formulas from statistical thermodynamics [53]. For the gas-phase species (X) at temperature (T) and pressure (P), the Gibbs free energy ($G_{\mathrm{X}}^{P,T}$) is given by:

$$G_{\mathrm{X}}^{P,T} = E_{\mathrm{X}} + E_{\mathrm{ZPE}} + \Delta H^{0,T} - TS^T + k_{\mathrm{B}}T\ln(P/P^0), \tag{4}$$

where E_{ZPE} is the zero point energy, $\Delta H^{0,T}$ is the enthalpy change due to increasing the temperature from 0 K to T, S^T is the entropy at T, k_{B} is Boltzmann's constant and P^0 is standard pressure (taken to be 1 bar). The equation for calculating the energy of the adsorbed species (X′) on metal (M), $E_{\mathrm{X'}}$, is given by: $E_{\mathrm{MX'}} - E_{\mathrm{M}}$. There is no pressure term and the enthalpy change is replaced by the change in internal energy. This leads to the following expression for ($G_{\mathrm{X'}}^{P,T}$):

$$G_{\mathrm{X'}}^{P,T} = E_{\mathrm{X'}} + E_{\mathrm{ZPE}} + \Delta U^{0,T} - TS^T. \tag{5}$$

The vibrational frequencies used within this work to determine E_{ZPE}, $\Delta U^{0,T}$ and S^T are calculated within the harmonic approximation (n.b. configurational entropy is not included). There are clearly issues regarding the validity of this approximation, particularly to the low frequency modes of surface species and internal molecular rotation around bonds. However, there is at present no simple alternative method. Given that we are considering temperatures on the order of 1000 K it is believed that a larger source of error would result from leaving the contributions out. Furthermore, only one set of vibrational calculations was carried out, on the Ru$\{10\bar{1}5\}$ surface, the values obtained were then used for the other metals. This was done primarily because carrying out the vibrational frequencies on every metal would be computationally expensive, and secondly in the spirit of utilizing the scaling relationships in order to reduce the computational cost; it would require full DFT calculations of every species on every surface to obtain all of the vibrational frequencies. Again there is undoubtedly some error introduced from this approximation, but it will still enable the essential aspects of the temperature dependency to be captured, and the variations in entropic contributions over the different surfaces are likely to be significantly smaller than the variations in adsorption energetics [54].

Once the thermodynamic quantities are determined, we are in a position to construct the kinetic model. In order to do this, two important relationships are needed. The first relates the standard free energy change of an elementary reaction step, to the equilibrium constant of a reaction:

$$K_i = \exp\left(\frac{-\Delta G_i^{0,T}}{k_{\mathrm{B}}T}\right), \tag{6}$$

where K_i is the equilibrium constant of elementary step i. The second relates the standard free energy of activation, $\Delta G_i^{\mathrm{Act.}}$ (for those steps that cannot be considered at equilibrium) to the rate constant (k_i), which in transition state theory is:

$$k_i = \frac{k_{\mathrm{B}}T}{h}\exp\left(\frac{-\Delta G_i^{\mathrm{Act.}}}{k_{\mathrm{B}}T}\right), \tag{7}$$

where h is Planck's constant. This expression can be evaluated for both the forward and reverse reaction, along with the relevant coverages or gas-phase pressure of an elementary step in order to obtain the net rate of the particular step in question. The elementary steps considered in the steam reforming reaction will be presented with some discussion later in the paper.

Table 1
Overview of the catalysts investigated in this paper. The varying treatments are given by aging time and temperature. This gives rise to varying particle sizes and dispersions. The activity is given as a turn-over frequency (TOF)

Catalyst	Support	Aging time (h)	Aging temperature (K)	Average particle diameter (nm)	Dispersion (%)	TOF at 773 K (s^{-1})
1 wt% Rh-1	ZrO_2	–	–	2.7/2.2[a]	32.3	12.5
1 wt% Rh-2	ZrO_2	228	1103	8.4	10.6	1.8
5 wt% Rh-3	ZrO_2	–	–	4.5	21.0	7.4
5 wt% Rh-4	ZrO_2	72	1103	8.2	11.0	3.6
5 wt% Rh-5	ZrO_2	600	892	6.5	12.7	6.2
5 wt% Rh-6	ZrO_2	600	946	7.0	12.8	4.7
5 wt% Rh-7	ZrO_2	600	1067	9.8	9.5	2.5
5 wt% Rh-8	ZrO_2	600	1096	11.1	7.6	2.0
1 wt% Ir-1	ZrO_2	–	–	1.4/1.7[a]	82.2	2.3
1 wt% Ir-2	ZrO_2	228	1103	2.9	28.4	2.1
1 wt% Ru-1	ZrO_2	–	–	4.2/2.1[a]	48.1	19.9
1 wt% Ru-2	ZrO_2	228	1103	7.2	10.8	1.1
1 wt% Pt-1	ZrO_2	–	–	1.9/2.3[a]	58.4	2.5
1 wt% Pt-2	ZrO_2	228	1103	3.9	23.8	0.5
1 wt% Pd-1	Al_2O_3	–	–	21	54.1	1.3
14.8 wt% Ni-1	$MgAl_2O_4$	–	–	6.1	20.0	1.0
2.4 wt% Ni-2	Al_2O_3	–	–	2.7/2.8[a]	35.9	1.9
10 wt% Ni-3	Al_2O_3	–	–	2.6	40.5	2.0

[a] *Ex situ*/*in situ* measurements.

3. Experimental methods

3.1. Catalyst preparation and pre-treatment

A series of eighteen different catalysts were prepared for studying the methane steam reforming reaction over noble metal catalysts. Three different support materials were used in the preparation, an yttrium (3 mol%) stabilised ZrO_2 support, a θ-Al_2O_3 support and a $MgAl_2O_4$ spinel support with BET areas of 16, 116 and 18 m^2/g, respectively.

The metals (Ru, Rh, Ir, Pt, Ni and Pd) were impregnated by the incipient wetness method using aqueous solutions of $Ru(NO)(NO_3)_3$, $Rh(NO_3)_3$, $IrCl_3{\cdot}4H_2O$, $Pt(NH_3)_4(NO_3)_2$, $Ni(HCOO)_2$, $Ni(NO_3)_2$ and $Pd(NH_3)_4(HCO_3)_2$. 1 wt% metal catalysts and 5 wt% Rh catalysts were prepared using the ZrO_2 carrier. On the Al_2O_3 support, three samples (2.4 wt% Ni, 10 wt% Ni and 1 wt% Pd) were made. Finally, a 14.8 wt% Ni sample was prepared by impregnation on the $MgAl_2O_4$ support. All the eighteen catalysts were subsequently heated to 723 K in air followed by reduction in pure hydrogen at 1 bar and 798 K according to [4,55].

To obtain varying particle sizes, six 5 wt% Rh/ZrO_2 catalysts were aged for up to 600 h at different temperatures between 873 and 1103 K in H_2O/H_2 mixtures ($H_2O{:}H_2 = 1{:}1$) at 31 bar total pressure. Samples of 1 wt% Rh/ZrO_2, 1 wt% Ir/ZrO_2, 1 wt% Ru/ZrO_2 and 1 wt% Pt/ZrO_2 were aged at 1103 K for 228 h in a similar gas mixture. The ageing procedures rendered a total of 18 catalysts, which are listed in Table 1.

After reduction or ageing treatments, all catalysts were exposed to N_2 while cooling to room temperature and passivated at room temperature by exposure to a flow of 1% air for several hours before exposure to air. After this passivation procedure the catalysts were removed from the reactor and transferred in ambient environment to the different characterization setups.

3.2. Activity measurements

The rates of steam reforming of the catalysts were measured using a fixed bed steel reactor with an internal diameter of 7.1 mm and a thermo well with a diameter of 1.8 mm mounted inside the reactor. 10–120 mg of each catalyst was crushed to a sieve fraction of 0.3–0.5 mm and mixed with catalytically inert $MgAl_2O_4$ with the same grain size to obtain a total mass of 300 mg. The mixture of catalyst and inert material was placed in the reactor on wads of quartz wool supported on a metal plate with holes. The resulting bed height was approximately 11–12 mm. After insertion, the catalysts were first re-reduced in H_2 at 1 bar and 623 K. Subsequently the rate of methane steam reforming was measured at 773 K using a gas mixture of 19% CH_4, 7% H_2 and 74% H_2O at a total flow of 21.6 Nl/h and ambient pressure. At the reactor outlet, steam was condensed and the composition of the dry gas was analysed by a gas chromatograph (GC). The conversion was calculated from the GC analysis and the rate of methane consumption in the reactor was determined based on the methane inlet flow. The overall conversion in the reactor was used to calculate the local rate of reforming at the top of the catalyst bed by assuming that the rate (r) is described by the following expression for reforming:

$$r = k(T)\,p(\mathrm{CH_4}) \tag{8}$$

in accordance with the results recently obtained by Wei and Iglesia [16]. In contrast to Wei and Iglesia, we have performed kinetic studies mainly around >723–823 K which represents typical temperatures at the inlet of tubular reformers and in pre-reformers [19]. At the higher temperatures used by Wei and Iglesia, the reaction gas will be close to equilibrium in a tubular reformer with the axial temperature gradient as the main driving force for the reaction [19]. The conversions were always small (<15%) and no corrections were therefore needed to account for the finite approach to equilibrium.

3.3. Transmission electron microscopy

All catalysts were investigated by means of transmission electron microscopy (TEM) in order to determine the particle size distributions (PSDs), an average metal particle diameter, and the metal dispersion. Measurements were done *ex situ* using a Philips CM200 FEG and a Philips CM300 FEG electron microscope. For *ex situ* microscopy, a TEM specimen was prepared of each catalyst under ambient conditions by crushing the passivated catalyst to a fine powder and dispersing the powder on Cu grid covered with a holey carbon film. TEM images were recorded using a $1k \times 1k$ CCD camera at different magnifications corresponding to an image pixel size in the range of 0.08 nm to 0.45 nm. In order to enhance image contrast of the metal nanoparticles, an objective aperture was employed with a cut-off at 0.20 nm (CM200) or 0.24 nm (CM300).

Experiments were also performed *in situ* using environmental TEM (ETEM) in order to explore whether passivation affects the metal particle size. The ETEM experiments were done using a Philips CM300 FEG electron microscope equipped with an environmental cell [56]. In the ETEM experiments, the catalyst powders were distributed on a Mo TEM grid and exposed to 2.0 mbar H_2 at 773 K for about 1 h to re-reduce the catalyst. Subsequently, images were recorded *in situ* with the catalyst exposed to 1.2–1.6 mbar H_2 at 773 K. TEM images were recorded using a $1k \times 1k$ CCD at a magnification corresponding to an image pixel size of 0.12 nm. An objective aperture was employed with a cut-off at 0.26 nm.

From the TEM or ETEM images, the metal nanoparticle diameters are determined from the projected area of the particles assuming that the particles are spherical. The resulting particle size distributions allow surface-averaged diameters to be compared to sulphur chemisorption experiments and volume-averaged particle diameters to be compared to the average particle diameters ob-

tained by XRD methods.[2] The surface-averaged particle diameter is given by

$$d_s = \frac{\sum n_i d_i^3}{\sum n_i d_i^2}$$

where n_i is the number of particles with diameter d_i. Likewise, the volume-averaged particle diameters are given by

$$d_v = \frac{\sum n_i d_i^4}{\sum n_i d_i^3}.$$

The dispersion can then be determined from the total surface area (A_{tot}) and the total volume (V_{tot}) determined from the particle size distributions by the following equation:

$$D = \frac{A_{tot}}{V_{tot}} \cdot \frac{v}{s} = 6 \cdot \frac{\sum n_i d_i^2}{\sum n_i d_i^3} \cdot \frac{v}{s}, \quad (9)$$

where v is the atomic volume and s is the surface area per atom. If we assume that the close-packed surfaces which have the lowest surface energies are dominant, then it is possible to calculate the dispersion for an fcc(111) metal particle by

$$D = \frac{\sum n_i d_i^2}{\sum n_i d_i^3} \cdot \frac{6a}{\sqrt{3}}$$

and for an hcp(0001) metal particle by

$$D = \frac{\sum n_i d_i^2}{\sum n_i d_i^3} \cdot 3 \cdot c,$$

with a and c being the lattice parameters.

3.4. X-ray powder diffraction

The 5 wt% Rh samples were analysed by X-ray powder diffraction (XRPD) to determine the average rhodium crystallite sizes of selected samples. It should be noted that crystallite sizes obtained by XRD are volume averaged. The XRD measurements were performed on a Philips X'Pert Pro θ–θ diffractometer with Bragg–Bretano geometry, a variable divergence slit and a graphite monochromator using Cu$K\alpha$ radiation. Average metal crystallite sizes were obtained from the line broadenings of the Rh(200) diffraction line, corrected for the instrumental broadening, using the Scherrer equation.

3.5. Sulphur chemisorption

Sulphur chemisorption was used for estimating the diameter of the metal crystals of the zirconia supported Rh catalyst according to [16,19]. As there are no systematic studies published on the H_2S/Rh system, the use of the correlation for metal crystal size and sulphur uptake as for nickel [19] represents a simplification. In brief, the catalysts were exposed to a H_2S/H_2 gas mixture until saturation. After sulphidation, the sulphur uptakes of the catalysts, in μg sulphur per gram catalyst (ppm), were determined by oxidation of the chemisorbed sulphur at high temperature and measuring the amount of generated SO_2 by means of infrared detection. The sulphur chemisorption capacity (s_{cap}) was used to estimate the dispersions and surface-averaged metal particle diameters. For nickel catalysts it is possible to correlate the sulphur chemisorption and the diameter [19]. However, for Rh catalysts the conversion of the sulphur uptake to a metal area, a surface-averaged metal-diameter and a metal dispersion is less well studied. The maximum coverage of sulphur at nickel is approximately 0.5 and this value is also assumed to be the maximum coverage of sulphur on Rh. The total number of metal surface atoms per weight, $N_{surface}$, may then be calculated from the sulphur capacity, $s_{cap.}$ (wt. ppm), the molar mass of sulphur, M_s (g/mol), the coverage of sulphur, θ_s, and Avogadros number N_A

$$N_{surface} = N_A \frac{s_{cap}}{M_s \theta_s} 10^{-6}. \quad (10)$$

The total number of Rh atoms in the catalyst can then be calculated from the weight percentage of the metal, X, and the molar mass of the Rh, M_x (g/mol)

$$N_{total} = N_A \frac{X}{M_x \cdot 100}. \quad (11)$$

Combining Eq. (10) and Eq. (11) it is then possible to estimate the dispersion of the metal based on a measurement of the sulphur capacity

$$D = \frac{1}{\theta_s} \frac{M_x}{M_s} \frac{s_{cap}}{X} 10^{-4}. \quad (12)$$

For Rh (fcc metal) is possible to estimate the average particle diameter based on the dispersion by combining Eq. (12) and Eq. (9)

$$d = \theta_s \frac{M_s}{M_x} \frac{X}{s_{cap}} \frac{6v}{s} 10^4, \quad (13)$$

where v and s are the volume and surface area of the metal x in the catalyst as given previously assuming closed packed surfaces.

4. Theoretical results

The theoretical part of the paper will develop the picture of steam reforming in a sequential manner. Starting from the simple energetic picture, we then build up the complexity by introducing reaction conditions such as pressure and temperature through thermodynamic considerations, and finally we turn the theoretical picture into a micro kinetic model of the steam reforming process. The discussion will unfold primarily to address what key parameters are important for the reaction and to establish a consistent picture of the reaction.

4.1. Thermodynamic analysis

We shall begin by considering what can be learnt by applying the scaling relationships to the construction of an energy diagram for steam reforming. Fig. 1 illustrates the overall energy diagram that can thus be constructed. Even this most simple diagram is extremely instructive, for a number of reasons. This allows one to momentarily take a step back from the intricate details, and to observe the overall trends in steam reforming reactivity of the pure metals. It is immediately observed that the noble metals Au, Ag and Cu are completely unsuitable for steam reforming with the reaction steps from $CH_4(g) + H_2O(g)$ all the way to $C^* + O^*$ being significantly uphill energetically. We can also consider the other extreme where W binds C^* and O^* so strongly that they are unlikely to react off easily, and in fact W is found to be oxidised under these conditions. In Fig. 1 a region of metals can be discerned, bounded by Pt and Ru, for which the reaction looks reasonably favourable.

When one considers the overall reaction, it can be seen that the reaction from left (reactants) to right (products) is uphill (endothermic) and it can also be observed from the stoichiometry of the reaction that the entropy is increasing (four product molecules

[2] There is not any particular merit to one or the other technique, but one needs to be aware of the subtle difference in the information obtained, due to the nature of the technique.

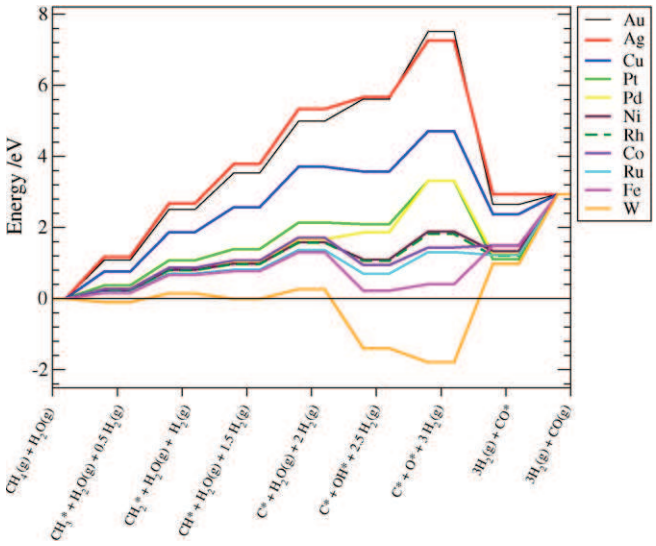

Fig. 1. The potential energy diagram for steam reforming, as determined from the linear scaling relationships. Here a range of metals from noble to highly reactive are considered.

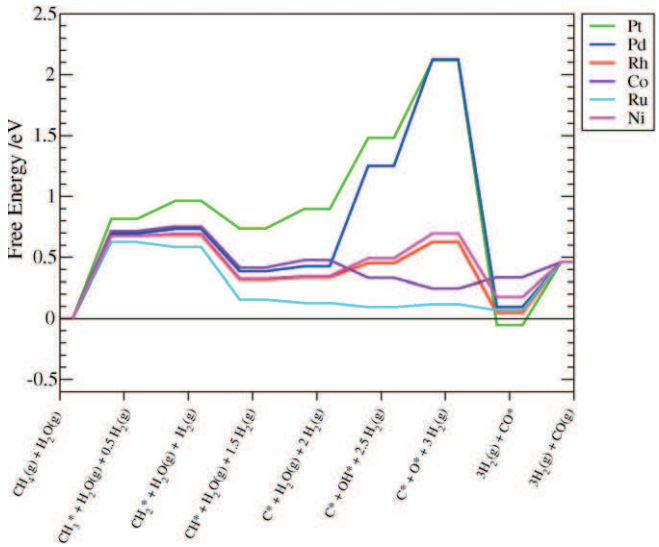

Fig. 2. Standard free energy reaction scheme for steam reforming at 773 K. The noble metals Cu, Ag and Au are now removed from consideration as are the metals that are to reactive and known to form oxides under the reaction conditions. DFT was used to calculate the energies of C*, O* and the gas phase species (as well as the Ru data which all other data was referenced to). Scaling relationships were used to determine the energies of the hydrogenated species. The data are calculated using scaling relationships to determine total energies of hydrogenated species and DFT of those remaining.

per two reactant molecules). This second point is particularly important because it implies that the $T\Delta S^T$ in the expression for the gas-phase free energy will become increasingly significant as the temperature increases. It is therefore essential to run the reaction at high temperature in order to obtain a significant conversion. Furthermore, it is important to consider the energetics under these elevated temperatures in order to simulate some of the subtleties that arise.

For clarity of discussion the focus will now be on the subset of most relevant metals, namely those in Fig. 1 that are bounded by Pt and Ru (i.e. Pt, Pd, Ni, Rh, Co, Ru). For these the thermodynamic terms at specific temperatures are now included for the purpose of calculating $\Delta G^{0,T}$. In order to facilitate the subsequent discussion, a temperature of 773 K will be used for the main body of the text. This is because the presented experimental work has been carried out at this temperature. In the supporting material graphs are included that correspond to higher temperatures (1000 K) as well as conditions which match those used in the work of Wei and Iglesia (873 K). Fig. 2 shows the reaction free energy profile at 773 K. It is observed that the overall standard free energy is increasing by a little less than 0.5 eV. It should be noted that we do not achieve a negative change in free energy at standard pressure for the reaction until ~900 K (however if we apply 1 bar of pressure and 10% conversion at 773 K we do in fact drive the final state down to the level of the initial state, implying that equilibrium at 773 K gives 10% conversion). What is clearly evident under these conditions is that Pt and Pd are very unfavourable for the adsorption and dissociation of molecular water. Furthermore, we can see that the entropy loss for the dissociative adsorption of molecular CH_4 has driven up the free energy level for this step, suggesting that this step could be rate determining under certain conditions.

We now turn our attention to Fig. 3 which is constructed using data at the same temperature as Fig. 2, but this time with the pressure contributions included, allowing us to get a different perspective. Fig. 3 illustrates the relative $\Delta G^{1,773}$ of each important surface intermediate, where rather than just examining the standard free energies we see the influence of varying the pressure upon the surface stability of each species. The conversion of methane is set at 10% and CO, CO_2, H_2 and H_2O are assumed to be equilibrated in the water gas shift reaction. The partial pressures for these four gasses are used to determine $\Delta G^{1,773}$ for each

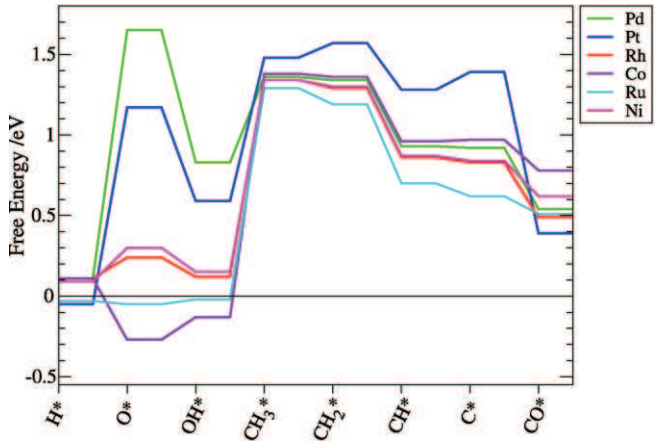

Fig. 3. Free energies of the most important surface species involved in steam reforming, referenced to CO(g), H_2O(g) and H_2(g) for steam reforming at 773 K, 10% conversion at 1 bar total pressure and assuming that the shift reaction is equilibrated. The data are calculated using scaling relationships to determine total energies of hydrogenated species, and DFT of those remaining.

surface species. Details are given in the supplementary material. Through this we can get an understanding of which species are likely to be present on the surface, and if indeed we would expect any poisoning effects. Co adsorbs O and OH more strongly than any of the other metals under consideration and it is therefore highly likely to be O poisoned (Ru is the only other metal, which has O and OH species at a negative free energy). Apart from these species it can be seen that we would expect the surface to be very clean under steam reforming conditions.

4.2. Analysis of reaction barriers

The important metals for steam reforming catalysis have now been identified and the thermochemistry of the reaction intermediates has been established. The next step is to consider the reaction barriers. In order to do this we shall first look at the

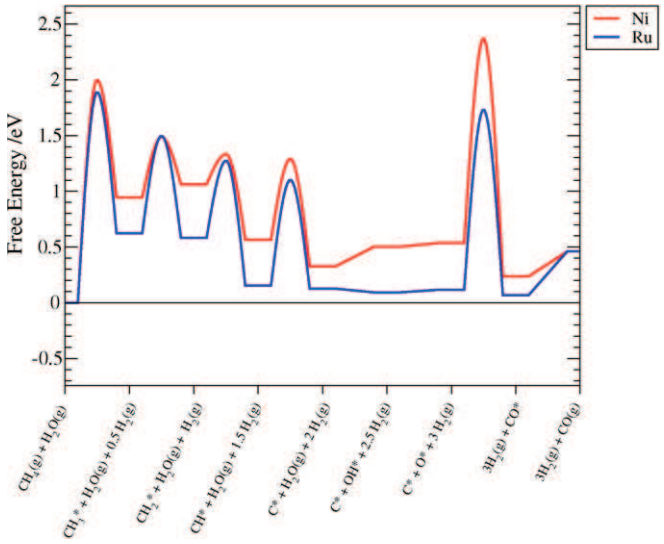

Fig. 4. Reaction free energy scheme including reaction barriers for steam reforming over stepped Ru and Ni. The plot has been constructed using DFT calculations and normal-mode analysis for the total free energies at 773 K.

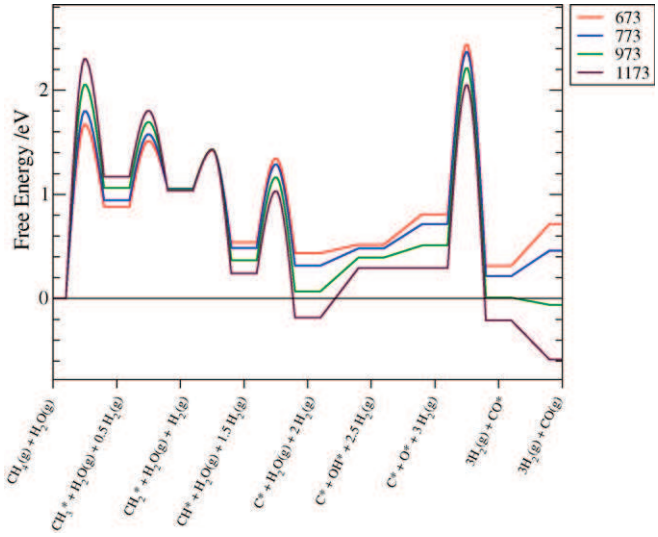

Fig. 5. Reaction scheme illustrating the temperature dependence of the steam reforming reaction over Ni at standard conditions, determined from DFT total energies.

DFT results for Ni and Ru. Ni is the metal of choice for the industrial process at present, primarily because of its abundance and therefore relatively low cost. Ru, as we have illustrated from the thermodynamic considerations, is likely to be a good candidate for the process as well, though significantly more expensive. Fig. 4 depicts the free energy diagram for Ni and Ru, along with the barriers for each hydrogenation step and the CO formation. A quick glance suggests that having a single rate determining step may be an over-simplification. In fact what what is seen is that for Ni the CO formation step looks difficult, however, on Ru there is very little to separate the CH_4 adsorption and the CO formation step.[3]

In order to answer the question of which step is the kinetically most important, we first consider the mechanism by which CO recombines. It was recently shown for methanation over Ni that at high coverages of CO (close to saturation of the preferred step site) that a dissociation mechanism involving a hydrogen atom was favoured [57]. This mechanism required the formation of a COH intermediate that then dissociated into C and OH. We might expect by time reversal that the reverse of this mechanism would hold for steam reforming. However, under steam reforming conditions we have a low CO coverage (Fig. 3). At these coverages the direct dissociation/association transition state is found to be the more stable pathway. For the CH_4 dissociation we have used a direct dissociation from the gas phase molecule, since this again is favoured at low coverages due to the need of an empty site in which to dissociate.

It has been shown recently by Inderwildi et al. [58,59] that on close packed surfaces a formyl pathway is favourable. In fact we find this pathway to be competitive for stepped Ru. However, in treating the general mechanistic overview for a series of metals the CO step is thought to be sufficient. Particularly in light of the fact that in the temperature ranges considered CH_4 activation dominates the Ru rate, and it is the less reactive metals (e.g., Ni) where the CO step competes. However, if one was to go to significantly lower temperatures where CH_4 did not dominate the reaction on Ru then an alternative mechanism would need to be included.

Using the thermodynamic analysis the discussion can be taken a step further and used to examine the reaction profile at different temperatures (see Fig. 5 for the plot corresponding to Ni). As the temperature increases the entropic contribution is such that it makes the barrier for CH_4 dissociation increase relative to the reactants free energy, whereas the free energy barrier for the CO formation step in fact decreases. This demonstrates clearly the importance of the reaction conditions on the rate of steam reforming, i.e. as T is increased the most important barrier switches from being CO formation to CH_4 dissociation. This can also be observed in the kinetic modelling to be discussed below.

The thermodynamics shows that under the experimental reaction conditions employed here, i.e. relative low temperatures, we might expect the CO formation step to be rate determining for most metals, but as the temperature is increased towards 1000 K one enters the regime where CH_4 dissociation is rate determining (passing through an intermediate regime where there is no single rate determining step). The conclusion that the CH_4 dissociation rate is rate-determining at higher temperatures, is in excellent agreement with the findings in the work of Wei and Iglesia, where relatively high temperatures (823–1023 K) were used.

A detailed picture of steam reforming has now been established, primarily based upon thermodynamic considerations of the stable species and the reaction barriers. The most promising metals have been found and subsequently the number of "good" metals has been narrowed down. The most stable species on the surface and the largest reaction barriers have been identified and the entropy dependence of the most important reaction steps has been established. This analysis will now be further developed and used to parameterise a microkinetic model.

4.3. Kinetic model

From the thermodynamic analysis it was seen that for the majority of metals under consideration the surface will be relatively clean. This implies that to a first approximation it is not necessary

[3] Here we should just point out that we are considering the rate determining step to be that which has the largest free energy barrier. This may be a reasonable assumption if one considers the expression for the rate constant and the fact that it depends exponentially on the size of the barrier. However, it is also important to consider coverage effects and this will be addressed in the modelling of the microkinetics.

explicitly to include lateral interactions.[4] We can write out our elementary steps for the steam-reforming process as follows:

$$CH_4(g) + 2^* \rightleftharpoons CH_3^* + H^*, \quad (ES1)^*$$

$$H_2O(g) + 2^* \rightleftharpoons OH^* + H^*, \quad (ES2)$$

$$OH^* + {}^* \rightleftharpoons O^* + H^*, \quad (ES3)$$

$$CH_3^* + {}^* \rightleftharpoons CH_2^* + H^*, \quad (ES4)$$

$$CH_2^* + {}^* \rightleftharpoons CH^* + H^*, \quad (ES5)$$

$$CH^* + {}^* \rightleftharpoons C^* + H^*, \quad (ES6)$$

$$C^* + O^* \rightleftharpoons CO^* + {}^*, \quad (ES7)^*$$

$$H^* \rightleftharpoons \frac{1}{2}H_2(g) + {}^*, \quad (ES8)$$

$$CO^* \rightleftharpoons CO(g) + {}^*. \quad (ES9)$$

If we treat all but steps (ES1)* and (ES7)* as quasi-equilibrated then the overall rate for this process (assuming steady state) can be written out as follows:

$$r_{\text{overall}} = r_1 = r_7 = k_1^+ P_{CH_4}\theta_*^2 - k_1^-\theta_{CH_3}\theta_H = k_7^+\theta_C\theta_O - k_7^-\theta_{CO}\theta_*. \quad (14)$$

From the expressions for the equilibrium constants it is possible to replace θ_{CO}, θ_O, and θ_C at the right side of the equation above:

$$\theta_{CO} = P_{CO}\theta_*/K_9, \quad (15)$$

$$\theta_O = K_2K_3K_8^2P_{H_2O}\theta_*/P_{H_2}, \quad (16)$$

$$\theta_C = K_4K_5K_6K_8^3\theta_{CH_3}/P_{H_2}^{3/2}. \quad (17)$$

At the left side of the expression for the overall reaction rate, θ_H equals:

$$\theta_H = P_{H_2}^{1/2}\theta_*/K_8. \quad (18)$$

θ_{CH_3} can be expressed as a function of θ_*, with all other unknowns (i.e. rate constants and equilibrium constants) being determined from DFT calculations or scaling relationships, as outlined in the methodology section:

$$\theta_{CH_3} = \frac{(A+B)}{(C+D)}\theta_*, \quad (19)$$

where:

$$A = k_1^+P_{CH_4}, \quad (20)$$

$$B = k_7^-\frac{P_{CO}}{K_9}, \quad (21)$$

$$C = k_1^-\frac{P_{H_2}^{1/2}}{K_8}, \quad (22)$$

$$D = K_2K_3K_4K_5K_6^5k_7^+\frac{P_{H_2O}}{P_{H_2}^{5/2}}. \quad (23)$$

By defining the coverage of species i as the product of a ratio (λ_i) and the coverage of empty sites (θ_*) we can now determine θ_*,

$$\theta_* = \frac{1}{1+\sum_i\lambda_i} \quad (24)$$

and consequently the overall rate expression given above. For the discussion we shall use the scaling relationships to determine the total energies and subsequently the rates. The scaling relations

[4] The coverage due to the calculation set up is effectively 0.5 monolayer with respect to the step sites. This corresponds to essentially non-interacting adsorbates, for example lowering the coverage along the step on Ni{211} to 0.25 monolayer has a negligible influence on the adsorption energy.

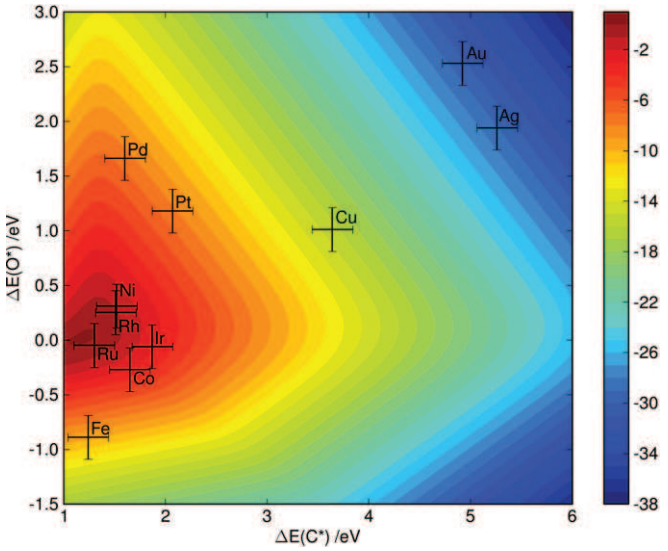

Fig. 6. Two-dimensional volcano-curve of the turn over frequency ($\log_{10}$) as a function of O and C adsorption energy. $T = 773$ K, $P = 1$ bar; 10% conversion. The error bars include an estimated 0.2 eV uncertainties in the adsorption energies.

possess particularly important properties. First of all, they show that to a first approximation only two independent variables, ΔE_C and ΔE_O, characterise the metals. All other adsorption energies and reaction barriers depend linearly upon these underlying variables. Secondly, rather than just calculating rates for discrete points given by the specific elements of the Periodic Table, it is possible to obtain the rate as a function of these two independent variables ($\Delta E_C, \Delta E_O$). This allows us to probe the rate of steam reforming in all of the T, P and adsorption energy phase space. It should be noted that this approach is generally applicable to many processes, where the elementary steps can be described by a scaling relationship. This greatly simplifies the understanding and reveals the trends in reactivity. One particular advantage of the scaling method is that it allows us to probe not only the influence of temperature and pressure on the reaction for each metal, but also permits variation of the adsorption energy of oxygen and carbon and hence rationalise their effect. Fig. 6 depicts the 2D plot comparing the influence of the C and O adsorption energy on the rate at 773 K, 1 bar of pressure having a conversion of 10%. It is seen that the peak of the volcano plot (i.e. where the rate is highest) lies close to the region of the Ni, Rh and Ru adsorption energies, in good agreement with the thermodynamic analysis. The peak lies in the region where the influence of the CO formation and CH_4 adsorption are roughly balanced and that there is competition between these two processes. We do not have a single descriptor as for some reactions, but instead require two descriptors to describe the complete phase space; this was also found to be the case for the water–gas shift reaction [60]. This is as expected from inspection of the BEP relations where the CH_4 dissociation barrier scales with the C adsorption energy, yet both the C and O energy are required to describe the CO formation barrier correctly.

5. Experimental results

The modelling in the previous section gave an estimate of the individual reactivity at a certain set of conditions. In the following experimental results at similar conditions from activity measurements and catalyst characterization are presented. Firstly, the TEM, XRD and sulphur chemisorption results for the average metal particle diameter and metal dispersion are described. Secondly, the structural results are combined with measured activities to deter-

mine the reactivity of methane per surface atom, represented as the turn-over frequency (TOF), for the different metal catalysts.

5.1. TEM measurements

From several TEM images acquired for each sample, the particle size distributions were determined from measurements of more than 400 individual particles. Fig. 7 shows representative *ex situ* TEM images for Rh catalysts in their fresh and aged states. From the particle size distributions, as shown in Fig. 8, the number-averaged particle sizes and dispersions were calculated and are shown in Table 1. A comparison of two individual data sets obtained for a single sample showed a statistical uncertainty (2σ) of 4% in the measurements of the average particle size. The uncertainty due to the microscope magnification calibration was ca. 10%. From these contributions, the absolute uncertainty of the average particle diameter is estimated to be approximately 14%. The TEM images in Fig. 7 and results in Table 1 shows that the fresh samples contained metal particles with an average diameter in the range 1–6 nm and that the particle diameters increased and the dispersion decreased correspondingly with ageing of the different metal catalysts.

It is well-known that Ru is prone to oxidation in the surface [61], and so one may speculate that the passivation procedure affected the Ru particle size so the *ex situ* TEM measurements revealed an incorrect particle size. The fact that the number-averaged particle diameter for the fresh Ru catalyst is about twice as large as for the other metals could reflect such an effect (Table 1). Environmental TEM (ETEM) measurements were therefore conducted to image *in situ* the fresh metal catalysts with 1 wt% metal loading. These catalysts have the smallest particle sizes and so an effect of passivation is expected to be most pronounced for these catalysts. ETEM images of the catalysts are obtained during exposure to 1.2–1.4 mbar of H_2 at 773 K and the analysis for average particle size and dispersion is carried out in the same way as for *ex situ* TEM measurements. Figs. 9a and 9b show representative TEM images of the Ru sample obtained *ex situ* and *in situ* and indicate that a larger fraction of smaller particles were present during in situ observations. The finding is further corroborated by the results presented in Table 1, which reveal that average particle size for the fresh Ru sample (Ru-2) was reduced by a factor of two to 2.1 nm in the ETEM experiment. In comparison, the fresh Rh, Pt, Ni, Pd, and Ir catalysts have also been investigated thoroughly by ETEM. For these catalysts, the results show no difference between the *ex situ* and *in situ* determination of the average particle sizes (Table 1). Since Ru seems to be the only metal affected by passivation, we also investigated the aged Ru catalyst (Ru-2) *in situ* in

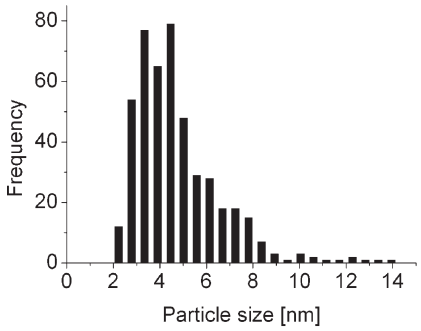

Fig. 8. The particle size distribution of the Rh-3 catalyst with an average particle size of 4.5 nm (i.e. 21% dispersion). A total of 466 particles are included.

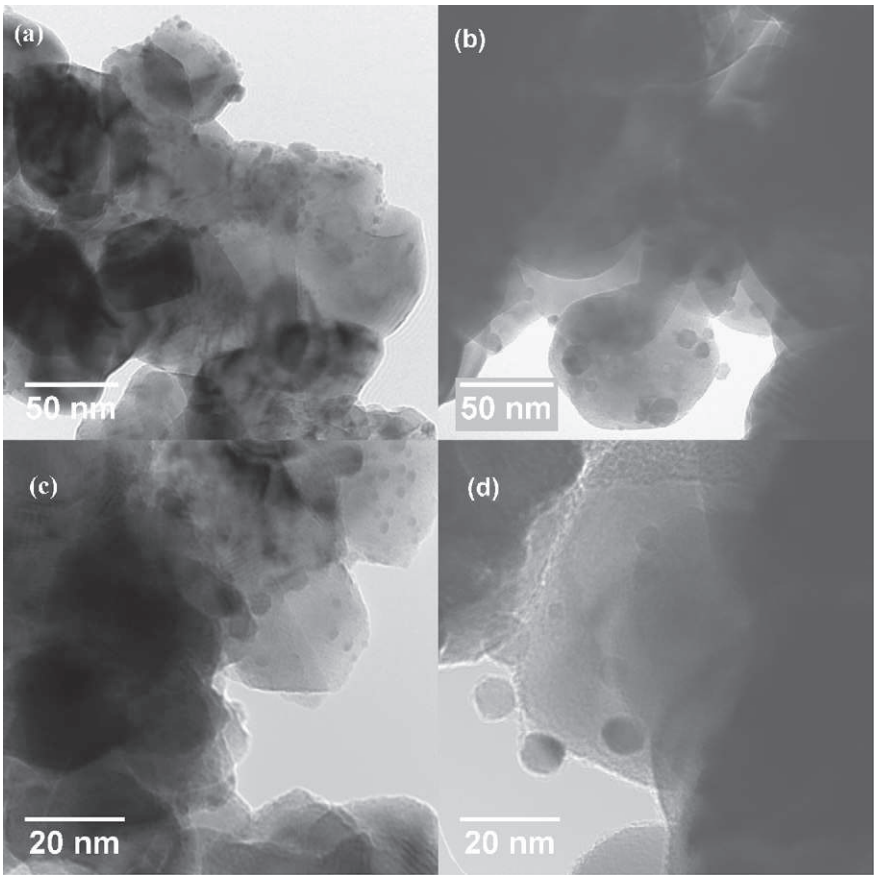

Fig. 7. TEM images of Rh/ZrO_2 catalysts showing the effect of ageing. (a) Fresh 5 wt% Rh-3 and (b) aged 5 wt% Rh-8 (600 h/1096 K) with the average particle diameters of 4.5 and 11.1 nm, respectively. (c) Fresh 1 wt% Rh-1 and (d) aged 1 wt% Rh-2 (228 h/1103 K) with average particle diameters of 2.7 and 8.4 nm, respectively.

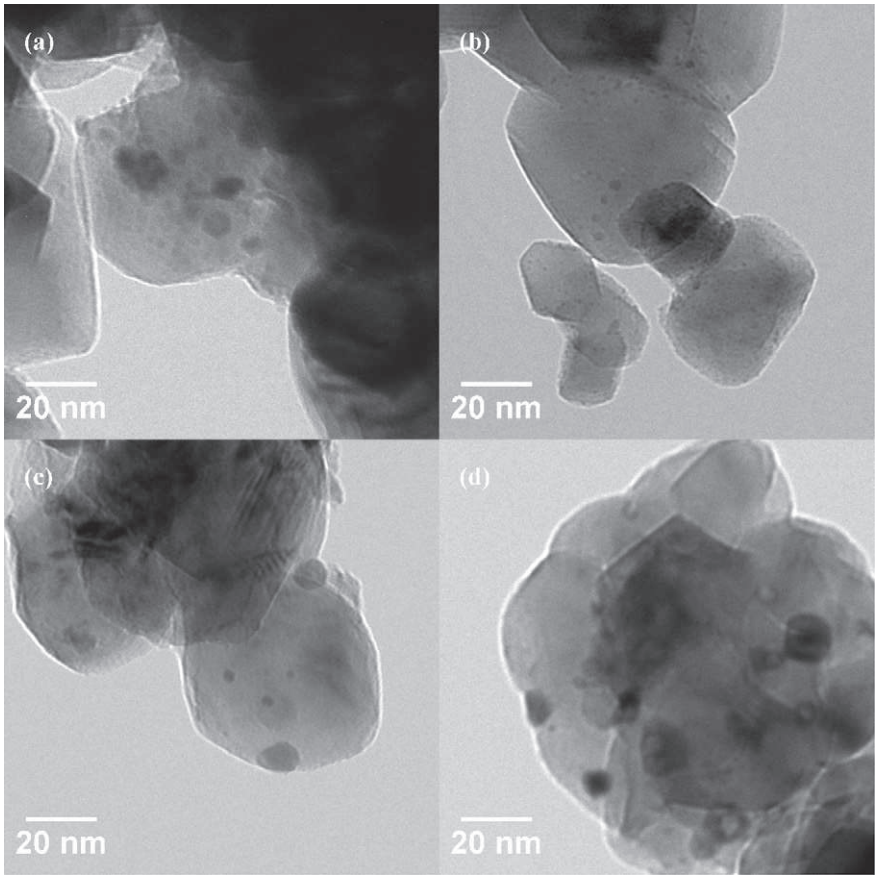

Fig. 9. *Ex situ* and *in situ* microscopy of Ru/ZrO_2. (a) TEM image and (b) ETEM image (1.4 mbar H_2, 773 K) of the fresh Ru catalyst (1 wt% Ru-1). The average particle size was 4.2 nm and 2.1 nm under *ex situ* and *in situ* conditions, respectively. (c) TEM image and (d) ETEM image (1.4 mbar H_2, 773 K) of the aged Ru catalyst (1 wt% Ru-2). The average particle size was 7.2 nm and 7.5 nm under *ex situ* and *in situ* conditions, respectively.

the H_2 environment by ETEM. Figs. 9c and 9d indicate that the Ru particles in the aged catalyst apparently had similar size in the *ex situ* and *in situ* observations and Table 1 further show that the average particle size was large (Ru-2: 7 ± 0.3 nm) and independent of whether the measurements were performed *in situ* or *ex situ*. Hence, the passivation procedure reduced the visibility of 2–4 nm wide Ru particles whereas the effect was less significant for the other metals and larger Ru particles. In order to accurately determine the TOF and dispersion of the fresh ruthenium catalyst, we therefore used the average particle size obtained from *in situ* observations using ETEM. For the other catalysts the particle diameters obtained *ex situ* were used.

5.2. Characterization by sulphur chemisorption and XRD

To confirm the average particle sizes determined by TEM, the 5 wt% Rh catalysts have been characterized by integral methods including sulphur chemisorption and XRD. In Fig. 10 (left) is shown the good correlation between the average diameter obtained by sulphur chemisorption and the surface-averaged diameter obtained by TEM. Fig. 10 (right) shows that the average crystal sizes determined by XRD show the same level as the volume-averaged diameter obtained by TEM. However, the crystallite diameter as obtained by XRD is smaller than actual particle size. The discrepancy could likely be due to twinning of the individual Rh particles (Fig. 11), which causes particles to appear as polycrystals so that the average crystal size becomes smaller than the average particle size. Hence, it is expected that the diameters determined by XRD fall below those obtained by TEM.

5.3. Activity measurements

All catalysts were tested for their activity in steam reforming of methane. The series of Rh catalysts were prepared to obtain a variation in particle sizes so that any structural effect on the activity can be revealed. The remaining Ru, Ir, Pt, Pd and Ni catalysts were tested to allow a ranking of the different metals with respect to their TOF. In the activity measurements, the catalyst amount was adjusted to a conversion of about 10%, and definitely less than 15%. The steam-to-carbon ratio was set to 4. The turnover rates of the catalysts are given in Table 1 and plotted versus dispersion in Fig. 12. For the Rh catalysts, there is a pronounced dependence of the turnover rate on the dispersion; i.e. the turnover number is increasing with higher dispersion and smaller particle sizes. This finding indicates that the activity depends on the detailed surface structure of the nanoparticles and that the low-coordinated surface sites play an important role for the relative activity of the active metals for steam reforming because smaller particles are expected to expose a larger fraction of low-coordinated sites than larger particles [62,63]. It is particularly interesting to note that for Rh, the turnover rate increases nearly linearly with dispersion. Fig. 12 shows that by comparing the different metals at the same dispersion (e.g., 0.4) that the activity is highest for Rh and Ru-based catalysts and is decreasing in the following order: Rh $\sim$ Ru $>$ Ni $\sim$ Ir $\sim$ Pt $\sim$ Pd.

6. General discussion

The 2D volcano plot of the steam reforming rate (Fig. 6) shows the peak activity to be at a slightly lower C adsorption energy than

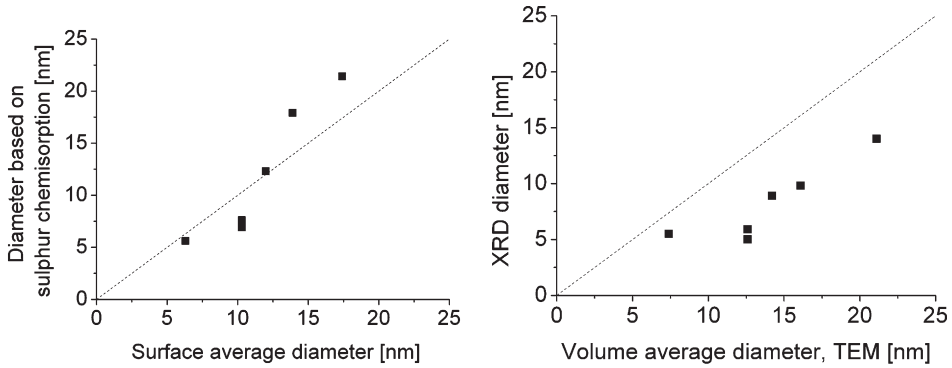

Fig. 10. Diameter by sulphur chemisorption vs. surface average diameter (left). Diameter by XRD vs. volume averaged diameter (right).

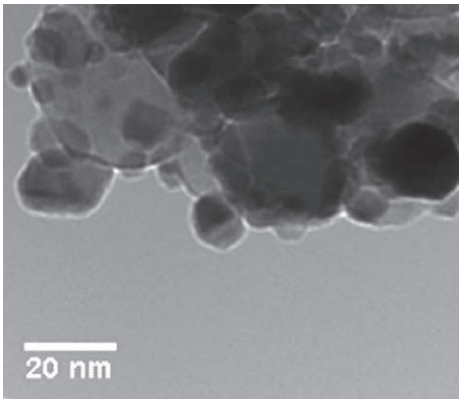

Fig. 11. TEM image of Rh/ZrO_2 (Rh-6) showing twinning plane in a Rh nanoparticle.

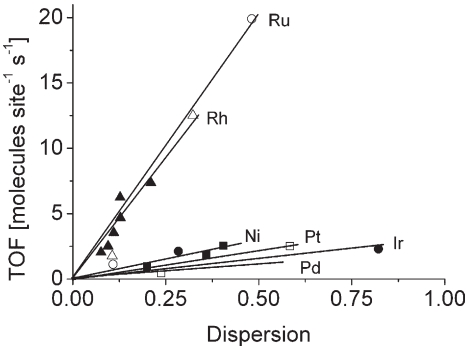

Fig. 12. Reaction rate as a function of dispersion for CH_4–H_2O reforming (773 K, 0.19 bar CH_4, 0.74 bar H_2O, 0.07 bar H_2). Ru (○), 5 wt% Rh (▲), 1 wt% Rh (△), Ni (■), Pt (□), Ir (●) and Pd (◆).

that of the pure metals with the highest activity (Ru, Rh and Ni). If we raise the temperature, the peak of the volcano moves out to even lower C adsorption energies, however, the general reactivity trend is maintained with the activities of Rh, Ni and Ru being almost indistinguishable (see supplementary materials for further information). If we turn our attention to the experimental order of reactivity (Fig. 12) at constant dispersion (e.g., 0.4) we see that Rh and Ru have a comparable and high activity while Ni, Pt, Ir, and Pd have lower and comparable activities at similar dispersions. It should be noted however that the theoretical determined rates drop off considerably faster than those determined experimentally, as one moves towards the more noble metals (see supporting material for more details). This is actually observed for several catalytically interesting systems [64] however up to now the precise reason has remained elusive. An important part of the answer is that the accuracy of calculated rates are considerably smaller away from the maximum where the compensation between different elementary reactions makes the overall rate quite independent of the absolute value of the interaction energies. Away from the maximum the error in an activation energy of the order $2kT$ will show up as an order of magnitude error in the rate. Other possible reasons may well be that the rate becomes so low out in the tail of the volcano that another process is causing the catalytic turnover. This could be a reaction path different from the one prevailing for the most active catalysts or it could be that defects or even impurities start to dominate. In these cases we are no longer measuring the rate due to the metal present. If other processes take over this is a sign that the rates are small anyhow and the calculations still describe the right trends. The important point is that we are able to get reasonable rates close to the maximum (where they are most interesting) and that we can describe the trends as discussed below.

Overall the picture we have is that under the assumption that the support effects are negligible the trend from our experimental work is as follows:

$$\text{Ru} \sim \text{Rh} > \text{Ni} \sim \text{Ir} \sim \text{Pt} \sim \text{Pd}$$

and the following trend from theory:

$$\text{Ru} > \text{Rh} > \text{Ni} > \text{Ir} > \text{Pt} \sim \text{Pd}.$$

Whereas there is not exact agreement the general trends are the same and it must be borne in mind that we have a number of sources of error both in the experiments and in the modelling. For instance, some of the discrepancy in the exact trend might result from the morphology of the nanoparticles under experimental conditions.

From inspection of the slopes in Fig. 12, it can be observed that there is a reasonably linear dependence between the TOF and dispersion. The TOF has been extracted from the experimental data assuming that the process proceeds at all surface sites i.e. $\text{TOF} = r/A$, where r is the rate and A is the surface area. However, this may not be the case since we have seen that the steps and defects are much more reactive due to under-coordination effects. Therefore the rate can be written not as due to atoms sitting at the terraces but due to those sitting at the steps and corners. It would be more correct to write the rate as a sum over these different contributions as follows:

$$r = k_t A_t + k_s A_s + k_c A_c, \tag{25}$$

where the subscript t, s, c referrers to terrace, steps, and corners respectively. This means that the TOF can be written as a sum that scales as:

$$\text{TOF} = r/A \cong k_t + k_s g_s \frac{1}{d} + k_c g_c \frac{1}{d^2} \cong k_t + k_s g_s' D + k_c g_c' D^2, \tag{26}$$

where the geometrical factors (g) are constants since the dispersion, $D = A/V$, where V is the volume, scales as $1/d$ for not too

small particles. The important message here is that if only the terrace atoms are active the TOF would appear constant as a function of dispersion, while if steps are dominant it would increase linearly and if corners are dominant it would increase by the square of the dispersion.

The observed increase in the TOF shown in Fig. 12 clearly indicates that the reactivity is dominated by steps and corners and is in good agreement with theoretical results. A more detailed description like the one found in [57] is not possible at this stage. The morphology may change with chemical gas composition and temperature and thereby also influence the reactivity.

The input energies for the kinetic model are all determined from the same technique (i.e. DFT and scaling relationships), rather than a mixture of experimental techniques and theory, hence we would expect most systematic errors to cancel out. However, there are potential errors we should consider: We expect the DFT adsorption energies to possess errors of approximately 0.2 eV, however, we expect energy differences to be more accurate. The applied scaling relationships show a mean absolute error of 0.14 eV as detailed in reference [49]. These uncertainties must also be considered in the context of the volcano plot, where such errors are not expected to perturb the reactivity trends significantly. Absolute rates may therefore deviate by a few orders of magnitude, but the calculated reactivity trend is not expected to deviate from experiment. This is particularly important when considering the predictive power of the theoretical model.

It is evident that both our theoretical and experimental reactivity trends are in reasonable agreement with Kikuchi et al. [13], Rostrup-Nielsen and Hansen [4,12] and Qin et al. [9]. However, the reactivity trend reported here is significantly different from that obtained by Wei and Iglesia [11], though all metals are within an order of magnitude. The reason for this discrepancy is not known, but we will now proceed to discuss some of the differences between the present experimental work and the work of Wei and Iglesia.

First the experimental conditions will be considered. Wei and Iglesia work at slightly higher temperatures than we do (823–1073 K vs. 773 K). They find the rate-determining step to be methane activation in good agreement with our theoretical work, which shows that the rate-determining step switches from the CO formation step to the methane activation step in this temperature regime in accordance with the previously suggested two-step mechanism. There is general agreement that steam reforming is first order in methane [4], but an overall negative pressure dependency in our previous measurements [4] differs from the results of Wei and Iglesia [11] that showed no impact from other reactants than methane. This may be explained by the different temperatures and pressures involved. Using extrapolation of data for the retarding effect of steam for ethane reforming [19] shows that it becomes negligible above 900 K.

Wei and Iglesia have in some cases used high conversion compared to what was used here, as indicated by their reported approach to equilibrium. We have therefore increased the conversion in our theoretical model to 30% in order to see what influence this may have. This has the effect of moving the peak of the volcano towards the Rh, Ni and Ru points, essentially leaving us with the same trend as we observed at the lower conversion of 10%. This evidence implies that it is not a difference in the conversion that is responsible for the difference in the reactivity trends. Theory also shows that the surface coverages are small at higher temperatures, which also corresponds with the work of Wei and Iglesia who report the same findings experimentally.

Support effects were mentioned in the introduction and it has previously been shown that the support has limited effect on the activity of the individual metals [12,15], provided that the support is alkali-free. Even traces of alkali may have a significant effect on the activity [4,12,19]. The only significant support effect expected here is the variance of metal dispersion on different supports [11]. Since the dispersion was determined here by various methods and very thoroughly by TEM, it is not likely that the reported differences arise from support effects. If neither the temperature, conversion nor the coverage effects account for the difference in the reactivity trends, then we can expand the considerations to the experimental set-up and analysis.

The initial catalyst grain size in this investigation was 300–500 μm. Interestingly, we observed in activity tests with smaller catalyst grains or very fine catalyst powder tabletted with catalytically inert material and crushed again according to the method used by Iglesia and Wei, resulted in a significant loss of activity at 823 K and above. After some time the activity stabilized but at a lower level than the activity obtained for the medium sized particles (300–500 μm). This phenomenon has been tested and observed for reforming catalysts containing Rh, Ru, and Ni. At present it is speculated that support effects are causing this deactivation, possibly a weak metal support interaction as observed for example for Rh on Al_2O_3 [65,66] and ZrO_2 [67]. This phenomenon justified the chosen catalyst particle size in our experiments. The temperature used in this study of 773 K was chosen to get a stable activity and to measure at a temperature where catalyst activity is most important in tubular steam reformers [19]. No quantitative measurements of the decrease in activity have been performed, but qualitatively a difference is observed in the effect on the different metal/support systems. Therefore deactivation of the catalyst to a different extent could change the ranking of the various metals with respect to their reforming activity. We note that if we extrapolate the TOFs measured by Iglesia and Wei to 773 K using their measured activation energy of 91 kJ/mol we estimate a TOF that is approximately 20 times smaller than our corresponding values. In relation to this we will turn to a discussion of measured methane sticking probability.

Iglesia and Wei suggest that there is a large discrepancy between the CH_4 sticking probabilities measured on single crystal Ru(0001) [18] and those extracted from their rate data. From the data of Wei and Iglesia [11] we estimate the CH_4 sticking coefficient as:

$$S(T) = kN_o\sqrt{2\pi m k_B T},$$

where k is the experimental rate constant of the methane dissociation (which under the assumption that the surface is free of adsorbates) is equivalent to the TOF in $s^{-1}\,Pa^{-1}$ and N_o is the area density of the exposed metal atoms on the catalyst at the hcp closed packed surface (e.g., $1.57 \times 10^{19}\,m^{-2}$ for Ru(0001)). This gives a value of 0.13×10^{-6}. The sticking coefficient measurements on single crystals were carried out between 500 K and 700 K [18]. Using the measured activation energy of $E_a = 0.55$ eV for the single crystal experiment, this value has been extrapolated to 873 K to give a sticking coefficient of 19×10^{-6}. As pointed out by Wei and Iglesia this is two orders of magnitude larger than their value. We can use a similar procedure to extract a sticking coefficient from our rate data. In the case of Ru at 873 K we get a value of 3.5×10^{-6}, much closer to the single crystal value. The DFT calculations give a value of 6.3×10^{-6}, but here the very good agreement is fortuitous, given the uncertainty in the calculated activation energy. All the numbers for sticking coefficients and TOF are summarized in Table 2.

We conclude that the CH_4 dissociation rate measured by Wei and Iglesia for methane decomposition over Ru is considerably lower than the one extracted from our catalytic data, which is in reasonable agreement with the single crystal data. Abbott and Harrison [17] suggested that the experimental conditions used during the methane decomposition measurement of the sticking coefficient of CH_4 on ruthenium by Wei and Iglesia [11] will lead to an

Table 2
Sticking coefficients at 873 K and CH_4 turnover rate at 773 K for Ru catalyst

	Sticking coefficient ($\times 10^6$) 873 K	Forward CH_4 turnover rate (s^{-1}) 773 K	Reference
DFT/scaling relations	6.3	0.64	This study
1.0 wt% Ru/ZrO_2	3.51	19.9[a]	This study
3.2 wt% Ru/γ-Al_2O_3	0.13	0.83	[6]
Ru(0001)	19		[18]

[a] 48.1% dispersion, 0.19 bar CH_4, 0.07 bar H_2, 0.74 bar H_2O. Total flow rate 24 Nl/min.

underestimation. At the conditions stated in [11], we calculate an ideal transient to pass through the catalyst bed in about 0.1 sec. The extracted sticking coefficient ($\sim 1.3 \times 10^{-7}$) will then lead to a conversion of methane of 0.33 and a deposition of one third of a monolayer of carbon in 0.1 second neglecting blocking the active sites by carbon. These figures and the challenges in establishing a transient of methane with a raise time of less than 0.1 second illustrate the difficulties in measuring the sticking coefficient of CH_4 at the experiment conditions used by Iglesia and Wei. The data indicate that the sticking coefficients of CH_4 derived by methane decomposition could easily be underestimated and it seems impossible to measure larger sticking coefficients than those reported by Iglesia and Wei. However, we do not think that the problems encountered in the measurements of the sticking of CH_4 by methane decomposition exist in the steam reforming rates measured in [11].

7. Conclusion

Firstly, we have been able to build up a complete picture of the reactivity of pure metal catalysts for steam reforming using recently identified scaling relationships. This has been combined with thermodynamic and kinetic models to get a fundamental insight into the steam reforming process. Experimental work has verified the picture, thereby validating such an approach. The calculations suggest that the rate is a function of two parameters, the O and C adsorption energies, and a volcano is found giving the trends in ranking. The volcano has a broad maximum and most metals considered here and in previous experiments, including Wei and Iglesia's, are found to lie close to the maximum. Considering the relative small difference between different late transition metal, both experiments and theoretical results agree with most of the earlier works that the most active pure metals for the steam reforming reaction are Ru and Rh, while Ni, Ir, Pt, and Pd are a little less active. Neither the detailed ranking nor the absolute activities agree with the recent work of Wei and Iglesia where it was found that Pt is the most active steam reforming metal.

Theoretically we are able to probe a wide range of temperatures and pressures and it is observed that at low temperatures and for the noble metals the CO formation step is kinetically the most important reaction step. However, as the temperature and reactivity of the metal increase i.e. the metal becomes less noble, the most kinetically relevant step switches from being CO formation to dissociative methane adsorption. This offers an explanation for the fact that different studies, carried out under different conditions, find different rate determining steps. For example the work of Wei and Iglesia was carried out between 873 K and 1073 K, which would be the correct conditions to observe methane activation as the rate determining step.

As well as presenting the fundamental picture from the corroboratory views of theory and experiment, we have also seen in this paper how the theoretical scaling relationships can be used. For simple hydrogenated species it has been shown that we can screen through a range of transition metals to determine where the optimal pure metal catalyst lies. Furthermore, by having the adsorption energies of hydrogenated species as a function of only two parameters (our C and O adsorption energies) we can rapidly probe all of the available adsorption energies to see what properties the ideal catalyst should posses. This scheme provides new insight into what direction to move in terms of surface reactivity for designing new and better catalysts.

Acknowledgments

Haldor Topsøe A/S acknowledges the participation of the CTCI Foundation, Taiwan, in establishing the ETEM facility. CINF is funded by the Danish National Research Foundation.

CAMD is funded by the Lundbeck Foundation. This work has been supported by the Danish Research Agency through frame work program #26-04-0047. The Danish Center for Scientific Computing is acknowledged for the provision of high performance computing facilities.

Supporting material

Supplementary material for this article may be found on ScienceDirect, in the online version.

Please visit DOI: 10.1016/j.jcat.2008.08.003.

References

[1] A.J. Ragauskas, C.K. Williams, B.H. Davison, G. Britovsek, J. Cairney, C.A. Eckert, W.J. Frederick Jr., J.P. Hallett, D.J. Leak, C.L. Liotta, J.R. Mielenz, R. Murphy, R. Templer, T. Tschaplinski, Science 311 (2006) 484.
[2] J.R. Rostrup-Nielsen, Science 308 (2005) 1421.
[3] G.W. Huber, J.N. Chheda, C.J. Barrett, J.A. Dumesic, Science 308 (2005) 1446.
[4] J.R. Rostrup-Nielsen, J. Sehested, J.K. Nørskov, Adv. Catal. 47 (2002) 65.
[5] J. Xu, G.F. Froment, AIChE J. 35 (1989) 88.
[6] J.M. Wei, E. Iglesia, J. Phys. Chem. B 108 (2004) 7253.
[7] J.R. Rostrup-Nielsen, J.-H.B. Hansen, J. Catal. 144 (1993) 38.
[8] J.M. Wei, E. Iglesia, J. Catal. 225 (1) (2004) 116.
[9] J.M. Wei, E. Iglesia, Phys. Chem. Chem. Phys. 6 (13) (2004) 3754.
[10] J.M. Wei, E. Iglesia, Angew. Chem. Int. Ed. 43 (2004) 3685.
[11] J.M. Wei, E. Iglesia, J. Phys. Chem. B 108 (13) (2004) 4094.
[12] J.R. Rostrup-Nielsen, J. Catal. 31 (1973) 173.
[13] E. Kikuchi, S. Tanoka, Y. Yamazaki, Y. Morila, Bull. Jpn. Pet. Inst. 16 (2) (1974) 95.
[14] D. Qin, J. Lapszewicz, Catal. Today 21 (1994) 551.
[15] R. Craciun, B. Shereck, R.J. Gorte, Catal. Lett. 51 (3-4) (1998) 149.
[16] J. Wei, E. Iglesia, J. Catal. 224 (2004) 370.
[17] H.L. Abbott, I. Harrison, J. Catal. 254 (2008) 27.
[18] R.C. Egeberg, S. Ullmann, I. Alstrup, C.B. Mullins, I. Chorkendorff, Surface Science 497 (2002) 183.
[19] J.R. Rostrup-Nielsen, in: J.R. Anderson, M. Boudart (Eds.), Catalysis, Science and Technology, vol. 5, Springer-Verlag, Berlin, 1984, chap. 1.
[20] H. Yang, J.L. Whitten, Surf. Sci. 289 (1–2) (1993) 30.
[21] J. Schule, P. Siegbahn, U. Wahlgren, J. Chem. Phys. 89 (1998) 6982.
[22] C.-T. Au, M.-S. Liao, C.-F. Ng, J. Phys. Chem. A 102 (1998) 3959.
[23] C.-T. Au, C.-F. Ng, M.-S. Liao, J. Catal. 185 (1999) 12.
[24] P. Siegbahn, I. Panas, Surf. Sci. 240 (1990) 37.
[25] P. Kratzer, B. Hammer, J.K. Nørskov, Catal. Lett. 40 (3–4) (1996) 131.
[26] H. Burghgraef, A.P.J. Jansen, R.A. van Santen, Surf. Sci. 324 (1995) 345.
[27] R.M. Watwe, H.S. Bengaard, J.R. Rostrup-Nielsen, J.A. Dumesic, J.K. Nørskov, J. Catal. 189 (2000) 16.
[28] I.M. Ciobica, F. Frechard, R.A. van Santen, A.W. Kleyn, J. Hafner, J. Chem. Phys. Lett. 311 (1999) 185.
[29] I.M. Ciobica, F. Frechard, R.A. van Santen, A.W. Kleyn, J. Hafner, J. Phys. Chem. B 104 (2000) 3364.
[30] A. Michaelides, P. Hu, in: M.A.C. Nascimento (Ed.), Theoretical Aspects of Heterogeneous Catalysis, Kluwer, Dordrecht, 2001.
[31] I.M. Ciobica, R.A. van Santen, J. Phys. Chem. B 106 (2002) 6200.
[32] G. Henkelman, H. Jonsson, Phys. Rev. Lett. 86 (4) (2001) 664.
[33] H.S. Bengaard, J.K. Nørskov, J. Sehested, B.S. Clausen, L.P. Nielsen, A.M. Molenbroek, J. Rostrup-Neilsen, J. Catal. 209 (2) (2002) 365.
[34] C.J. Zhang, P. Hu, J. Chem. Phys. 116 (2002) 322.
[35] A.T. Anghel, D.J. Wales, S.J. Jenkins, D.A. King, Phys. Rev. B 71 (11) (2005) 113410.
[36] M.A. Petersen, S.J. Jenkins, D.A. King, J. Phys. Chem. B 108 (2004) 5909.
[37] M.A. Petersen, S.J. Jenkins, D.A. King, J. Phys. Chem. B 108 (2004) 5920.

[38] A. Kokalj, N. Bonini, S. de Gironcoli, C. Sbraccia, G. Fratesi, S. Baroni, J. Am. Chem. Soc. 128 (38) (2006) 12448.
[39] A. Kokalj, N. Bonini, C. Sbraccia, S. de Gironcoli, S. Baroni, J. Am. Chem. Soc. 126 (51) (2004) 16732.
[40] B. Hammer, L.B. Hansen, J.K. Nørskov, Phys. Rev. B 59 (1999) 7413.
[41] H.S. Taylor, Proc. R. Soc. London Ser. A 108 (1925) 105.
[42] T. Zambelli, J. Wintterlin, J. Trost, G. Ertl, Science 273 (1996) 1688.
[43] P. Kratzer, E. Pehlke, M. Scheffler, M.B. Raschke, U. Höfer, Phys. Rev. Lett. 81 (1998) 5596.
[44] S. Dahl, A. Logadottir, R. Egebjerg, J. Larsen, I. Chorkendorff, E. Tørnqvist, J.K. Nørskov, Phys. Rev. Lett. 83 (1999) 1814.
[45] F. Abild-Pedersen, O. Lytken, J. Engbæk, G. Nielsen, I. Chorkendorff, J. Nørskov, Surf. Sci. 590 (2005) 127.
[46] T. Bligaard, J.K. Nørskov, S. Dahl, J. Matthiesen, C.H. Christensen, J. Sehested, J. Catal. 224 (2004) 206.
[47] H.J. Monkhorst, J.D. Pack, Phys. Rev. B 13 (1976) 5188.
[48] D. Vanderbilt, Phys. Rev. B 41 (1990) 7892.
[49] F. Abild-Pedersen, J. Greeley, F. Studt, J. Rossmeisl, T.R. Munter, P.G. Moses, E. Skúlason, T. Bligaard, J.K. Nørskov, Phys. Rev. Lett. 99 (2007) 016105.
[50] G. Jones, T. Bligaard, F. Abild-Pedersen, J.K. Nørskov, J. Phys. Condens. Mater. 20 (2008) 064239.
[51] V. Pallasana, M. Neurock, J. Catal. 191 (2000) 301.
[52] J.K. Nørskov, T. Bligaard, A. Logadottir, S. Bahn, L.B. Hansen, M. Bollinger, H. Bengaard, B. Hammer, Z. Sljivancanin, M. Mavrikakis, Y. Xu, S. Dahl, C.J.H. Jacobsen, J. Catal. 209 (2002) 275.
[53] J.H. Noogle, Physical Chemistry, Little Brown and Co, Boston, 1985.
[54] T. Bligaard, K. Honkala, A. Logadottir, J.K. Nørskov, S. Dahl, C.J.H. Jacobsen, J. Phys. Chem. B 107 (2003) 9325.
[55] J. Sehested, J.A.P. Gelten, S. Helveg, Appl. Catal. 309 (2006) 237.
[56] P.L. Hansen, S. Helveg, A.K. Datye, Adv. Catal. 50 (2006) 77.
[57] M.P. Andersson, F. Abild-Pedersen, I. Remediakis, T. Bligaard, G. Jones, J. Engbaek, O. Lytken, S. Horch, J.H. Nielsen, J. Sehested, J.R. Rostrup-Nielsen, J.K. Nørskov, I. Chorkendorff, J. Catal. 255 (2008) 6.
[58] O.R. Inderwildi, S.J. Jenkins, D.A. King, J. Phys. Chem. C 112 (2008) 1305.
[59] O.R. Inderwildi, S.J. Jenkins, D.A. King, J. Am. Chem. Soc. 129 (2007) 1751.
[60] N. Schumacher, A. Boisen, S. Dahl, A.A. Gokhale, S. Kandoi, L.C. Grabow, J.A. Dumesic, M. Mavrikakis, I. Chorkendorff, J. Catal. 229 (2005) 265.
[61] P.G.J. Koopman, A.P.G. Kieboom, H. van Bekkum, J. Catal. 69 (1981) 172.
[62] C.H. Jacobsen, S. Dahl, P.L. Hansen, E. Toernqvist, H. Topsøe, D.V. Prip, P.B. Møenshaug, I. Chorkendorff, J. Mol. Catal. A Chem. 163 (2000) 19.
[63] K. Honkala, A. Hellman, I.N. Remediakis, A. Logadottir, A. Carlsson, S. Dahl, C.H. Christensen, J.K. Nørskov, Science 307 (2005) 555.
[64] H. Falsig, T. Bligaard, J. Rass-Hansen, A.L. Kustov, C.H. Christense, J.K. Nørskov, Top. Catal. 45 (2007) 117.
[65] J.G. Chen, M.L. Colaianni, P.J. Chen, J.T. Yates Jr., J. Phys. Chem. 94 (1990) 5059.
[66] C. Wong, R.W. McCabe, J. Catal. 119 (1989) 47.
[67] A. Gervasini, F. Morazzoni, D. Strumolo, F. Pinna, G. Strukul, L. Zanderighi, J. Chem. Soc. Faradray Trans. I 82 (1986) 1795.

Applied Catalysis A: General 377 (2010) 158–166

Contents lists available at ScienceDirect

Applied Catalysis A: General

journal homepage: www.elsevier.com/locate/apcata

Steam and CO_2 reforming of methane over a Ru/ZrO_2 catalyst

Jon Geest Jakobsen [a,b,*], Tommy L. Jørgensen [a], Ib Chorkendorff [b], Jens Sehested [a]

[a] Haldor Topsøe A/S, Nymøllevej 55, DK-2800 Kgs. Lyngby, Denmark
[b] Center for Individual Nanoparticle Functionality (CINF), Department of Physics, Building 312, Technical University of Denmark, DK-2800 Kgs. Lyngby, Denmark

ARTICLE INFO

Article history:
Received 15 December 2009
Received in revised form 21 January 2010
Accepted 22 January 2010
Available online 1 February 2010

Keywords:
Methane steam reforming
TEM
Kinetics
Ruthenium

ABSTRACT

The kinetics of methane steam reforming over a Ru/ZrO_2 catalyst was studied at 1.3 bar total pressure and in the temperature range 425–575 °C. These data were fitted by combining a reactor model with a series of kinetic models. The best fit was obtained by a model with methane dissociative adsorption as the rate limiting step and with CO and H adspecies partly blocking the active sites. The Ru/ZrO_2 catalyst was characterized by TEM and H_2 chemisorption. By comparison of *ex situ* and *in situ* TEM, it is evident that Ru particles with diameters of <2 nm are difficult to observe with *ex situ* TEM due to oxidation when exposed to air.

1. Introduction

The conversion of hydrocarbons with steam is the preferred way of producing synthesis gas. Synthesis gas is a mixture of H_2, CO and CO_2, which can be used for both chemical, fuel and power production. CO_2 may be used as a reactant to adjust the composition of the synthesis gas. It is usually an advantage to pre-reform the hydrocarbon feed into a mixture of primarily methane, H_2, CO_2 and water in an adiabatic reactor. Traditionally, nickel-based catalysts are used for methane steam reforming and are used in the vast majority of industrial applications. Recently natural gas in remote areas – also called stranded gas – is converted to valuable liquid products like diesel and methanol in very large Gas-to-Liquid (GTL) plants using autothermal reforming [1]. For GTL applications it is interesting to develop other steam reforming catalysts that are able to operate at low steam/carbon ratios, where nickel catalysts form carbon whiskers. These carbon whiskers will eventually destroy the catalysts [2]. One solution to this problem is to use noble metals. Noble metal catalysts such as Ru, Rh, Ir, Pt, and Pd are more resistant to the formation of carbon whiskers [3], and these catalysts may be used for production of synthesis gas at very low steam/carbon ratios. Previous studies showed that Ru is among the most active metals for catalyzing the methane steam reforming reaction [3,4]. Other noble metals such as Rh, Pt, Pd, and Ir also show good methane steam reforming activity although different relative reactivities were observed [4,5]. The kinetics of the steam and CO_2 reforming reactions over a Ru/ZrO_2 catalyst are the main topics of this article.

The kinetics of methane steam reforming was studied intensively over a long period and most studies were conducted for nickel-based catalysts. A range of kinetic expressions for methane steam reforming over nickel were proposed including Langmuir–Hinshelwood, power laws, and expressions based on micro kinetic analysis [1,4]. Generally, the dissociative methane adsorption reaction is thought to be the rate determining step for nickel-based catalysts at most conditions [1,6].

For supported ruthenium catalysts, specific studies of the kinetics for methane steam reforming are more limited [3,7–11]. In a thorough study by Wei and Iglesia [7], they found the following rate expression for methane conversion over ruthenium:

$$R = k(T)P_{CH_4} \quad (1)$$

In this expression the rate of methane conversion is proportional to the methane partial pressure. This methane dependency is explained by dissociative adsorption of methane as the rate limiting step, and kinetic isotope experiments were used to support this conclusion. The rate expression (Eq. (1)) was derived from experiments in the temperature range, 550–700 °C, using total pressures of 1–5 bar. No dependency of steam or CO_2 was observed, hence the rates of steam and CO_2 reforming were equal. In contrast to that study, observations by Rostrup-Nielsen and Hansen [3] show that there is a significant difference between steam and CO_2 reforming at 550 °C, where the lower activity for CO_2 reforming is speculated to be caused by CO adsorption on the

* Corresponding author at: Haldor Topsøe A/S, Nymøllevej 55, 2800 Lyngby, Denmark. Tel.: +45 45272497; fax: +45 45272999.
E-mail addresses: jgja@topsoe.dk, geest@fysik.dtu.dk (J.G. Jakobsen).

0926-860X/$ – see front matter © 2010 Elsevier B.V. All rights reserved.
doi:10.1016/j.apcata.2010.01.035

surface. The partial pressure of CO is significantly higher during CO_2 reforming reaction conditions than during steam reforming.

Studies by Berman et al. of methane steam reforming over ruthenium at different temperatures (450, 500 and 700 °C) show a significant variation of the reaction order of methane [9]. At low temperatures (450/500 °C), the reaction order of methane was found to be significantly below 1, while at higher temperatures (700 °C) the reaction rate was proportional to the methane partial pressure. The high temperature observations are in line with the observations by Wei and Iglesia.

DFT calculations of steam reforming over transition metals show that the rates of dissociative methane adsorption and the direct CO formation reaction are of the same order of magnitude at low temperatures [4]. The rate of methane dissociation was found to be rate limiting at high temperature for the most active metals. The model proceeds via methane decomposition to carbon atoms at the active surface. We assumed that CO are formed from C and O atoms even though reaction pathways such as CO formation via CHO and CHOH intermediates [12–14] could have significantly lower barriers for CO formation at some conditions. Especially for higher coverages of adsorbed species, CO formation could proceed via CH_xO species [12].

Various forms of support effects were also observed. The Berman et al. study found a negative reaction order in water at high temperatures, and the authors speculated that adsorption of water takes place on an Al_2O_3/MnO_x support [9]. Based on studies of CO_2 reforming over a Ru/La_2O_3 catalyst, Carrara et al. [10] proposed a kinetic model where CO_2 interacts with the La support. A temperature decrease from 590 to 510 °C induced a lower dependency of the partial pressure of methane and higher dependency of the CO_2 partial pressure. This is explained by the slow reaction of CO_2 bound to the La support and carbon from the methane dissociation at the Ru surface. Other studies [4,7] have shown no influence of support on the reactivity, although these studies do not include La oxide.

Studies of CO_2 reforming by Ferreira-Aparicio et al. [11] also indicate that Al_2O_3 support significantly influences the coverages of surface species. According to these authors OH radicals are formed on the support by reduction of CO_2. These OH radicals are proposed to diffuse back to the ruthenium surface enhancing the oxidation of carbonaceous species.

This short overview of the limited studies of methane steam reforming over Ru-based catalysts shows that the kinetics might not be as simple as indicated by Eq. (1). This simple dependency of methane may account for the kinetics at higher temperatures, i.e. above 600–700 °C depending on gas pressures. The study reported here is focused on experiments in the temperature range 425–575 °C and 1.3 bar absolute pressure. Methane dissociative adsorption is an important kinetic step in the reaction. DFT calculations indicate that the direct CO formation step might be rate limiting at low temperature [4]. However, kinetically it can be shown that if the direct CO formation step is significant, there will be a large negative effect of increasing the H_2 partial pressures on the overall reactivity, which is not found in our kinetic measurements. In the following, kinetic expressions with methane dissociation as the rate determining step and either one or two adsorbates are used to model the experimental data.

2. Experimental

A 1 wt% Ru catalyst was prepared for use in the kinetic measurements with incipient wetness impregnation of a ZrO_2 (15 m^2/g, 95% tetragonal/5% monocline) support with an aqueous solution of $Ru(NO)(NO_3)$. The sample was dried at 80 °C in ambient air and subsequently reduced at 600 °C in H_2 for 4 h. To achieve a stable catalyst, the samples were aged at 750 °C for 336 h in a H_2O/H_2 (ratio ~1) gas mixture at 31 bar total pressure. The activity measurements were performed in a 8.5 mm inner diameter plug flow reactor tube, with catalysts in a size fraction of 125–300 μm. In total 1.00 g of catalyst and inert material ($MgAl_2O_4$) were used during the experiments, with the catalyst amount accounting for 25–30 mg. The total bed height was 15 mm. The catalyst amount was chosen to obtain conversions of <15% apart from the highest temperatures (≥550 °C). In fact all the experiments were carried out far from equilibrium as the approach to equilibrium for steam and CO_2 reforming was $\beta_{SR} < 9.6 \times 10^{-3}$ and $\beta_{CO_2\ reforming} < 1.4 \times 10^{-3}$ under all conditions. β is the approach to equilibrium, and β_{SR} and $\beta_{CO_2\ reforming}$ are given by Eqs. (2) and (3):

$$\beta_{SR} = \frac{P_{CO}P_{H_2}^3}{P_{CH_4}P_{H_2O}} \cdot \frac{1}{K_{p,SR}} \quad (2)$$

$$\beta_{CO_2\ reforming} = \frac{P_{CO}^2P_{H_2}^2}{P_{CH_4}P_{CO_2}} \cdot \frac{1}{K_{p,CO_2\ reforming}} \quad (3)$$

Here P_j is the partial pressures of species j while $K_{p,SR}$ and $K_{p,CO_2\ reforming}$ are equilibrium constants based on partial pressures. Inlet gases of CH_4, CO_2, N_2 and H_2 were premixed with steam before entering the catalyst bed. The total inlet gas flow was 12.1 Nl/h, and the reactor was operating at 425–575 °C. The dried outlet gas was analyzed by gas chromatography (GC) with three measurements at each set of conditions. A thermocouple was placed in the center of the bed, measuring the catalyst temperature. To control the reactor temperature a thermometer was placed on the outer wall, giving a reference temperature for the heat balance calculations.

The experimental procedure commenced with re-reduction of the sample at 350 °C in H_2 at 1 bar for 1 h. Then the catalyst temperature was increased to 825 °C to ensure that the catalyst was stable during the kinetic measurements. The individual gas flows were altered while keeping a constant inlet flow (12.1 Nl/h), and the effects of changing the flows of the CH_4, H_2O and H_2 gases were investigated at 500 °C. Furthermore, the rates of steam and CO_2 reforming were measured in the temperature range 425–575 °C with constant gas flows. As a check of the stability of the catalyst, standard activity measurements were made between each series of variations of inlet flows and/or temperatures. A standard activity measurement corresponds to the following conditions at the entrance of the catalyst bed: 16.7% CH_4, 16.7% N_2, and 66.6% H_2O at 500 °C and 1.3 bar. The standard activity measurements showed that the catalyst deactivation was small during the experiments. During a measurement period of 14 days, the total deactivation of the catalyst as calculated by Eq. (1) amounted to 16%, which was compensated for by a linear correction of the rates followed by calculations of the conversions using Eq. (1).

Transmission electron microscopy (TEM) was used to determine the particle size distribution for the Ru/ZrO_2 catalyst. According to previous reports it is necessary to study the catalyst *in situ* to image small Ru particles [4]. Measurements were performed at 60,000× and 200,000× magnification using a Philips CM300 FEG electron microscope equipped with an environmental cell. The sample was crushed and dispersed on a Mo TEM grid and measured *ex situ* at vacuum conditions and subsequently exposed to 1.5 mbar H_2 at 500 °C for about 1 h to re-reduce the catalyst before the *in situ* measurements was initiated. The diameters of the Ru particles were obtained from the TEM and ETEM images by measuring the projected particle area of the 2D images and calculating the diameter assuming spherical particles. From this particle size distribution, the number average particle size and the surface average particle size were determined [1].

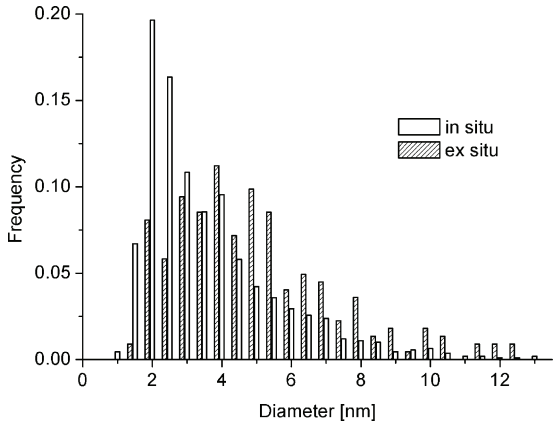

Fig. 1. Particle size distributions (PSD) for the Ru/ZrO_2 catalyst obtained from *ex situ* measurements (*white*) and from *in situ* measurements at reducing conditions, i.e. 500 °C and 1.5 mbar H_2 (*black*). Average particle sizes are 4.9 and 3.5 nm, respectively. The PSDs were based on 223 (*ex situ*/*white*) and 1042 (*in situ*/*black*) measured particles, respectively.

The resulting surface average particle size was compared to the results from H_2 and sulfur chemisorption measurements. Volumetric H_2 chemisorption, used to determine the active surface area of the catalyst, was initiated by drying the sample at 120 °C in He and followed by re-reduction at 400 °C in H_2 for 2 h. After cooling to 40 °C, a H_2 chemisorption isotherm was measured between 2.5 and 112 kPa. The isotherm was extrapolated to zero H_2 pressure to calculate the uptake of chemisorbed H_2. Generally, it is assumed that one H atom chemisorbs on each ruthenium surface atom. Sulfur chemisorption measurements can also be used to estimate the average particle size. After sulfidation of the sample, the sulfur uptake can be determined by high temperature oxidation and infrared measurements of the released SO_2. It is possible to correlate the amount of adsorbed sulfur to a specific surface area [4].

3. Experimental results

The focus of the experimental work was to obtain good kinetic data for the Ru/ZrO_2 catalyst, which may be used for optimization of a kinetic model. The corresponding experimental results from catalyst characterization and activity measurements are thus presented below.

3.1. Characterization

The Ru/ZrO_2 catalyst was characterized using TEM and reducing ETEM conditions. The particle size distributions (PSD) for the Ru/ZrO_2 catalyst are presented in Fig. 1. The data obtained at *ex situ* conditions show a broad distribution of particle sizes and an average particle diameter of 4.9 nm. The equivalent particle size distribution obtained at reducing conditions is much sharper and has an average particle diameter of 3.5 nm. There is a significant difference between the particle size distributions for the same sample obtained under different conditions.

The reason for this difference in the PSDs is almost certainly due to surface oxidation of ruthenium particles. The ruthenium particle on the ZrO_2 support in Fig. 2 (left) has a 1 nm edge of amorphous material at *ex situ* conditions. The amorphous material is assumed to be ruthenium oxide, and the inner core of the particle is seen to be crystalline. In the *ex situ* measurements the particle size includes the oxide surface, which yields further complications during size estimation. A similar size particle at reducing conditions of 500 °C and 1.5 mbar H_2, Fig. 2 (right) does not have the amorphous layer and the particle appear faceted. The resolution is lower due to the presence of a relative high gas pressure in the *in situ* cell. Based on these images and the PSDs, we suggest that the smallest ruthenium particles will form amorphous ruthenium oxide at ambient conditions, making them difficult to be identified in the TEM images. Hence at *ex situ* conditions nanoparticles smaller than 2–3 nm will not be distinguishable from the support. Therefore the PSD obtained using 60k× ETEM images will be used in the following, and the average diameter and dispersion were determined to be 3.5 nm and 20%, respectively. The Ru/ZrO_2 catalyst was also characterized by H_2 chemisorption and sulfur chemisorption, and the dispersions were determined to be 32% and 23%, respectively.

3.2. Activity measurements

In the following the focus will be a detailed investigation of steam and CO_2 reforming over the Ru/ZrO_2 catalyst. A series of

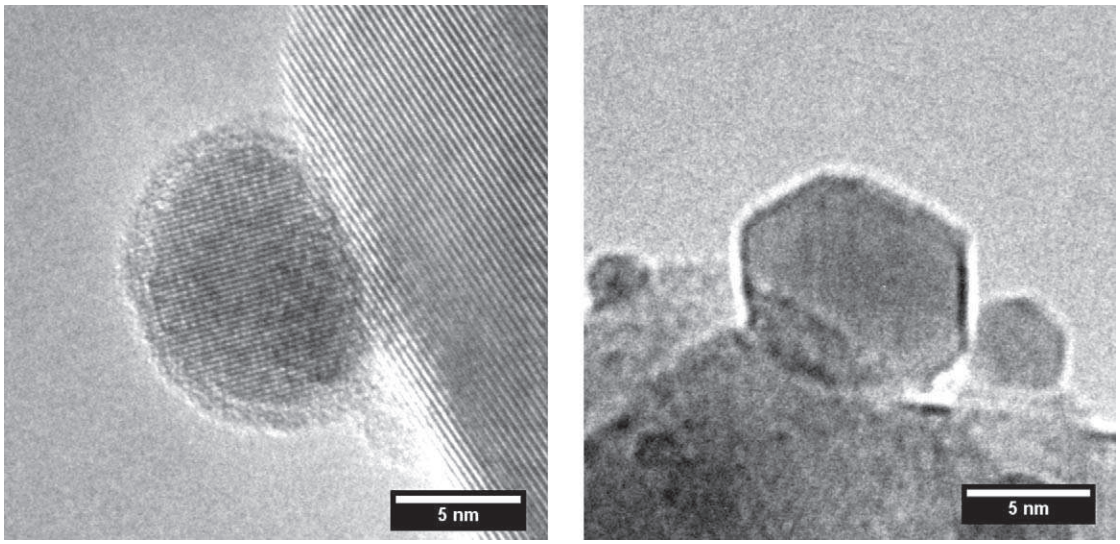

Fig. 2. 22 × 22 nm TEM images obtained with 200k× magnification. At *ex situ* conditions of Ru/ZrO_2 a 1 nm layer of RuO_2 is observed at the edge of the Ru particle (left). At *in situ* ETEM conditions of 1.5 mbar H_2 and 500 °C a faceted Ru particle is observed (right).

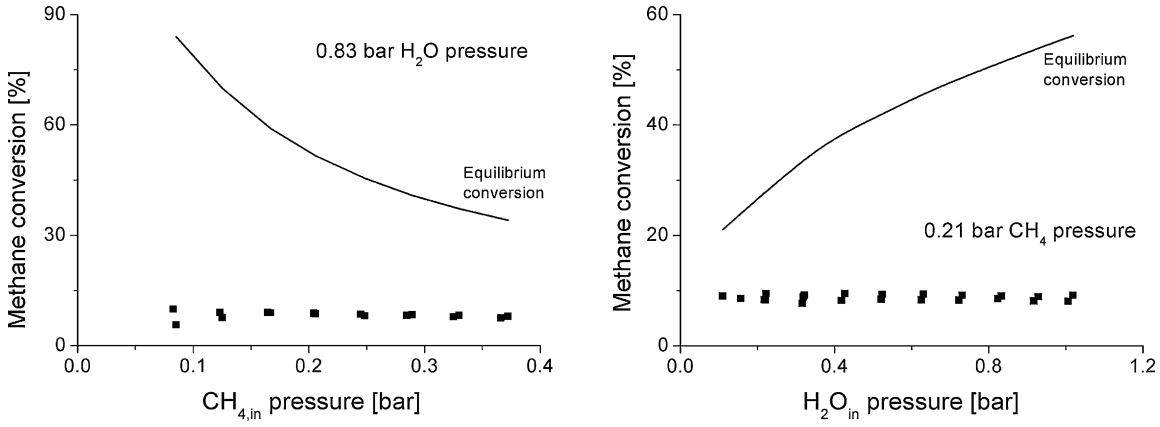

Fig. 3. Methane conversions at 500 °C for the Ru/ZrO_2 catalyst as a function of $P(CH_4)_{in}$ (left), and as a function of $P(H_2O)_{in}$ (right). The total inlet flow rate was $\upsilon_{T,in}$ = 12.1 Nl/h. Total pressure P = 1.3 bar, N_2 balance.

experiments were performed to elucidate the influence of the CH_4, H_2O and H_2 partial pressures, and the temperature on the rate of methane steam reforming and methane CO_2 reforming.

The dependencies of CH_4 and H_2O are given in Fig. 3. First of all the reaction rate appears to be first order in methane as the conversion is almost independent of $P(CH_4)_{in}$. The conversion decreases slightly for increasing inlet partial pressures of methane, but this may be caused by an indirect effect as one or several reaction intermediates or products may cover part of the active surface. In Fig. 3 (right) the reaction rate is seen to be nearly independent of the inlet partial pressure of water. The methane conversion decreases by 28% as the inlet partial pressure of H_2 increases from 0.04 to 0.2 bar as seen in Fig. 4 (left). As also observed in previous studies [3], the methane conversion and hence the reaction rates are significantly higher for steam reforming than for CO_2 reforming at otherwise similar conditions – see Fig. 4 (right). This effect may be caused by reaction intermediates or products covering a relatively larger part of the ruthenium surface during CO_2 reforming than during steam reforming. Before discussing the kinetics of steam and CO_2 reforming further, the water gas shift reaction will be considered. During similar studies of ruthenium catalysts used for steam and CO_2 reforming, it was found that the water gas shift reaction is close to equilibrium [7]. In this context the approach to equilibrium for the water gas shift reaction is defined as follows:

$$\beta_{WGS} = \frac{P_{CO_2} P_{H_2}}{P_{CO} P_{H_2O}} \cdot \frac{1}{K_{p,WGS}} \quad (4)$$

In the present work the approach to equilibrium was evaluated at the outlet of the catalyst bed. The approach to equilibrium for the water gas shift reaction may be calculated from the experimental data. However, β_{WGS} is uncertain primarily due to the low CO content. Nevertheless, we conclude that the vast majority (84%) of the β_{WGS} values were within a range of $\beta_{WGS} \in [0.60; 1.40]$. The results obtained by model fitting will therefore rely on the assumption that the water gas shift reaction is in thermodynamic equilibrium at all conditions in agreement with [7].

4. Modeling

Modeling of the experimental data will be described in the following. To be able to quantify the observed effects measured, it is necessary to model the data. To include possible transport effects, the reactor has been modeled as a one-dimensional, non-isothermal plug flow reactor [15]. Steam reforming kinetics for the Ru/ZrO_2 catalyst was modeled using an Arrhenius type expression, where adsorbate effects have been taken into consideration.

4.1. Reactor modeling

A one-dimensional reactor model was chosen as the radial temperature, and concentration gradients in the reactor were small because low conversions were generally attained, i.e. the conversions were <15% apart from the highest temperatures (≥550 °C). For the few experiments at higher temperatures, conversions of up to 30% were measured. The steam reforming

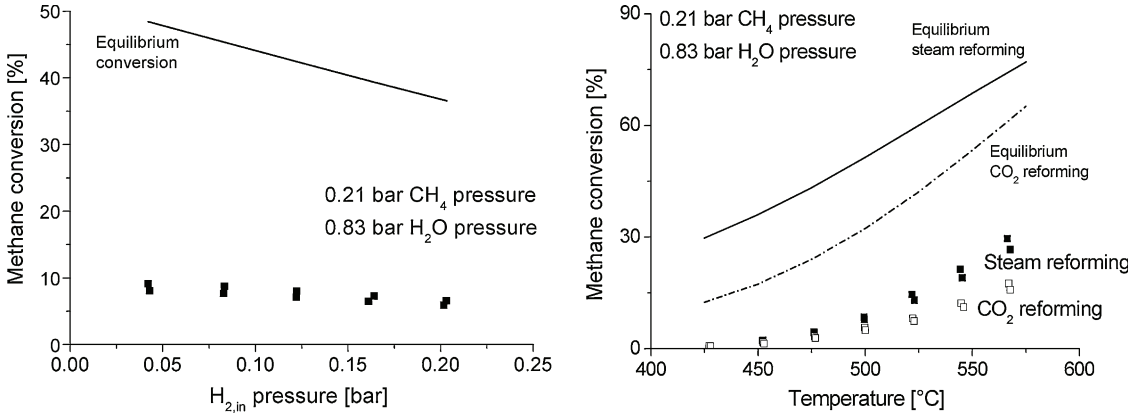

Fig. 4. Methane conversions at 500 °C for the Ru/ZrO_2 catalyst as a function of $P(H_2)_{in}$ (left), temperature variations for steam reforming and CO_2 reforming (right). The total inlet flow rate was $\upsilon_{T,in}$ = 12.1 Nl/h. Total pressure P = 1.3 bar, N_2 balance.

reaction and the water gas shift reaction were considered:

$$CH_4(g) + H_2O(g) \rightleftharpoons CO(g) + 3H_2(g) \quad (5)$$

$$CO(g) + H_2O(g) \rightleftharpoons CO_2(g) + H_2(g) \quad (6)$$

The two degrees of conversion, X_5 and X_6, were defined as:

$$X_5 = \frac{\text{Moles of } CH_4 \text{ converted in reaction(5)}}{\text{Moles of } CH_4 \text{ in the feed stream}} = \frac{F_{CH_4,in} - F_{CH_4}}{F_{CH_4,in}} \quad (7)$$

$$X_6 = \frac{\text{Moles of } CO_2 \text{ generated in reaction(6)}}{\text{Moles of } CH_4 \text{ in the feed stream}} = \frac{F_{CO_2} - F_{CO_2,in}}{F_{CH_4,in}} \quad (8)$$

A mole balance results in the following relation between the reaction rates and the conversion:

$$R_5 = F_{CH_4,in} \cdot \frac{dX_5}{dW'} \quad (9)$$

$$R_6 = F_{CH_4,in} \cdot \frac{dX_6}{dW'} \quad (10)$$

Eqs. (9) and (10) give the overall reaction rates of the steam reforming reaction (i.e. mole CH_4 converted $(g\ cat)^{-1}\ h^{-1}$) and the water gas shift reaction (i.e. mole CO_2 generated $(g\ cat)^{-1}\ h^{-1}$), respectively. Eq. (9) can be rewritten where the reaction rate is given as a function of conversions and temperature:

$$\frac{dX_5}{dW'} = \frac{R_5(X_5, X_6, T)}{F_{CH_4,in}} \quad (11)$$

W' is the mass of catalyst from the inlet to a given position in the reactor and $F_{CH_4,in}$ is the molar flow rate of methane at the inlet to the packed bed. Eq. (11) specifies how the conversion of methane varies through the catalyst bed. As indicated, the overall reaction rate of the steam reforming reaction will depend on X_5, X_6 and the temperature T. Here X_6 will be a function of X_5 due to the assumption that the water gas shift reaction is fast enough to reach equilibrium at all conditions:

$$X_6 = f(X_5) \quad (12)$$

Since the overall reaction is strongly endothermic, there is a significant heat loss during reaction. An energy balance is used to obtain a differential equation that describes the temperature variation through the catalyst bed[1]:

$$\frac{dT}{dW'} = \frac{U \cdot (a/(\rho_{bed,bulk} \cdot \omega_{bed})) \cdot (T_{wall,outer} - T) - R_5 \cdot \Delta_r H_5 - R_6 \cdot \Delta_r H_6}{F_{T,in}(\bar{C}_{p,in} + y_{CH_4,in} X_5 \Delta C_{p,5} + y_{CH_4,in} X_6 \Delta C_{p,6})} \quad (13)$$

During the measurements, heat is transported into the bed through the tube wall, and U is the overall heat transfer coefficient from the outer side of the reactor tube wall to the center of the bed. It consists of three resistances towards heat transfer if the temperature at the outer tube wall is known: one in the reactor tube wall, one at the inner wall of the bed, and finally one in the bed itself. U is found to be in the range 400–800 $kcal/m^2/h/K$. A connection between the reaction rates R_5 and R_6 exists, again due to the assumed equilibrium of the water gas shift reaction. Therefore, R_6 can be evaluated based on X_5, X_6 and T so that the above differential equation for the temperature variation can be used:

$$R_6 = R_5 \cdot \frac{dX_6}{dX_5} = f(X_5, X_6, T) \quad (14)$$

[1] U, overall heat transfer coefficient; a, ratio between wall area and volume of bed; $\rho_{bed,bulk}$, bulk density of bed; ω_{bed}, mass fraction of catalyst in the bed; R_i, reaction rate; ΔH_i, reaction enthalpy of reaction i; $F_{T,in}$, total molar flow rate at the inlet; $\Delta C_{p,i}$, net change in the heat capacity for reaction i.

Thus Eqs. (11) and (13) are coupled differential equations, but they can be solved numerically by also applying Eqs. (12) and (14). Furthermore, to ensure an accurate simulation of the experiments, it is necessary to correct the reaction rates in the reactor calculations by a bulk effectiveness factor η because the rates within the catalyst particles may be lower than the rate corresponding to bulk conditions due to possible transport limitations. The bulk effectiveness factor considers the potential resistances between the bulk phase and the surface of a catalyst particle as well as the resistances within the particle itself, such as pore diffusion [16]. Hence the bulk effectiveness factor is both a function of transport properties and reactivity:

$$\eta = f(\text{transport properties}, \text{reactivity})$$

Therefore $\eta \approx 1$ when the steam reforming reaction limits the overall rate while $\eta \ll 1$ when transportation of reactants, products, and/or energy limits the overall rate. This bulk effectiveness factor for the steam reforming reaction was calculated by collocation [17], and the reaction rate corresponding to bulk conditions was corrected in every step down through the reactor. The effectiveness factors satisfied the condition $\eta > 80\%$ at all conditions, and for the vast majority η was >90%. This indicates that only minor transport limitations existed at the experimental conditions applied. Hence the kinetic studies in this work were based on near-intrinsic activity measurements.

With the above one-dimensional reactor model it was possible to perform integration over the catalyst mass for each of the experiments, which were carried out in the laboratory. This calculation was performed for all experiments, $k = 1, 2, 3, \ldots, N_{exp,total}$, where k is the experiment number, and $N_{exp,total}$ is the total number of experiments. This provided calculated methane conversions, $X_{5,out,calc,k}$, in the outlet of the reactor corresponding to each experiment. These values were compared to the corresponding measured conversions in the outlet of the reactor, $X_{5,out,meas,k}$, by the following sum of square:

$$SSQ = \sum_{k=1}^{N_{exp,total}} (X_{5,out,meas,k} - X_{5,out,calc,k})^2 \quad (15)$$

In this way the entire dataset was simulated by means of the above reactor model and a reaction rate expression R_5 for the rate of steam reforming over ruthenium. The issue of finding appropriate reaction rate expressions is considered in the next section, and the optimal parameters of these reaction rate expressions were all determined by integration over the catalyst mass for each of the experiments and by minimizing the above sum of square.

4.2. Micro kinetic modeling

In order to determine the possible reaction barriers for steam reforming over ruthenium, it is necessary to evaluate how the reaction proceeds at the atomic level. For this purpose the following micro kinetic model with elementary reaction (ER) steps is proposed in [4]:

$$CH_4(g) + 2^* \underset{k_1^-}{\overset{k_1^+}{\rightleftharpoons}} CH_3^* + H^* \quad (ER1)$$

$$H_2O(g) + 2^* \underset{k_2^-}{\overset{k_2^+}{\rightleftharpoons}} OH^* + H^* \quad (ER2)$$

$$OH^* + {}^* \underset{k_3^-}{\overset{k_3^+}{\rightleftharpoons}} O^* + H^* \quad (ER3)$$

$$CH_3^* + {}^* \underset{k_4^-}{\overset{k_4^+}{\rightleftharpoons}} CH_2^* + H^* \quad (ER4)$$

$$CH_2^* + * \underset{k_5^-}{\overset{k_5^+}{\rightleftharpoons}} CH^* + H^* \quad \text{(ER5)}$$

$$CH^* + * \underset{k_6^-}{\overset{k_6^+}{\rightleftharpoons}} C^* + H^* \quad \text{(ER6)}$$

$$C^* + O^* \underset{k_7^-}{\overset{k_7^+}{\rightleftharpoons}} CO^* + * \quad \text{(ER7)}$$

$$H^* \underset{k_8^-}{\overset{k_8^+}{\rightleftharpoons}} \frac{1}{2} H_2(g) + * \quad \text{(ER8)}$$

$$CO^* \underset{k_9^-}{\overset{k_9^+}{\rightleftharpoons}} CO(g) + * \quad \text{(ER9)}$$

Possible reaction barriers for steam reforming are also considered in [4] by use of DFT calculations. These calculations indicate that both dissociative adsorption of methane (ER1), and/or the direct CO formation (ER7) may have significant influence on the overall rate although the hypothesis that CO formation is the rate determining step is not supported by the experimental data. There would be an inhibition by H_2 corresponding to $P_{H_2}^{-3}$ if CO formation was rate determining which was not observed in this experimental study. We therefore assume below that dissociative adsorption of methane is rate determining at the conditions used here. By using the above elementary reactions (ER1–ER9) and considering the dissociative adsorption step of methane to be rate determining while the remaining eight reactions are quasi-equilibrated, we derive an expression for the overall reaction rate of methane steam reforming over ruthenium:

$$\begin{aligned} R_{\text{overall}} &= k_1^+ P_{CH_4} (1 - \beta_{SR}) \cdot \theta_*^2 \\ &= A_1^+ \cdot \exp\left(\frac{-E_{a,1}}{RT}\right) \cdot P_{CH_4} \cdot (1 - \beta_{SR}) \cdot \theta_*^2 \end{aligned} \quad (16)$$

Here θ_* is the fraction of the active surface that is free. θ_* accounts for the fact that the various reaction species may be able to block the active sites:

$$\theta_* = \frac{1}{\begin{aligned} &1 + (\theta_{CO}/\theta_*) + (\theta_H/\theta_*) + (\theta_{OH}/\theta_*) + (\theta_O/\theta_*) \\ &+ (\theta_C/\theta_*) + (\theta_{CH}/\theta_*) + (\theta_{CH_2}/\theta_*) + (\theta_{CH_3}/\theta_*) \end{aligned}} \quad (17)$$

The terms in Eq. (17) are given by:

$$\frac{\theta_{CO}}{\theta_*} = \frac{P_{CO}}{K_9} \quad (18)$$

$$\frac{\theta_H}{\theta_*} = \frac{P_{H_2}^{1/2}}{K_8} \quad (19)$$

$$\frac{\theta_{OH}}{\theta_*} = \frac{K_2 K_8 P_{H_2O}}{P_{H_2}^{1/2}} \quad (20)$$

$$\frac{\theta_O}{\theta_*} = \frac{K_2 K_3 K_8^2 P_{H_2O}}{P_{H_2}} \quad (21)$$

$$\frac{\theta_C}{\theta_*} = \frac{1}{K_2 K_3 K_7 K_8^2 K_9} \cdot \frac{P_{CO} P_{H_2}}{P_{H_2O}} \quad (22)$$

$$\frac{\theta_{CH}}{\theta_*} = \frac{1}{K_2 K_3 K_6 K_7 K_8^3 K_9} \cdot \frac{P_{CO} P_{H_2}^{3/2}}{P_{H_2O}} \quad (23)$$

$$\frac{\theta_{CH_2}}{\theta_*} = \frac{1}{K_2 K_3 K_5 K_6 K_7 K_8^4 K_9} \cdot \frac{P_{CO} P_{H_2}^2}{P_{H_2O}} \quad (24)$$

$$\frac{\theta_{CH_3}}{\theta_*} = \frac{1}{K_2 K_3 K_4 K_5 K_6 K_7 K_8^5 K_9} \cdot \frac{P_{CO} P_{H_2}^{5/2}}{P_{H_2O}} \quad (25)$$

It can be shown that Eq. (16) is also valid for CO_2 reforming when the water gas shift reaction is assumed to be in equilibrium. Hence it is with this assumption possible to calculate the rates of CO_2 reforming. The fast WGS equilibrium gives the H_2O needed for the methane steam reforming reaction to proceed as modeled by Eq. (16). When Eq. (16) is considered, it is clear that a new reaction rate model will appear every time a new reaction specie or combination of reaction species is considered in the denominator of θ_*.

5. Results of fitting reaction rate models

Based on the reactor and micro kinetic modeling already described, ten different reaction rate models were tested against the obtained experimental data. In total 62 experiments were used in the model fitting (both steam and CO_2 reforming experiments). The difference between the rate models was the appearance of the denominator of θ_*. The following species were tried out in the denominator of θ_*: clean surface, CO, H, OH, O, C, CH, CH_2, CH_3, and CO + H. Hence Eq. (16) was combined with Eqs. (18)–(25), either using one equation or for the last model (CO + H) using both coverages given by Eqs. (18) and (19). Effectively coverage effects of the possible surface species were thus studied by modeling our experimental results. In the following only the results based on the reaction rate models of clean surface, CH, CH_2, and CO + H in the denominator of θ_* will be commented as the latter three models provide the best agreement with the experimental data, and the clean surface will be included as a reference for these models. In Table 1 the pre-exponential factor A_1^+, the activation energy $E_{a,1}$, and the adsorption parameters are provided for the reaction rate models of clean surface, CH, CH_2, and CO + H in the denominator of θ_*. The corresponding sum of square as given by Eq. (15) is also shown for each fit. Moreover, the global predictions of the four models are compared to the measured conversions for each of the variations of partial pressures and temperature in Figs. 5 and 6.

The simple model with no reaction species able to block part of the active sites has been proposed by Wei and Iglesia to model the kinetic data given by their experimental observations [7] at 550–700 °C. However, Table 1 shows that the performance of this model is poor for the data obtained in this study at 425–575 °C. The residual of optimizing this model is much higher than for the remaining models given in Table 1. This is also seen in Fig. 6 where the clean surface model predicts too low conversions for most of the steam reforming experiments, while it predicts too high conversions for the CO_2 reforming experiments. The model considering CH inhibition gives reasonable results, and the main reason is the good capture of the reaction rate behavior during the experiments with H_2 addition. However, the model shows a strong tendency to underestimate the conversions at low partial pressures of water. The model considering CH_2 inhibition also captures the negative influence of H_2 on the reaction rate quite well. However, it underestimates the conversions even more than the previous model at low partial pressures of water. Of all the models the model considering CO and H species on the surface provides the best fit to the overall dataset because this model estimates the conversions at low partial pressures of water correctly. Furthermore, this model provides a good agreement with the measured conversions during both temperature variations, and it also captures the negative influence of H_2 addition with reasonable accuracy.

It is interesting to consider the observations above in the light of the recently reported DFT calculations in Ref. [4] of the most important surface species involved in steam reforming. Here the abilities of various reaction species to bind to ruthenium surfaces during steam reforming were studied. In these DFT calculations, a temperature of 500 °C, a conversion of 10%, and an absolute pressure of 1 bar were used for the calculations of free energy.

Table 1
Results of fitting the overall rate model to the experimental kinetic data for the Ru/ZrO_2 catalyst. In total 62 experiments were used in the model fitting. The pre-exponential factor, activation energy and adsorption parameters are provided for the reaction rate models containing clean surface, CH, CH_2, and CO + H in the denominator of θ_*. The corresponding sum of squares as given by Eq. (15) is also shown.

Reaction species in denominator of θ_*	A_1^+ (mol g^{-1} h^{-1} bar^{-1})	$E_{a,1}$ (kJ/mol)	AD_{CH}, AD_{CH_2} or AD_{CO}($bar^{-3/2}$, bar^{-2} or bar^{-1})	Q_{CH}, Q_{CH_2} or Q_{CO} (kJ/mol)	AD_H ($bar^{-1/2}$)	Q_H (kJ/mol)	SSQ (%^{2})
Clean surface	1.38×10^7	102.3	–	–	–	–	247.58
CH	1.74×10^8	118.0	6.01×10^{-12}	−213.2	–	–	21.59
CH_2	3.35×10^8	122.0	6.93×10^{-10}	−195.5	–	–	24.12
CO and H	4.39×10^7	107.9	2.19×10^{-5}	−87.4	7.31×10^{-6}	−71.0	10.98

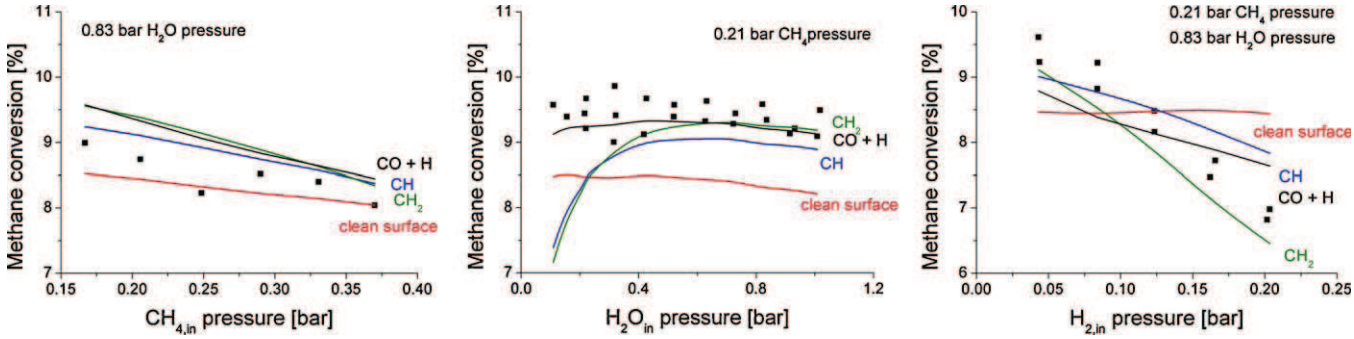

Fig. 5. Experimental conversions and global model data by four models; clean surface, CH, CH_2 and CO + H in the denominator of θ_*. Predictions of methane conversions at varying methane partial pressure (left), water partial pressure (middle) and H_2 partial pressure (right). The total inlet flow rate was $\nu_{T,in}$ = 12.1 Nl/h. Total pressure P = 1.3 bar, N_2 balance. T_{in} = 500 °C.

Furthermore, we assumed that the water gas shift reaction is equilibrated, and thus these conditions correspond well with those employed in this study. The analysis showed that the surface species CO, H, O, and/or OH may be present at the ruthenium surfaces during steam reforming, whereas it is unlikely that C, CH, CH_2 and CH_3 will have any significant coverage [4]. As explained earlier the models considering O and OH inhibition were also fitted to the experimental data, but neither of them gave reasonable results. On the other hand the model considering CO and H species on the surface provides the best agreement with the experimental data, and furthermore the calculations in [4] suggest that these species may likely stick to ruthenium surfaces at the conditions used here. Therefore these facts indicate that the model considering CO and H inhibition is valid during methane steam reforming at low pressure. The final model with CO and H inhibition rightly contains 6 parameters, whereas especially the two other models (CH and CH_2) only have 4 parameters. One should be critical when adding parameters for modeling experimental data. However, we still believe that it captures the right trends and makes a solid theoretical basis at the actual reaction conditions.

6. Discussion

First, the dispersions were determined by TEM, H_2 chemisorption, and sulfur chemisorption. The three methods give slightly different dispersions, and an average of the dispersions was used together with the activity to obtain a good estimate of the turn over frequency (TOF) for comparison with previous results. The average dispersion is 25%, and the resulting TOF is 11.1 s^{-1} at 500 °C. When comparing absolute rates of methane reforming, we found that our TOF agrees within a 20% uncertainty with the data presented in a previous investigation [4]. Therefore both the absolute activity and subsequently sticking coefficient are more than an order of magnitude larger than those observed in the study of Wei and Iglesia [7].

Second, we will discuss the kinetics of methane steam reforming. Studies have previously shown that methane dissociative adsorption is a rate limiting step at some conditions [4,7], and this basic model is also consistent with the data obtained here. Nevertheless, we show above that methane steam reforming at 500 °C cannot be modeled by a simple first order dependency of

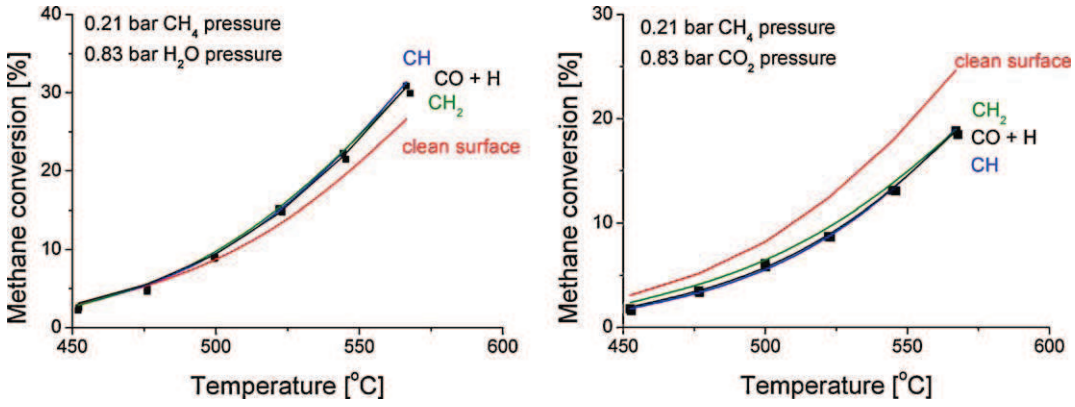

Fig. 6. Prediction of methane conversions during steam reforming (left) and CO_2 reforming (right). Experimental conversions and global model data by four models; clean surface, CH, CH_2 and CO + H as the denominator of θ_*. The total inlet flow rate was $\nu_{T,in} \approx$ 12.1 Nl/h, P = 1.3 bar, N_2 balance and with varying temperatures (425–575 °C).

methane as observed at higher temperatures [7]. In this study we observe a significant influence of the inlet partial pressure of H_2. Furthermore, the steam and CO_2 reforming rates are not equal, which makes it is necessary to include a term in the kinetics that takes this observation into account. The difference between methane steam and CO_2 reforming activities were previously described by Rostrup-Nielsen and Hansen [3] for a series of noble metal catalysts and was attributed to higher partial pressures and surface coverage of CO during CO_2 reforming. The difference between methane steam and CO_2 reforming activities is also ascribed to high CO coverages in the model developed here. Furthermore, we observe that the difference between steam and CO_2 reforming activities is approximately the same as the difference found in the previous study at 550 °C using a MgO supported ruthenium catalyst [3], where the activity for steam reforming was between 2 and 3 times higher than CO_2 reforming.

Another explanation of the lower activity of CO_2 reforming compared to steam reforming could be that CO_2 has a direct effect on the reaction rate. However, the binding energy of CO_2 to ruthenium is so small that the coverage of CO_2 at Ru will be negligible [4]. A study of CO_2 reforming over a Ru/La_2O_3 catalyst showed that CO_2 addition increases the methane conversion, and this was ascribed to an interaction with the support [10]. With regard to steam, we found no dependency of the steam content on the rate of steam reforming at 500 °C, and this observation is also in agreement with previous work [3,7].

The kinetic studies of steam reforming over ruthenium reported in the literature and the work presented here point to methane dissociative adsorption as the rate determining step. At high temperature the active surface is free, but at lower temperatures CO and hydrogen are present at the surface and reduces the activity due to blockage of the active sites. Thus, there is a qualitative agreement between the kinetic model reported here and the data obtained by Rostrup-Nielsen and Hansen [3] along with the data and model presented by Wei and Iglesia [7]. We also examined whether there is a quantitative agreement between the present models and that obtained in [7]. We find that the level of site blockage in the steam and CO_2 reforming experiments reported by Wei and Iglesia [7] is in the order of 10% at 600 °C at the highest conversion used using our model.

DFT calculations demonstrate the importance of reaction conditions on the rate of steam reforming over ruthenium because the most important barrier switches from being direct CO formation to methane dissociation as the temperature is increased [4]. Based on the DFT calculations at low temperatures (e.g. $T < 500$ °C) one may expect the direct CO formation step to be rate determining, while an intermediate regime may exist where there is no single rate determining step.

The results show that the direct CO formation is not the rate determining step. It is possible that the rate of CO formation is higher than predicted by DFT in Ref. [4] as we assume that CO formation proceeds via recombination of C and O. This is the most likely reaction path at low coverages; however, at higher coverages other reaction paths for CO formation at the surface of ruthenium may be important. CHO species may be formed from CH_2O or CH and O, and this intermediate (CHO) could then dissociate into CO and H. This mechanism was recently suggested to be the main reaction path for methane steam reforming over nickel catalysts [13], but the mechanism may also be relevant for steam reforming over ruthenium. The reaction barriers for the formation of CO by this alternative route are expected to be minor than the corresponding barrier for the direct CO formation step. At low temperature the methane dissociative adsorption step would then still be rate determining.

In the following CO adsorption at ruthenium will be discussed. When CO is adsorbed on a ruthenium surface, it is predominantly molecularly adsorbed [18]. Adsorption experiments using both single crystals and nanoparticles show a large difference in adsorption energies for low and high CO coverages. The initial CO binding energy is about 150–175 kJ/mol but decrease to about 100 kJ/mol for higher CO coverages, see Table 2. A CO adsorption energy of 87 kJ/mol is found using our model, which reasonably agrees with the high coverage values of the CO adsorption energy found in the literature. There may be two reasons for this. First, our value most likely corresponds to the high coverage adsorption energy of CO as Q_{CO} was mainly determined by the data at the relative high coverages of CO during CO_2 reforming. Second, even though our binding energy of CO is in the low end of the range reported in the literature, the temperature independent factor of the CO adsorption constant is relatively high, 2.19×10^{-5} bar^{-1}. For example the temperature independent factor for CO adsorption to nickel is about two orders of magnitude lower [19]. The low temperature independent factor could be due to a compensation effect between the pre-factor and the adsorption energy [20].

The adsorption energies of CO reported in Table 2 were mainly derived using temperature programmed desorption (TPD). Few studies of the energetics of CO adsorption at high temperatures, i.e. of the order of 500 °C have been carried out, but Dulaurent et al. [21] studied Ru/Al_2O_3 catalysts and CO adsorption in the temperature range of 100–430 °C and at a constant background pressure of 1000 Pa CO. The CO coverage was studied by FTIR spectroscopy and significant coverages were obtained even at high temperatures. By using their model at our conditions (both steam and CO_2 reforming at 500 °C), we obtain CO coverages of 10–40%, which explain the observed differences in activity between steam and CO_2 reforming.

DFT calculations [22] suggest that at the gas and temperature conditions used in our study, the surface will be partly covered by hydrogen. So it is likely that the kinetics will also be influenced by hydrogen as found in our study. As Table 3 shows the H adsorption energy of 71 kJ/mol found here is higher than the energy obtained in single crystal and nanoparticle studies. Furthermore, the temperature independent factor for H atom adsorption at nickel is estimated to be approximately two orders of magnitude higher than obtained here [19]. These deviations from the literature values are most likely due to a compensation effect as the overall adsorption constant is well determined, whereas the temperature independent factor and the activation

Table 2
Experimental CO adsorption/desorption energies (kJ/mol).

Ru surface	Q_{CO} at low coverage (kJ/mol)	Q_{CO} at high coverage (kJ/mol)	Analytical method	Ref.
Ru $(10\bar{1}0)$	−145		TPD	[28]
Ru (109)	−165	−50	FTIR and TPD	[29]
Ru $(10\bar{1}0)$	−157	−100	TPD	[30]
Ru $(11\bar{2}0)$		−103	TPD	[31]
Ru/HOPG[a]		−113	TPD	[18]
Ru/Al_2O_3	−175	−115	FTIR and adsorption model	[21]
Ru/ZrO_2		−87	Kinetic model	This work

[a] Highly ordered pyrolytic carbon.

Table 3
Experimental H adsorption energies (kJ/mol) at low H coverage.

Ru surface	Q_H (kJ/mol)	Analytical method	Ref.
Ru $(10\bar{1}0)$	−40	TPD	[32]
Ru (0001)	−46	TPD	[33]
Ru (0001)	−62	TPD	[34]
Ru (0001)	−54	TPD	[35]
Ru/SiO_2 nanoparticles	−40	Calorimetric	[36]
Ru (0001)	−35	TPD	[37]
Ru/ZrO_2	−71	Kinetic model	This work

energy are highly correlated. At the experimental conditions our model predicts hydrogen coverages in the range of 2–20%, with the highest coverage when hydrogen was added at the inlet and lowest during CO_2 reforming.

The potential importance of the interaction between CO and H should also be considered. Co-adsorption of CO and H at ruthenium catalysts was studied in some detail [23–27], and we observed that for CO there is either no influence [26,27] or weaker CO bonding [25] in the presence of hydrogen. Furthermore, the studies reported in the literature do not agree on whether the CO–H interaction is repulsive [26] or attractive [23]. It is likely that the binding of H atoms is more affected than CO in this co-adsorption situation [26,27]. Generally, it cannot be concluded with certainty that there is any significant co-adsorption effect.

7. Conclusion

The activity of a Ru/ZrO_2 catalyst was measured at varying conditions, and subsequently the reactivity was modeled by combining a reactor model and a kinetic model. At the conditions and temperatures relevant for this study, the data obtained here are consistently modeled using methane dissociative adsorption as the rate limiting step. CO and H adsorb and partly cover the active sites and thereby influence the overall activity. The kinetic expression for methane steam reforming over the Ru/ZrO_2 catalyst is given by a Langmuir–Hinshelwood type expression:

$$R = \frac{4.39\times10^{7}\,[\mathrm{mol\,g^{-1}h^{-1}bar^{-1}}]\exp(-108\,[\mathrm{kJ/mol}]/\mathrm{RT})\cdot P_{\mathrm{CH_4}}\cdot(1-\beta_{\mathrm{SR}})}{\left(1+2.19\times10^{-5}\,[\mathrm{bar^{-1}}]\exp(87\,[\mathrm{kJ/mol}]/\mathrm{RT})\cdot P_{\mathrm{CO}} + 7.31\times10^{-6}\,[\mathrm{bar^{-1/2}}]\exp(71\,[\mathrm{kJ/mol}]/\mathrm{RT})\cdot P_{\mathrm{H_2}}^{1/2}\right)^{2}}$$

The catalyst (Ru/ZrO_2) is most likely representative for other ruthenium catalysts since support effects are reported to be negligible [7], except for La_2O_3 [10].

The Ru/ZrO_2 catalyst was characterized using TEM and H_2 chemisorption. A notable feature of the TEM analysis is that ruthenium particles form a small amorphous ruthenium oxide surface layer of about 1 nm thickness when exposed to air at room temperature. Therefore ETEM has to be used for determining particle size distributions of Ru catalysts, especially for Ru samples with small Ru particles since small ruthenium particles will be fully oxidized.

Acknowledgements

We would like to thank Stig Helveg for support in connection with the ETEM work and analysis. Furthermore we thank the Danish Agency for Science Technology and Innovation for financial support of this work. CINF is funded by the Danish National Research Foundation.

References

[1] J.R. Rostrup-Nielsen, J. Sehested, J.K. Norskov, Hydrogen and Synthesis Gas by Steam- and CO_2 Reforming, Adv. Catal. 47 (2002) 65–139.
[2] P.K. Bakkerud, Catal. Today 106 (2005) 30–33.
[3] J.R. Rostrup-Nielsen, J.-H.B. Hansen, J. Catal. 144 (1993) 38–49.
[4] G. Jones, J.G. Jakobsen, S.S. Shim, J. Kleis, M.P. Andersson, J. Rossmeisl, F. Abild-Pedersen, T. Bligaard, S. Helveg, B. Hinnemann, J.R. Rostrup-Nielsen, I. Chorkendorff, J. Sehested, J.K. Nørskov, J. Catal. 259 (2008) 147–160.
[5] J.M. Wei, E. Iglesia, J. Phys. Chem. B 108 (2004) 4094–4103.
[6] J.M. Wei, E. Iglesia, J. Catal. 224 (2004) 370–383.
[7] J.M. Wei, E. Iglesia, J. Phys. Chem. B 108 (2004) 7253–7262.
[8] M.C.J. Bradford, M.A. Vannice, J. Catal. 183 (1999) 69–75.
[9] A. Berman, R.K. Karn, A. Epstein, Appl. Catal. A 282 (2005) 73–83.
[10] C. Carrara, J. Munera, E.A. Lombardo, L.M. Cornaglia, Top. Catal. (2008) 98–106.
[11] P. Ferreira-Aparicio, I. Rodriguez-Ramos, J.A. Anderson, A. Guerrero-Ruiz, Appl. Catal. A 202 (2000) 183–196.
[12] M.P. Andersson, F. Abild-Pedersen, I.N. Remediakis, T. Bligaard, G. Jones, J. Engbæk, O. Lytken, S. Horch, J.H. Nielsen, J. Sehested, J.R. Rostrup-Nielsen, J.K. Norskov, I. Chorkendorff, J. Catal. 255 (2008) 6–19.
[13] D.W. Blaylock, T. Ogura, W.H. Green, G.J.O. Beran, J. Phys. Chem. C 113 (2009) 4898–4908.
[14] S.G. Wang, X.Y. Liao, J. Hu, D.B. Cao, Y.W. Li, J.G. Wang, H.J. Jiao, Surf. Sci. 601 (2007) 1271–1284.
[15] O. Levenspiel, Chemical Reaction Engineering, John Wiley & Sons, 1999.
[16] G.F. Froment, K.B. Bischoff, Chemical Reactor Analysis and Design, John Wiley & Sons, Inc., 1990.
[17] J.V. Villadsen, M.L. Michelsen, Solution of Differential Equation Models by Polynomial Approximation, Prentice-Hall, Eaglewood Cliffs, NJ, 1978.
[18] R.M. Nielsen, The Structure and Reactivity of Ruthenium Nanoparticles, Ph.D. Thesis, Technical University of Denmark, 2009.
[19] J. Sehested, S. Dahl, J. Jacobsen, J.R. Rostrup-Nielsen, J. Phys. Chem. B 109 (2005) 2432–2438.
[20] T. Bligaard, K. Honkala, A. Logadottir, J.K. Norskov, S. Dahl, C.J.H. Jacobsen, J. Phys. Chem. B 107 (2003) 9325–9331.
[21] O. Dulaurent, M. Nawdali, A. Bourane, D. Bianchi, Appl. Catal. A 201 (2000) 271–279.
[22] F. Faglioni, W.A. Goddard, J. Chem. Phys. 122 (2005).
[23] H.M. Miura, M.L. Mclaughlin, R.D. Gonzalez, J. Catal. 79 (1983) 227–232.
[24] N.M. Gupta, V.P. Londhe, V.S. Kamble, J. Catal. 169 (1997) 423–437.
[25] D.L. King, Prepr. Am. Chem. Soc., Div. Pet. Chem. 23 (1978) 482–494.
[26] I.M. Ciobica, A.W. Kleyn, R.A. van Santen, J. Phys. Chem. B 107 (2003) 164–172.
[27] D.W. Goodman, T.E. Madey, M. Ono, J.T. Yates, J. Catal. 50 (1977) 279–290.
[28] M. Kiskinova, M. Tikhov, Surf. Sci. 194 (1988) 379–396.
[29] T. Zubkov, G.A. Morgan, J.T. Yates, O. Kühlert, M. Lisowski, R. Schillinger, D. Fick, H.J. Jänsch, Surf. Sci. 526 (2003) 57–71.
[30] G. Lauth, T. Solomun, W. Hirschwald, K. Christmann, Surf. Sci. 210 (1989) 201–224.
[31] J. Wang, Y. Wang, K. Jacobi, Surf. Sci. 488 (2001) 83–89.
[32] G. Lauth, E. Schwarz, K. Christmann, J. Chem. Phys. 91 (1989) 3729–3743.
[33] L.R. Danielson, M.J. Dresser, E.E. Donaldson, J.T. Dickinson, Surf. Sci. 71 (1978) 599–614.
[34] P. Feulner, D. Menzel, Surf. Sci. 154 (1985) 465–488.
[35] J.A. Schwarz, Surf. Sci. 87 (1979) 525–538.
[36] S. Bhatia, F. Engelke, M. Pruski, B.C. Gerstein, T.S. King, J. Catal. 147 (1994) 455–464.
[37] H. Shimizu, K. Christmann, G. Ertl, J. Catal. 61 (1980) 412–429.

Methane steam reforming kinetics for a rhodium-based catalyst

Jon Geest Jakobsen[a,b,*], Martin Jakobsen[a], Ib Chorkendorff[b], Jens Sehested[a],

[a]Haldor Topsøe A/S, Nymøllevej 55, DK-2800 Kgs. Lyngby, Denmark

[b]Center for Individual Nanoparticle Functionality (CINF), Department of Physics, Building 312, Technical University of Denmark, DK-2800 Kgs. Lyngby, Denmark

[*]To whom correspondence should be addressed: E-mail: jgja@topsoe.dk, Fax: +45 45272999, Tel: +45 45272497

Keywords: **Methane steam reforming, Kinetics, Rhodium**

Running head: **Methane steam reforming on Rh/ZrO_2**

Abstract: Methane steam reforming is the key reaction to produce of synthesis gas and hydrogen at the industrial scale. Here the kinetics of methane steam reforming over a rhodium-based catalyst is investigated in the temperature range 500-800°C and as a function of CH_4, H_2O and H_2 partial pressures. The methane steam reforming reaction cannot be modeled without taking CO and H coverages into account. This is especially important at low temperatures and higher partial pressures of CO and H_2. For methane CO_2 reforming experiments, it is also necessary to consider the repulsive interaction of CO that lowers the absorption energy at high CO coverage. The CO-CO interaction is supported by comparison with fundamental surface science studies.

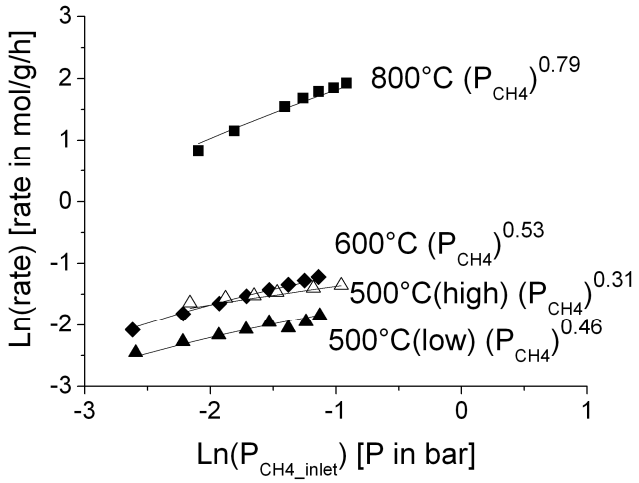

Graphical abstract. Kinetic modeling and experimental results for the methane dependency in the methane steam reforming reaction on a Rh catalyst.

1. Introduction

Steam reforming is the preferred process for production of hydrogen and synthesis gas today [1]. By combining steam and CO_2 reforming, it is possible to vary the H_2/CO ratio over a wide range and by adjusting to the right H_2/CO ratio synthesis gas can be used as a precursor for the formation of various chemicals and fuels. The methane steam (Eq. 1) and CO_2 (Eq. 2) reforming reactions investigated in this work are given below.

$$CH_4(g) + H_2O(g) \rightleftharpoons CO(g) + 3H_2(g) \quad (1)$$

$$CH_4(g) + CO_2(g) \rightleftharpoons 2CO(g) + 2H_2(g) \quad (2)$$

Several papers deal with the kinetics of methane steam reforming over nickel catalysts [2,3]. The nickel-based catalysts are preferred due to the relative low price of nickel compared to other transition metals (Rh, Ru, Pt, Pd, Ir etc.) that also catalyze conversion of methane to synthesis gas. The majority of the authors find that the most active metals for methane steam reforming are Rh and Ru [4-8], whereas varying relative reactivities have been determined for Ni, Pt, Ir and Pd. We recently found these four transition metals to have quite similar activities [8]. It should be mentioned that Wei and Iglesia recently reported a different relative reactivity of the transition metals: Pt > Ir > Ni > Rh > Ru [9].

Noble metals have a higher barrier for carbon formation during operation than nickel. Especially whisker carbon formation can at severe conditions be problematic for an effective performance of the catalyst and the catalyst may eventually break down [2,3]. Noble metals are much more expensive than nickel, but they also have an advantage due to the higher barrier towards carbon formation and in some cases industrial use of noble metals may be economically feasible [4].

Several different mechanisms for methane steam reforming kinetics over transition metals have been proposed, but the main part of the work was done for nickel-based catalysts.

The work reported here focuses on the kinetics of a rhodium-based catalyst as a continuation of our previous studies for ruthenium-based catalysts [10]. The kinetics for methane CO_2 reforming [11-16] and methane steam reforming [4,17,18] on rhodium have been investigated with different results. Rostrup-Nielsen and Hansen reported that steam reforming is faster than CO_2 reforming at 550°C. The difference was ascribed to CO partly covering the active sites [4]. On the contrary, investigations of CO_2 reforming by Bhat and Sachtler showed that the reaction is first order in the partial pressure of methane at 600°C and that there is no influence of the CO_2 partial pressure [11]. Investigations of steam and CO_2 reforming at 550-700°C by Wei and Iglesia gave the same conclusions as Bhat and Sachtler – i.e. the reaction is first order in CH_4 and no other species influence the reaction rate [18]. Múnera et al. [14] performed CO_2 reforming at 550°C and found a positive reaction order of CO_2 and the follow rate equation; $r = k\left(P_{CH4}\right)^{0.61}\left(P_{CO2}\right)^{0.37}$ using a Rh/La_2O_3 catalyst. They suggested that La_2O_3 has a stronger adsorption of CO_2, resulting in an increase in the rate at elevated CO_2 partial pressure.

Support effects for steam or CO_2 reforming reactions have been debated. In recent investigations, we found metal particle size effects [8,18]. We obtained different particle sizes on different supports, and it seems most likely that the dominant effect on the reaction rate is the particle size and that the nature of the support is of minor importance [18].

Our previous investigations on steam reforming kinetics over ruthenium-based catalysts showed that there is a strong adsorbance of CO and H at low temperature experimental conditions [10]. Based on the similarities in the observed kinetics and the nature of rhodium and ruthenium, the steam reforming kinetics for rhodium used here is based on the same kinetic and reactor models as previously described for ruthenium [10]. In other studies, the adsorbance of CO and H at low

temperature (400-600°C) also showed to be relevant for the methane steam reforming conditions present in our investigation [19]. It was also found that the water gas shift reaction is equilibrated for the reaction conditions for rhodium [19] as it was for ruthenium [10].

2. Experimental methods

A 1% Rh/ZrO_2 catalyst was prepared by incipient wetness impregnation with an aqueous solution of $Rh(NO_3)_3$ of a 15 m^2/g ZrO_2 (95% tetragonal / 5% monocline) support. The catalyst was calcined in air at 450°C for 4 hours and reduced in 1 bar hydrogen at 550°C. To obtain a stable catalyst, it was aged at 830°C for 228 h in a H_2O/H_2 mixture ($H_2O:H_2$ = 1:1) at 31 bar total pressure. Before exposure of the reduced catalyst to air, the catalyst was passivated at room temperature by exposure to a flow of 1% air for several hours.

To circumvent transport restrictions during the kinetic measurements, the catalyst pellets were crushed to less than 45 µm and mixed 1:10 with inert ZrO_2 support and pressed to tablets. The final catalyst particle size of the diluted particles was 125-300 µm. The catalyst was characterized as described elsewhere [8], and an average Rh particle diameter of 8.4 nm was determined by transmission electron microscopy corresponding to a metal dispersion of 10.6%.

2.1 Measurements of H_2O and CO_2 reforming activities

The type of measurements used in this study is described in more detail in [10] and will only be described briefly here. Six experimental series were performed with a total of 78 individual measurements. Catalytic activity was measured by placing a catalyst sample (25-500 mg diluted catalyst, 125-300 µm) in a stainless steel tube (8.5 mm inner diameter). The catalyst granules was further diluted with inert $MgAl_2O_4$ (125-300 µm) to a total catalyst bed weight of 1000 mg. The reactor was mounted with an internal thermo well with an outer diameter of 3.2 mm. A

thermocouple was placed inside the thermo well to measure the catalyst temperature. A pretreatment procedure was enabled for reduction and stabilization of the catalytic activity at a high temperature of 800°C. We observed that the catalyst continuously deactivates at medium temperatures of 500-600°C, if this pretreatment is not performed. As will be discussed later, the reduction and stabilization procedure resulted in different stable activities for the different experimental series. This was accounted for in the modeling of the experimental data.

The flow rate in all measurements was kept constant at 200 Ncm^3/min and the effect of CH_4, H_2O, H_2 and CO_2 partial pressures were investigated in a temperature range of 500-800°C. The reaction was studied at 1.3 bar total pressure with a mixture of CH_4, H_2O, H_2 and CO_2 as the inlet gases. After condensing the steam, the composition of the outlet gas was measured by an HP gas chromatograph.

2.2 Reactor modeling

The reactor can be described and modeled as a fixed bed plug flow reactor. The reactor model was discussed in more detail in a previous publication dealing with steam and CO_2 reforming on Ru catalysts [10]. Briefly, mass and heat transport considerations were included in the model due to inter-particle diffusion and the strongly endothermic reaction. The reactor was modeled as a one-dimensional, non-isothermal plug flow reactor. The bulk effectiveness factors (η) were calculated to be above 0.8 for 90% of the measurements; hence the intrinsic rate controls the majority of the measurements. For the remaining measurements, η is larger than 0.6.

The model was optimized by a sum of squares (SSQ) of the outlet methane conversion in Eq. 3, where the calculated conversions, X_{calc}, were compared to the corresponding measured conversions, X_{meas}.

$$SSQ = \sum_{k=1}^{N} \left(X_{calc} - X_{meas} \right)^2 \quad (3)$$

Where N is the total number of measurements and the model is optimized by the six variables in Eq. 13 to describe the reaction rate.

3. Kinetic modeling

The expression for modeling of the reaction rate is given by Eq. 4, which can be derived from simple kinetic considerations from dissociative adsorption of methane as the rate limiting step [10].

$$rate = A_1 \cdot \exp\left(\frac{-E_a}{RT} \right) \cdot P_{CH_4} \cdot \theta_*^2 \quad (4)$$

Where θ_* is the fraction of free active sites. Kinetics of steam reforming over rhodium was studied by Wei and Iglesia [18] who observed no influence of CO_2, H_2O, CO or H_2 inlet partial pressures on the rate of reaction and further found that the only relevant kinetic step was found to be methane dissociative adsorption at a clean active surface, i.e. $\theta_* = 1$. The clean surface was most likely obtained due to high temperatures and low conversions. If other elementary steps are important, then it is necessary to propose a more complicated model. We previously showed that the CO formation step could be relevant at low temperatures [8]. If this elementary step is dominant, then we can calculate that the rate will depend on the partial pressure of H_2 as $P_{H_2}^{-3}$ [8]. Such a dependency was not observed experimentally neither in this investigation nor in our recent study of the kinetics of ruthenium [10].

Instead it is possible to include a blockage of the active sites to explain the experimental results in our present study. Our previous work showed on ruthenium-based catalysts showed that CO and

hydrogen atoms partly cover the surface at low temperatures and thereby reduce the methane steam reforming activity [10]. Maestri et al. [19] found a significant effect of CO and H coverage on Rh catalysts even for diluted systems (>95% N_2, atmospheric conditions). The influence of CO on the activity was introduced by assuming that CO in the gas phase is in equilibrium with CO at the active sites as given by Eq. 5.

$$CO(g) + {}^{*} \underset{k_1^-}{\overset{k_1^+}{\rightleftharpoons}} CO^{*} \tag{5}$$

The equilibrium for this reaction is found by Eq. 6 and written in Eq. 7.

$$\frac{d\theta_{CO}}{dt} = 0 = k_1^+ P_{CO} \theta_* - k_1^- \theta_{CO} \tag{6}$$

$$K_{CO} = \frac{k_1^+}{k_1^-} = \frac{\theta_{CO}}{P_{CO}\theta_*} \tag{7}$$

Where K_{CO} is the equilibrium constant for adsorption of CO molecules to the active sites, k_1^+ and k_1^- are the forward and reverse rate constants for Eq. 5, respectively. P_{CO} is the partial pressure of CO, and θ_{CO} and θ_* are the fractional of coverages of CO and free active sites, respectively. Similar equations are set up for hydrogen in Eq. 8-10, where we assume that an equilibrium between gas phase hydrogen molecules and adsorbed hydrogen atoms is established.

$$\frac{1}{2} H_2(g) + {}^{*} \underset{k_2^-}{\overset{k_2^+}{\rightleftharpoons}} \theta_H \tag{8}$$

$$\frac{d\theta_H}{dt} = 0 = k_2^+ P_H^{½} \theta_* - k_2^- \theta_H \tag{9}$$

$$K_H = \frac{k_2^+}{k_2^-} = \frac{\theta_H}{P_{H_2}^{½}\theta_*} \tag{10}$$

Taking the presence of these two species on the Rh surface into account, the fraction of free sites can be calculated from the partial pressures of CO and H_2. The number of free sites is given by Eq. 11 and the equilibrium constants in Eq. 12.

$$\theta_* = \frac{1}{1+\frac{\theta_{CO}}{\theta_*}+\frac{\theta_H}{\theta_*}} = \frac{1}{1+K_{CO}P_{CO}+K_H P_{H_2}^{½}} \tag{11}$$

$$K_x = A_x \cdot \exp\left(\frac{-\Delta H_x}{RT}\right) \tag{12}$$

The reaction kinetics of the steam reforming or CO_2 reformation reactions can then be calculated using Eq. 4, where the number of free sites is found by combining Eq. 11 and 12. This overall rate is given by Eq. 13 corresponding to the equation obtained in our study of the kinetics of steam reforming over ruthenium-based catalysts [10].

$$rate = \frac{A_1 \cdot \exp(\frac{-E_1}{RT}) \cdot p_{CH_4} \cdot (1-\beta)}{\left(1+A_{CO} \cdot \exp\left(\frac{-\Delta H_{CO}}{RT}\right) p_{CO} + A_H \cdot \exp\left(\frac{-\Delta H_H}{RT}\right) p_{H_2}^{½}\right)^2} \tag{13}$$

A_x is the prefactor for the CO and H equilibrium constants, and ΔH_x is the adsorption enthalpy. We assume that at the temperatures studied in this paper, the water gas shift reaction is in equilibrium at all conditions in accordance with the results obtained in this study and in previous studies of this reaction [19]. We observed that a pretreatment procedure at high temperatures was necessary to obtain stable catalytic activity. The catalyst partly deactivates during the pretreatment procedure and hence the activity is not the same for each set of experiments. The procedure ensured that the catalyst was stable (±15%) but at different activity levels. It is of course not ideal to have this

difference in absolute activity. However, a similar deactivation phenomenon has previously been observed for rhodium-based, catalytic partial oxidation (CPO) catalysts [20,21]. The authors proposed that defect Rh sites favor carbon deposition reactions which predominantly occur in the medium temperature regime of 500-700°C. High temperature treatment at 850°C for several hours reduces the problem, but they showed that an initial deactivation occurred even at this high temperature, and a continuous re-activation was observed for several hours. The authors proposed that steps and kinks play an important role for the phenomena and that the high temperature treatment reduces the number of surface defect sites, and thereby reduce the carbon deposition reactions [20,21].

Our investigations support the observations of the deactivation phenomena found at the medium temperature range of 500-700°C. Neither our studies nor the studies by Beretta et al. [21] found that activity was reduced in a similar manner for each individual experiment. The differences between the absolute activities for the different set of experiments were included in the modeling procedure by using a factor multiplied to A_1 in Eq. 13, when modeling the experimental data. These factors were determined by standard measurements before and after each experimental series.

4. Results

Modeling of the results is divided in two parts for steam reforming and CO_2 reforming, respectively, to distinguish between the differences in the modeling of these types of experiments.

4.1 Steam reforming

In the following, we report on our findings for the kinetics of steam reforming of CH_4 using a 1.0 wt% Rh/ZrO_2 catalyst (10.6% dispersion). All steam reforming data are modeled together. The

results obtained by modeling of the 62 steam reforming experimental measurements using Eq. 13 are given in table 1 and Fig 1-4.

Table 1. Results of fitting the overall rate model to the experimental data. In total 62 steam reforming measurements were fitted by the model. The prefactor, activation energy and adsorption parameters are provided by the reaction rate model. The corresponding sums of squares (SSQ) as given by Eq. 3 are also shown.

Reaction species in denominator of θ_*	A_1 [mol/g/h/bar]	E_1 [kJ/mol]	A_{CO} [bar^{-1}]	ΔH_{CO} [kJ/mol]	A_H [$bar^{-½}$]	ΔH_H [kJ/mol]	SSQ [$\%^2$]
Clean surface	$2.04 \cdot 10^9$	147.7	-	-	-	-	2556
CO and H	$6.89 \cdot 10^6$	89.2	$2.29 \cdot 10^{-5}$	-126.6	$1.99 \cdot 10^{-5}$	-82.1	30.29

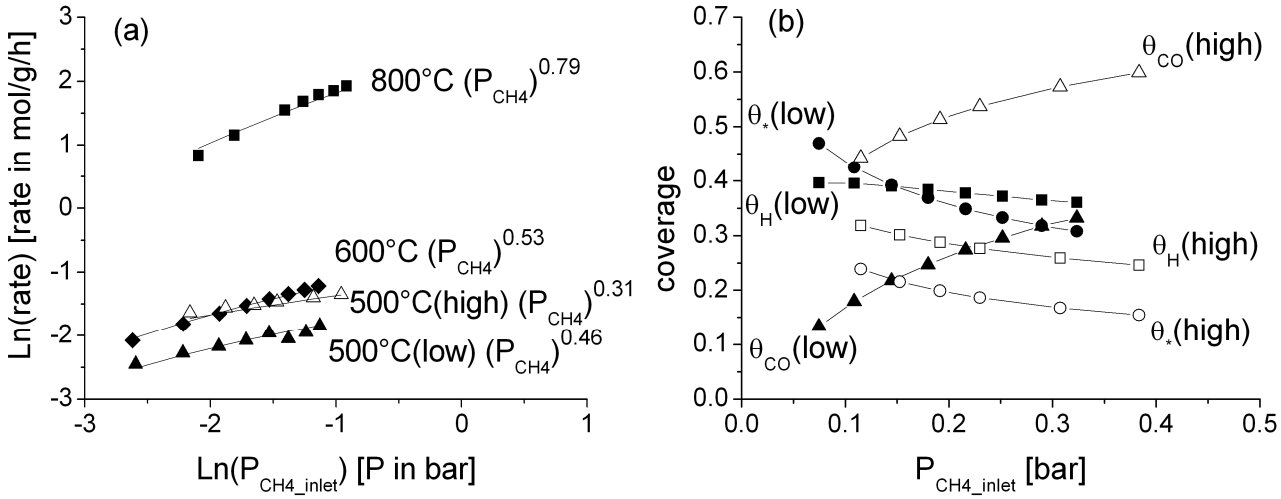

Figure 1. (a) Comparison between the model and the measured overall apparent CH_4 steam reforming rates. The observed reaction orders of methane are shown. The inlet pressure of H_2O was 0.66 bar and N_2 was used as the balance. (b) The average CO and H coverages based on the model are shown for low and high conversions at 500°C, respectively.

In table 1 we compare the results obtained using a simple first order dependency with no coverage dependence to those obtained by Eq. 13. As shown by the big difference in SSQ, a simple first order model is too simple to give a reasonable fit to the data. The data in Fig. 1 (a) also show that we cannot use the simple first order rate expression to explain the experimental results obtained here as the reaction order in methane partial pressure should in that case be one. The observed reaction order in methane increases with temperature and decreases with conversion. These observations are ascribed to indirect effects of changes in CO and H coverages. When comparing experiments at 500°C for high (9-22%) and low (5-11%) conversions, the effect of higher CO and H_2 partial pressures for higher conversions results in a lower observed reaction order in methane. This can also be seen by the CO and H coverages in Fig. 1 (b), where there are significantly more free sites for the low conversions than the high conversions. Similarly, orders increase with temperature in the observed reaction as the coverage of CO and H decreases with T. The observed reaction orders in methane are only phenomenological as the reaction is temperature and coverage dependent.

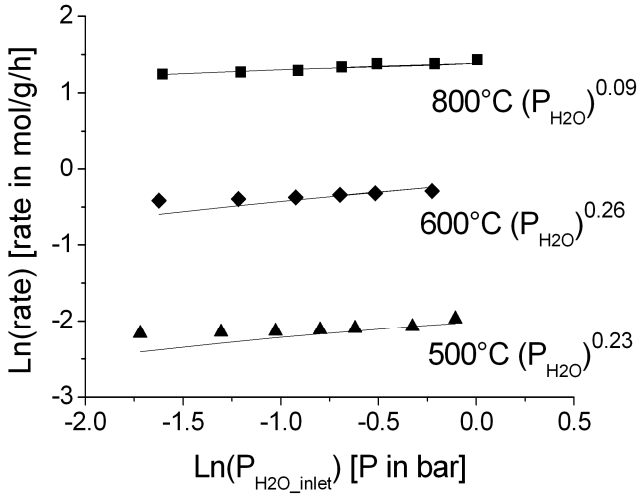

Figure 2. Comparison between model results and experimental data. Overall apparent CH_4 steam reforming rate plotted as a function of the partial pressure of steam with 0.17 bar CH_4 and balance N_2.

The effect of steam partial pressure on the reaction rate was rather small as shown in Fig. 2. There was a reasonable agreement between the modeled results and the experimental data. The effect of steam corresponded to previously observed results for rhodium steam reforming catalysts, where steam was found to have a minimal effect on the steam reforming rate [18,19].

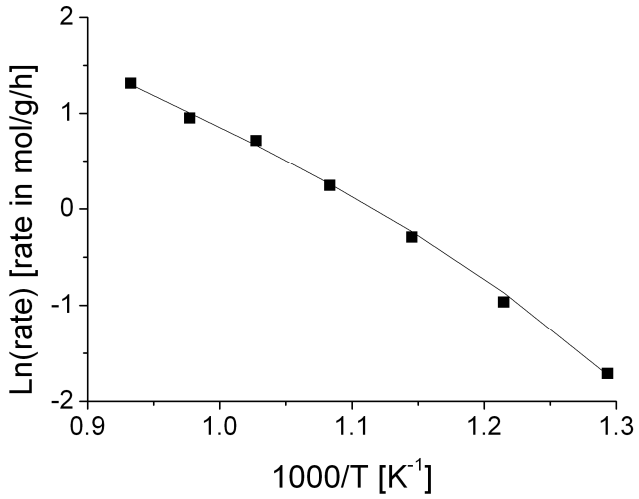

Figure 3. Observed temperature dependency of the steam reforming rate plotted as a function of 1000/T. The gas composition consists of 0.8 bar H_2O, 0.2 bar CH_4 and balance N_2.

The temperature dependency on the rate is shown in Fig. 3. The results are obtained in the temperature range of 500-800°C with corresponding conversions between 3% (500°C) and 62% (800°C). The change in temperature, CO and H partial pressures give a slightly curved graph when plotting ln(rate) vs. 1/T. In a typical Arrhenius plot, the gradient can be converted to an observed activation energy. Here the observed activation energy can be estimated to vary between 91 kJ/mol (500°C) and 46 kJ/mol (800°C). These values are valid for the specific conditions used in this experimental set, but serve as a good indication of the difficulty in estimating the activation energy. Detailed modeling as shown here is critical to describe the change in the reaction rate with temperature.

Finally, the effect of H_2 at low temperature was measured. Additional hydrogen was added at the reactor inlet to obtain higher H_2 partial pressures through the reactor. As shown in Fig. 4 the model and the experimental data both show a clear negative effect of hydrogen on the methane steam reforming rate. This was ascribed to the adsorption term for hydrogen in Eq. 13.

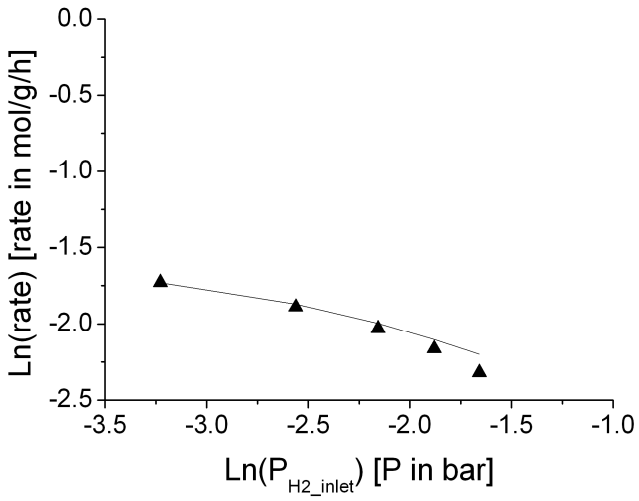

Figure 4. Comparison between model results and experimental data. Average CH_4 steam reforming rate as a function of the inlet H_2 partial pressure. (0.8 bar H_2O, 0.17 bar CH_4, balance N_2)

4.2 CO_2 reforming

We attempted to model the CO_2 reforming data with the model obtained by fitting the steam reforming data, but the model gave too low activities. The most likely explanation is that the model fails to take the effects of surface coverage on the CO adsorption energy into consideration. One way to solve this apparent discrepancy was to adjust the CO adsorption energy and take the remaining values in the models from table 1. This procedure will be justified in the discussion section. The CO_2 reforming data at 500°C and 600°C can be modeled well with an average CO adsorption energy that is 16.3 kJ/mol lower than that obtained from the steam reforming data with low CO levels. As shown in Fig. 5, the model gives a good description of the experimental data.

The average CO coverage is between 0.75 and 0.8, and minimal H coverages for all the CO_2 reforming experiments are obtained.

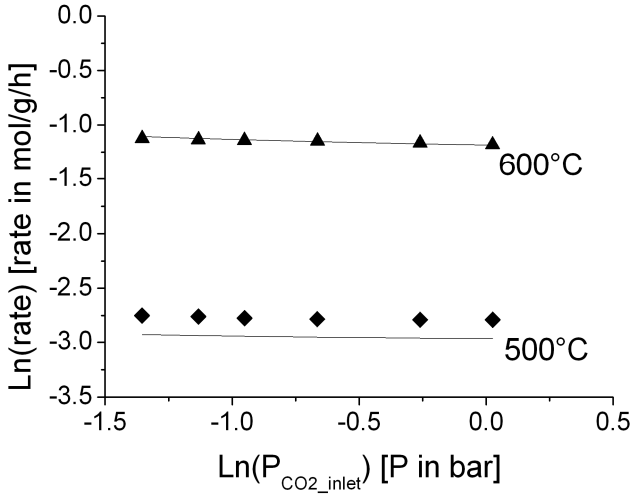

Figure 5. Comparison between model results and experimental data. Average CO_2 reforming rates as a function of inlet CO_2 partial pressure. 0.2 bar CH_4, N_2 balance. The model is given by Eq. 13 and the data in table 1, except ΔH_{CO} = -110.3 kJ/mol.

5. Discussion

Several different kinetic models for steam and dry reforming over Rh based catalysts have been published. Both empirical overall kinetic models [19,22-24] and micro-kinetic models [18,25] have been reported in the literature. When applying detailed kinetic modeling, it is necessary to have a very detailed understanding of the surface sites on the catalyst. In this investigation the focus was on determining the main trends for the steam reforming reaction and relate that to the CO_2 reforming experiments.

The first order in methane observed in other studies [18,19] is also valid for our experimental data when taking product inhibition into consideration. H_2O and CO_2 do not directly influence the reaction rate, although there may be an indirect influence through the production of CO and H_2 via the shift reaction. The adsorbance of CO and H, which is used on our model to describe the steam reforming kinetics on rhodium, is similar to the adsorbents used in the kinetic model developed in a

paper by Maestri et al. [19]. They find that both CO and H_2 influence the reaction rate. This is due to the adsorption of CO and H that both have a significant influence at low temperatures (<600°C). The influence of CO and H_2 was reported to be neglectable by Wei and Iglesia [18] at 600°C. This is most likely due to the high temperature and possibly very low conversions used in their study. The inhibition effect of CO on rhodium-based steam reforming catalysts is also been noted elsewhere [4,25]. The adsorption energy estimated here was 126.3 kJ/mol for steam reforming at low CO coverage, in good agreement with other reports [26,27]. Studies of Rh catalysts at ambient conditions show that there is a significant CO coverage at temperatures of around 450°C [26]. Dulaurent et al. show both linear and bridged CO species at 450°C by in situ infrared spectroscopy when exposing a Rh catalyst to a 1%CO/He gas mixture at atmospheric pressure. The CO coverage was approximately 65% at these conditions. The model by Dulaurent et al. and the model obtained in this study approximately predict a 30% CO coverage at 500°C at typical experimental conditions used in the present investigation (0.18 bar CH_4, 0.72 bar H_2O, balance N_2, total pressure 1.3 bar, 7% conversion)

The CO adsorption energy shows to depend on the CO surface coverage [26,28]. The initial adsorption energy is determined to 165-175 kJ/mol [28] on a Rh/Al_2O_3 catalyst and 195 kJ/mol for another Rh/Al_2O_3 catalyst [26]. Higher coverages are also interesting to review due to a significant amount of CO in the gas phase in the experiments. In Fig. 6 the CO adsorption energy is shown as a function of CO coverage for rhodium [28]. For a Rh/Al_2O_3 catalyst, a plateau between θ = 0.05-0.6 shows a constant adsorption energy (115-120 kJ/mol) and at higher coverages (θ = 0.6-0.9) this levels off to approximately 95 kJ/mol [28]. These numbers agree well with our observations at different plateaus and the relative difference in adsorption energy at low and high coverage of approximately 16 kJ/mol found in our modeling of the steam and CO_2 reforming experiments.

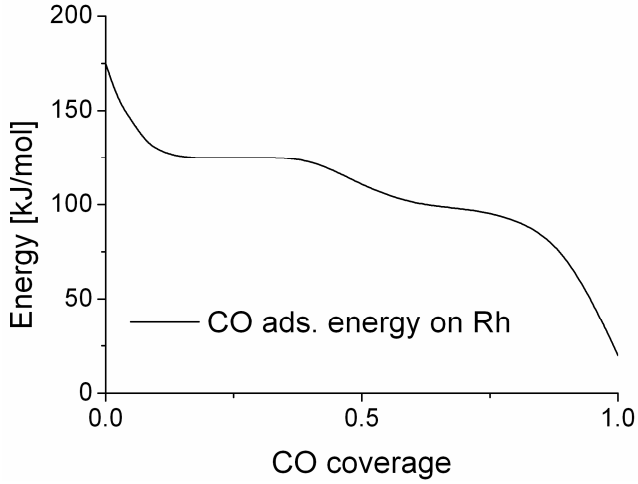

Figure 6. The CO adsorption data for Rh/Al_2O_3 [28].

We found experimentally that there is a stronger adsorption of CO on Rh than on Ru. On Ru we found a CO adsorption energy of 87 kJ/mol, where the adsorption energy was largely controlled by CO_2 reforming experiments with an average CO coverage of 0.4-0.5 [10]. It was not necessary to take the adsorption energy dependency of the CO coverage into consideration for the Ru kinetics, probably because the coverages of CO on Ru were below 0.5 during CO_2 reforming and very low CO coverages in the steam reforming experiments. The adsorption energy of CO on Ru corresponded well with other high CO coverage adsorption energies for Ru [10].

The stronger adsorption of CO on Rh than on Ru is also evident from temperature-programmed desorption (TPD) experiments at similar conditions. On single crystal closed packed surfaces, CO are adsorbed on Ru(0001) [30] and Rh(100) [31]. The experimental conditions are almost equal, making ground for a fair comparison. In Fig. 7 the CO TPD experiments with medium and high initial coverages are shown. The relative strength of CO adsorption on Ru and Rh is supported theoretically by adsorption and desorption calculations on closed packed surfaces at low coverages. These show that CO binds more strongly to Rh than to Ru [32].

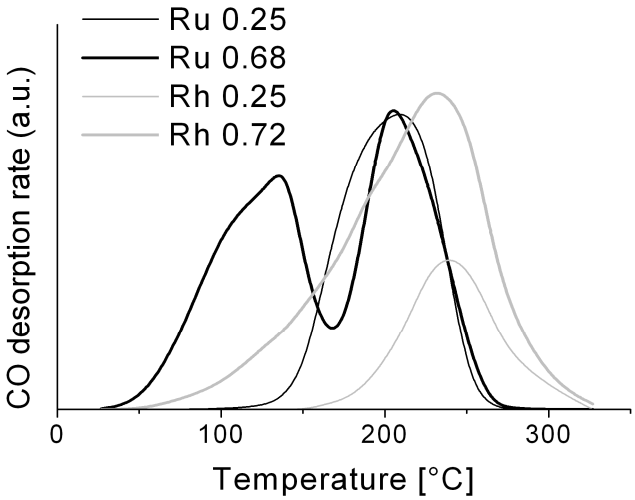

Figure 7. CO TPD data for Ru(0001) [30] and Rh(100) [31]. CO is pre-adsorbed at temperatures below -143°C for both sets of experiments. Initial CO coverages of 0.25 and ~0.7 (0.68 for Ru and 0.72 for Rh) were used. β = 5 °C/s.

Hydrogen adsorption also has an effect on the overall activity, but to a smaller extent than CO. This also limits the effect of the adsorption energy as a function of coverage. The adsorption energy of hydrogen have been reported to be up to 80 kJ/mol at low coverages and level out to approximately 35-50 kJ/mol at a coverage of θ = 0.4-0.6 [28]. For H chemisorbed at the conditions present in these experiments, no experiments are reported. However, detailed DFT and kinetic modeling were carried out and it is estimated that there is a significant coverage of hydrogen on rhodium at atmospheric pressure of H_2 at 500°C [33]. These models were confirmed by experimental TPD and metal-hydrogen binding energies [33].

The coadsorption of CO and hydrogen was included in the model, whereas any interaction was disregarded. Studies of coadsorption of CO and hydrogen on Rh(100) show that hydrogen is destabilised and that some of the hydrogen desorbs at a lower temperature [31]. When there are a low number of free sites, the surface will predominantly be covered by CO. Our model predicts that

the coverages for the two species, CO and H, are similar at steam reforming conditions as shown on Fig. 1(b), but that CO is dominating for CO_2 reforming conditions.

Different values of the activation energy for steam reforming were reported: we show that while the model had an activation energy of 89 kJ/mol, the observed activation energy was in the range of 46-91 kJ/mol for our reaction conditions. Wei and Iglesia's study found an activation energy of 109 kJ/mol [18] for an assumed clean surface, which is not too far from what we found in this study. Maestri et al. included coverage effects in determining the activation energy and estimated an activation energy of 62 kJ/mol at $\theta_{CO} = 0.15$ and $\theta_H = 0.2$, which corresponds well with our observed values that also include a partly coverage of CO and H.

6. Conclusions

This investigation contributes to the understanding of the methane steam reforming kinetics for rhodium-based catalysts. The reaction was first order in methane, but was strongly influenced by CO and hydrogen adsorbing to the surface. This product inhibition was especially important at temperatures of 500-600°C and at high conversions. A good model for our steam reforming experiments is given by Eq. 14. The rates of CO_2 reforming cannot be described by the equation below. This is ascribed to a coverage dependence of the CO adsorption energy reported in the literature. Instead, it was necessary to lower the energy of CO adsorption by 16 kJ to model our CO_2 reforming experiments.

$$R = \frac{6.89 \cdot 10^6 \left[\frac{mole}{g \cdot h \cdot bar}\right] \exp\left(\frac{-89[kJ/mole]}{RT}\right) \cdot P_{CH_4} \cdot (1-\beta_{SR})}{\left(1 + 2.29 \cdot 10^{-5}\left[bar^{-1}\right] \exp\left(\frac{127[kJ/mole]}{RT}\right) \cdot P_{CO} + 1.99 \cdot 10^{-5}\left[bar^{-1/2}\right] \exp\left(\frac{82[kJ/mole]}{RT}\right) \cdot P_{H_2}^{1/2}\right)^2} \quad (14)$$

Acknowledgement

Our work has been financially supported by the Danish Agency for Science Technology and Innovation. CINF is funded by the Danish National Research Foundation.

Reference List

1. J.R. Rostrup-Nielsen, Catal. Today 63 (2000) 159-164.

2. J.R. Rostrup-Nielsen, J. Sehested, J.K. Nørskov, Adv. Catal. 47 (2002) 65-139.

3. J.R. Rostrup-Nielsen, in Catalysis - Science and Technology, eds. J.R. Anderson and M. Boudart (Springer, Berlin, 1984)

4. J.R. Rostrup-Nielsen and J.-H.B. Hansen, J. Catal. 144 (1993) 38-49.

5. E. Kikuchi, S. Tanaka, Y. Yamazaki, Y. Morita, Bull. Jpn. Pet. Inst. (1974) 95-98.

6. D. Qin and J. Lapszewicz, Catal. Today 21 (1994) 551-560.

7. J.R. Rostrup-Nielsen, J. Catal. 31 (1973) 173-199.

8. G. Jones, J.G. Jakobsen, S.S. Shim, J. Kleis, M.P. Andersson, J. Rossmeisl, F. Abild-Pedersen, T. Bligaard, S. Helveg, B. Hinnemann, J.R. Rostrup-Nielsen, I. Chorkendorff, J. Sehested, J.K. Nørskov, J. Catal. 259 (2008) 147-160.

9. J.M. Wei and E. Iglesia, J. Catal. 224 (2004) 370-383.

10. J.G. Jakobsen, T.L. Jørgensen, I. Chorkendorff, J. Sehested, Appl. Catal. A 377 (2010) 158-166.

11. R.N. Bhat and W.M.H. Sachtler, Appl. Catal. A 150 (1997) 279-296.

12. H.Y. Wang and E. Ruckenstein, Appl. Catal. A 204 (2000) 143-152.

13. M.J. Hei, H.B. Chen, J. Yi, Y.J. Lin, Y.Z. Lin, G. Wei, D.W. Liao, Surf. Sci. 417 (1998) 82-96.

14. J.F. Munera, L.M. Cornaglia, D.V. Cesar, M. Schmal, E.A. Lombardo, Ind. & Eng. Chem. Res. 46 (2007) 7543-7549.

15. J.F. Munera, S. Irusta, L.M. Cornaglia, E.A. Lombardo, D.V. Cesar, M. Schmal, J. Catal. 245 (2007) 25-34.

16. M.C.J. Bradford and M.A. Vannice, Catal. Rev. – Sci. & Eng. 41 (1999) 1-42.

17. P.O. Graf, B.L. Mojet, J.G. van Ommen, L. Lefferts, Appl. Catal. A 332 (2007) 310-317.

18. J.M. Wei and E. Iglesia, J. Catal. 225 (2004) 116-127.

19. M. Maestri, D.G. Vlachos, A. Beretta, G. Groppi, E. Tronconi, J. Catal. 259 (2008) 211-222.

20. A. Beretta, T. Bruno, G. Groppi, I. Tavazzi, P. Forzatti, Appl. Catal. B 70 (2007) 515-524.

21. A. Beretta, A. Donazzi, G. Groppi, P. Forzattl, V. Dal Santo, L. Sordelli, V. De Grandi, R. Psaro, Appl. Catal. B 83 (2008) 96-109.

22. D.A. Hickman and L.D. Schmidt, AIChE J. 39 (1993) 1164-1177.

23. A.B. Mhadeshwar and D.G. Vlachos, J. Phys. Chem. B 109 (2005) 16819-16835.

24. R. Schwiedernoch, S. Tischer, C. Correa, O. Deutschmann, Chem. Eng. Sci. 58 (2003) 633-642.

25. I. Tavazzi, A. Beretta, G. Groppi, P. Forzatti, J. Catal. 241 (2006) 1-13.

26. O. Dulaurent, K. Chandes, C. Bouly, D. Bianchi, J. Catal. 192 (2000) 262-272.

27. D.N. Belton and S.J. Schmieg, Surf. Sci. 202 (1988) 238-254.

28. A. Maroto-Valiente, I. Rodriguez-Ramos, A. Guerrero-Ruiz, Catal. Today 93-5 (2004) 567-574.

29. G. Rotaris, A. Baraldi, G. Comelli, M. Kiskinova, R. Rosei, Surf. Sci. 359 (1996) 1-9.

30. H. Pfnur, P. Feulner, D. Menzel, J. Chem. Phys. 79 (1983) 4613-4623.

31. M.M.M. Jansen, J. Gracia, B.E. Nieuwenhuys, J.W. Niemantsverdriet, Phys. Chem. Chem. Phys. 11 (2009) 10009-10016.

32. E.D. German and M. Sheintuch, J. Phys. Chem. C 112 (2008) 14377-14384.

33. F. Faglioni and W.A. Goddard, J. Chem. Phys. 122 (2005) 14704.